REDUCING MOISTURE-CONTENT VARIATIONS IN KILN-DRIED TIMBER

J.J. Nijdam

A Thesis Submitted in fulfilment of the requirement for the Degree of Doctor of Philosophy in Chemical and Process Engineering to the University of Canterbury.

Department of Chemical and Process Engineering
University of Canterbury
1998

ACKNOWLEDGMENTS

I wish to thank my supervisor Professor R.B. Keey for his valuable guidance and support throughout the course of this research. He proved to be a mine of incredibly useful information and continually amazed me with his awesome grasp of the English language. I would never have used words such as 'whilst' and 'whence' if it were not for him.

I would also like to express my gratitude to Dr J.C.F. Walker for his support in a number of my endeavours, and for his infectious enthusiasm. He encouraged me to see matters from a more practical perspective which helped me to keep my focus on the research goals of this work.

My sincere thanks are due to Dr T.A.G. Langrish for being a surrogate co-supervisor. He jump-started my research progress on numerous occasions with his ever-ready and intelligent advice. The use of his super-duper computer is very much appreciated.

I also wish to thank the departmental technicians for their time spent constructing the hydraulic kiln. Frank Weerts deserves particular mention for his hard work and skill.

Finally, I am especially grateful to my parents, siblings, and friends for their moral support and encouragement, and without whom it would have been considerably more difficult to finish this work.

CONTENTS

SUMMARY

This thesis examines the kiln drying of timber with particular reference to *Pinus radiata*, a highly permeable softwood which is the most important commercially grown species in New Zealand. It is the aim of this thesis to develop new methods, or suggest improvements of existing methods, for reducing the variability in moisture contents of kiln-dried timber.

In the first stage of this thesis, the high-temperature drying of *Pinus radiata* was modelled. New gaseous diffusion and liquid permeability models were developed, and the moisture-transport mechanism between irreducible saturation and fibre saturation was elucidated. The simulations were compared with experimental data from the literature to validate the model. The predicted temperature and average moisture content profiles with respect to time were in good agreement with the experimental data. Comparison between the experimental and predicted within-board moisture content profiles illustrated the importance of accounting for heterogeneities due to the presence of growth rings, and their effect on density and liquid permeability, in modelling the drying process.

Following from this work, the kiln-wide drying behaviour of timber was examined by developing a rigorous batch-drying model which coupled the high-temperature drying model with a turbulent flow model. Thus, temperature, humidity, and moisture content fields throughout a timber stack and with time could be determined. This model was used to evaluate the accuracy of a simplified kiln model. One assumption associated with the simplified model is that the characteristic drying curve, which describes the internal drying behaviour of the timber, is independent of the external flow conditions. The simulations showed that leading edge effects invalidate this assumption for the first two or three boards from the leading edge, although the assumption is valid over the remaining boards. Thus, the simple model should accurately describe the kiln-wide drying behaviour for most of the timber in stack provided that variations in the mass-transfer coefficients are considered. The thickness of the board was shown to affect the magnitude of the critical point. Moreover, the two-dimensional nature of the moisture transfer in a stack also influences the magnitude of the critical point. On the other hand, two-dimensional effects in single-board laboratory tests are more severe than are found in a typical timber stack. Thus, kiln-stacking arrangements should be borne in mind when conducting and analysing single-board laboratory tests.

The drying of stacked *Pinus radiata* boards was investigated by the use of the simplified kiln model which incorporated airflow reversals. Only one reversal is needed to reduce significantly both the drying time and variations in the extent of drying through the stack. Variations in moisture content of the boards are caused by the progressive humidification of air and the maldistribution of airflow. These variations are predicted for two existing kilns for which their respective flow distributions are known from kiln audits. The use of airflow reversals is more effective than increasing the air flowrate in reducing the moisture variations caused by air humidification. However, increases in flowrate reduce moisture variations caused by

airflow maldistribution more significantly than reversals. The calculations illustrate the effect of air bypassing the stack in limiting the drying process.

Even drying of stacked timber boards in a kiln depends, amongst other things, on having a uniform airflow through the pile. A study of airflow maldistribution in existing kilns has been carried out using a Perspex model of a kiln, with water as the fluid, which has been designed to be geometrically similar to an actual kiln and have dynamically similar flows. Measurements of local velocities were possible by tracing the flow of fine gas bubbles. The standard kiln arrangements result in significant recirculation zones before the stack, with a non-uniform incident velocity profile. Different design alternatives for the geometry of the plenum spaces on either side of the stack have been investigated. The recirculation zone can be eliminated by streamlining the sharp right-angled turn to the plenum space from the ceiling space, where the fan is located. This method is only effective when the plenum-space width is less than or equal to the height of the ceiling space.

Conformal transformations were used to determine the flow patterns of irrotational flow through a right-angled bend and a sudden contraction. This work has applications for designing timber kilns with reduced non-uniformity of flow across the face of the timber stack. An entrance length equal to the width of the plenum chamber is required between the right-angled bend and the top of the timber stack to reduce the velocity distribution across the width the plenum chamber below 5%. This result is based on the assumptions that the flow path is streamlined so that boundary-layer separation does not occur, and that the Reynolds number is high so that the boundary layer hugs the walls very closely and the flow in the mainstream is irrotational.

The final part of this thesis evaluates the performance of a one-dimensional mathematical model for flow through a timber-drying kiln. There was close agreement between theory and experiment. This model was used to develop recommendations for the design of the plenum chambers on either side of the timber stack. A width of the plenum chambers equal to the sum of the thickness of the fillets was shown to be effective in reducing flow maldistribution across timber stacks in single-track kilns. The width of the plenum chambers of double-track kilns may be reduced to three-quarters of the sum of the thickness of the fillets, because the increase in timber-stack resistance to airflow mitigates the effect of pressure variations down the vertical length of the plenum chambers.

CHAPTER ONE

INTRODUCTION

Wood is humankind's oldest natural resource. Because of its wide distribution, ready availability, variety of uses, and relative ease in handling and conversion, wood has been indispensable since humans existed on earth. Early humankind could not have survived without wood for fuel, for construction of shelter, and for making weapons for protection and to hunt food. Today, wood is no less important with a myriad of wood-based products being produced by a wide range of wood-conversion processes. In fact, the worldwide demand for wood is increasing (Food and Agriculture Organisation of the United Nations [1993]). Consequently, the need for a thorough understanding of wood, its properties and ways it is grown and converted are becoming increasingly important.

The utilisation of wood as a raw material or in a finished product depends to a great extent on the physical properties of the material. Wood is very strong, yet light in weight and is therefore an extremely useful building material. Moreover, the attractive colours and grains in wood, as well as its ease of cutting and fabrication, make it an ideal medium for artists, craftsmen, and designers, in whose work appearance is of paramount importance.

Of the many types of wood products available today, timber (lumber) is probably the most familiar. It is a versatile material, adapted to a multitude of uses and applications, although a large portion is used for residential and commercial construction (Walker [1993]). In New Zealand, 3.0 million m^3 of sawn timber were produced in 1997. This compares with the pulp industry (3.8 million m^3) and log exports (5.6 million m^3) which utilised the greatest shares of wood (NZ Forest Owners Association [1997]). Clearly, the business of converting trees into timber occupies an important place in the industrial economy, and it is probable that timber will continue to be an important wood product from a volume standpoint for many years to come. The three main activities associated with timber production are sawing, grading, and drying (seasoning). In this thesis, the drying process is of primary concern.

1.1 Moisture in Wood

The honeycomb structure of wood allows it to hold large amounts of water, as much as two or three times the weight of the wood substance itself. A freshly felled tree is usually in a practically green condition, which means that the moisture content is very high. The moisture content of wood is important because it affects properties such as the strength, insulation, durability and machined surface quality of the wood.

Moisture is present in green wood in two forms: it fills or partially fills the cell spaces, and it is present in the cell walls. The amount of moisture held in the cell walls is roughly the same for all timber species - approximately 30% of the dry weight of wood at room temperature. This moisture is usually referred to as 'bound' moisture to distinguish it from 'free' water which occurs in the cell voids and makes up the remaining moisture content of wood. The fibre saturation point is defined as the moisture content of wood at which the cell walls are saturated with bound moisture but no free water remains in the cell voids. This moisture content is important because timber begins to shrink as moisture is lost below fibre saturation owing to a loss of moisture in the cell wall.

There are various reasons why much of the moisture must be removed before timber is used.

1) The presence of moisture in the cell walls causes them to swell such that the microfibrils of the cell walls separate. Dried wood has lost most of the water molecules in the cell wall structure, and therefore the microfibrils of the cell walls draw closer together, forming a stiffer and generally stronger material. It is therefore beneficial to remove all of the free water and most of the bound moisture by drying wood, which improves its strength and durability.

2) Wood shrinks when dried below fibre saturation point, and if it is not dried prior to being put into service, the shrinkage occurring in fabricated items or structures can be quite damaging. The wood must be dried as closely as possible to the moisture content it will assume in use if dimensional changes are to be minimised.

3) Because it is an organic material, wood is subject to attack by wood-staining or wood-destroying fungi, and insects. The organisms which cause such degradation will not normally live in timber which has a moisture content below 20%. Furthermore, they will not usually survive exposure to temperatures in excess of 50 °C (Brown *et al.* [1958]). Therefore, if wood is dried at high temperatures, then the portions which are already infected with organisms will be sterilised, and the low final moisture content will ensure that the wood is less prone to degradation while it is in use.

4) Wood which is used in damp conditions must be treated with a preservative if it is to last for any length of time. Preservatives, to be effective, must penetrate the surface of the wood for some distance to prevent fungi from infiltrating and growing from within. In order that preservatives may enter the wood, at least all of the free water and much of the bound moisture must be removed (Evans [1995]).

5) The weight of wood is greatly reduced when dried because the water in green wood sometimes comprises over half its total weight. The lighter weight not only makes handling of the timber easier, but also reduces shipping costs.

6) Wood must be dry if it is to take paints, to be polished or glued, as very few finishes and glues will adhere properly to a wet surface.

The reasons for drying wood may then be summarised as follows: (1) to increase its strength and stability, (2) to improve its resistance to decay, (3) to help it absorb preservatives more readily, (4) to reduce its weight, and (5) to allow it to take paints, polishes, and glues if necessary.

The most common methods of drying timber are to either air season or kiln dry. Both methods rely on the circulation of air over the surfaces of the timber to evaporate and remove moisture. The advantage of kiln drying timber is a faster drying rate compared with air drying, because the circulation of air over the timber surfaces is considerably more rapid, and higher temperatures cause the moisture within the timber to move more quickly to the surface from which it can be evaporated. For some species, the drying time can be reduced from months for air seasoning to a matter of days for kiln drying (Walker [1993]).

A further advantage of kiln drying is that conditions can be closely controlled to minimise the drying time and drying defects. Air seasoning of wood is dependant on the vagaries of wind, sun and rain, and so is extremely difficult to control. The various types of dry kilns commonly used for the drying of timber are equipped so that the temperature, relative humidity and velocity of the air in contact with the timber can be closely controlled.

1.2 Forced-Circulation Kiln

A kiln is a chamber, for containing stacked timber to be dried, provided with means for heating the air and circulating it through the timber stack. Provision is also made for humidifying the air so that the rate of evaporation may be kept within safe limits to avoid degrade due to differential shrinkage of the timber. The most common type of kiln is the forced-circulation kiln which provides air movement by the action of fans which force air through the load of stacked timber. Air circulation serves the dual purpose of conveying heat to the timber boards and carrying off moisture which has been evaporated.

Figure 1.1 shows the cross-sectional view of a typical forced-circulation kiln with overhead fans. Air passes through the fans, turns by 90 degrees, and enters vertically into the space between the chamber wall and the timber stack, which is usually referred to as the plenum chamber. The function of the plenum chamber is to distribute the air evenly into the spaces separating the timber boards. By reversing the direction of the fans periodically, the air can be delivered into the plenum chambers on the either side of the timber stack. This is essential for reducing the moisture content variation across the stack. After passing through the timber stack, the air returns to the top of the kiln where it is reheated, dehumidified and recirculated. Fresh air is taken in and spent air exhausted via vents on the roof. The chief function of ventilation is to remove hot, moisture laden air from the kiln and to replace it with fresh, cold air to lower the relative humidity in the kiln to a point where timber drying can proceed.

Modern kilns are generally constructed from insulated aluminium panels on an internal or external frame of aluminium or steel. The foundation of the kiln is usually

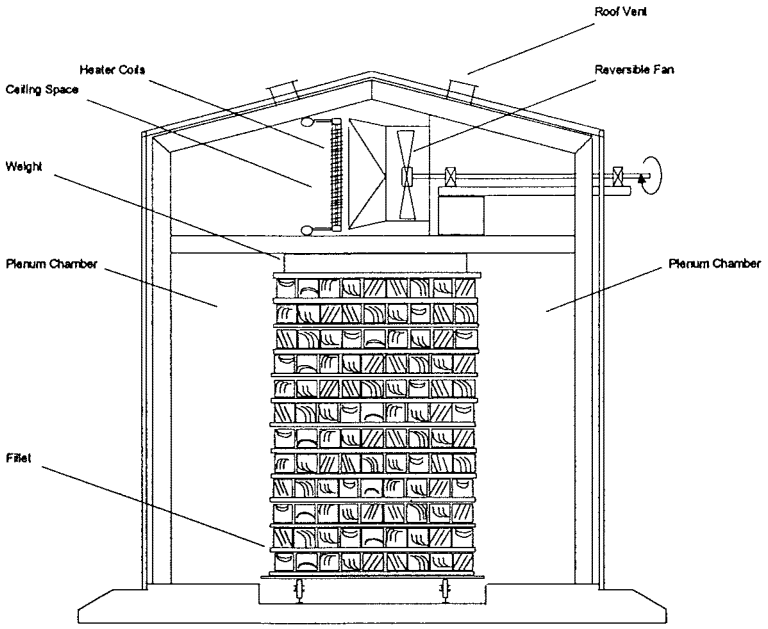

Figure 1.1. A kiln holding a stack of stickered timber.

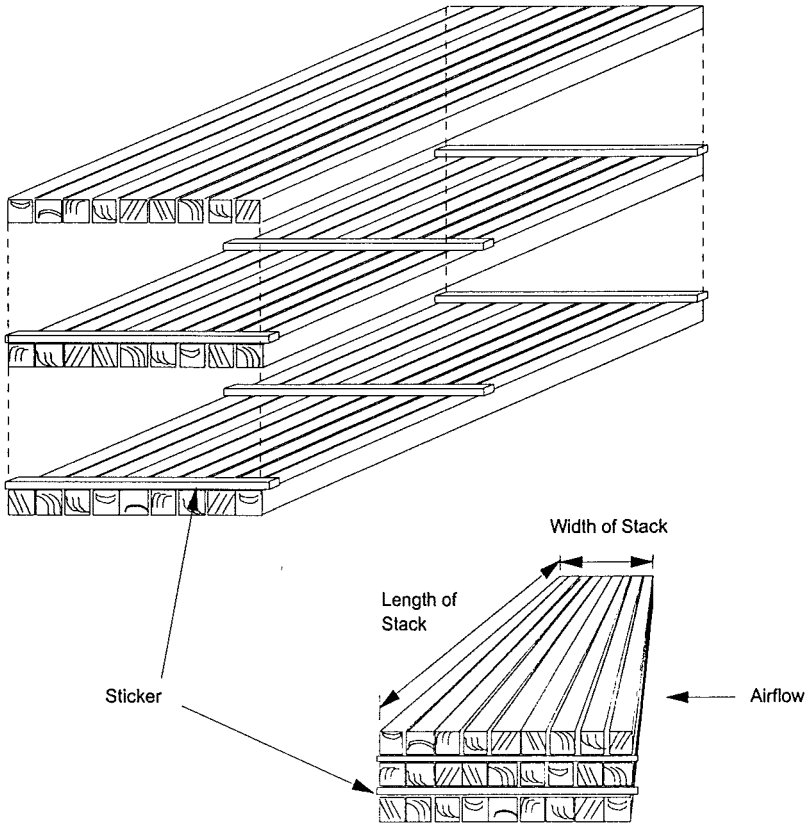

Figure 1.2. A small timber stack: exploded and isometric views.

concrete. The most common kiln design in New Zealand accommodates a single rail track mounted with a 2.4 m wide stack of timber on a trolley (Ministry of Forestry [1996]). In general the dimensions of a kiln taking a stack of timber 2.4 m wide and 3.5 m high, is 5m from floor to ceiling and 4.5 m in width. The kiln width includes the stack plus two plenum chambers about 1m wide on either side of the stack. The length of the kiln is determined by the range of timber lengths to be dried. For example, timber which is predominantly 6 m in length will require a kiln length in multiples of 6 m, plus an allowance for gaps and minor length variations.

Kiln conditions are usually controlled automatically. Thermostats are used to automatically control and record dry and wet-bulb temperatures. Changes in the temperature at the control bulbs result in the activation of electrically driven motor valves. One motor valve controls stream flow into the heating coils, another controls the flow of steam or water used for humidification, and a third controls the opening and closing of the vents. These instruments maintain the temperature and humidity as constant as possible throughout the kiln.

Kilns are normally classified according to their temperature operating range. Conventional kilns operate at temperatures below 100 °C, whereas high-temperature kilns operate with air temperatures exceeding 100 °C but usually below 150 °C in New Zealand. High-temperature drying can significantly reduce the drying time and save energy compared with conventional kilns. However, due to drying defects such as checking and distortion, the high-temperature drying process has been restricted to permeable softwoods such as *Pinus radiata*. Kiln schedules are employed, which in some cases consist of a series of dry and wet-bulb temperature changes so that the driving force for moisture evaporation from the surface is increased in a step-wise fashion. Thus, the timber is dried at a satisfactory rate without causing objectionable drying defects, which is especially important during the early stages of drying when timber is prone to degrade (Brown *et al.* [1958]).

1.3 Timber Stack and Baffles

The objective when stacking timber is to maximise the volume of timber put into the kiln, while giving a uniform airflow through the fillet spaces and restraining all boards. Unless good timber-stacking techniques are employed, the timber may well leave the kiln with an undesirable range of moisture contents, and unnecessary degrade. The usual method of stacking is to arrange the boards in horizontal layers one above the other, separated by a series of cross-piling sticks (called stickers or fillets). Figure 1.2 shows a typical stacking arrangement. Fillets are normally made of 20-25 mm by 30 mm well-seasoned, straight-grained timber that is free from resin that might stain the timber boards. Within a particular layer, the fillets are spaced at intervals of 300 to 900 mm depending upon the thickness of the wood and its tendency to distort. Each line of fillets is aligned vertically and is fully supported by a bearer on the kiln trolley so that the weight of the stack is directly transmitted through the lines of fillets to the bearers below. Poor alignment of the fillets can cause kinking in the timber.

The sides of the stack are made as even as possible with no boards jutting out appreciably into the plenum chambers. Misaligned boards tend to act as air deflectors causing an excess of air to pass through one or two spaces at the expense of others. It is also important to sort the lengths of timber when handling boards of uneven length. A square-ended, even-sided stack will ensure uniform flow through the timber stack and reduce drying degrade. The last step is to weight the top of the stack with concrete slabs or other suitable materials to help minimise the amount of distortion in the otherwise unrestrained top rows.

The use of baffles is important in preventing air from short circuiting around the timber stack (Culpepper [1990]). Baffles are installed at the ends of the stack (to allow for length variation), on both sides of the stack below the partition separating the stack from the ceiling space (to allow for stack height variation), and in the space between the trolley and the floor. Thus, the spaces around the timber stack are closed off with snug-fitting baffles so that air is forced through the fillets, and very little bypass of air around the stack can occur.

1.4 The Tree

A thorough understanding of the process of timber drying requires knowledge of the structure and physical characteristics of wood. The basic composition of wood determines its relationship to water and its response to drying. Knowing the role that the wood structure plays in the drying process can help determine appropriate drying conditions. It can also provide explanations for certain drying effects.

Trees have three main parts: the roots, the trunk, and the leaves (Desch [1953]). The roots anchor the tree in the ground, and take in water and mineral salts in dilute solution from the soil. The trunk conducts these solutions from the roots to the leaves, it stores food materials, and it has mechanical rigidity, supporting the leaves above competing vegetation. The leaves absorb gases from the atmosphere and, with energy obtained from sunlight, manufacture complex organic substances for carrying on the life process.

The trunk is of primary interest in this thesis. The trunk has an outer covering, called bark, which protects the wood from extreme temperatures, drought, and mechanical injury. Between the bark and the wood is a thin, delicate tissue, known as the cambium which forms a sheath around the trunk and branches. This tissue produces bark towards the outside and wood towards the inside of the tree. The increase in diameter of the trunk and branches is caused by the activity of the cambium sheath.

Under the bark is a cylinder of wood. The wood of trees grown under seasonal conditions consists of a series of concentric layers of tissue called growth rings. These rings, which are produced by the cambium, extend the full height of the tree, with a new layer being added each growing season. Growth rings are apparent because the wood produced at the beginning of the growth season is different in character from that formed later in the season. Thus, the zones of earlywood and latewood may be distinguished.

The work of food storage and sap conduction is performed by the outer-growth layers which are known as sapwood. The central part of the tree provides mechanical rigidity to the trunk and is known as heartwood. Heartwood in *Pinus radiata* contains dead cells with much less moisture than sapwood, since it no longer takes part in the active upward transport of water, and is usually darker in colour because any remains of stored food material are converted to tannins and other substances which tend to be coloured (Brown [1965]).

Internal Structure

Commercial timbers fall into two main groups: softwoods and hardwoods. The former are conifers or cone-bearing plants, characteristically with needle-shaped leaves with 'naked' seeds; the latter are characterised by broad leaves, and seeds which are enclosed in a seed-case. The terms 'soft' and 'hard' is a misnomer since hardwoods are not necessarily harder than softwoods. However, there is a distinct difference in the structures of hardwoods and softwoods. This thesis is concerned with softwoods, specifically *Pinus radiata.*

Wood is built of individual units called cells (Figure 1.3). There are several different types of cell which may be present. In softwoods, the moisture conducting and mechanical support functions are performed by a single type of cell called a tracheid. Tracheids form approximately 95% of the total wood volume in *Pinus radiata* (Kininmonth [1991]). They are hollow, closed, needle-shaped units which are relatively long and narrow (generally 1-5 mm in length by about 0.04 mm in width). Tracheids are closely packed together so that a cross section through them resembles a honeycomb.

In the living tree, water is transported up the tree towards the leaves by moving from one tracheid to another through bordered pits in the cell walls. These bordered pits, which connect adjacent tracheids, appear as disks with an impermeable central area, known as the torus, and a web-like region surrounding the torus called the margo (Figure 1.4). The cell wall of the pit overarches the central membrane with dome-like structures, which exist on both sides of the pit, that have apertures (openings linking the lumen to the pit chamber) which are smaller than the diameter of the torus (Figure 1.5). The liquid in the lumen of a tracheid can flow through the pit aperture, the margo, and the following pit aperture, and enter into the lumen of the adjacent tracheid. Moisture movement through the bordered pits is controlled by the torus, which can move from side to side to regulate the pit opening. The torus is able to move so as to completely seal off one of the pit apertures (Figure 1.4). This process is called pit aspiration and is irreversible. It is the trees natural defence, when it has been injured in some way, to protect wood in areas adjacent to the damaged regions.

The thickness of the cell walls and size of the cell cavities vary depending on the location of the cell within the tree and its purpose. In the tree, the thin-walled tracheids with large cavities are primarily concerned with the conduction of sap, and the thick-walled ones with maintaining mechanical rigidity, although the latter may also play some part in conduction. The thin-walled, conducting tracheids are laid down at the beginning of the growth season, when the water requirements of the

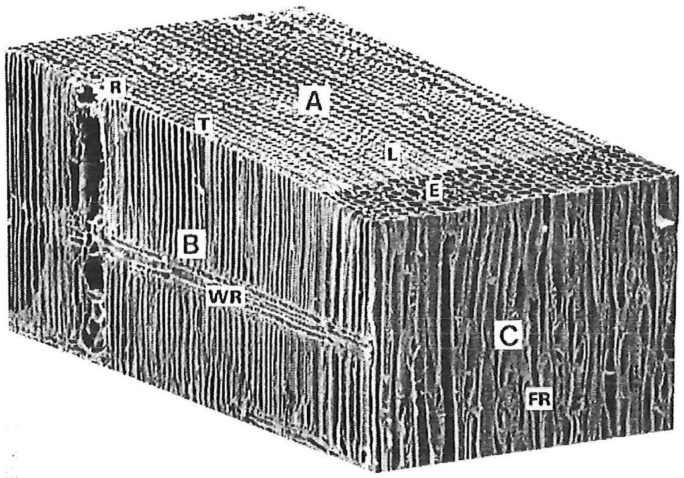

Figure 1.3. The microstructure of *Pinus radiata* wood in three directions (after Kininmonth *et al.* [1991])

Face A, Transverse: T-cut ends of tracheids; L-latewood; E-earlywood; R-resin canal
Face B, Radial/longitudinal: WR-wood ray
Face C, Tangential/longitudinal: FR-fusiform ray

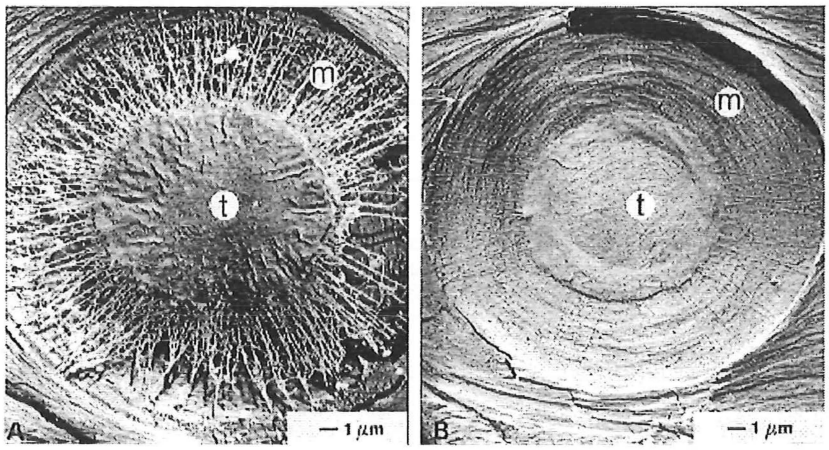

Figure 1.4. Bordered pit membranes in the earlywood tracheids of *Pinus radiata* sapwood: unaspirated (left), aspirated (right); t-torus; m-margo.

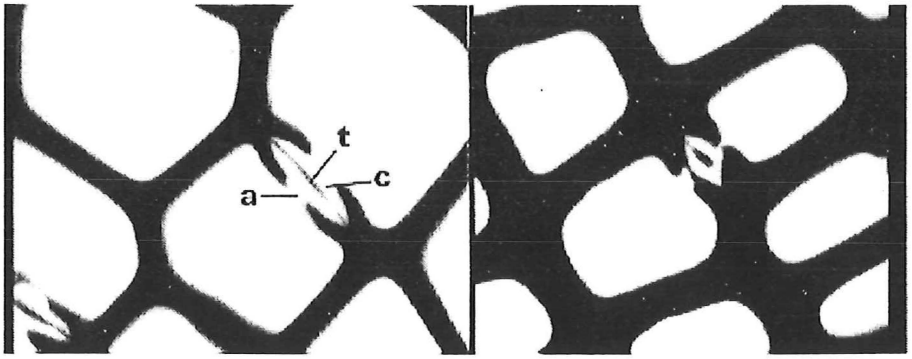

Figure 1.5. A bordered pit between two tracheids in *Pinus radiata*: earlywood (left), latewood (right); a-pit aperture; t-torus; c-pit chamber.

leaves are at a maximum, whereas the thick-walled strengthening tracheids are formed later. Thus, alternating zones of thin and thick-walled cells are present which are visible to the naked eye as earlywood and latewood (Figure 1.3). Earlywood is lighter because it contains a smaller proportion of the wall substance and is therefore less dense.

The other important cell in softwood is the ray parenchyma or wood ray (Figure 1.3). These cells are brick-shaped with relatively thin walls and numerous pits. They occur in narrow, horizontal bands which radiate outwards from the centre of the tree to the bark. Their function is to store food, and to convey liquids in the radial direction. Wood rays account for only a small fraction of the wood volume in *Pinus radiata* (approximately 4%); however, they contribute in a significant but not major degree to the conduction of moisture during the seasoning process (Stamm [1964]).

Pinus radiata also contains resins canals, which are continuous tubes extending both vertically in the stem and horizontally in the rays (Figure 1.3). They occupy only 1 % of the wood volume (Panshin *et al.* [1964]) and are almost always clogged with resin. Therefore, resin canals are, in general, ineffective for movement of fluids in the living tree (Stamm [1964]) and during seasoning.

1.5 Problems in Drying

The major problems associated with kiln drying, especially under high-temperature drying conditions, are (1) uneven moisture-content distributions due to variations in timber properties (primarily permeability) from board to board, flow maldistribution across the stack, and progressive humidification of air through the stack, and (2) the development of drying defects such as checking and distortion which is caused by rapid drying rates. All these problems will be discussed in turn below, although this thesis is concerned with final moisture-content variations which result from flow maldistribution and progressive humidification of air through the stack.

Permeability

The variation in the internal structure of the timber will affect the permeability of wood to both liquid and gas flows, and hence the ease of drying. Heartwood has a lower initial moisture content, but the wood is less permeable and liquid flow is insignificant due to the extent of pit aspiration in the greenwood (Booker [1990]). In contrast, the permeability to liquid flow is higher for the much wetter sapwood because almost all of the bordered pits in the tracheid walls of green sapwood are open. They only aspirate when moisture is lost. When the board consists of both sapwood and heartwood, the moisture movement becomes complicated as some moisture migrates through the heartwood layer while other moisture moves across the sapwood zone (Pang [1994]).

Booker [1990] has observed that permeability varies with direction (radial, tangential, and longitudinal), so that timber orientation in the different sawn direction will also affect the drying behaviour of the board. Since the radial permeability to liquid flow in green sapwood is much lower than that in the tangential direction, when a board is

exactly flat-sawn, the liquid flow perpendicular to the airflow direction may not be as high as that in a quarter-sawn board. Another factor which affects the drying behaviour of wood is the progressive aspiration of bordered pits as green sapwood is dried, which effectively reduces the permeability of the timber (Walker [1993]). In addition, the permeability of earlywood to liquid water is greater than for latewood, and therefore the seasoning process will be affected by the distribution and orientation of growth rings within the boards.

Flow Maldistribution

One necessary condition for producing evenly dried timber is to ensure that the air velocity is uniform across the stack. Good baffling systems, and regular stacking arrangements will reduce, to a certain extent, the degree of flow maldistribution across the stack (Culpepper [1990]). However, the presence of the abrupt right-angled turn from the ceiling space into the inlet plenum chamber which occurs in most existing kilns, and the branching points at each fillet location make flow maldistribution unavoidable. Several studies have shown how special equalising and distribution devices, and sufficiently smooth transitions from the ceiling space into the plenum chamber may be employed to minimise flow maldistribution across the stack (Kröll [1978], Sturany [1952], and Werner [1958]). However, these techniques are quite often impractical due the shear size of most industrial-scale kilns which makes it difficult to install distribution devices, or manufacture contoured plenum chambers and ceiling spaces.

Thus, criteria have been developed for the design of box-shaped plenum chambers to reduce flow maldistribution across the stack (Arnaud [1991], Kröll [1978]). These criteria usually specify minimum geometric ratios; for example, a general rule of thumb is that the plenum chambers should be at least equal to one-third of the stack height in width to ensure even air flow across the stack (Ministry of Forestry [1996]).

Progressive Humidification

As the airstream sweeps over the rows of boards, moisture is picked up by the air and, hence, the humidity of the air increases and its temperature drops. Thus, the driving forces for heat and mass transfer decrease in the airflow direction. Moreover, the local heat and mass-transfer coefficients decrease exponentially from a peak value at the inlet face of the stack (Kho *et al.* [1989]). These variations in the external conditions and in the transfer coefficients result in non-uniform drying rates and a subsequent poor distribution of final moisture along a row of boards. The boards near the air offtake dry more slowly than those at the air intake, and therefore the final moisture content of the timber boards near the leading edge of the row of boards is usually much lower than at the trailing edge. Switching the fan direction over so that air flows in the opposite direction through the stack will mitigate these effects. Thus, the drying rate becomes enhanced over the wetter section of the boards, and retarded over the drier portions (Keey [1992], Pang [1994]).

Timber Degrade

Kiln drying involves the removal of moisture from the surfaces of pieces of timber. This means that the surfaces exposed to the air must inevitably dry faster than the interior portion of the wood. Thus, the surface will shrink before the centre. Moreover, when timber dries it does not shrink by equal amounts in all directions. Shrinkage is not the same in the different grain directions (Brooke *et al.* [1997]). The greatest shrinkage occurs in a direction tangential to the growth rings. The shrinkage in a radial direction is nearly always considerably smaller than the tangential shrinkage, whilst the shrinkage along the grain is very small and can usually be neglected. Differential shrinkage caused by moisture-content gradients, and differences in shrinkage along the three directions are practically entirely responsible for all the warping and checking that occurs in timber. These drying defects represent a loss of board quality since the tensile strength is reduced, and the appearance of the material is spoiled.

1.6 Overview of the Problem

This thesis is concerned with the reduction of variability in final kiln-wide moisture-content variations resulting from non-uniform airflow across the stack, and progressive humidification of air through the stack. Stress development in timber drying is outside the scope of this work, although some of the ideas that are presented in this thesis could be useful in the development of a comprehensive stress-strain model. In particular, it is the aim of this thesis to improve on existing methods, or develop new methods, for designing kilns and kiln schedules which optimise the drying process. These methods will then be used to explore possible design options, which could be incorporated into new kiln designs and kiln schedules.

The problem may be divided into two parts: the *drying problem*, and the *external-flow problem*. The *drying problem* involves the development of kiln schedules that reduce final moisture-content variability across the timber stack. Thus, the effect of airflow reversals and air-circulation speed on moisture-content variations caused by flow maldistribution and progressive humidification will be investigated. This requires knowledge of the transfer processes that occur within both the timber and the external airflow, and their relationship to each other. The *external-flow problem* examines the effect of kiln geometry on the uniformity of flow across the stack. If the kiln can be designed to reduce flow maldistribution across the timber stack, then final moisture content variations will likewise be reduced.

Two strategies have been employed in the past for analysing the *drying problem* using computational techniques. Workers such as Ashworth [1977] and Pang [1994] have employed batch-drying calculations, which depend upon lumped-parameter models of the moist timber, for investigating the effect of airflow reversals and air-circulation speed on moisture-content variation. Other workers such as Pang [1994], Stanish *et al.* [1986], Plumb *et al.* [1985], and Perré *et al.* [1993] have simulated the internal heat and moisture movement in timber using more rigorous transport-based drying models. Both lumped-parameter and transport-based models have proved useful for analysing the performance of kiln schedules.

The *drying problem* has also been investigated experimentally by Pang [1994] and Northway [1989]. These workers monitored the temperatures at different depths of a board to give temperature variations both with distance from the surface and with elapsed time. Changes in average moisture content were also monitored by measuring the sample's weight during drying. Pang [1994] used his experimental results to test his transport-based drying model.

Until recently, the *external-flow problem* has been investigated experimentally by only a few workers such as Arnaud [1991], Kröll [1978], Sturany [1952], and Werner [1958]. Computational fluid dynamics (CFD) methods have not been possible until recently owing to the complexity of the underlying behaviour, which precluded a description of fluid flows that was at the same time economical and sufficiently complete. However, the availability of affordable high-performance computing hardware and the introduction of user-friendly interfaces, such as CFX and Fluent, have made it possible to calculate the complex flows generated in kilns. Workers such as Arnaud [1991] and Langrish [1992] have pioneered CFD analysis of fluid flow in kilns.

The next sections give a brief literature survey of the previous work done by various researchers on the *drying problem* and the *external-flow problem*, and explains how this work is extended in this thesis.

Lumped-Parameter Model

Van Meel [1958] derived a simple set of differential equations to model convective batch drying by assuming that a common normalised curve could describe the variation of drying rates with moisture content throughout the whole dryer. This curve has become known as the characteristic drying curve. Ashworth [1977] studied the concept of the characteristic drying curve extensively to determine its validity. He concluded that the concept was useful for slabform materials, such as timber boards, provided the characteristic drying curve was derived from data on material of the same thickness.

Ashworth [1977] went on to solve the batch-drying equations numerically, using arbitrary characteristic drying curve functions to express the drying behaviour, and incorporating effects such as airflow reversals and flow maldistribution. He showed that a single early flow reversal is effective in smoothing the moisture-content distribution irrespective of the specific drying behaviour of the timber species. Pang [1994], using a similar approach, corroborated Ashworth's conclusions. He found that not many reversals were needed to reduce moisture content variations, and that the first airflow reversal is critical to reduce moisture-content variations. Pang found that a single reversal after 4 hours from the start of drying is adequate to give a reasonable degree of uniformity in the drying. However, this single-reversal policy was not optimised, and its effect on the drying time was ignored.

Steven and Johnstone [1957] showed experimentally that frequent airflow reversals do not necessarily reduce moisture-content variations across the stack. They state that the

advantages to be gained from airflow reversals is marked in the early stages of drying; however, once the surface moisture is evaporated and internal resistance becomes important, the advantages offered by air flow reversals diminish in value. This result agrees with the later conclusions of Ashworth [1977] and Pang [1994]. Clearly, the first reversal is critical to reduce moisture-content variations, and subsequent reversals become progressively less effective.

Ashworth [1977] suggested that flow maldistribution across the timber stack could be investigated by decomposing the stack into a number of smaller sections, the air velocity being constant for each section. The simple batch drying equations are then applied to each section. Using kiln-wide air velocity distributions found by Malmquist and Meichsner [1958], Ashworth illustrated the effect of flow maldistribution on the variation in moisture contents of the dried timber. He concluded that one necessary condition for optimising a kiln's performance is to ensure that the airflow is uniform across the stack.

Neither Pang [1994] nor Ashworth [1997] investigated the effect of bypass of air around the stack on the drying time and variability in moisture contents of the dried timber boards. Furthermore, no attempt was made by these workers to incorporate all of the major aspects of kiln drying, such as airflow reversals, airflow maldistribution, and bypass of air around the stack, into one model. Useful information about the influence of airflow reversals and air-circulation speeds on kiln-wide moisture content variations can be investigated using a comprehensive model of this type. In addition, optimum reversal policies can be determined, and the effectiveness of such reversal policies on a timber load with boards of varying density and green-moisture content evaluated. Some workers have recommended so-called 'hi-low' schedules that involve stepwise reduction in the airflow rate as the timber boards are dried (Bachrich [1980]). In these schedules, high airflow rates are used at the start of drying, when the external resistance to moisture movement controls the drying rate, and the airflow rate is reduced once the internal resistance of the timber board becomes predominant. The effectiveness of such schedules can also be investigated using the batch-drying equations.

Thus, one of the aims of this thesis is to develop a comprehensive kiln-wide model, based on Van Meel's batch-drying equations, which models the three-dimensional drying behaviour of a stack of timber. Within-board moisture-content profiles cannot be calculated using this approach. Nevertheless, this model is a useful tool for evaluating the performance of new schedules for kilns with flow maldistribution across the stack, bypassing air around the stack, variations in green moisture content and density, and in which progressive air humidification is an important element.

Transport Model

The analysis of the drying process within a board is usually conducted by solving transport equations for heat and mass transfer resulting from the differential balance laws. The geometric complexity of the solid matrix inside wood prevents a general solution of the detailed velocity and temperature field at the tracheid scale. Therefore, most workers use the continuum approach to describe physical phenomenon in timber

drying. The flow field is discretised into a number of elements each of which is small compared with the overall dimensions of the porous body, but large compared with the dimensions of the pores. Thus, the characteristic-length scale of the elements is significantly greater than the characteristic-length scale of the tracheids so that variations in fluxes in the microscopic scale (pore scale) become averaged at the macroscopic scale (elemental scale). Whitaker [1977] derived the transport equations at the elemental scale by averaging the transport equations at the microscopic scale over the element. Plumb *et al.* [1985], Stanish *et al.* [1986], Perré *et al.* [1993], and Pang [1994] have solved these macroscopic-scale equations in order to investigate the internal moisture and heat transport processes that occur when timber dries.

The results of these workers are essentially the same. They show that there is an initial constant-rate period when the drying rate is essentially independent of time and externally controlled by the rate of heat transfer to the wood surface. Moisture evaporates at the surface and free water moves from the interior to the surface through the capillary structure of the cell cavities and the interconnecting pits provided the pits are not aspirated and the moisture content is greater than the irreducible moisture content when liquid continuity ceases. The constant-rate period is followed by the first falling-rate period when the evaporation front retreats within the wood resulting in a wet core separated from the surface by dry zones on either side. In the dry zone, which is below fibre-saturation point, moisture migration is by bound-water diffusion across the cell walls and vapour diffusion across the cell cavities. In the wet zone, moisture migration is by capillary action. Eventually, the evaporative front recedes to the centre of the wood. This marks the start of the second falling-rate period when no free water remains in the wood and moisture migration takes place solely by bound-water diffusion and vapour diffusion, until the equilibrium moisture content is reached.

None of these workers have obtained satisfactory agreement between experiment and theory. One problem with the mathematical model is that the transport mechanisms have not been adequately described. In fact, there appears to be disagreement in the literature on which mechanisms are responsible for moisture transport between irreducible saturation, when liquid continuity ceases, and fibre saturation. Pang [1994] assumes that there is no transport of moisture between these moisture contents. Chen *et al.* [1996] assume that vapour diffusion is responsible for moisture movement between these points, while Perré *et al.* [1993] appears to rely on vapour diffusion, vapour-phase pressure-driven moisture fluxes, and liquid-capillary flows between irreducible and fibre-saturation point. Thus, another aim in this thesis is to elucidate the transport mechanisms between irreducible and fibre saturation, and to improve on existing flux models for the wet and dry zones.

Interfacial Phenomena

Masmoudi *et al.* [1991] developed a numerical method allowing heat and mass transfer between a porous medium and the external airflow to be determined. They simulated the drying process of a non-hygroscopic porous medium using Luikov's [1966] transport based model for capillary bodies, and the laminar boundary-layer equations for the external flow. The boundary conditions at the interface were the continuity of flux densities, and the no-slip condition for the external flow. No one has

attempted to simultaneously model the external and internal drying processes for timber. Such a rigorous model would be useful in testing the simplifying assumptions which were made in the development of Van Meel's [1977] batch drying equations. Therefore, an additional aim in this thesis is to couple the transport-based timber drying model developed by Whitaker [1977], with the external flow equations in the manner described by Masmoudi *et al.* [1991].

Experimental Flow Visualisation

Kröll [1978] has described a study of airflow in tray dryers using transparent models with water as the fluid. His flow visualisations show that a sharp right-angled bend, from the ceiling space into the inlet plenum chamber, induces a recirculation zone downstream of the bend that severely retards the flow through the uppermost gaps in the stack. According to Kröll, pressure variations down the length of the inlet plenum chamber are also responsible for variations in velocities between the fillet spaces. Flow guides, sloping walls, and various types of screens were placed within the inlet plenum chamber of his transparent model in an attempt to even the distribution of flows over the height of the stack. Sturany [1952] and Werner [1958] tried similar solutions to even the flow distribution across the stacks. These workers showed that a smoother transition in the right-angled bend removes the recirculation zone thereby improving the uniformity of flow across the stack.

Moreover, increasing the pressure drop across the stack of trays, by placing screens over the inlet face of the stack, was shown to effectively swamp the variations in pressure down the plenum chambers, thus improving the velocity distribution across the stack. The drawback of screens for improving flow uniformity is that they increase the pressure loss through the kiln, which affects the power requirement of the fan. Kröll [1978] has presented data for the pressure changes across various points along the circulation path in a kiln with a distribution screen placed in front of the inlet face of the stack. The pressure drop across the distribution screen was about 6 times larger than the pressure drop across the stack. Clearly, the power required by the fan will increase significantly with the inclusion of a distribution screen.

Kröll [1978] showed that curved flow guides, placed within the inlet plenum chamber, were quite effective in smoothing the transitions in flow direction and cross-sectional area. However, flow guides are difficult to install due to the size of most industrial-scale kilns. Therefore, the most effective method for reducing flow maldistribution across a timber stack is to change the size and shape of the plenum chambers on either side of the stack, and to prevent boundary-layer separation by smoothing the surfaces of the transitions. Thus, the problem is reduced to determining the geometric ratios of the important kiln dimensions, such as plenum-chamber width, ceiling-space height, fillet-space width, and radius of the rounded section, which will improve the uniformity of flow across the timber stack.

Kröll [1978] has also described the effect of plenum-chamber width on the velocity distribution. He states that the ratio of the plenum chamber width to the widths of the gaps between boards should be at least equal to unity to mitigate the effect of pressure variations down the length of the inlet plenum chamber.

Arnaud *et al.* [1991] also studied the influence of various geometric ratios on the velocity distribution across the stack. Their experimental work involved measuring the airflow across a stack of timber in a pilot-scale kiln using pitot tubes. The velocity field was visualised by photographing tufts tied on iron threads that stretched between the ceiling and floor. These photographs show large recirculation zones near the uppermost boards, which are generated by the sharp right-angled bend from the ceiling space into the inlet plenum chamber. The recirculation zones appear to shrink in size as the plenum-chamber width is reduced; however, the velocity distributions across the stack become more non-uniform. Arnaud *et al.* concluded that the plenum-chamber width should be at least equal to the height of the ceiling space in order to produce a uniform velocity distribution across the stack of timber.

Idelchik's [1991] investigation into pipe flows in right-angled bends suggests that the design criteria of Arnaud *et al.* can be improved upon. Idelchik shows that when the outlet width of a right-angled bend is greater than the inlet width, then flow separation at the corner worsens because the flow diverges in the expansion. He suggests that the corner be streamlined to eliminate flow separation, and that the outlet width of the right-angled bend be less than or equal to the inlet width so that the flow converges in the bend. This is exactly the opposite conclusion drawn by Arnaud *et al.* [1991]. Idelchik recommends that the radius of the corner be at least equal to one-quarter of the outlet width of the right-angled bend to eliminate the recirculation zone downstream of the bend.

Clearly, more work needs to be done to determine which policy is most effective in reducing flow maldistribution across the stack. In addition, more realistic design options than those suggested by Kröll [1978] need to be investigated, and the ideas of Idelchik [1991] for pipe flows in right-angled bends should be tested on the right-angled bends in a kiln. The aim of this section of the work is to broaden the current understanding of flow in batch-drying kilns by investigating flow phenomena in kilns over a wider range of flow conditions than described by Kröll [1978] and Arnaud *et al.* [1991]. It is also aimed to investigate realistic design options for reducing flow maldistribution across the timber stack.

Computational Fluid Dynamics (CFD)

Kröll [1978] has shown that the flow phenomena within a dryer can be elucidated by visual inspection of the flow patterns in a hydraulic model. Commercial CFD packages can also be used to model such flow patterns with relative ease compared with the experimental technique. However, assumptions are usually required in this approach to reduce the complexity of the system to a manageable level while preserving the salient features of the problem in hand. Moreover, a number of mathematical models of varying complexity are usually available in most commercial CFD codes. The appropriateness of the simplifying assumptions, and the accuracy of the mathematical model chosen governs to a great extent the quality of information generated by CFD. Thus, analysis of the flows by a CFD approach cannot be considered reliable until it has been verified by comparison with experimental work. Such data are scarce in the literature. Nijdam [1997] has shown that the experimental

data of Kröll for flow in a hydraulic model (presented in Charm [1963]) could not be predicted accurately using CFD since insufficient data were given about the geometry and flows within his hydraulic model. Therefore, the secondary aim of this study into the *external-flow problem* is to generate experimental data which can be used to test CFD predictions of the flow phenomena in kilns.

1.7 Scope

The purpose of this thesis is to develop new methods, or improve on existing methods, for reducing the variability in final kiln-wide moisture-content variations which result from non-uniform airflow across the stack, and progressive humidification of air through the stack.

The first two chapters are concerned chiefly with the internal drying kinetics of timber, and the effect of the external flow on such drying phenomena. In particular, Chapter 2 considers improvements to the one-dimensional, transport-based, timber-drying model developed by Pang [1994]. The validity of the new ideas developed in this chapter will be tested by comparing the theory with the experimental data of Pang [1994]. Chapter 3 will treat the simultaneous modelling of the internal drying kinetics of timber and the external flow phenomena. In this chapter, the improved drying model presented in Chapter 2 will be extended to the two-dimensional form so that the drying behaviour of a row of boards in a timber stack may be investigated. Although Masmoudi *et al.* [1991] assumed the flow was laminar, flow in a kiln is mainly in the turbulent regime. Therefore, the turbulent-flow behaviour will be modelled by including a turbulence model. A mass fraction and enthalpy equation are also necessary for modelling the humidity and temperature variations along the fillet spaces. One of the aims of this chapter is to investigate the validity of various assumptions made in the development of Van Meel's batch-drying equations.

Chapters 4, 5 and 6 involve the development of experimental and computational methods for analysing the effectiveness of kiln designs and schedules in reducing moisture content variability in dried timber. In Chapter 4, a comprehensive kiln-wide model will be developed which will account for bypass of air around the stack, flow maldistribution across the stack, and progressive humidification of air through the stack. This model will be used to investigate the effect of air speed and airflow reversals on final moisture-content variability. Chapter 5 redesigns the kiln to encourage an even distribution of flows from the top down to the bottom of the timber stack. The method of direct flow visualisation through transparent models, in which water takes the place of air, will be employed to determine the flow details. The advantage of this method is that both qualitative and quantitative data can be derived from the obtained flow picture with only minimal physical interference with the flow. Following from this work, Chapter 6 presents mathematical methods for the design of kilns.

Chapter 7 ties together the ideas presented in the previous chapters. It is the purpose of Chapter 7 to summarise the methods uncovered in this thesis for reducing the variability in moisture-content variations of kiln-dried timber.

1.8 References

Arnaud, G., Fohr, J.P., Garnier, J.P., Ricolleau, C., 1991, Study of the air flow in a wood drier, *Drying Technology*, 9 (1): 183-200.

Ashworth, J.C., 1977, The mathematical simulation of batch drying of softwood timber, PhD thesis, Department of Chemical Engineering, University of Canterbury, New Zealand.

Bachrich, J.L., 1980, Dry kiln handbook, H.A. Simons (Internal) Ltd, Vancouver, Canada.

Booker, R.E., 1990, Changes in transverse wood permeability during the drying of Dacrydium cupressinum and Pinus radiata, *NZ J Forest Science*, 20 (2):231-244.

Brooke, A.S., Langrish, T.A.G., 1997, The simulation of stresses and strains in the drying of *Pinus radiata* sapwood: the effects of board geometry, *Computers Chem.Engng.*, 21 (11):1271-1281.

Brown, W.H., 1965, An introduction to the seasoning of timber, Pergamon Press, New York.

Brown, N.C., and Bethel, J.S., 1958, Lumber, 2nd edition, John Wiley & Sons, Inc, New York.

Charm, S.E., 1963, The fundamentals of food engineering, The AVI Publishing Company, Inc., Westport, Connecticut.

Culpeper, L. 1990, High temperature drying-enhanced kiln operations, Miller Freeman Publications, Inc, San Fransico.

Desch, H.E., 1953, Timber: its structure and properties, MacMillan & Co Ltd, London.

Evans, J.M., 1995, The vapour boron timber treatment process, PhD thesis, Department of Chemical and Process Engineering, University of Canterbury, New Zealand.

Food and Agriculture Organisation of the United Nations, 1993, Forestry Statistics today for tomorrow:1961-1991-2010, Rome.

Idelchik, I.E., 1991, Fluid dynamics of industrial equipment: flow distribution design methods, Hemisphere Publishing Corporation, New York.

Keey, R.B., 1992, Drying of loose and particulate materials, Hemisphere Publishing Corporation, New York.

Kho, P.C.S., Keey, R.B., Walker, J.C.F., 1989, Effect of minor board irregularities and air flows on the drying rate of softwood timber boards in kilns, *Proc. IUFRO International Drying Symposium*, Seattle, Washington, 150-157.

Kininmonth, J.A., Whitemann, L.J., 1991, Properties and uses of New Zealand Radiata Pine, Vol 1, New Zealand Ministry of Forestry.

Kröll, K., 1978, Trockner und trocknungsverfahren, 2nd edition, Springer-Verlag, Berlin, Heidelberg, New York.

Langrish, T.A.G., Kho, P.C.S., Keey, R.B., Walker, J.C.F., 1992, Experimental measurements and numerical simulation of local mass-transfer coefficients in timber kilns, *Drying Technology*, 10 (3): 753-781.

Luikov, A.V., 1966, Heat and mass transfer in capillary-porous bodies, Pergamon Press, Oxford.

Malmquist, L., Meichsner, H., 1958, Investigations on high temperature kilns, Holz als Roh und Werkstoff, 16:263-273.

Masmoudi, W., Prat, M., 1991, Heat and mass transfer between a porous medium and a parallel external flow. Application to drying of capillary porous materials, Int J. Heat Mass Transfer, 34:1975-1989.

Ministry of Forestry and New Zealand Forest Research Institute Limited, 1996, Producing quality kiln-dried timber in New Zealand, NZFRI Ltd, Rotorua.

New Zealand Forest Owners Association, 1997, NZ Forestry Facts and Figures, Wellington, NZ

Nijdam, J.J., 1997, Flow Visualisation Data, Research Report, Chemical and Process Engineering, University of Canterbury, Christchurch, New Zealand.

Northway, R., 1989, Moisture profiles and wood temperature during very high temperature drying of *Pinus radiata* explain lack of degrade, Proceedings of the 2nd IUFRO International Wood Drying Symposium, Seattle, 24-28.

Pang, S., 1994, High-temperature drying of *Pinus radiata* boards in a kiln, Phd thesis, Department of Chemical and Process Engineering, University of Canterbury, New Zealand.

Panshin, A.J., Zeeuw, C.D., Brown, H.P., 1964, Textbook of wood technology, 2nd edition, McGraw-Hill Book Co., New York.

Perre, P., Moser, M., Martin, M., 1993, Advances in transport phenomena during convective drying with superheated steam or moist air, *Int. J. Heat and Mass Transfer*, 38 (11):2725-2746.

Plumb, O.A., Spolek, G.A., Olmstead, B.A., 1985, Heat and Mass transfer in wood during drying, *Int. J. Heat Mass Transfer*, 28 (9):1669-1678

Stanish, M.A., Schajer, G.S., Kayihan, F., 1986, A mathematical model of drying hygroscopic porous media, *AIChE J.*, 32(8):1301-1311.

Sturany H., 1952, Questions of flow in the drying of wood, *Holz als Roh-und Werkstoff*, 10 (5): 201-207.

Van Meel, D.A., 1958, Adiabatic convection batch drying with recirculation of air, *Chem. Eng. Sci.*, 9:36-44.

Walker, J.C.F., 1993, Primary Wood Processing, Chapman & Hall, London.

Werner, H., 1958, Methods of air and heat distribution in convective dryers, *Chem. Ing. Techn.*, 44 (8): 570-576.

Whitaker, S., 1977, Simultaneous heat, mass and momentum transfer in porous media. A theory of drying in porous media, *Advances in Heat Transfer*, 13:119-200.

CHAPTER TWO

TRANSPORT MODEL

2.1 Introduction

Radiata pine (*Pinus radiata*) is a commonly planted softwood in the Southern Hemisphere. The timber enjoys the reputation of being a species which can be rapidly and economically kiln-dried with little degrade provided good stacking and drying methods are employed. To comply with the latter criterion, kiln schedules must be designed which dry the timber boards uniformly in the shortest possible time, with acceptable quality, and with the least amount of energy use. A trial-and-error approach may be used by a kiln operator to determine a suitable drying schedule; however, this is a lengthy and expensive task. A reliable method is thus required to predict the moisture content and temperature fields as functions of time and various locations through a timber board for a particular schedule. These fields provide the basis for estimating stress development during drying. In this way, the performance of a given kiln-drying schedule may be evaluated.

Kilns for drying softwood timber boards operate across a range of temperatures. High-temperature kilns operate at dry-bulb temperatures above 100 °C, whereas conventional kilns operate at much lower temperatures (of order 60 °C). Accelerated conventional schedules use intermediate temperatures (of order 90 °C) and are favoured for appearance-grade timbers. High-temperature kiln drying offers the benefits of significantly reduced drying times and energy savings for framing and structural grades. However, harsher drying conditions can potentially result in more discolouration and more distortion of the timber boards and the development of internal and surface checks, offset by increased plasticity of the wood at the higher temperatures. A complete understanding of the mechanisms involved in the high-temperature drying process can aid in developing strategies to reduce such drying defects.

According to Pang *et al.* [1994], the process of high-temperature drying a highly permeable softwood like *Pinus radiata* can be divided into three periods. During the first and second periods there exists an evaporative plane at which all the free water evaporates. In the first period, the plane is located near the exposed surface, but in the second, this plane recedes into the material as drying proceeds. The evaporative plane divides the material into two parts: a wet zone within the core and a much drier zone in the outer portion. In the drier zone, moisture is assumed to exist as bound water and water vapour. Bound water will be in local thermodynamic equilibrium with the water vapour at the local temperature. The moisture content in this zone is less than the fibre-saturation moisture content. In the wet zone, moisture exists as unbound water, water vapour and bound water; however, only unbound water fluxes are considered

significant. The moisture content in the wet zone is higher than the moisture content at which the cell-wall tissue is saturated (fibre saturation). The third drying period begins when the evaporative plane has reached the mid-plane of the board. At this point, drying is controlled by bound-water and water-vapour diffusion.

There are several discrepancies between the predictions of Pang's mathematical model and available experimental data (Pang [1994], Northway [1989]). Firstly, Pang's model does not allow any transport of moisture between irreducible and fibre saturation. This assumption produces a sharp discontinuity in the within board moisture-content profile in which the moisture content jumps from below fibre saturation to a value above irreducible saturation. However, experimental moisture content profiles do not exhibit such discontinuity. This implies that a mechanism for moisture transport exists in this range of moisture contents. Secondly, Pang's model does not take account of shrinkage of the timber below fibre saturation which attenuates the moisture-vapour diffusion. This has a significant effect on the rate at which the evaporative plane can recede into the board. Finally, the experimental data of Tesoro *et al.* [1974] for liquid permeability above irreducible saturation show that more pits aspirate near green moisture content than expected from the permeability correlation used by Pang.

The aim of this chapter is to develop a more satisfactory drying model based on the models of Pang *et al.* [1994] and Stanish *et al.* [1986]. Special attention will be paid in the development of this model to the experimental temperature and moisture content profiles for the high-temperature drying of *Pinus radiata* obtained by Pang [1994] and Northway [1989]. The experimental data of Luikov [1966], Choong [1963] and Stamm [1959] will be used to improve the moisture flux ideas of Pang *et al.* [1994] and Stanish *et al.* [1986], and a model will be postulated to account for moisture flow between fibre saturation and irreducible saturation, where liquid continuity breaks down. The new high-temperature drying model will be validated against the experimental data of Pang [1994].

It is envisaged that at a later date, this model will be coupled with a stress-strain model as developed by Chen *et al.* [1997]. High-temperature drying schedules for softwoods can then be optimised to minimise degrade of the timber due to internal checking and warping in a similar manner to the optimisations for hardwoods by Langrish *et al.* [1997].

2.2 Aspects of Timber Drying

2.2.1 Heartwood and Sapwood

The principal feature of the anatomy of a softwood like *Pinus radiata* is the system of longitudinal hollow fibres known as tracheids which are aligned in the direction of the stem, and which can occupy up to 95% of the wood volume. Longitudinal tracheids have a number of pits on the cell walls whose function are to provide flow paths for liquids in the living tree. These pits appear as pit pairs, or bordered pits, with borders on either side of the double cell wall between adjacent tracheids.

The bordered pits are generally aspirated or closed for green heartwood *Pinus radiata*, and therefore the liquid flow in the wet zone during the drying process is very small in heartwood. Furthermore, the moisture content of heartwood is normally close to the irreducible moisture content where capillary-driven liquid flows cease due to a loss in continuity in the liquid flow path. Therefore, the first period in heartwood drying is very short and may be neglected. The pits in sapwood are usually not aspirated when the sapwood is green, since the pits are required for the transport of liquid nutrients, but aspirate only when the sapwood is damaged or dried. Moreover, the moisture content of sapwood is considerably higher than the irreducible moisture content by at least a factor of 2 to 3, so that significant liquid flows are possible within the wet zone during the first and second drying periods.

The experimental profiles of Pang [1994] support this view that significant liquid flows are possible only in sapwood. Figures 2.1 and 2.2 show the temperature and average moisture-content profiles for sapwood and heartwood boards, respectively. In the sapwood profiles, a quasi-steady state is reached in which the surface temperature rises to an asymptotic value well below the external air temperature and remains there for a short period (approximately 118 °C for Figure 2.1a, 98 °C for Figure 2.1b, and 110 °C for Figure 2.1c). This temperature eventually rises, marking the end of the first drying period and the beginning of the second drying period when the evaporative plane recedes into the board. No such quasi-steady state is observed in the heartwood profiles, which suggests that the evaporative plane recedes immediately into the board at the start of drying; thus, the first drying period is non-existent for heartwood. The evaporative plane is able to recede immediately in heartwood drying because there are no significant liquid flows in the wet zone to maintain the position of the evaporative plane near the surface. The difference between the drying behaviour of sapwood and heartwood is that liquid flow in the wet zone for sapwood has a significant influence on the time at which the evaporative front recedes and the velocity with which it recedes.

2.2.2 Damaged Surface Layer

During the milling process, the surface fibres of the timber boards are damaged and water can evaporate from these tracheids. The pits in the damaged tracheids are likely to be aspirated. Therefore, before the kiln-seasoning process even begins, an evaporative zone will be located a short distance into the board. This thin layer of surface fibres will be at a moisture content which is in equilibrium with the surrounding environment, while the rest of the timber will remain close to its green moisture content. Careful drying experiments with sapwood samples cut so that evaporation takes place at right angles to the growth rings have shown that the moisture content over the surface growth ring is low and remains constant while the core moisture falls (McCurdy [1998]).

Water-soluble materials and resins, which form a brown stain when exposed to oxygen (Evans *et al.* [1962]), are able to diffuse towards the surface as far as the evaporative front which marks the inner boundary of the damaged layer. Therefore, the position of the evaporative zone in the first period is rendered visible in practice

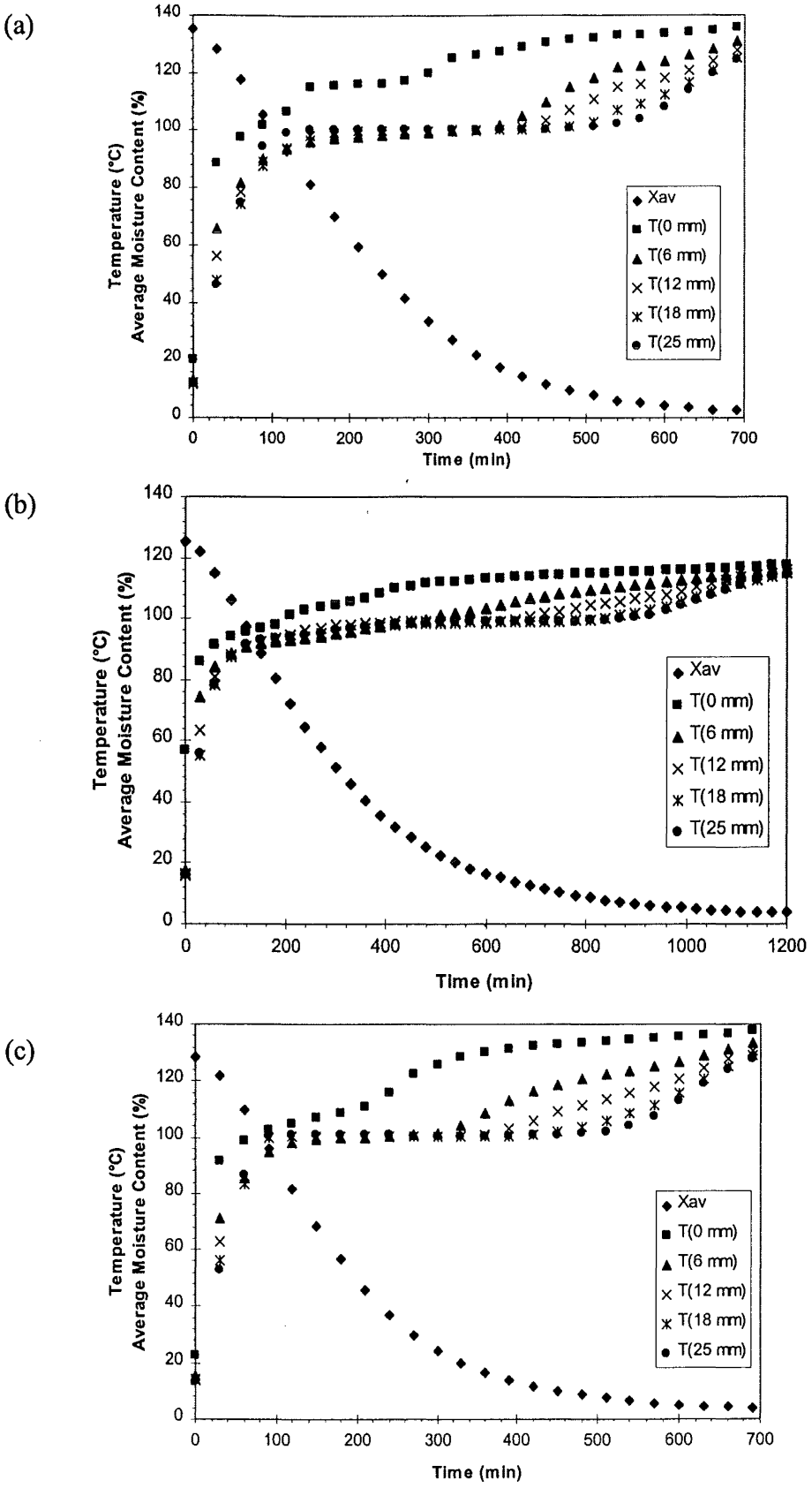

Figure 2.1. The temperature and moisture content profiles within a 50 m thick sapwood board: (a) 140/65 °C, air flow 5 m/s, dry density 438 kg/m^3
(b) 120/85 °C, air flow 5 m/s, dry density 469 kg/m^3
(c) 140/85 °C, airflow 5 m/s, dry density 447 kg/m^3

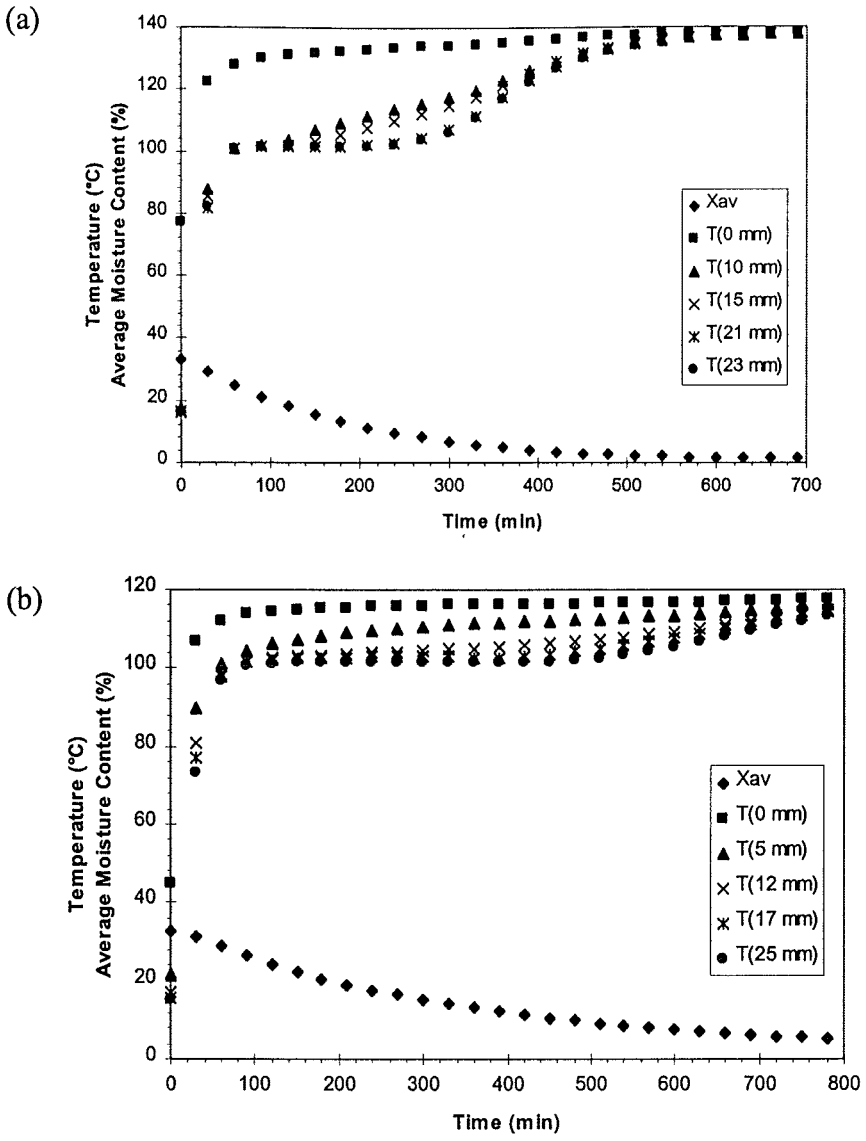

Figure 2.2. The temperature and moisture content profiles within a 50 mm thick heartwood board: (a) 140/65 °C, air flow 5 m/s, dry density 375 kg/m^3 (b) 120/85 °C, air flow 5 m/s, dry density 387 kg/m^3

by brown stain. Pang [1994] states that brown stain in *Pinus radiata* lies between 0.5 and 1.5 mm below the surface of the board and is from one-third to two-thirds of the damaged layer thickness wide. Evans *et al.* [1962] has observed that, in western hemlock (*Tsuga heterophylla*), brown stain occurs in a layer approximately 0.5 mm thick at the surface of a kiln-dried board. They attribute this phenomenon to the movement of materials from the interior of a board to the surface and subsequent concentration there as the water evaporates.

The presence of the damaged layer near the surface of the timber boards may also be deduced from the experimental temperature profiles of Pang [1994] for sapwood (Figure 2.1), and more clearly in the recent experiments of McCurdy [1998]. As described above, the surface temperature often approaches an asymptotic value well below the external air temperature when drying sapwood under high-temperature conditions. This suggests that a quasi-steady state has been reached in which the

evaporative plane remains stationary at its initial position beneath the surface of the board even though moisture is being lost. In many of these profiles, the surface temperature during this period is significantly greater than the temperatures at various points beneath the surface, which are approximately equal to or less than the boiling point of water. This suggests that the surface is below fibre saturation, whereas the interior points are above it. Thus, a relatively dry layer exists at the surface which is below fibre saturation. Pang's profiles indicate that this dry layer is less than 6 mm in width; however, the temperature profiles of Northway [1989], which have greater resolution, show that this layer is thinner and less than 3 mm in width.

2.2.3 Transport mechanisms for moisture flow

There may exist three distinct zones within a timber board as it dries out.

Zone 1

In the first zone, the moisture content is greater than the irreducible saturation value and the liquid phase is continuous. Capillary pressure causes the liquid to move towards the drying surface. In the living tree, the sap is held under tension in the lumens of the tracheids. Cavitation can take place during drying, with the spontaneous formation of bubbles. The relative vapour pressure in these bubbles is very close to unity. Stamm [1964] points out, that a relative vapour pressure of unity is not reached until all of the void structure is full with liquid water. This only occurs at relatively high moisture contents. Therefore, for *Pinus radiata*, it is possible for some movement of water vapour to occur even at moisture contents approaching the green conditions. Chen *et al.* [1996] assume that water-vapour movement by diffusion is significant only at moisture contents below the irreducible moisture content. In this thesis, it is assumed that water-vapour diffusion is insignificant above the fibre-saturation point because the relative humidity, which is the driving force for water vapour movement above the fibre saturation point, varies only slightly from a value of about 0.99-0.995 at the fibre-saturation point when the lumens are empty to a value of 1.0 when the lumens are completely filled with liquid water.

Zone 2

In the second zone, the moisture content is between the irreducible and fibre-saturation points. There are different views on the mechanism for moisture transport in this zone.

Zero moisture-transport theory -

Pang *et al.* [1994] assume that both liquid and gas transport are negligible. They assume that the relative humidity of the gas at the fibre saturation point is unity, and therefore no vapour-pressure gradients are possible above the fibre-saturation point. Gas flows due to convection are considered negligible and no liquid flow is possible at moisture contents below irreducible saturation. Thus, zone two is non-existent in their model.

Whitaker [1985] points out that the assumption of negligible liquid and gas flows between the irreducible and zero-saturation points in a non-hygroscopic porous body results in a discontinuity at the evaporative front across which the moisture content jumps from zero saturation to a value above irreducible saturation. When the moisture content at a point in the wet zone drops to irreducible saturation, it remains there until the evaporative front has receded passed that point in the porous body, because no driving force for moisture transport is available at that point. Similar discontinuous profiles have been reported by Chen *et al.* [1996] for timber drying except that, in their profiles, the moisture content jumps from a value below fibre saturation to a value above irreducible saturation.

Liquid transport by convection theory -

Whitaker [1985] presents the data of Ceaglske *et al.* [1937] for drying beds of sand which show that moisture flow is possible between the irreducible saturation and zero saturation values. Whitaker concludes from the results of a sensitivity analysis that gas-phase convective transport is negligible in this range of moisture contents, so that only liquid-phase convective mass transport occurs. He uses the concept of the capillary pressure-saturation curve to model the moisture flow, but assumes that the capillary pressure tends towards infinity at a saturation value well below the experimental irreducible saturation values found by many workers. The assumed capillary pressure-saturation curve is almost identical with the experimental one except at very low saturation values. He is able to match experimental and theoretical moisture-content profiles on this basis.

Gas transport by convection theory -

Perré *et al.* [1986] have presented discontinuous fronts for timber similar to those of Whitaker's profiles for sand, when negligible moisture flows between the irreducible and zero saturation (or fibre saturation for timber) are assumed. They conclude, however, that gas-phase convective flows must be possible in this range while liquid flows are negligible. The gaseous convective flow results from a total pressure gradient between the evaporative front and the surface of the board which, in turn, results from the resistance of the porous medium to gas migration generated by diffusion.

Moyne *et al.* [1985] and Perré *et al.* [1993] show experimentally and numerically that total overpressures of up to one atmosphere are possible at the centre of a timber board dried under high-temperature conditions. They conclude that when timber is dried at temperatures above the boiling point of water, the pressure gradient in the gas phase is a significant driving force for gaseous transport and therefore convective gas flows should be taken into account. However, their sensitivity analysis on the transport properties used in their mathematical model, shows that permeability strongly influences the pressure level inside a timber board. They state that with a highly permeable species, significant total pressure gradients may not be observed within a timber board.

As Pang [1994] has pointed out, *Pinus radiata* is more permeable than many coniferous species which may explain why the experimental wet-zone temperature profiles for sapwood *Pinus radiata* of several workers (Northway [1989], Pang [1994]) approach the boiling point of water at atmospheric pressure. Heartwood is less permeable than sapwood which would explain why the wet-zone temperature in some of the experimental profiles of Pang [1994] rise above 100 °C. This suggests that, in some cases, convective gas flows may be needed to model the drying of *Pinus radiata* heartwood because the total overpressures that can be generated would set up pressure gradients with subsequent convective flows. However, sapwood is more permeable and therefore convective gas flows may be ignored in this wood.

Water Vapour transport by diffusion theory -

Chen *et al.* [1996] have assumed that vapour diffusion is possible between fibre saturation and irreducible saturation due to a slight positive vapour pressure gradient. Stamm [1971] has reported that the relative vapour pressure, or relative humidity, at fibre saturation is about 0.995. Skaar [1988] takes a value for the relative humidity of 0.99 at the fibre-saturation point. This depression of the relative humidity at fibre saturation is presumed to be caused by both condensation of water at the lumen ends and the tiny micropores and/or cavities in the cell wall. According to Kelvin's equation, a vapour-pressure lowering corresponding to a relative humidity of 0.995 corresponds to a capillary size of 0.1 μm.

Other assorted theories -

Huang [1979] gives a detailed description of the pendular state in the drying of porous media, when the moisture content is below the irreducible saturation value and liquid pockets exist throughout the porous body. He describes a dual capillary and evaporation-condensation mechanism in which vapour is transported by a vapour pressure gradient across air-filled pores and condenses on the liquid pockets, or on the interior surface of the solid matrix to form a film. Liquid flows in the pockets are caused by capillary action due to changes in the curvature of the menisci at the edges of the pockets which result from condensation and evaporation at these edges. In his view, the flux through the liquid islands readjusts itself to carry on the vapour moisture flux. He assumes that the mobility of both liquid pockets and films is insignificant and that vapour movement is the major mechanism for moisture transfer.

Przesmycki *et al.* [1985] assume that both liquid and gas flows are possible in zone two which they call the evaporating zone. They claim that, even though free liquid continuity does not exist, water molecules adsorbed on the inner surfaces of a hygroscopic porous medium form bridges between places of higher moisture content. Therefore, liquid transfer due to surface diffusion is possible. Diffusion-type expressions are used to model both liquid and gas flows in their simulations.

Adesanya *et al.* [1986] claim that in the wet zone (above the irreducible saturation) both Fickian diffusion and capillary action occur simultaneously. They state that moisture migration is by liquid diffusion in the finer pore structure (in the cell wall), and by capillary action in the larger tracheid-pit structure. While Adesanya's theory

would allow liquid diffusion to occur below the irreducible moisture content via the fine pore structures which are postulated to exist in wood, Spolek *et al.* [1981] show experimentally that liquid flow by capillary action is not possible below the irreducible moisture content.

Summary of theories -

The mechanisms suggested by several workers for transport of moisture between fibre saturation (timber) or zero saturation (sand), and irreducible saturation have been described above. Although gas diffusion is possible above the fibre-saturation point due to a gradient in the relative humidity, this flow must be negligible because of the small relative humidity potential available. Empirical evidence suggests that convective gas flows are insignificant for the drying of *Pinus radiata* sapwood. Therefore, liquid transport might occur between the irreducible and fibre-saturation points. Many workers have shown that liquid transport by capillary action is not possible below the irreducible saturation point (for example, Spolek *et al.* [1981]). Therefore, in this thesis, it is assumed that a diffusive-type liquid-transport mechanism occurs below irreducible saturation either through any small-pore structure in the cell wall, as Adesanya *et al.* [1986] have assumed, or by surface diffusion on the inner surface of the cell walls, as Przesmycki *et al.* [1985] claim. Liquid diffusion must also be possible above the irreducible-saturation point, but is small compared to liquid convection resulting from capillary action.

The force which is responsible for 'liquid diffusion' between irreducible saturation and fibre saturation has not been identified. It is unclear what mechanism is responsible for liquid movement in this range of moisture contents. In this thesis, liquid flows are modelled by a diffusive mechanism, although this does not necessarily imply that diffusion is the transport mechanism prevailing. This approach is necessary in order to avoid the problem of the discontinuity which arises in the moisture content profiles predicted by Whitaker [1985] and others, who use the continuum mechanics approach.

Experimental evidence

Voigt *et al.* [1940] have found experimentally the relationship between diffusion coefficient and moisture content from fibre saturation to green moisture content for Beech wood (*Fagus* sp.). Their data indicate significant diffusion between fibre saturation and irreducible saturation (Figure 2.3). Kerdemelidis *et al.* [1987] have also shown that significant diffusion coefficients occur in this range of moisture contents for *Pinus radiata*. Luikov [1966] present data of diffusion coefficients versus moisture content for pinewood which show non-zero diffusion coefficients between the irreducible and fibre-saturation points (Figure 2.3). Clearly, some moisture movement is possible in this range.

In this chapter, a diffusion equation will be used to model moisture flow between irreducible and fibre saturation. It is not possible to resolve the two different driving forces above irreducible saturation (diffusion caused by concentration differences and convection caused by capillary pressure) using the data given by Luikov [1966].

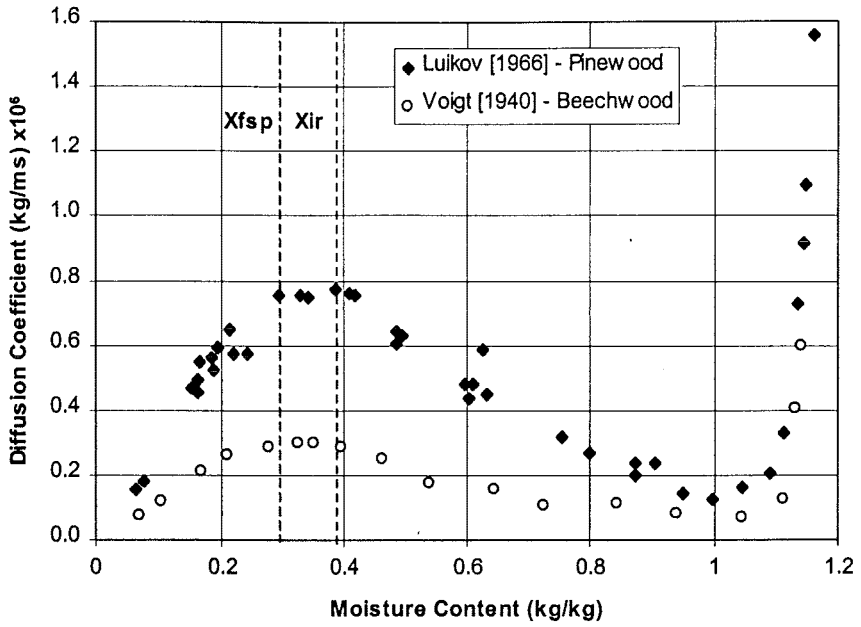

Figure 2.3. Variation of diffusion coefficient of pinewood (*Pinus* sp.) as a function of moisture content at 30 °C.

Therefore, above irreducible saturation, the capillary pressure will be used as the driving force, and diffusion will be accounted for by lumping the diffusion and convection coefficients together into an effective permeability coefficient.

Zone 3

In the third zone, diffusion occurs due to bound moisture migration and variations in partial pressure with temperature and moisture content. Gas-phase convective transport is assumed to be negligible for the drying of sapwood *Pinus radiata* because the experimental temperature profiles of Pang [1994] indicate that significant total pressure gradients do not occur.

2.2.4 Model adopted in this thesis

In this thesis, the wet zone will be defined by the range of moisture contents from fibre saturation to the green condition. Liquid diffusion will occur everywhere in the wet zone; however, its contribution will be small compared to liquid convection which only occurs at moisture contents greater than irreducible saturation. A normalised permeability correlation will be fitted to the experimental data presented by Luikov [1966] for pinewood, and a green permeability value in the range of those measured by Booker [1990] and Kininmonth *et al.* [1991] for *Pinus radiata* will be used to dimensionalise this equation.

Below fibre saturation, the vapour pressure will be used as the driving force for vapour diffusion. Air diffusion will occur to replace vapour which is lost in the drying zone. Air diffusion need not be modelled directly because it can be related to the vapour flow if it is assumed that the gas mixture is ideal. Vapour diffusion and bound-

moisture diffusion are assumed to occur in parallel. Bound moisture diffuses through the woody substance. Vapour follows a more tortuous path involving diffusion across the void tracheids, followed by condensation on the cell walls, bound moisture diffusion across the cell walls, and subsequent evaporation at the adjacent cell wall. Stanish *et al.* [1986] have derived an equation for bound-moisture diffusion which assumes that chemical potential is the driving force. It has been found, using this equation, that bound-moisture fluxes are negligible in comparison with vapour-diffusion fluxes when drying under high-temperature conditions and, therefore, in this thesis bound-moisture fluxes are ignored. Convective gas flows are not modelled because it is assumed that they are negligible.

2.3 Theory

Mass Balance Equations

Water in wood consists of three components: unbound water, water vapour and bound water. The continuity equations for these water components are

$$\frac{\partial \rho_f}{\partial t} + \frac{\partial j_{wf}}{\partial z} = -\dot{m}_{fv} \tag{2.1}$$

$$\frac{\partial \rho_v}{\partial t} + \frac{\partial j_{wv}}{\partial z} = \dot{m}_{fv} + \dot{m}_{bv} \tag{2.2}$$

$$\frac{\partial \rho_b}{\partial t} = -\dot{m}_{bv} \tag{2.3}$$

The following equations for density and flux apply for the water species:

$$\rho_w = \rho_f + \rho_v + \rho_b \tag{2.4}$$

$$j_w = j_{wf} + j_{wv} \tag{2.5}$$

The moisture content of timber is defined as the mass of moisture per mass of dry solid. Therefore,

$$X = \frac{\rho_w}{\rho_s} \tag{2.6}$$

Thus, the sum of the continuity equations for the relevant water components (Equations (2.1)-(2.3)) can be written

$$\frac{\partial}{\partial t}(\rho_s X) + \frac{\partial}{\partial z}(j_{wf} + j_{wv}) = 0 \tag{2.7}$$

Thermal Energy Equation

The heat balance is

$$\frac{\partial}{\partial t}\left[H_f\rho_f + H_v\rho_v + H_b\rho_b + H_s\rho_s + H_a\rho_a\right] = \frac{\partial}{\partial z}\left(k\frac{\partial T}{\partial z}\right) - \frac{\partial}{\partial z}\left(H_f j_{wf} + H_v j_{wv} + H_a j_a\right) \tag{2.8}$$

The enthalpies may be expressed in terms of heat capacities and temperatures, and enthalpies of phase change, assuming that the heat capacities are constant over the temperature range tested. Thus,

$$H_a = Cp_a T \tag{2.9}$$
$$H_f = Cp_f T \tag{2.10}$$
$$H_s = Cp_s T \tag{2.11}$$
$$H_b = H_f - H_{sorp} \tag{2.12}$$
$$H_v = Cp_f T_{dew} + H_{vap} + Cp_v(T - T_{dew}) \tag{2.13}$$

The total density of the wood-air-water system is

$$\rho = \rho_w + \rho_a + \rho_s \tag{2.14}$$

Substituting Equation (2.6) into (2.14) gives

$$\rho = \rho_s(1+X) + \rho_a \tag{2.15}$$

If it is assumed that $\rho_s(1+X) >> \rho_a$, then the effective heat capacity of moist wood can be derived from the sum of the individual heat capacities as follows

$$\left(Cp_f\rho_f + Cp_v\rho_v + Cp_b\rho_b + Cp_s\rho_s + Cp_a\rho_a\right) = \rho_s Cp(1+X) \tag{2.16}$$

so that the heat balance becomes

$$\frac{\partial}{\partial t}\left[\rho_s Cp(1+X)T + \rho_v\left(H_{vap} + T_{dew}\left(Cp_f - Cp_v\right)\right) - \rho_b H_{sorp}\right] = \frac{\partial}{\partial z}\left(k\frac{\partial T}{\partial z}\right) - \frac{\partial}{\partial z}\left(H_f j_{wf} + H_v j_{wv} + H_a j_a\right) \tag{2.17}$$

where Cp is the heat capacity of moist wood.

Assuming that H_{vap} and $T_{dew}\left(Cp_f - Cp_v\right)$ do not vary appreciably with distance and time, and given that H_{sorp} is close to zero at the evaporative front, then Equation (2.17) may be transformed to

$$\frac{\partial}{\partial t}\left[\rho_s Cp(1+X)T\right] - \rho_b \frac{\partial H_{sorp}}{\partial t} = \frac{\partial}{\partial z}\left(k\frac{\partial T}{\partial z}\right) - \frac{\partial}{\partial z}\left[\left(Cp_f j_{wf} + Cp_v j_{wv} + Cp_a j_a\right)T\right] - \left(H_{vap} + T_{dew}\left(Cp_f - Cp_v\right) + H_{sorp}\right)\left(\dot{m}_{fv} + \dot{m}_{bv}\right) \tag{2.18}$$

Moyne *et al.* [1985] assume that the accumulation term in Equation (2.2) is small compared with the evaporation and convective flux terms. On this basis

$$\frac{\partial j_{wv}}{\partial z} = \dot{m}_{fv} + \dot{m}_{bv} \tag{2.19}$$

In addition, Perré *et al.* [1993] assume that H_{sorp} is independent of time. The final form of the heat balance is therefore

$$\frac{\partial}{\partial t}\left[\rho_s Cp(1+X)T\right] = \frac{\partial}{\partial z}\left(k\frac{\partial T}{\partial z}\right) - \frac{\partial}{\partial z}\left[\left(Cp_f j_{wf} + Cp_v j_{wv} + Cp_a j_a\right)T\right] - \left(H_{vap} + T_{dew}\left(Cp_f - Cp_v\right) + H_{sorp}\right)\frac{\partial j_{wv}}{\partial z} \tag{2.20}$$

Boundary Conditions

The surface fluxes are calculated using heat and mass-transfer coefficients and corresponding potentials. Continuity of moisture transfer must occur at the surface; thus,

$$j_{wv} + j_{wf} = \beta^*\left(P_{vg} - P_v\right) \tag{2.21}$$

where P_v is the vapour pressure at the surface and P_{vg} is the vapour pressure of the bulk of the cross-circulating air at the specified dry and wet-bulb temperatures. The star on the mass-transfer coefficient indicates that the mass-transfer coefficient is influenced by the flux of mass from the surface. This effect is known as the 'blowing' effect. The mass-transfer coefficient β^* is equal to the mass transfer coefficient β, which has been measured by many workers (Kho *et al.* [1990]), multiplied by the Ackermann correction factor for high mass-transfer rates.

The continuity equation for heat transfer at the surface is

$$j_{wf} H_{vap} + k\frac{\partial T}{\partial z} = h^*\left(T - T_g\right) \tag{2.22}$$

where T_g is the bulk gas temperature and T is the surface temperature. Again, the 'blowing' effect at the surface of the timber board is taken into account which is indicated by the star on the heat-transfer coefficient. The heat-transfer coefficient h^* is equal to the heat transfer coefficient h, which can be related to the mass-transfer coefficient β by the principle of analogy between convective processes, multiplied by the Ackermann correction factor for heat transfer.

Due to the symmetry of the timber board, the gradients with respect to distance in temperature, moisture content and vapour pressure are zero at the core.

Vapour-air movement

Vapour and air fluxes are made up of a convective and a diffusive term:

$$j_{wv} = \left[x_v (N_v + N_a) - cD \frac{\partial x_v}{\partial z} \right] M_v \varepsilon \tag{2.23}$$

$$j_a = \left[x_a (N_a + N_v) - cD \frac{\partial x_a}{\partial z} \right] M_a \varepsilon \tag{2.24}$$

where ε is the fractional voidage of the timber. In this chapter, it is assumed that the convective gas flows, which are pressure-driven, are negligible. On assuming that the gas mixture is an ideal gas of constant total pressure, then Equations (2.23) and (2.24) can be transformed to

$$j_{wv} = -\frac{M_v \varepsilon D}{RT} \frac{\partial P_v}{\partial z} \tag{2.25}$$

$$j_a = +\frac{M_a \varepsilon D}{RT} \frac{\partial P_v}{\partial z} \tag{2.26}$$

The effective diffusivity can be taken to be equal to the binary gas diffusivity of water vapour and air multiplied by an attenuation factor α. This factor arises because vapour must follow a more tortuous path than described by mere diffusion through air over a given distance z. The vapour pathway involves: (1) changes in direction because of non-alignment of connecting pores, aspirated (closed) pits, and blockages due to extraneous materials such as resins, and (2) condensation on cell walls, followed by bound-moisture diffusion across the cell walls, followed by evaporation at adjacent cell walls. The effective diffusivity is defined by the equation

$$D = \alpha D_{AB} \tag{2.27}$$

The attenuation factor α is the inverse of the diffusional resistance coefficient in the German literature (Krischer *et al.* [1978], Vanek and Telschinger [1980]). The binary diffusivity of the air-vapour mixture may be estimated from the equation (Sherwood [1975])

$$D_{AB} = 1.17564 \times 10^{-9} T^{1.75} \tag{2.28}$$

The vapour partial pressure can be calculated as a function of local temperature and relative humidity using the relationship

$$P_v = \psi P_{vs} \tag{2.29}$$

where the saturation vapour pressure, P_{vs}, may be estimated using the Antoine equation which has been fitted to vapour pressure-temperature data from steam tables.

The relative humidity may be estimated using a relationship given by Simpson *et al.* [1981] for the sorption equilibrium of timber at elevated temperatures:

$$\psi = 0.5\left[Z_1 + \sqrt{\left(Z_1^2 + \frac{4}{K_1 K_2^2}\right)}\right] \tag{2.30}$$

where

$$Z_1 = \frac{(1 - Z_2)}{K_2} - \frac{(1 + Z_2)}{K_1 K_2} \tag{2.31}$$

$$Z_2 = \frac{18}{WX} \tag{2.32}$$

and

$$K_1 = -45.70 + 0.3216T - 5.012 \times 10^{-4} T^2 \tag{2.33}$$

$$K_2 = -0.1722 + 4.732 \times 10^{-3} T - 5.553 \times 10^{-6} T^2 \tag{2.34}$$

$$W = 1417 - 9.430T + 1.853 \times 10^{-2} T^2 \tag{2.35}$$

In this chapter, the sorption isotherms are scaled so that the equilibrium moisture content at a relative humidity of unity is equal to the fibre-saturation moisture content. The fibre-saturation moisture content is calculated using the correlation of Siau [1984],

$$X_{fsp} = 0.3 - 0.001(T - 293.15) \tag{2.36}$$

which implies the fibre-saturation point takes a value of 0.3 kg/kg at 20 °C.

The Simpson equation is considered appropriate for a softwood such as *Pinus radiata*, as limited data obtained by Cunningham and Sprott [1984] indicated similar sorption data to those presented by Stamm [1964] for *Picea sitchensis*.

Liquid moisture movement

The movement of unbound water above irreducible saturation is assumed to follow Darcy's law for flow through a porous media. Therefore, the flux is proportional to the gradient in pressure within the liquid:

$$j_{wf} = -E_l \frac{\partial P_l}{\partial z} \tag{2.37}$$

The liquid pressure gradient is equal to the difference between the gas pressure gradient and the capillary pressure gradient. The vapour pressure in the wet zone remains constant, being equal to the value at the evaporative plane, for reasons mentioned above. Therefore, the unbound water flux is given by the equation

$$j_{wf} = E_l \frac{\partial P_c}{\partial z} \tag{2.38}$$

in which E_l the effective permeability to water flow, may be related to the commonly measured permeability, k_l by the equation

$$E_l = \frac{k_l \rho_l}{\mu_l} \tag{2.39}$$

For softwoods, Spolek *et al.* [1981], have measured the capillary pressure in Southern Pine wood and assume that it is related to the relative saturation by the following equation:

$$P_c = 12400 S^{-0.61} \tag{2.40}$$

in which

$$S = \frac{X - X_{fsp}}{X_{max} - X_{fsp}} \tag{2.41}$$

where X_{max} is the moisture content of the wood if the entire void structure were filled with liquid. They show that liquid flow ceases at a relative saturation value of 0.1. It is explained that this is caused by the relative location of the bordered pits and the tips of the tracheids so that unbound water may be trapped at the tips of the tracheids after the meniscus that separates the vapour and unbound water phases has moved passed the pits. The moisture content at which this occurs is called the irreducible moisture content, X_{ir}. Chen *et al.* [1996] estimate that the irreducible saturation may occur at a higher relative saturation value. Besides trapped moisture in the tips of tracheids, it is possible that full lumens can become isolated by being completely surrounded by tracheids which have already aspirated. However, in this thesis, irreducible saturation is set to 0.1 (Spolek *et al.* [1981]).

The maximum moisture content is related to the voidage, the dry wood density ρ_s, and the density of water by the equation

$$X_{max} = \varepsilon \frac{\rho_{water}}{\rho_s} \tag{2.42}$$

where the voidage is given by

$$\varepsilon = \frac{\rho_{cw} - \rho_s}{\rho_{cw}} \tag{2.43}$$

The cell wall density ρ_{cw} is approximately 1500 kg/m^3 and independent of species (Kininmonth *et al.* [1991]).

Liquid permeability and diffusivity for unbound liquid flow

The liquid flux equation in the wet zone may be defined in two ways: using (1) the capillary pressure, and (2) using the moisture content as the driving force. That is,

$$j_{wf} = \frac{k_l \rho_l}{\mu_l} \frac{\partial P_c}{\partial z} \tag{2.44}$$

$$j_{wf} = -D \frac{\partial X}{\partial z} \tag{2.45}$$

Both equations are equivalent except that the coefficients of proportionality (k_l and D) become different functions of moisture content.

Equating these equations and substituting the derivative of Equation (2.40) with respect to moisture content gives

$$k_l = \frac{D v_l \left(X - X_{fsp}\right)^{1.61}}{7564 \left(X_{max} - X_{fsp}\right)^{0.61}} \tag{2.46}$$

which can be rearranged to

$$k_l = \frac{D S^{1.61} v_l \left(X_{max} - X_{fsp}\right)}{7564} \tag{2.47}$$

Luikov [1966] has obtained data for the diffusion coefficient of pinewood (*Pinus* sp.) for moisture contents between the fibre-saturation moisture content and the maximum possible moisture content, X_{max} (Figure 2.3). These data, when substituted into Equation (2.47), can be plotted against saturation as in Figure 2.4. At irreducible saturation (S=0.1), the liquid diffusion (surface diffusion on the cells walls, or flow through any fine pore structure) can be represented as an effective permeability. Thus,

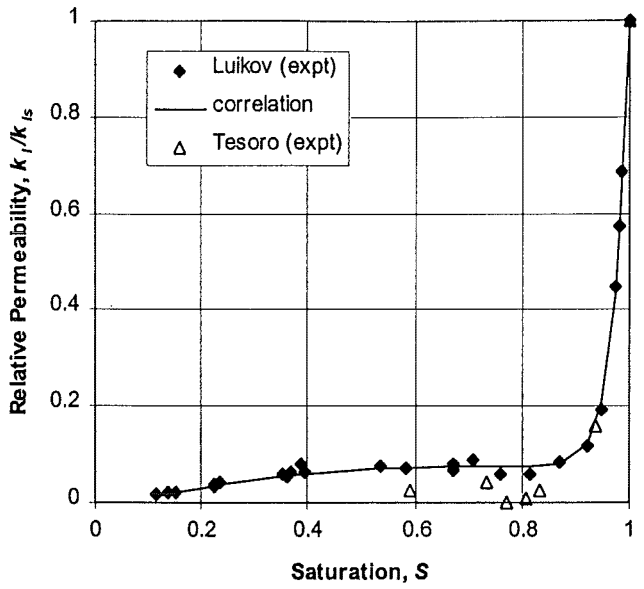

Figure 2.4. Variation of relative permeability with saturation.

the following fitted correlation for effective liquid permeability above irreducible saturation lumps together both diffusion and convection terms:

$$\frac{k_l}{k_{ls}} = \frac{S^{1.61}e^{-2.2S} + 1.5S^{35.61}}{e^{-2.2} + 1.5} \tag{2.48}$$

Figure 2.4 compares the data points produced when Luikov's diffusion coefficients are substituted into Equation (2.47), against the fitted permeability correlation (Equation (2.48)), and the experimental data of Tesoro *et al.* [1974] for the sapwood of baldcypress (*Taxodium distichum*) which is a softwood. Equation (2.48) is a good fit of Luikov's data. The difference between Luikov's and Tesoro's data probably reflects the relatively greater permeability of the pine.

The maximum permeability corresponds to a saturation value of unity. This occurs when the entire void space is filled with water. As moisture is lost, the bordered pits which connect adjacent tracheids will progressively aspirate. This reduces the number of flow paths for liquid, thus reducing the liquid permeability. The steep slope close to the saturation value of unity suggests that the initial rate of pit aspiration is very high compared to aspiration rates at lower saturation values. This contrasts with the ideas of Chen *et al.* [1996] who assume random pit aspiration takes place at a constant rate.

A diffusion-type process is assumed to occur between irreducible and fibre saturation, either by surface diffusion on the cell walls, or diffusion in any fine-pore structure. Therefore, the flux is proportional to the gradient in moisture content within the liquid:

$$j_{wf} = -D\frac{\partial X}{\partial z} \tag{2.49}$$

The data of Luikov [1966] show that the diffusion coefficient between fibre saturation and irreducible saturation is approximately constant at the irreducible saturation value (Figure 2.3). The diffusion coefficient between fibre and irreducible saturation can be calculated by substituting Equation (2.48) into Equation (2.47), and incorporating the irreducible saturation value of 0.1.

Attenuation factor for vapour flow

The attenuation factor is a function of both moisture content and temperature. The form of this function may be extracted from the experimental data of Choong [1963]. In these experiments the two opposite faces of a block of wood, with an average moisture content below the fibre-saturation point, were subjected to different temperatures. This piece of wood was left for a period of time to reach steady state before temperature and moisture content values throughout the wood samples were taken. Figure 2.5 shows an example of the temperature and moisture content profiles measured by Choong. Using Simpson's isotherm correlations (Equations (2.30)-(2.35)) it is possible to convert these profiles into vapour-pressure profiles (Figure 2.5).

Moisture below fibre saturation flows either in vapour or bound-water form. Stanish [1986] has suggested that these two flows are in parallel - (1) bound moisture through the woody substance, and (2) vapour diffusion across the cell voids, followed by condensation on the cell walls, followed by bound moisture diffusion across the cell walls, followed by evaporation at the adjacent cell wall. Choong [1963] proposes that

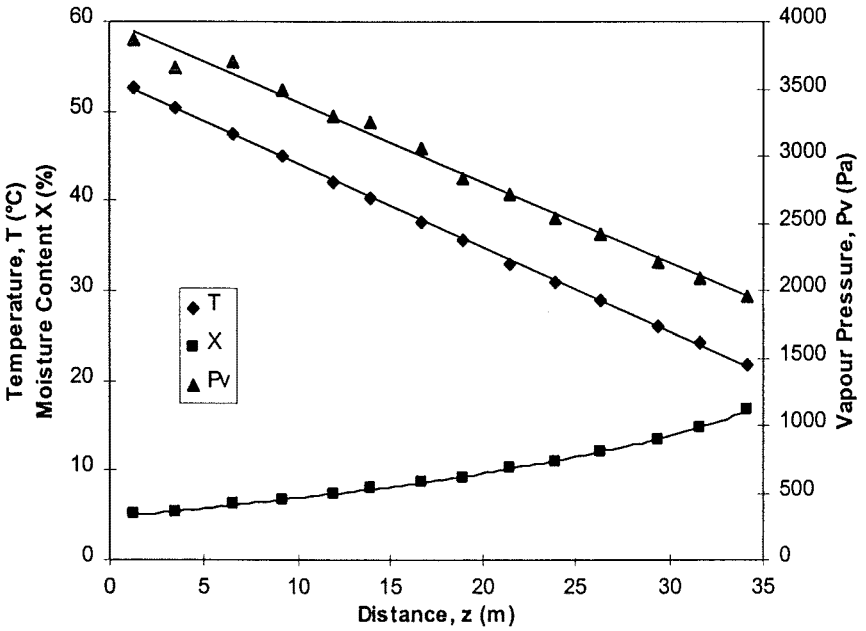

Figure 2.5. Moisture content, temperature, and vapour pressure profiles in a timber sample (Western Fir, *Abies* sp.) subjected to an imposed temperature gradient in the radial direction.

at steady state, vapour flows in one direction due to the vapour-pressure gradient, and bound-moisture flows in the opposite direction due to the bound-moisture content gradient, and that these flows balance (the total moisture flux at any point in the wood must be zero at steady state).

Stanish [1986] has argued that chemical potential should be used as the driving force for bound moisture flow. In fact, his calculations show that bound-moisture content works nearly as well as chemical potential as a driving force for bound moisture flow. The difference is that the diffusion coefficient becomes a more complex function of moisture content and temperature when moisture content is used as the driving force. No data are available on how the diffusion coefficient based on chemical potential varies with temperature and moisture content, but such data exist, courtesy of Stamm [1959], for moisture content as the driving force. Therefore, bound moisture content was used as the driving force for bound water flows in the following calculations to deduce the form for the attenuation factor. Vapour pressure was used as the driving force for vapour flows.

A moisture balance at any point within the piece of wood when at steady state yields:

$$\frac{D_{AB}\alpha\varepsilon M_v}{RT}\frac{\partial P_v}{\partial z} + D_b\frac{\partial X_b}{\partial z} = 0 \tag{2.50}$$

where

$$X_b = \frac{\rho_b}{\rho_s} = X - \frac{\rho_v}{\rho_s} \tag{2.51}$$

The bound moisture content X_b may be approximated as the total moisture content X since the amount of water vapour is small compared with the bound liquid.

On using the data of Choong [1963] it is possible to calculate the ratio of the bound-moisture diffusion coefficient D_b and attenuation factor α from the experimentally determined gradients of moisture content and vapour pressure. Figure 2.6 shows that this ratio is an exponential function of moisture content and is independent of temperature. Stamm [1959] demonstrates that bound-moisture diffusion coefficients vary exponentially with moisture content (Figure 2.7). Clearly, the attenuation factor must also vary exponentially with moisture content. This variation is also observed in the transverse and radial diffusional resistance coefficients reported by Vanek and Teischinger [1989] for oak (*Quercus* sp.) and beech (*Fagus* sp.) for moisture contents below fibre saturation. Stamm's experimental results also show that the bound-moisture diffusion coefficient varies between the second and third power of the temperature. Therefore, the following form is used for the attenuation factor

$$\alpha = A\left(\frac{T-273.15}{100}\right)^n exp\left(B\frac{X}{0.22}\right) \tag{2.52}$$

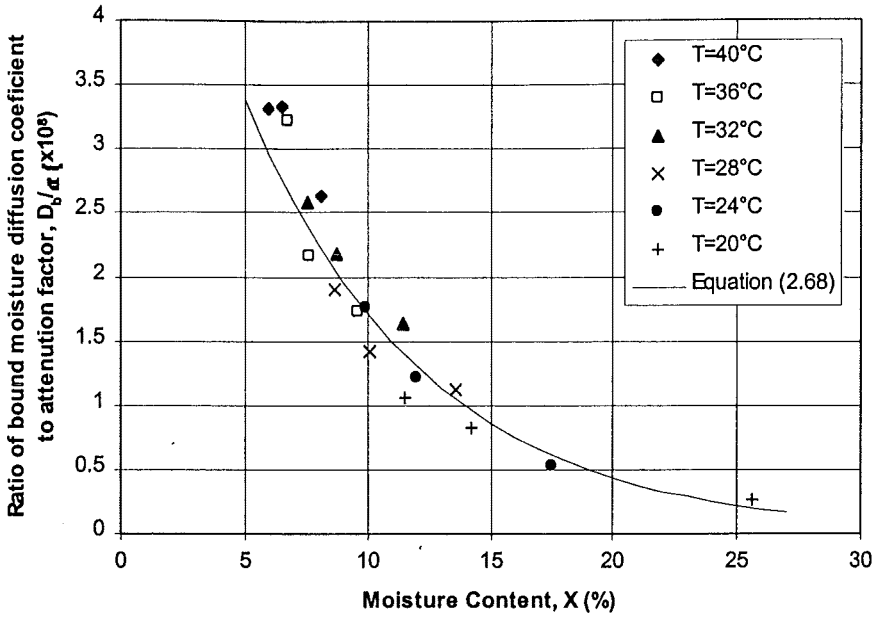

Figure 2.6. The ratio of bound moisture diffusion coefficient to attenuation factor as a function of moisture content for Western Fir (*Abies* sp.).

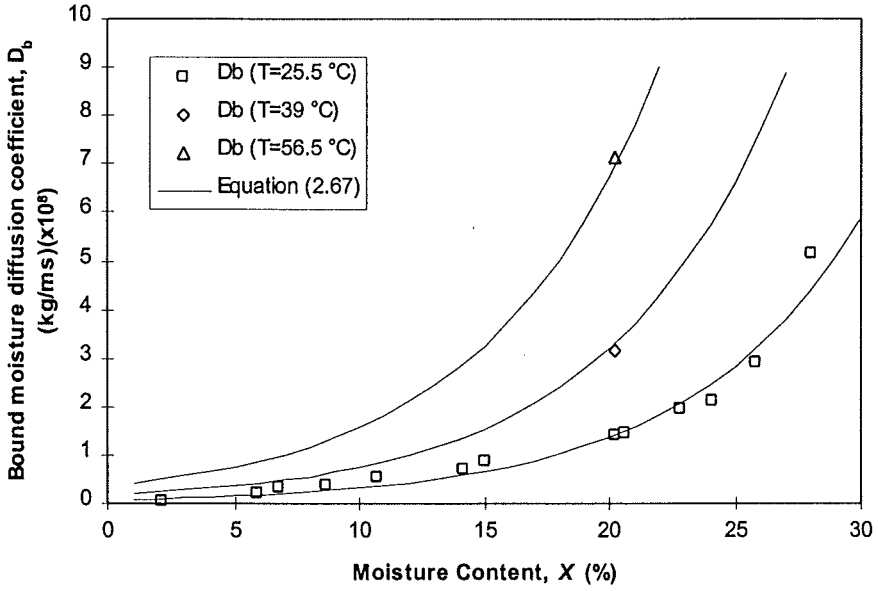

Figure 2.7. Bound moisture diffusion coefficient against moisture content for *Pinus radiata* in the radial direction.

A physical explanation why the attenuation factor decreases with decreasing moisture content is that the cell wall shrinks as moisture is lost and the remaining moisture is more tightly bound to the polymeric substrate. Therefore, bound moisture diffusion across the cell walls becomes gradually more restricted and, hence, the flow path becomes effectively more tortuous and the attenuation factor decreases. Note that, in this thesis, vapour flows are evaluated separately from bound-moisture flows even though the vapour flow path involves some bound-moisture diffusion.

Thermodynamic relationships

The density and viscosity of liquid water used in the permeability flux equation were correlated with temperature using data from steam tables. Polynomial forms were used for these correlations. Enthalpies were calculated from heat capacities assuming that the heat capacities were constant over the temperature range tested. The following values were used: air (Cp_a) 1000 $Jkg^{-1}K^{-1}$; water vapour (Cp_v) 1950 $Jkg^{-1}K^{-1}$; liquid water (Cp_f) 4180 $Jkg^{-1}K^{-1}$. Stanish *et al.* [1986] give correlations for both the heat of vaporisation H_{vap} (J/kg) and the dewpoint temperature T_{dew} (K)

$$H_{vap} = 2.792\times10^{6} - 160T_{dew} - 3.43T_{dew}^{2} \tag{2.53}$$

$$T_{dew} = 230.9 + 2.10\times10^{-4}(P_v) - 0.639(P_v)^{1/2} + 6.95(P_v)^{1/3} \tag{2.54}$$

The heat of sorption (J/kg) was calculated using a correlation given by Skaar [1988]:

$$H_{sorp} = 1.172\times10^{6} e^{-14X} \tag{2.55}$$

The heat capacity and thermal conductivity of moist wood are functions of both moisture content and temperature. Shubin [1990] shows that the heat capacity does not depend on the wood species and density. The thermal conductivity, however, will vary with density. The heat capacity and thermal conductivity have been calculated using the following correlations which have been fitted to data from Shubin using an equation similar in form to the heat capacity correlation of Kayihan [1982].

Heat Capacity (J/kg):

$$C_{pw} = \frac{(0.219+X)^{0.781}}{1+X}\left[8.5(T-273.15)+5300\right] \tag{2.56}$$

Thermal Conductivity ($Wm^{-1}K^{-1}$):

$$k = \frac{(0.26+X)^{0.95}}{1+X}\left[0.0035X(T-273.15)+0.53\right]\left[1.7\frac{\rho_s}{1000}+0.16\right] \tag{2.57}$$

where T is temperature in Kelvin, and ρ_s is the basic wood density (kg/m^3).

2.4 Specifications

Surface heat and mass-transfer coefficients from correlation

The local external mass-transfer coefficient, which corresponds to a certain cross-circulation velocity, may be obtained by using the correlation of Kho *et al.* [1990] for airflow over a timber board at a position x from the leading edge:

$$Sh_x = 0.084\, Re_x^{0.75}\, Sc^{0.33} \tag{2.58}$$

where

$Re_x = \dfrac{ux}{\nu}$ is the local Reynolds number based on the swept length x

$Sc = \dfrac{\nu}{D_{AB}}$ is the Schmidt number

$Sh_x = \dfrac{K_c x}{D_{AB}}$ is the local Sherwood number

The mass-transfer coefficient may be averaged over any two points along the swept length by integrating between these points:

$$\overline{K}_c = \frac{\int_{x_1}^{x_2} K_c\, dx}{\int_{x_1}^{x_2} dx} = \frac{0.112 D_{AB}\left(Re_{x_2}^{0.75} - Re_{x_2}^{0.75}\right) Sc^{0.33}}{x_2 - x_1} \tag{2.59}$$

According to Treybal [1969] the mass-transfer coefficient based on the partial pressure difference β may be related to the mass-transfer coefficient based on the molar concentration K_c in the following manner:

$$\beta = \frac{M_v K_c}{RT} \tag{2.60}$$

The external heat-transfer coefficient h may be estimated from the Chilton-Colburn analogy:

$$h = K_c \rho C_p \left(\frac{Sc}{Pr}\right)^{2/3} \tag{2.61}$$

The timber samples used in Pang's experiments [1994] were 100-mm wide with a dummy board, also 100-mm wide, placed in front of the sample. When humid air at 140 °C with velocity 5 m/s is flowing across the two timber boards, the average values of h and β over the sample board are 36.7 W/m²K and 24.0x10^{-8} s/m, respectively.

These transfer coefficients may be affected by the bulk motion of gas across the surface. This is called the 'blowing' effect which will be at its peak during the constant rate period when the flux of moisture across the surface is the greatest. Bird *et al.* [1960] show that the Ackermann correction factor for mass and heat transfer during the constant rate period, when the air flux at the surface is negligible, is equal to

$$\theta = \frac{\phi}{e^{\phi} - 1} \tag{2.62}$$

where for mass transfer

$$\phi = \frac{j_{wv}}{\beta P_{atm}} \tag{2.63}$$

and for heat transfer

$$\phi = \frac{j_{wv} C_{pv}}{h} \tag{2.64}$$

The steady state vapour flux from the surface may be calculated from the maximum slope of the moisture content profile (Figure 2.1) using the following equation:

$$j_{wv} = \left|\frac{\Delta X}{\Delta t}\right| \rho \frac{b}{2} \tag{2.65}$$

where b is the thickness of the timber board (50 mm in this case). These maximum surface fluxes are 0.00085 and 0.00056 kg/m²s for the 140/85 °C and 120/85 °C moisture-content profiles, respectively. Substituting into Equations (2.62) the maximum vapour flux extracted from Pang's data, and the mass-transfer coefficient of 24.0×10^{-8} s/m, which was calculated from Kho's [1990] correlation, gives an Ackermann correction factor for mass transfer of 0.9827. This value is very close to unity which suggests that the mass-transfer coefficient is not affected by the 'blowing' effect at the low mass-flux levels experienced by timber during the high-temperature drying process.

A similar analysis shows that the heat-transfer coefficient is likewise not affected by the 'blowing' effect. The Ackermann correction factor is 0.9762 when the maximum vapour flux from Pang's data, and a heat transfer coefficient of 36.7 W/m²K (calculated from the mass-transfer coefficient using the Chilton-Colburn analogy, Equation (2.61)) is substituted into Equation (2.62).

Surface heat and mass-transfer coefficients from experimental data

The heat-transfer coefficient may also be extracted from the experimental temperature and moisture profiles for sapwood *Pinus radiata* of Pang [1994] (Figure 2.1). During

the first drying period when the evaporative plane is stationary close to the surface of the board, the surface temperature approaches a constant value between the wet and dry-bulb temperatures. Providing the internal resistance to moisture flow is negligible compared with the external resistance to moisture flow, then the drying rate becomes approximately constant and therefore the average moisture content drops linearly with time. A simple steady state heat and mass balance around an envelope described by the surface of the timber board and the evaporative plane beneath the surface can be used to calculate the local heat-transfer coefficient.

Quite often, three periods are used to describe the characteristic drying behaviour of timber (Pang [1994]). In the first period, the evaporative plane remains near the exposed surface while liquid water is drawn outwards from the interior region. The drying rate is assumed to be independent of moisture content during this period, which is known as the constant rate period. In the second period, the evaporative front recedes into the board and the drying rate drops due to an increasing internal resistance to moisture flow. This period is known as the first falling-rate period. The third period begins when the evaporative plane has reached the centre of the board, at which point the drying rate falls even more rapidly. This period is known as the second falling-rate period.

The drying behaviour described above is exhibited in a plot of Pang's experimental data for sapwood of relative drying rate versus average moisture content (Figure 2.8). This curve is commonly known as the characteristic drying curve. The relative drying rate f is defined as the ratio of the drying rate at any given time to the maximum drying rate. In Figure 2.8, the maximum drying rate occurs at a moisture content of about 95% and above in sapwood. At lower moisture contents, the drying rate begins to drop because the internal resistance to moisture flow becomes increasing more important. The plot also shows the variation of local surface temperature with average moisture content. The thermocouple used to measure the local surface temperature

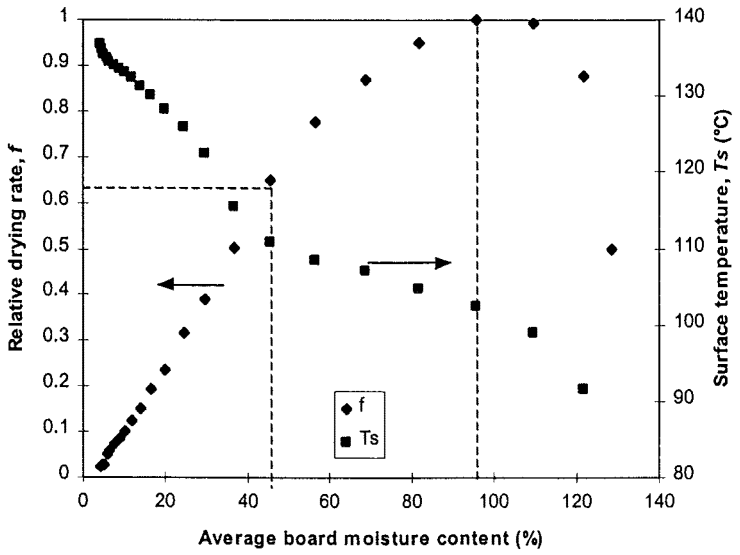

Figure 2.8. Relative drying rate and local surface temperature versus average moisture content (sapwood data: 140/85 °C).

was positioned 60-mm from the leading edge of the 100-mm wide sample board. The local surface temperature appears to approach an asymptotic value of 110 °C at an average moisture content of 45% before rising sharply at lower moisture contents (Figure 2.8). This cusp represents the moment at which the local evaporative front, positioned within the timber board just below the surface-mounted thermocouple, begins to withdraw into the timber board.

These results show that the recession of the evaporative front within the solid is not entirely a one-dimensional process as has been assumed in this chapter. The inevitable appearance of gaps (of up to 1.0 mm) between adjacent boards in a stack of timber generate additional turbulence in the cross-circulating air, which enhances the transfer coefficients over the leading portion of each timber board (Kho [1993]). The transfer coefficients over the leading edge of each timber board can be more than twice those at the trailing edge (Kho [1993]). Therefore, the local evaporative front will recede more quickly at the leading edge of the timber board than at the trailing edge. Furthermore, the timber boards tested by Pang had three surfaces exposed to the external airflow. Two of these were the drying surfaces tangential to the airflow direction; the third was the trailing edge of the timber board beyond which the airflow formed a wake. Although the third exposed surface was painted to eliminate mass transfer, heat transfer was still possible through this interface. Given that the drying process is predominantly heat-transfer controlled under high-temperature drying conditions, then the extra source of heat through the third exposed surface would have influenced the time and rate at which the local evaporative plane receded within the board at the trailing edge.

Figure 2.8 shows that the local evaporative front, at a point 60 mm from the leading edge of the timber board, was stationary close to the surface of the timber board even though the relative drying rate of the board had fallen below unity. Clearly, the relative drying rate of the timber board was falling because the evaporative front had already begun to recede at another point within the timber board. The two-dimensional drying behaviour of timber is investigated in more detail in Chapter 3.

The term 'constant rate' is used even though no such period can be seen in Figure 2.8. The warming-up period effectively obscures the constant rate period. If the warming-up period could be avoided by heating up the timber sufficiently before moisture was lost, then the drying rate would reach the same maximum value at a moisture content greater than the values shown in Figure 2.8, and remain there until the internal resistance became significant. The surface temperature would also reach the same asymptotic value but at a higher moisture content. In order to calculate the surface heat-transfer coefficient using a steady-state analysis, the drying rate and surface temperature during the constant rate period are required. These values may be extrapolated from the asymptotic values shown in Figure 2.8. The steady-state drying rate is the maximum possible value. The surface temperature is the value at the cusp when the evaporative plane begins to withdraw into the board.

A heat balance around an envelope described by the evaporative plane and timber surface is given by the expression

$$h^{*}\left(T_s - T_g\right) = j_{wv} H_{vap} \tag{2.66}$$

The steady state moisture flux may be evaluated using Equation (2.65). The latent heat of vaporisation should be evaluated at the temperature of the evaporative front which is equal to the mid-plane temperature at steady state (100 °C for Figure 2.1c, and 94°C for Figure 2.1b). The surface temperature can be readily taken off the temperature profiles: 110 °C for Figure 2.1c, and 98 °C for Figure 2.1b. Thus, the average heat-transfer coefficient is approximately 60 W/m²K. This is about 23 W/m²K higher than the value calculated using Kho's correlation which suggests that there is significant contribution to heat transfer from radiation in Pang's experiments [1994]. Keey [1978] notes that in many convective drying situations at temperatures of order 120 °C, radiation from the moist air and other hot surfaces is likely to make a significant contribution to the overall heat transfer.

Physical Properties of Wood

Green Permeability

The permeability of wood to water plays a major role in the drying of a board because it reflects the ease with which the water flows through it. The permeability of timber is likely to vary with factors such as species of the tree, the location of the wood in the tree trunk, the orientation of the sample, the density of the wood and seasonal changes. Timber boards are normally sawn in the direction parallel to the tree stem. In the drying of these boards, air sweeps over the surface perpendicular to the lengthwise direction of the timber boards. Therefore, moisture is lost at right angles to the grain direction. Thus, longitudinal permeability (or permeability in the grain direction) is not significant in the drying process, and only radial permeability (or permeability at right angles to the growth ring) and tangential permeability (or permeability tangent to the growth ring) are considered important. The higher longitudinal permeability, however, ensures that the moisture-content contours in the wood remain relatively flat during the drying process, except close to the ends of the boards.

As the permeability is a very variable property of any wood, a large range in the permeability values can be found, even for the same species. Table 2.1 gives some data for the radial and tangential permeabilities of green *Pinus radiata* found by Booker [1990] and Kinninmonth *et al.* [1991]. In order to dimensionalise the permeability correlation (Equation (2.37)) the permeability value when the entire void space of the timber is filled with water is required. This may not necessarily correspond to the green permeability. The reason why there is so much variability in the experimentally determined permeabilities is that only a small change in saturation is required, when the moisture content of the timber is close to full saturation, for a significant change in permeability to occur. Figure 2.4 shows that the relative permeability drops by an order of magnitude when the saturation is reduced from unity to 0.9. It is therefore likely that the higher permeabilities shown in Table 2.1 correspond to the permeability of fully saturated wood.

		radial	tangential
Green sapwood liquid permeability $1x10^{-15}$ m²	Booker (1990)	0.018-0.168	0.169-0.774
	Kininmonth (1991)	0.310-3.8	2.9

Table 2.1. The permeability of green sapwood *Pinus radiata* to liquid flow.

Attenuation Factor

Approximate values for the constants given in Equation (2.52) may be extracted from the bound-moisture diffusion coefficient data for Sitka spruce (*Picea sitchensis*) in the longitudinal direction (Stamm [1959]), and the ratio of attenuation factor to bound moisture diffusion coefficient for western fir (*Abies* sp.) in the radial direction (Choong [1963] - Figure 2.6). Stamm [1960] shows that it is possible to scale the bound-moisture diffusion coefficients to account for grain direction and species differences by using an analogy between electrical conductivity and bound-moisture diffusion coefficient. The bound-moisture diffusion coefficients for *Pinus radiata* in the radial direction, which were calculated from the data for Sitka spruce (*Picea sitchensis*) using the scaling technique described by Stamm, are shown in Figure 2.7, and the following equation was fitted to these data,

$$D_b = 1.15 \times 10^{-8} \left(\frac{T - 273.15}{100} \right)^2 exp\left(3.2 \frac{X}{0.22} \right) \tag{2.67}$$

The following exponential form was fitted to the experimental data for western fir (*Abies* sp.) in the radial direction with a ratio of attenuation factor to bound moisture diffusion coefficient (Figure 2.6),

$$\frac{D_b}{\alpha} = 6.71 \times 10^{-8} exp\left(-3.0 \frac{X}{0.22} \right) \tag{2.68}$$

It is expected that *Pinus radiata* being a softwood, will have ratios of attenuation factor to bound moisture diffusion coefficient of similar order of magnitude to western fir (*Abies* sp.). Thus, the attenuation factor takes the form

$$\alpha = 0.17 \left(\frac{T - 273.15}{100} \right)^2 exp\left(6.2 \frac{X}{0.22} \right) \tag{2.69}$$

Equation (2.69) results in attenuation factors significantly greater than unity at moisture contents approaching fibre saturation which is physically unrealistic. This might be caused by the complications inherent in the measurements made by both Stamm [1959] and Choong [1963]. It is also possible that as the fibre-saturation moisture content is approached, the mechanism for moisture movement becomes transitional between bound-moisture transport and unbound moisture transport which has the effect of skewing the results. However, such errors should not affect the general form of Equation (2.69).

Vapour-Diffusion Model

The convective term (the first terms in Equations (2.23) and (2.24)) may be expressed in the form of Darcy's law for flow through porous medium. In the case of vapour flow, this term becomes

$$\frac{\rho_v}{\varepsilon}\frac{k_g \rho_g}{\mu_g}\frac{\partial P}{\partial z} \tag{2.70}$$

where P is the total gaseous pressure and k_g is the vapour permeability. It has been argued that no total pressure gradients occur in *Pinus radiata* because it is very permeable. Thus, gaseous flow by convection is negligible and only gaseous diffusion need be modelled. Perré *et al.* [1993] give two criteria for assuming a purely diffusive type model. The first criterion is

$$\frac{k_g \rho_g}{\mu_g} >> \frac{DM_v}{RT} \tag{2.71}$$

where k_g is the gaseous permeability, and D is the effective diffusivity which accounts for the complex structure of the wood. The ratio of the terms in this equation represent the relative magnitude of the convective and diffusive driving forces. The second criterion is

$$j_{wv} z << \frac{k_g \rho_g}{\mu_g} P_{atm} \tag{2.72}$$

where j_{wv} is the mass flux of vapour and z is the thickness of the gaseous zone.

Booker [1990] has found experimentally that the gaseous permeabilty in *Pinus radiata* lies within the range from 32 to 138 $x10^{-15}$ m^2. The attenuation factor takes on a maximum value of unity. Substituting these values in Equation (2.71) shows that the convective term is between 30 and 350 times greater than the diffusive term and most likely even higher when a lower attenuation factor is used. The vapour flux during the constant-rate period, when the evaporative plane remains stationary close to the surface of the timber board, may be extracted from the data of Pang [1994] (Figure 2.1). This value ranges from 0.00056 to 0.00085 kg/m^2s for the 50mm timber board. If it is assumed that the thickness of the dry layer near the surface during the constant rate period is 1 mm, then the right-hand term of Equation (2.72) is at least 430 times greater than the left-hand term. This is a fairly strong indication that a purely difffusive model will suffice for the dry zone.

Numerical Solution

The partial differential equations were discretised using a finite-difference approach. The grid layout, which was fixed with respect to time, is shown in Figure 2.9. The

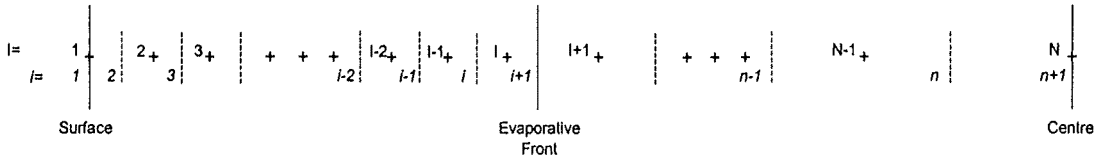

Figure 2.9. Grid layout.

control volume interfaces were equispaced in the thin-dry layer at the surface, and increased in distance into the board with separation distances following a geometric series. Thus, the grid was concentrated near the surface where the gradients with respect to time and space change most rapidly, especially in the initial stages of drying. All nodes were located at the centre of the control volumes except for the centre-line and surface nodes which were located on the centre-line and surface, respectively.

The fluxes of energy and mass across each control volume interface were required for the numerical solution. Thus, gradients of temperature, vapour pressure and moisture content were calculated at these interfaces. These gradients were normally determined by differences using the values at the nodes on either side of the control volume interface. For example, the moisture content gradient was given by

$$\left.\frac{\Delta X}{\Delta z}\right|_{I} = \frac{X_I - X_{I-1}}{\Delta z_{i-1}} \tag{2.73}$$

However, the evaporative front was treated specially. At any given time, the evaporative front was assumed to be located at a control volume interface between two nodes with moisture contents less than and greater than the fibre-saturation point. Thus, there is a rapid transition in moisture content over a very short distance which may only be one or two tracheids wide. On the dry-zone side of the interface, the moisture content and relative humidity at the interface were assumed to be equal to the fibre saturation point and unity, respectively. The vapour pressure gradient in the vapour flux formulation was estimated using a backward difference:

$$\left.\frac{\Delta P_v}{\Delta z}\right|_{i+1} = \frac{P_{sat} - P_v|_I}{\Delta z_i / 2} \tag{2.74}$$

The temperature at the evaporative plane is not fixed at a constant value during the entire drying time. It only becomes constant when the temperature at the front reaches the boiling point of water. When this happens, the temperature-distance profile becomes dicontinuous at the evaporative front. Therefore, the normal temperature difference was used except when the evaporative front reached boiling temperature, T_b at which point the following difference was used:

$$\left.\frac{\Delta T}{\Delta z}\right|_{i+1} = \frac{T_b - T_I}{\Delta z_i / 2} \tag{2.75}$$

A backward difference should approximate the moisture content gradients at the evaporative front more accurately than a difference calculated using values at the nodes on either side of the evaporative plane because this plane represents a discontinuity. The advantage of using this approach is that steep gradients in moisture content and vapour pressure, especially in the initial stages of drying, are avoided to yield improved numerical stability.

This approach will be accurate during the first drying period, when the evaporative plane remains stationary near the surface of the timber board. However, once the evaporative plane begins to recede, its location will lie somewhere between the two grid points at any given time, and will not necessarily be positioned at a control volume interface. The consequence of not tracking the evaporative front properly is a noisy numerical solution in the time domain. However, this problem can be mitigated by concentrating nodes near the evaporative plane which in effect gives a more accurate estimate of the exact position of the evaporative front. The tracking of a moving boundary is usually referred to as a 'Stefan' problem; however, this approach was not attempted in this thesis.

It was assumed that the centreline of the timber board was a symmetry plane. Therefore, gradients in moisture content, vapour pressure and temperature were set equal to zero in the core. The surface continuity equations (Equations (2.21) and (2.22)) were used in conjunction with the mass and energy equations (Equations (2.7) and (2.20)) at the surface node.

After the equations have been discretised, they can then be rearranged into a system of ordinary differential equations of the form

$$\left.\frac{dX}{dt}\right|_I = A_I \tag{2.76}$$

$$\left.\frac{dT}{dt}\right|_I = B_I \tag{2.77}$$

where A_I and B_I are functions of moisture content, temperature, distance and time. These equations were solved simultaneously for each time step using an ordinary differential equation solver for stiff equations called DVODE which was developed by Brown *et al.* [1989].

The experimental profiles of Pang [1994b] and Northway [1989] for the high-temperature drying of sapwood *Pinus radiata* show that the temperature in the wet zone never exceeds 100 °C. This temperature, which is the boiling point of water at one atmosphere, is a thermal barrier. Only when the total pressure in the wet zone exceeds one atmosphere can this maximum temperature rise above 100 °C. The mathematical model does not 'know' about this natural thermal limit. There is nothing in the equations which prevents the temperature increasing above 100 °C. Therefore, the temperature gradient with respect to time is set equal to zero whenever a control

volume located within the wet zone of the timber board reaches 100 °C. Once, the moisture content in that control volume reduces below the fibre-saturation point, the temperature gradient with respect to time is calculated in the normal fashion such that the temperature is free to increase above 100 °C. Moyne *et al.* [1985] take a similar approach by limiting the temperature of the surface to 100 °C when its moisture content is greater than fibre saturation.

2.5 Results

In his experiments, Pang [1994] measured continuously, as the board was dried, the dry and wet-bulb temperatures, the temperatures at six different within-board locations including the surface and centre, and the average moisture content of the board. Each sample was a 100 mm x 50 mm undressed, flat-sawn board of green *Pinus radiata* consisting entirely of either sapwood or heartwood. Density measurements of each sample were made prior to drying. The boards were dried in a tunnel dryer at dry-bulb temperatures ranging from 120 to 140 °C, and wet-bulb temperatures ranging from 65 to 85°C, with a constant air velocity of 5 m/s. The results of some of these experiments are shown in Figures 2.1 and 2.2.

These experimental results were compared with the model predictions to verify the simulations. Three model parameters - liquid permeability, vapour tortuosity, and thin-dry layer width - are the initial input variables required for the simulations. The liquid permeabilities used in the sapwood simulations fell within the range of values measured by Booker [1990] and Kininmonth [1991] for green sapwood *Pinus radiata* (Table 2.1). The variation in permeability between samples is attributed to the biodiversity within timber of the same species.

Only limited experimental data are available for the tortuosity factor. The coefficients in Equation (2.69), which were found by least-squares fitting, resulted in attenuation factors greater than unity which are not physically realistic. Therefore, the coefficients B and n of Equation (2.52) were approximated by fitting the simulation results to a base set of experimental drying data, and using the resultant coefficients in all other drying simulations. Fitting the simulation results to the data of Pang [1994] for the drying conditions of 140/65 °C (Figure 2.1a) yielded values for B and n of 1.5 and 2.5, respectively. The coefficient A in Equation (2.52) is a fitting parameter which is dependant on the physical variability which exists among different samples of the same species.

The width of the thin-dry layer at the start of drying was given a value within the range of 0.5 to 1.5 mm. The moisture content in this thin layer was set to the equilibrium moisture content at ambient conditions (12.4% at 20/15 °C). The average densities of the timber samples were measured by Pang [1994]. These values which are given in the captions of Figures 2.1 and 2.2 were used in the simulations.

It has been shown that the mass-transfer coefficient is not affected by the mass flux from the surface when high-temperature drying of *Pinus radiata* in the range of external conditions tested. Therefore, the mass-transfer coefficient at the surface is close to the values measured by many workers (Kho *et al.* [1990]). The mass-transfer

coefficient based on vapour pressure was given a value of 24×10^{-8} s/m which corresponds to an air velocity of 5 m/s. This value was calculated from the correlation of Kho *et al.* [1990] for mass transfer over a row of timber boards (Equation (2.58)). The heat-transfer coefficient was set to a value of 60 W/m²K which was extracted from the experimental data of Pang [1994]. This value is considered to be the average heat-transfer coefficient over the width of the board, even though it actually represents the local heat-transfer coefficient 60 mm from the leading edge of the sample board. The effect of variable transfer coefficients in the airflow direction are considered in Chapter 3.

The temperature and moisture-content profiles predicted by the model for sapwood and heartwood are given in Figures 2.10 and 2.11, respectively, together with the experimental data of Pang [1994]. The fitted parameters (liquid permeability, k_{ls}, vapour-diffusion attenuation factor, A, and thin-dry layer width, ξ) are given below the figures. The effect of using an attenuation factor that is a function of moisture content and temperature is shown in Figure 2.12. A comparison between the within-board moisture content profiles and the experimental profiles of Pang [1994] is shown in Figure 2.13.

2.6 Discussion

Sapwood experimental profiles

The following observations can be made of the experimental data of Pang [1994] for sapwood *Pinus radiata* (Figure 2.1). In all cases, the surface temperature rises to a plateau between the wet and dry-bulb temperatures and remains there for a short time. During this period, the evaporative plane remains stationary close to the surface of the timber board while moisture is lost. The evaporative plane does not move because moisture flows from the interior zones are able to maintain the position of the plane.

The temperature at points beneath the surface also rise to a plateau; however, these temperatures are lower than the surface temperature. This difference in plateau temperatures is caused by the presence of the thin-dry layer near the surface. When the heat flux to the surface is relatively high, for example when drying at 140 °C, the plateau for within board temperatures in the wet zone is at the boiling point of water. When the surface heat flux is lower, for example when drying at 120 °C, the temperature plateau in the wet zone lies between the wet-bulb temperature and the boiling point of water. Temperatures in the dry zone fall between the surface and wet-zone temperature limit.

The evaporative plane begins to withdraw into the timber board after a while, because moisture flows towards the surface are not large enough to sustain the position of the plane. The beginning of this period is marked by an increase in the surface temperature which rises towards the dry-bulb temperature. The wet-zone temperatures either rise towards the boiling point of water, or if they are already at this temperature, remain constant until the moisture content at each point within the wet zone falls below the fibre-saturation point. They then rise up towards the dry-bulb temperature.

(a)

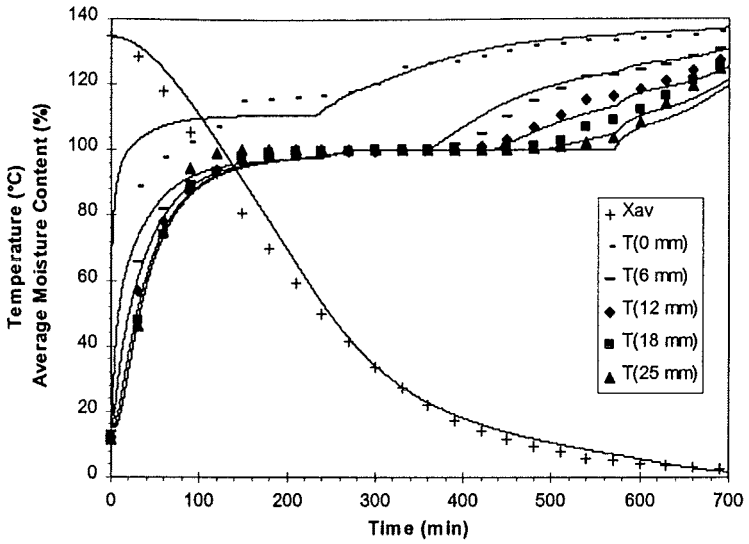

(b)

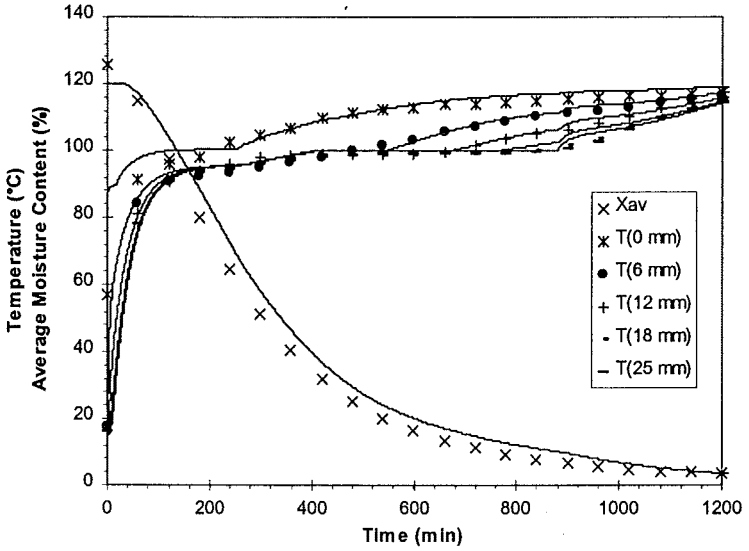

(c)

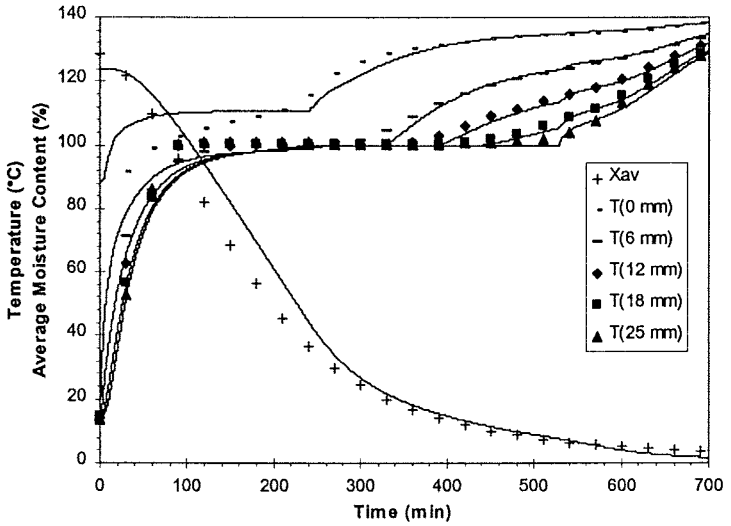

Figure 2.10. Comparison of the simulation results from the present model with experimental data of Pang [1994] for sapwood *Pinus radiata*.

(a) 140/65 °C, K_{ls}=2.5x10^{-15} m ^{2}, A=0.06, ξ=1.5 mm.

(b) 120/85 °C, K_{ls}=1.3x10^{-15} m ^{2}, A=0.06, ξ=1.0 mm.

(c) 140/85 °C, K_{ls}=3.2x10^{-15} m ^{2}, A=0.10, ξ=1.5 mm.

(a)

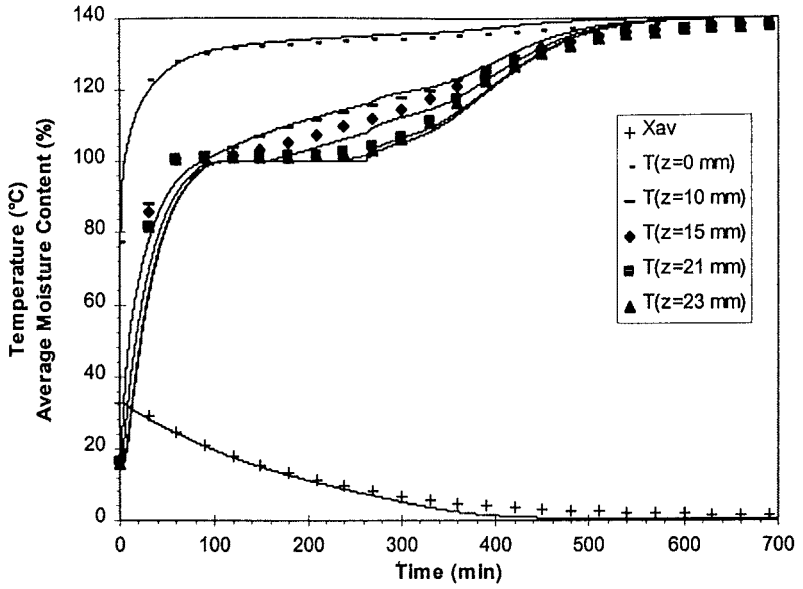

(b)

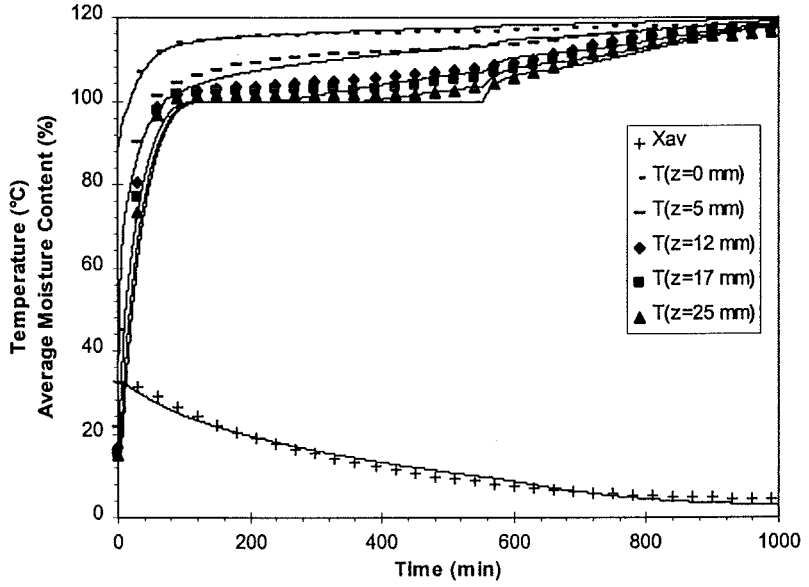

Figure 2.11. Comparison of simulation results from the present model with experimental data of Pang [1994] for heartwood *Pinus radiata*: 140/65 °C, 120/85 °C.
(a) 140/65 °C, D=1.7x10^{-4} kg/ms, A=0.07, ξ=1.5 mm.
(b) 120/85 °C, D=1.0x10^{-4} kg/ms, A=0.04, ξ=1.0 mm.

This period lasts until the centre-line moisture content falls below the fibre-saturation point. This is evident in the profiles of Pang [1994] by an increase in the centre-line temperature above the boiling point of water.

No wet zone exists during the remaining portion of the drying schedule; that is, the moisture content everywhere in the timber board is below the fibre-saturation point.

Heartwood experimental profiles

The heartwood profiles (Figure 2.2) are similar to the sapwood profiles. One difference is that the surface temperature rises towards the dry-bulb temperature

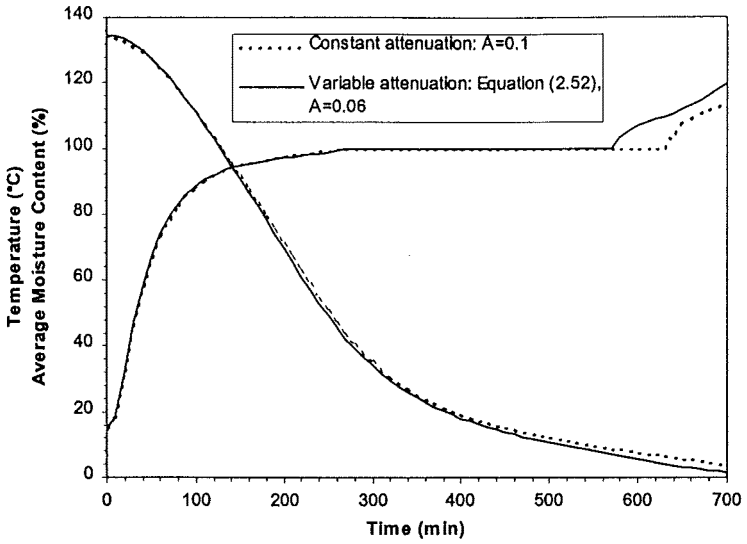

Figure 2.12. The effect of a variable attenuation factor on the drying predictions for sapwood *Pinus radiata*: 140/65 °C, K_{ls}=2.5x10^{-15} m^2, ξ=1.5 mm.

(a)

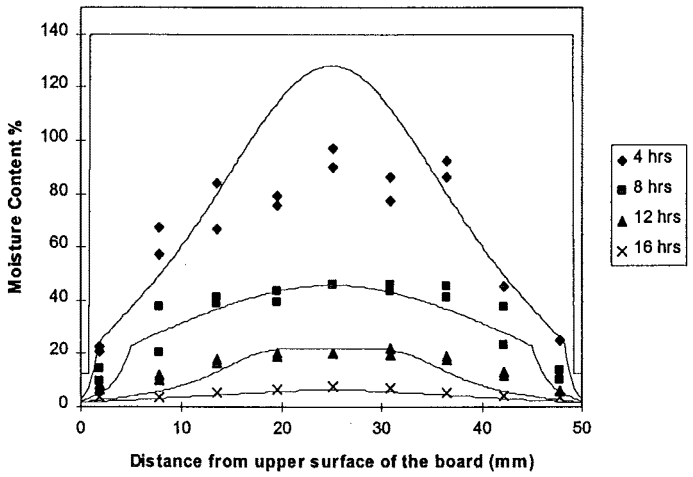

(b)

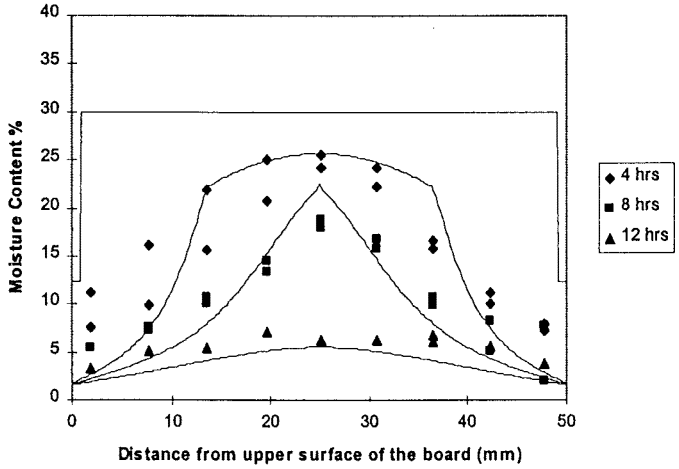

Figure 2.13. Comparison of simulation results of the present model with experimental data of Pang [1994] for sapwood and heartwood: 120/65 °C.

(a) Sapwood, K_{ls}=1.2x10^{-15} m^2, A=0.08, ξ=1.0 mm

(b) Heartwood, D=1.2x10^{-4} kg/ms, A=0.08, ξ=1.0 mm

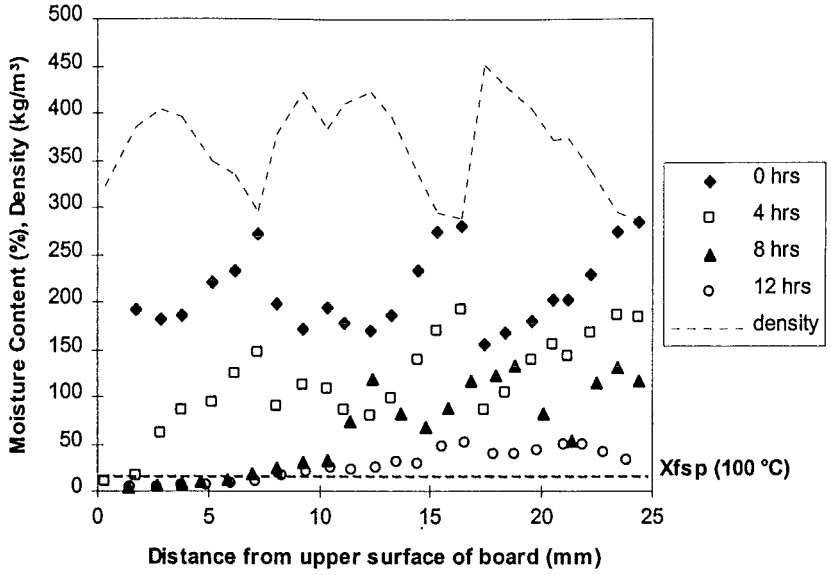

Figure 2.14. Variation of density and moisture content with depth from the outer surface in the drying of a sapwood, flat-sawn board, 50 mm thick, at 120/70 °C (McCurdy and Keey [1998]).

without resting at an intermediate temperature. Thus, the evaporative plane begins to withdraw into the board immediately upon drying. This suggests that no significant interior flows occur to sustain the position of the evaporative plane. The other noteworthy difference is that the initial average moisture content is significantly lower for heartwood by a factor of 2 to 3.

Simulations

There is good agreement between theory and experiment (Figures 2.10 and 2.11). The predicted moisture content and temperature profiles follow the experimental profiles quite closely, and the lengths of each drying period are predicted reasonably accurately. To obtain agreement between theory and experiment required that the liquid permeability and vapour-diffusion attenuation varied between timber samples. The permeability k_{ls} needed to be varied from 1.3 to 3.2×10^{-15} m² which was well within the experimental range of values cited by Kininmonth [1991].

The drying model predicts a slightly lower overall evaporation rate during the initial stages of drying than in practice (compare the average moisture content profiles for the predicted and experimental results (Figure 2.10)). This discrepancy is attributed to an underestimated value for the heat-transfer coefficient. The heat-transfer coefficient extracted from Pang's [1994] experimental data (60 W/m²K) is actually a local heat-transfer coefficient (at a position 60 mm from the leading edge of the board) and is not representative of the entire surface of the board. In fact, a higher heat-transfer coefficient can be expected given that the local transfer coefficients are enhanced at the leading edge of the board and approach an asymptotic value close to 60 W/m²K in this case at the trailing edge (Kho [1993]). A higher heat transfer-coefficient would increase the evaporation rate during the initial stages of drying when the drying process is predominantly heat-transfer controlled.

In the simulations of Stanish *et al.* [1986] and Pang *et al.* [1994], the attenuation factor is given a constant value. However, it is clear from the results of Choong [1963] and Stamm [1959] that this attenuation is dependant on both moisture content and temperature. The attenuation factor decreases when the moisture content is reduced because the woody material shrinks, and diffusion becomes restricted.

Figure 2.12 compares the predicted average moisture content and centre-line temperature profiles for the cases when variable and constant attenuation factors are employed. Note that the profiles for the variable attenuation factor case are also presented in Figure 2.10a. The value for the constant attenuation factor (A=0.1) was chosen so that the resultant profiles matched the profiles for the variable attenuation factor case as closely as possible during the early stages of drying. The remaining model parameters are exactly the same in both cases. Clearly, the attenuation factor has a significant effect on the rate at which the evaporative front recedes within the board. When a constant attenuation factor is employed, the model predicts that the evaporative front reaches the centre-line of the timber board approximately half an hour later than when a variable attenuation factor is used. The application of a variable attenuation factor improves the predicted rate at which the evaporative plane recedes within the board because the amended drying model accounts for changes in the diffusivity of vapour at different moisture contents and temperatures.

It might be expected that a wetting period, during which the average moisture content increases, should be evident in all of the experimental profiles while the temperature of the surface is below the wet-bulb temperature. However, Figures 2.1 and 2.2 show that the average moisture content drops rapidly during the initial stages of drying, even for the sapwood timber sample dried at 120/85°C for which the surface temperature only rises above the wet-bulb temperature after nearly 60 minutes. The surface temperature measured by Pang [1994] is a local temperature which is not representative of the entire surface of the sample board. Clearly, enhanced local transfer coefficients at the leading edge of the sample board have resulted in the leading portion of the board losing moisture more rapidly than any gain in moisture near the trailing portion, where the thermocouple for measuring the surface temperature was located. This illustrates the importance of accounting for the two-dimensional drying behaviour of the timber in the simulations. However, in this chapter a one-dimensional drying model was assumed which predicts a wetting period while the surface temperature is below the wet-bulb temperature. This effect was removed from the numerical calculations by reducing the green moisture content slightly, and setting the moisture fluxes to zero while the surface vapour pressure was less than the external vapour pressure.

The width of the thin-dry layer determines to a certain extent what quasi-steady state surface and wet-zone temperatures are reached during the constant-rate period. For example, when there is no thin-dry layer, and the surface is completely saturated, then the wet-zone temperature during the constant rate period is near the wet-bulb temperature. As the width of the thin-dry layer is increased, so the wet-zone and surface quasi-steady state temperatures increase, although the wet-zone temperature is limited by the boiling point of water. In the simulations, the thin-dry layer was assumed to range from 1.0 to 1.5 mm in width.

The within-board density and moisture content profiles of McCurdy and Keey [1998] show that there are great variations in density and green moisture content due to the presence of growth rings (Figure 2.14). The profiles show large peaks and troughs, with high moisture contents associated with low densities, and conversely, low moisture contents associated with high densities. Density variations have a significant effect on the moisture content profiles as flat-sawn timber dries during the initial stages of drying. However, as the average moisture content falls, the dependence of the within-board moisture-content profiles on density wanes and the profiles become smoother. Figure 2.13 indicates that variations in density and liquid permeability caused by growth rings must be accounted for in the early stages of drying if the within board moisture-content profiles are to be predicted successfully. However, the growth rings have a lesser effect on the attenuation factor and liquid permeability of the timber at the lower moisture contents. The effect is also less likely to be observed in quarter-sawn timber where the growth rings lie normal to the exposed drying faces of the board.

The density variations in Pang's experimental within-board moisture content profiles were not provided in his work. Therefore, variations in density within the board, and their effect on permeability, were not taken into account. Neglect of such variations may be responsible for the deviation of the simulations from experiment in the moisture content profile for sapwood at 4 hours (Figure 2.13a). The experimental profile is less peaky than the predicted one. Increasing the liquid permeability (and reducing the reference attenuation factor to compensate) flattens the moisture-content profile within the wet zone to a certain extent; however, this is not sufficient to match closely theory with experiment. Pang's experimental profiles do not show the great variations in moisture content exhibited by the profiles of McCurdy and Keey [1998] because these variations are smoothed out in Pang's use of wider slices (by a factor of 6) for the same thickness of board.

Figure 2.13a shows that at 8, 12, and 16 hours, the predicted moisture-content profiles in sapwood are in reasonable agreement with the simulations. The most significant difference between these profiles is that theory predicts that the surface moisture content approaches the equilibrium moisture content more rapidly than in practice. This can be clearly seen in the heartwood profiles (Figure 2.13b). Thus, the moisture-transport model for the dry zone (below fibre-saturation) is still not accurate enough, even though the model has been improved by incorporating a variable attenuation factor. Another indicator that the dry-zone transport mechanisms are not being modelled correctly is the surface-temperature profile, which rises too quickly during the heating-up period (Figure 2.10).

The model predicts a discontinuity at the fibre-saturation point. This discontinuity is not clearly evident in the within-board profiles of Pang [1994] (Figure 2.13). However, the experimental within board moisture-content profiles of McCurdy *et al.* [1998] (Figure 2.14) and Northway [1989], which have greater resolution, also show a discontinuity at the fibre-saturation point. Their profiles are in agreement with the profiles predicted in this thesis, which show that once the moisture content at a point in the wet-zone falls to the fibre-saturation point, then it will remain at that value until

the evaporative plane has passed that point within the board, at which time it falls below fibre saturation. This discontinuity differs from the one reported by Chen *et al.* [1996] and Perré *et al.* [1986] in which the moisture content jumped from below fibre saturation to above irreducible saturation.

In heartwood, liquid fluxes above fibre-saturation are not significant enough to maintain the position of the evaporative front near the surface of the timber board as with sapwood. However, Figure 2.13b shows that liquid flows still occur above fibre saturation (otherwise the moisture content in the wet-zone would remain at the green value). In fact, the liquid fluxes in heartwood are of the same order of magnitude as the liquid fluxes experienced by sapwood between fibre and irreducible saturation. It is assumed that liquid migration in heartwood occurs either by surface diffusion on the cell walls or by diffusion through any fine pores by a similar mechanism to moisture movement in sapwood between fibre and irreducible saturation. The diffusion coefficient in Equation (2.49) replaces the liquid permeability as the fitting parameter for the wet zone in the heartwood simulations.

2.7 Conclusions

A model of heat and mass transfer in a highly permeable board of softwood (*Pinus radiata*) has been developed. The moisture-transport mechanisms involved in this model are vapour diffusion in the dry zone (below fibre saturation), and liquid diffusion and convection in the wet zone (above fibre saturation). It is postulated that gaseous-convective fluxes are negligible because total pressure gradients do not build up within the wood due to its high permeability.

The vapour-diffusion flux in the dry zone depends on the tortuosity of the path, which becomes more severe as moisture is lost due to shrinkage of the cell wall and other effects. Liquid can migrate by surface diffusion on the cell wall, or diffusion through the fine pores everywhere in the wet zone. However, liquid-diffusive fluxes are small in comparison to capillary-driven liquid-convection fluxes which only occur above irreducible saturation. The liquid-convection fluxes are dependant on the rates of pit aspiration which are considered to be very rapid near the green condition of the timber.

The predictions of the model compare well with the experimental drying data available in the literature. The calculations demonstrate the importance of accounting for the effect of density variations on the liquid permeability, especially at high core moisture contents, and two-dimensional convective effects which result from enhancement of the local transfer coefficients at the leading edge of the timber boards.

2.8 Symbols

A, B	constants for attenuation factor correlation
b	timber thickness, m
c	molar density, mol/m^3
Cp	heat capacity, J/molK

C_p heat capacity of the humid air flowing over the timber board, J/molK
D effective gas diffusivity (m^2/s), diffusion coefficient, kg/ms
D_{AB} bulk binary diffusivity for air water vapour mixture, m^2/s
E_l effective permebility to liquid flow, s
h surface heat transfer coefficient, W/m^2K
H enthalpy, J/kg
H_{sorp} enthalpy of sorption, J/kg
H_{vap} enthalpy of vaporisation, J/kg
j flux, kg/m^2s
k thermal conductivity of moist wood, W/mK
k_g permeability of moist solid to gaseous flow, m^2
k_l permeability of moist solid to liquid flow, m^2
k_{ls} permeability of satuated solid to liquid flow, m^2
K_1, K_2 parametric functions for bound water sorption correlations
K_c local mass transfer coefficient based on molar concentration, m/s
$\overline{K_c}$ average mas-transfer coefficient based on molar concentration, m/s
$\dot{m}$ phase change rate, kg/m^3s
M molar mass, kg/mol
n constant for attenuation factor correlation
N molar flux, mol/m^2s
P total pressure, Pa
P_{atm} atmospheric pressure, Pa
P_c capillary pressure, Pa
P_v partial pressure of vapour, Pa
P_l liquid presure, Pa
q_o heat transfer rate from surface, W/m^2
R gas constant, J/molK
S saturation
t time, s
T temperature, K
u external velocity, m/s
W parametric functions for bound-water sorption correlations
x distance from leading edge of boards, m
x_v mol fraction of water vapour
X moisture content of timber, kg/kg
X_{ir} irreducible moisture content of timber, kg/kg
X_{max} maximum moisture content of timber, kg/kg
X_{fsp} fibre saturation moisture content of timber, kg/kg
z spatial coordinate measured normal to the surface, m
Z_1, Z_2 parametric functions for bound-water sorption correlations

Greek Letters

α attenuation factor for vapour diffusivity in wood
β mass transfer coefficient based on partial pressure, s/m

ε void fraction
κ ratio of electrical conductivities
λ thermal conductivity of external air, W/mK
μ dynamic viscosity, kg/ms
ν kinematic viscosity, m^2/s
θ Ackermann correction factor
ρ density, kg/m^3
ψ relative humidity

Subscripts

a air
b bound water, boiling point
cw cell wall
dew dew point
f free water
g gas
l liquid water
s surface, wood
v water vapour
w water

Dimensionless Numbers

Pr local Prandtl number
Re local Reynlds number
Sc local Schmidt number
Sh local Sherwood number

2.9 References

Adesanya, B.A., Beard, J.N., Nanda, A.K., 1986, Moisture distribution during high temperature drying of yellow poplar, Drying '86 edited by Mujumdar, A.S., Hemisphere Publishing Corporation, New York, 375-381.

Bird, R.B., Stewart, W.E., Lightfoot, E.N., 1960, Transport phenomena, John Wiley & Sons, Inc, New York.

Booker,R.E., 1990, Changes in transverse wood permeability during the drying of Dacrydium cupressinum and Pinus radiata, *NZ J Forest Science*, 20 (2):231-244.

Brown, P.N., Byrne, G.D., Hindmarsh, A.C., 1989, VODE: A variable coefficient ODE solver, *SIAM J. Sci. Stat. Comput.*, 10:1038-1051.

Ceaglske, N.H., Hougan, O.A., 1937, Drying granular solids, *Ind. Eng. Chem.*, 29:805-813.

Chen, G., Keey, R.B., Walker, J.C.F., 1996, Moisture content profiles in sapwood boards on drying, *Proc 10th International Drying Symposium, Krakow*, Vol A:679-687.

Chen, G., Keey, R.B., Walker, J.C.F., 1997, The drying stress and check development on high-temperature kiln seasoning of sapwood *Pinus radiata* boards. Part 1: Moisture movement and strain model. *Holz als Roh- und Werkstoff*, 55:59-64.

Choong, E.T., 1963, Movement of moisture through a softwood in the hygroscopic range, *Forest Products Journal*, 13 (11): 489-498.

Cunningham, M.J., Sprott, T.J., 1984, Sorption Properties of New Zealand Building Materials, Research Report, R43, Building Research Association of New Zealand.

Evans, R.S., Halvorson, H.N., 1962, Cause and Control of Brown Stain in Western Hemlock, *Forest Products Journal*, 12 (8):367-373.

Huang, C.L.D., 1979, Multi-phase moisture transfer in porous media subjected to temperature gradient, *International Journal Heat and Mass Transfer*, Vol 22:1295-1307.

Kayihan, F., 1982, Simulation heat and mass transfer with local three-phase equilibria in wood drying, *Proc 3rd International Drying Symposium, Birmingham*, Vol 1:123-134.

Keey, R.B.,1978, Introduction to Industrial Drying Operations, Pergamon, Oxford

Kerdemelidis, C., Keey, R.B., 1987, The determination of moisture permeability in Pinus Radiata at moisture contents above the fibre-saturation point using the moment method, BRANZ Contract, Department of Chemical and Process Engineering, University of Canterbury, New Zealand.

Kho, P.C.S., Keey, R.B., Walker, J.C.F., 1990, The variation of local mass transfer coefficients in streamwise direction over a series of in-line blunt slabs, *Proceedings of Chemeca*, Auckland, New Zealand, 1:348-355.

Kininmonth, J.A., Whitehouse, L.J., 1991, Properties and uses of New Zealand radiata pine: volume 1-wood properties, New Zealand Ministry of Forestry, New Zealand Forest Research Institute, Rotorua, New Zealand.

Krischer, O., Karst, W., 1978, Die Wissenschaftlichen Grundlagen der Trocknungstechnik, Springer-Verlag.

Langrish, T.A.G., Brooke, A.S., Davis, C.L., Musch, H.E., Barton, G.W., 1997, An improved drying schedule for Australian Ironbark timber: optimisation and experimental validation, *Drying Technology*, 13(1):47-70.

Luikov, A.V., 1966, Heat and mass transfer in capillary-porous bodies, Pergamon Press, Oxford.

McCurdy, M., Keey, R.B., 1998, Determination of Moisture Saturation Profiles in *Pinus radiata* during high-temperature drying, *Proceedings IPENZ Annual Conference*, Institution of Professional Engineers, New Zealand Inc., 3:22-25.

Moyne, C., Degiovanni, A., 1985, Drying '85 edited by Mujumdar, A.S., Hemisphere Publishing Corporation, New York, 109-115.

Northway, R., 1989, Moisture profiles and wood temperature during very high temperature drying of Pinus radiata explain lack of degrade, Proceedings of the 2nd IUFRO International Wood Drying Symposium, Seattle, 24-28.

Pang, S., Langrish, T.A.G., Keey, R.B., 1994, Moisture movement in softwood timber at elevated temperatures, *Drying Technology*, 12(8):1897-1914.

Pang, S., 1994, High-temperature drying of Pinus radiata boards in a batch kiln. PhD Thesis, University of Canterbury, New Zealand.

Perré, P., Ben Nasrallah, S., Arnaud, G., 1986, A theoretical study of drying: numerical simulations applied to clay-brick and softwood, Drying '86 edited by Mujumdar, A.S., Hemisphere Publishing Corporation, New York, 382-390.

Perré, P., Moser, M., Martin, M., 1993, Advances in transport phenomena during convective drying with superheated steam or moist air, *Int J Heat and Mass Transfer*, 38 (11):2725-2746.

Przesmycki, Z., Strumillo, C., 1985, The mathematical modelling of drying process based on moisture transfer mechanism, Drying '85 edited by Mujumdar, A.S., Hemisphere Publishing Corporation, New York, 126-134.

Schlünder, E.U., 1988, On the mechanism of the constant drying rate period and its relevance to diffusion controlled catalytic gas phase reactions, *Chem. Eng. Science*, 43(10): 2685-2688.

Sherwood, T. K., 1975, Mass Transfer, McGraw-Hill, New York.

Shubin, G.S., 1990, Drying and heat treatment of wood, Lesnaia Promyshlennost, Moscow.

Siau, J.F., 1984, Transport Process in Wood, Springer-Verlag, Berlin.

Siau, J.F., Avramidis, S., 1996, The surface emission coefficient, *Wood and Fibre Science*, 28(2): 178-185.

Simpson, W.T., Rosen, H.N., 1981, Equilibrium moisture content of wood at high temperatures, *Wood and Fibre Science*, 13 (3):150-158.

Skaar, C., 1988, Wood-water Relations, Springer-Verlag, New York.

Spolek, G.A., Plumb, O.A., 1981, Capillary pressure in softwood, *Wood Science and Technology*, Vol 15:189-199.

Stamm, A.J., 1959, Bound-water diffusion into wood in the fibre direction, *Forest Products Journal*, 9 (1): 27-32.

Stamm, A.J., 1960, Bound-water diffusion into wood in the across the fibre directions, *Forest Products Journal*, 10:524-528.

Stamm, A.J., 1964, Wood and Cellulose Science, The Ronald Press Company, New York.

Stamm, A.J., 1971, Review of nine methods for determining the fibre saturation point of wood and wood products, *Wood Science*, Vol 4:114-128.

Stanish, M.A., Schajer, G.S., Kayihan, F., 1986, A mathematical model of drying hygroscopic porous media, *AIChE J*, 32(8):1301-1311.

Stanish, M.A., 1986, The roles of bound water chemical potential and gas phase diffusion in moisture transport through wood, *Wood Sci. Technology*, 19:53-70

Suzuki, M., Maeda, S., 1968, On the mechanism of drying of granular beds: mass transfer from a discontinuous source, *J. Chem. Eng.* Japan, 1: 26-31.

Tesoro, F.O., Choong, E.T., Kimbler, O.K., 1974, Relative permeability and the gross pore structure of wood, *Wood and Fibre Science*, 6(3):226-236.

Treybal, R.E., 1968, Mass Transfer Operations, 2nd Edition, McGraw-Hill, New York.

Van Brakel, J., Heertjes, P.M., 1978, On the period of constant drying rate , *Proc. 1st Int. Symp. on Drying, Montreal* (edited by A.S. Mujumdar), pp 70-75, Science Press, Princton, New Jersey.

Vanek, M., Telschinger, A., 1989, Diffusion coefficients and dimensional resistance factors for different kinds of wood (in German), *Holzforschung und Holzverwertung*, 1:3-6.

Voight, H., Krischer, O., Schauss, H., 1940, (Movement of moisture in the evaporation drying of wood), *Holz Roh-Werkstoff*, 3(10):305-321.

Whitaker, S, 1985, Moisture transport mechanisms during the drying of granular porous media, Drying '85 edited by Mujumdar, A.S., Hemisphere Publishing Corporation, New York, 21-32.

CHAPTER THREE

CONJUGATE TRANSPORT MODEL

A mathematical model was developed in the previous chapter to simulate the movement of moisture and heat within a timber board during the process of drying. The model consisted of one-dimensional partial differential mass and heat balance equations, and expressions for the transport rates of moisture. Convective mass and heat-transfer coefficients were employed at the timber surface to account for the influence of the cross-circulating air. In this chapter, the model developed in the previous chapter will be extended to two dimensions so that the drying behaviour of a row of timber boards can be simulated. Heat and moisture fluxes at the surface of the timber boards will be determined by solving the transport equations for fully turbulent fluid flow through the fillet spaces that separate the timber boards. The resultant set of equations form a rigorous batch-drying model which is a powerful tool for evaluating the accuracy of much simpler drying models such as the batch-drying model developed by Van Meel [1958].

The simplicity of Van Meel's [1958] batch-drying model makes it useful for modelling the kiln-wide drying behaviour of timber in a stack. Two partial differential equations are specified in his model; one is a balance on moisture within the timber, and the second equation forms a mass balance on vapour in the cross-circulating air. A lumped-parameter model for characterising the internal drying kinetics of the timber completes the set of equations which form Van Meel's batch-drying model. A number of simplifying assumptions were made in the development of Van Meel's model. The validity of some of these assumptions will be investigated in this chapter by comparing the results of the simple model with the new rigorous model. In Chapter 4, a kiln-wide model will be developed, based on Van Meel's batch-drying equations, which predicts the drying process of a stack of timber with a maldistribution of fillet space velocities. A number of assumptions must be made in the development of the kiln-wide model which are also investigated in this chapter.

In the first section of this chapter, Van Meel's model will be derived to determine the underlying assumptions involved. The second section covers briefly the concepts of turbulence modelling, which will lead to the presentation of the turbulence flow model and the solution method used in this thesis. The third section will state the internal timber-drying model and the boundary conditions at the interface of the external and internal flow domains. This section will also discuss various assumptions that must be made when coupling the internal and external transport equations. Finally, the solution method for the coupled transport equations and the solutions of the simple and rigorous batch-drying models will be presented in the fourth and fifth sections, respectively.

3.1 Van Meel's Batch-Drying Equations

The concept of the characteristic drying curve is useful for the process design and analysis of kilns for drying timber. This concept involves characterising the drying behaviour of a timber species using a common normalised curve. This curve, known as the characteristic drying curve, is independent of the external drying conditions and, hence, characterises the transport kinetics within the timber. Van Meel's batch-drying equations are formed by incorporating a single characteristic drying curve with a simple moisture balance. Using this model, it is possible to calculate the variation of kiln-wide timber drying rates under different drying conditions of air velocity, temperature and humidity, and thus determine the moisture content profiles throughout a kiln.

The characteristic drying curve describes a functional relationship between a relative drying rate and a normalised moisture content, which are defined by the expressions

$$f = \frac{N_v}{N_{cr}} \tag{3.1}$$

and

$$\Phi = \frac{X - X_e}{X_{cr} - X_e} \tag{3.2}$$

where N_v and X are the drying rate and mean moisture content at any location, and X_e is the equilibrium moisture content corresponding to the external dry and wet-bulb temperatures. N_{cr} and X_{cr} are the drying rate and mean moisture content at the critical point.

The concept of the characteristic drying curve relies on the validity of certain simplifying assumptions. These are:

(1) The critical moisture content is invariant and is independent of the initial moisture content and the external conditions,

(2) All drying curves for a specific substance are geometrically similar; that is, the shape of the curve is independent of the external conditions.

In the drying of heartwood, the critical moisture content is likely to be coincident with the initial moisture content. Therefore, the concept of the characteristic drying curve is unlikely to be valid for a timber stack comprised of heartwood boards with a wide range of green moisture contents. In this chapter, the drying of sapwood timber boards is simulated which avoids this problem.

A number of assumptions must also be made in the development of the moisture balance equations which constitute Van Meel's batch drying model. These assumptions will be outlined in the following brief derivation of the batch-drying equations.

A tall-narrow rectangular element is defined which encompasses the height of the timber stack and an infinitesimally short distance along the width of the stack. A mass balance over this element on each component (vapour in the void space separating timber boards, and water in the wood) gives

$$\frac{\partial \rho_v}{\partial t} + \frac{\partial j_v}{\partial x} + \frac{\partial j_v}{\partial y} = \dot{m}_{lv} \tag{3.3}$$

$$\frac{\partial \rho_l}{\partial t} + \frac{\partial j_l}{\partial x} + \frac{\partial j_l}{\partial y} = -\dot{m}_{lv} \tag{3.4}$$

where $\dot{m}_{lv}$ is the rate of evaporation.

The moisture content of the timber is given by the expression

$$X = \frac{\rho_l}{\rho_s} \frac{1}{1-\varepsilon} \tag{3.5}$$

where ε is the void space in the stack, and ρ_s is the density of the oven-dry timber.

The humidity of the air in the void space is expressed as

$$Y_G = \frac{\rho_v}{\rho_G} \frac{1}{\varepsilon} \tag{3.6}$$

where ρ_G is the density of dry air.

Summing Equations (3.3) and (3.4), and substituting Equations (3.5) and (3.6) into the resultant equation gives

$$\rho_G \varepsilon \frac{\partial Y_G}{\partial t} + \rho_s (1-\varepsilon) \frac{\partial X}{\partial t} + \frac{\partial}{\partial x}(j_v + j_l) + \frac{\partial}{\partial y}(j_v + j_l) = 0 \tag{3.7}$$

Timber boards are butted against each other to form a row and these rows of timber boards are piled above each other, separated by fillets, to form a stack. Air flows through the fillet spaces over the rows of boards. It is assumed that there is no liquid water migration in the airflow direction (x-direction) because liquid water is constrained within each timber board. Furthermore, it is assumed that there is no bulk flow perpendicular to the direction of the mainstream. Thus, vapour is not able to move between fillets via the narrow gaps between adjacent boards.

The flux of vapour in the airflow direction is given by the equation

$$j_v = \left[x_v (N_v + N_a) - D_{AB} \frac{\partial \rho_v}{\partial x} \right] M_v \tag{3.8}$$

It is assumed that the gaseous mixture in the void space moves in plug flow with

velocity u. Thus, the vapour flux is

$$j_v = u\rho_G \varepsilon Y_G - D_{AB}\rho_G \varepsilon \frac{\partial Y_G}{\partial x} \tag{3.9}$$

Substitution of Equation (3.9) into (3.7) and making use of the above listed assumptions gives,

$$\rho_G \varepsilon \frac{\partial Y_G}{\partial t} + \rho_s (1-\varepsilon)\frac{\partial X}{\partial t} + G\frac{\partial (Y_G)}{\partial x} - D_{AB}\rho_G \varepsilon \frac{\partial^2 Y_G}{\partial x^2} = 0 \tag{3.10}$$

where

$$G = u\rho_G \varepsilon \tag{3.11}$$

is the flux of vapour in the void space. Ashworth [1977] shows that the last term in Equation (3.10), known as the dispersion term, can be ignored in all industrial dryers using air as the drying medium. He also shows that the time derivative term for humidity can be neglected.

Equation (3.4) and (3.5) give the expression for the rate of evaporation from the surface of the timber boards

$$\rho_s (1-\varepsilon)\frac{\partial X}{\partial t} = -\dot{m}_{lv} \tag{3.12}$$

The rate of evaporation from a moist surface may be given by the expression (Keey [1978])

$$\dot{m}_{lv} = [f\beta\phi(Y_w - Y_G)]a \tag{3.13}$$

where f is the relative drying rate (or characteristic drying curve) which is a function of moisture content, ϕ is the humidity-potential coefficient, β is the mass transfer coefficient based on the humidity-difference driving force, a is the exposed surface area per volume of dryer, and Y_w is the saturation humidity at the local temperature and pressure.

Equations (3.10)-(3.13) form the mass balance. It is convenient to simplify these equations by defining the following dimensionless parameters:

$$\Pi = \frac{Y_W - Y_G}{Y_W - Y_G^o} \tag{3.14}$$

$$\Phi = \frac{X - X_e}{X_{cr} - X_e} \tag{3.15}$$

$$\xi = \frac{\beta\phi a}{G}x \tag{3.16}$$

$$\theta = \frac{\beta\phi a\left(Y_w - Y_G^o\right)}{\left(X_{cr} - X_e\right)\rho_s\left(1-\varepsilon\right)}t \tag{3.17}$$

Thus, the mass balance simplifies to

$$-\frac{\partial \Pi}{\partial \xi} = -\frac{\partial \Phi}{\partial \theta} = f\Pi \tag{3.18}$$

which are Van Meel's batch drying equations.

Scope

It is the aim of this chapter to determine the validity of the assumption that the characteristic drying curve is independent of the external flow conditions. The validity of further simplifying assumptions, which are made in the development of the kiln-wide model of Chapter 4, are also investigated The most important of these assumptions is that the mass-transfer coefficient is constant over a row of timber boards. This assumption allows the dimensionless length of a row of timber boards cross-circulated with a given velocity to be related to the dimensionless length of another row of boards which is cross-circulated with a different air velocity. However, Kho's [1993] work indicates that the board-averaged mass transfer coefficient varies by a factor of at least 2 over the first three or four boards along a row, and reaches a constant value from the fifth board onwards. It is also assumed that the critical moisture content is independent of the air velocity so that a single characteristic drying curve can be used to describe the internal drying behaviour of every board within the stack, no matter where it is located.

3.2 Overview of Turbulence Modelling

The following section is a brief introduction to turbulence modelling. Thorough reviews on this subject can be found in works by Rodi [1980], Launder and Spalding [1974], and the ASCE Task Committee [1988].

The Navier-Stokes equations and the scalar-transport equations for heat and mass fraction (Table 3.1) describe all the details of the turbulent fluctuating motion of airflow in a kiln. However, the computing power required for the direct solution of these equations for fully turbulent flows is enormous. In fact, turbulent flows cannot presently be resolved by a numerical calculation procedure because they produce eddying motion of a wide range of length and time scales, and enormous computing meshes are required to describe the processes at all of these scales. Fortunately, details of each and every eddy in the flow are not required and only the average quantities are of interest.

Navier-Stokes Equations

Continuity
$$\frac{\partial \rho}{\partial t} + div(\rho \mathbf{u}) = 0$$

x-momentum
$$\frac{\partial (\rho u)}{\partial t} + div(\rho u \mathbf{u}) = -\frac{\partial P}{\partial x} + div(\mu grad u) + S_{Mx}$$

y-momentum
$$\frac{\partial (\rho v)}{\partial t} + div(\rho v \mathbf{u}) = -\frac{\partial P}{\partial y} + div(\mu grad v) + S_{My}$$

z-momentum
$$\frac{\partial (\rho w)}{\partial t} + div(\rho w \mathbf{u}) = -\frac{\partial P}{\partial z} + div(\mu grad w) + S_{Mz}$$

Scalar-Transport Equation

$$\frac{\partial (\rho \Phi)}{\partial t} + div(\rho \Phi \mathbf{u}) = div(\Gamma_{\Phi} grad \Phi) + S_{\Phi}$$

Table 3.1. Governing equations of the flow of a compressible Newtonian fluid.

Continuity

$$\frac{\partial \rho}{\partial t} + div(\rho \overline{\mathbf{U}}) = 0$$

Momentum

$$\frac{\partial (\rho \overline{U})}{\partial t} + div(\rho \overline{U}\, \overline{\mathbf{U}}) = -\frac{\partial P}{\partial x} + div(\mu grad \overline{U}) + \left[-\frac{\partial (\rho \overline{uu})}{\partial x} - \frac{\partial (\rho \overline{uv})}{\partial y} - \frac{\partial (\rho \overline{uw})}{\partial z} \right] + S_{Mx}$$

$$\frac{\partial (\rho \overline{V})}{\partial t} + div(\rho \overline{V}\, \overline{\mathbf{U}}) = -\frac{\partial P}{\partial y} + div(\mu grad \overline{V}) + \left[-\frac{\partial (\rho \overline{uv})}{\partial x} - \frac{\partial (\rho \overline{vv})}{\partial y} - \frac{\partial (\rho \overline{vw})}{\partial z} \right] + S_{My}$$

$$\frac{\partial (\rho \overline{W})}{\partial t} + div(\rho \overline{W}\, \overline{\mathbf{U}}) = -\frac{\partial P}{\partial z} + div(\mu grad \overline{W}) + \left[-\frac{\partial (\rho \overline{uw})}{\partial x} - \frac{\partial (\rho \overline{vw})}{\partial y} - \frac{\partial (\rho \overline{ww})}{\partial z} \right] + S_{Mz}$$

Scalar Transport

$$\frac{\partial (\rho \overline{\Phi})}{\partial t} + div(\rho \overline{\Phi}\, \overline{\mathbf{U}}) = div(\Gamma_{\overline{\Phi}} grad \overline{\Phi}) + \left[-\frac{\partial (\rho \overline{u\varphi})}{\partial x} - \frac{\partial (\rho \overline{v\varphi})}{\partial y} - \frac{\partial (\rho \overline{w\varphi})}{\partial z} \right] + S_{\overline{\Phi}}$$

Table 3.2. Turbulent Mean-Flow Equations for compressible flows

The details of the turbulence fluctuations can be avoided by adopting the statistical approach in which only the average effect of the turbulence fluctuations on the mean quantities is considered. Average quantities are defined as follows

$$\overline{\Psi} = \frac{1}{\Delta t}\int_0^{\Delta t} \Psi dt \tag{3.19}$$

where the averaging time, Δt, is long compared with the time scales of the turbulent motion but small compared with that of the mean flow in transient problems. The quantity Ψ represents a velocity component, heat, or concentration (humidity). Transport equations for these average quantities can be derived by separating the instantaneous values of the various quantities into mean and fluctuating parts,

$$\Psi = \overline{\Psi} + \psi \tag{3.20}$$

then introducing Equation (3.20) into the original time-dependant Navier-Stokes and scalar-transport equations (Table 3.1), and finally averaging as indicated by Equation (3.19). The resulting equations for the mean flows are shown in Table 3.2.

The instantaneous continuity, Navier-Stokes, and scalar equations (Table 3.1) form a closed set of five equations with five unknowns (u, v, w, P, and Φ) and are therefore solvable. This form of the transport equations is often used to calculate laminar flows. The turbulent mean-flow equations (Table 3.2), however, do not form a closed set. They are similar to the original Navier-Stokes and scalar-transport equations presented in Table 3.1, but the process of time-averaging has introduced new unknown terms, involving products of fluctuating velocities and/or scalars ($\overline{uu}$, $\overline{uv}, \overline{w\varphi}$, etc.), in the resulting time-average momentum and scalar equations. Physically, these terms represent the rate of transport (or fluxes) of momentum, heat or concentration due to the fluctuating turbulent motion. The velocity terms appear to act as stresses on the fluid and are therefore called turbulent or Reynolds stresses. The turbulent mean-flow equations can only be solved for the average dependant variables when the turbulence terms can be determined in some way. Thus, the task of any turbulence model is to represent the turbulence terms in the mean-flow equations in a way that closes these equations by relating the turbulence terms to the average dependant variables.

A parameter used in many turbulence models is the eddy viscosity, μ_t, which was introduced by Boussinesq on the assumption that, by analogy to the viscous stresses in laminar flow, the turbulent stresses are proportional to the mean-velocity gradients:

$$\tau_{ij} = -\rho\overline{u_i u_j} = \mu_t\left(\frac{\partial \overline{U}_i}{\partial x_j} + \frac{\partial \overline{U}_j}{\partial x_i}\right) - 2\rho k\delta_{ij} \tag{3.21}$$

where δ_{ij} is the Kronecker delta (δ_{ij}=1 if i=j, and δ_{ij}=0 if $i \neq j$). The eddy viscosity μ_t is, in contrast to the molecular viscosity μ, not a fluid property but depends

strongly on the state of the turbulence and may vary considerably over the flow field. Hence, an eddy-viscosity turbulence model has in general the task of determining the distribution of the eddy viscosity μ_t over the flow field.

In direct analogy to the turbulent momentum transport, the turbulent heat or concentration transport is often related to the gradient of the transport quantity:

$$-\rho\overline{u_i\varphi} = \Gamma_t \frac{\partial \overline{\Phi}}{\partial x_i} \tag{3.22}$$

where Γ_t is the turbulent diffusivity. Like the eddy viscosity, Γ_t is not a fluid property but depends on the state of the turbulence and must be specified as part of the turbulence models. In most models, Γ_t is directly related to the eddy viscosity by the equation

$$\Gamma_t = \frac{\mu_t}{\sigma_t} \tag{3.23}$$

where σ_t is the turbulent Prandtl number, for the heat-transport equation, or the turbulent Schmidt number, for the concentration-transport equation. Constant values are usually assumed for σ_t.

A wide variety of turbulence models have been proposed, ranging from the use of constant eddy viscosities μ_t over the flow field to differential transport equations for the turbulent momentum and heat/concentration fluxes. The k-ε model was employed in this chapter because it is the most widely used and validated turbulence model. It uses the eddy-viscosity hypothesis for the turbulence. Two transport equations are solved: one for the turbulent kinetic energy k and one for the rate of dissipation of turbulence kinetic energy ε. The quantities k and ε characterise the local state of the turbulence. The two transport equations account for the effects of the transport of turbulence in space and time by convection due to the mean motion of the fluid and by diffusion resulting from the turbulent motion, and for the production and destruction of turbulence.

In the development of the k-ε model, it is assumed that one velocity scale ϑ and one length scale l suffice to describe the effects of turbulence. On dimensional grounds, the kinematic turbulent viscosity ν_t, which has dimensions m²/s, can be expressed as a product of the turbulent-velocity scale ϑ (m/s) and a turbulent-length scale l (m):

$$\nu_t = C\vartheta l \tag{3.24}$$

where C is a constant of proportionality. Thus, the dynamic turbulent viscosity is given by the equation

$$\mu_t = C\rho\vartheta l \tag{3.25}$$

The velocity scale ϑ, which characterises the velocity fluctuations, is defined by $\sqrt{k}$ where k is the kinematic energy of the turbulent motion per unit mass as defined by the equation

$$k = \frac{1}{2}\left(u^2 + v^2 + w^2\right) \tag{3.26}$$

The length scale l, characterising the size of the eddies which contribute to the turbulent stresses, is defined by the equation

$$l = \frac{k^{3/2}}{\varepsilon} \tag{3.27}$$

Thus, the eddy viscosity is related to k and ε by the following equation:

$$\mu_t = \rho C_\mu \frac{k^2}{\varepsilon} \tag{3.28}$$

Exact forms of the transport equations for k and ε can be derived from the Navier-Stokes equations, although these equations contain certain higher-order terms which must be approximated by models in order to achieve closure. The resultant turbulence model becomes rather empirical in nature. The standard form of the steady two-dimensional k-ε model is given in Table 3.3. The empirical constants σ_k, σ_ε, C_1, C_2, and C_μ take on the values of 0.09, 1.44, 1.92, 1.0, and 1.3, respectively. These values were found by comprehensive data fitting for a wide range of turbulent flows. The continuity, momentum, heat, and concentration transport equations are also shown in Table 3.3. Note that the dependent variables u, v, H, and Y, are now defined as the averaged velocity components, averaged enthalpy, and averaged vapour mass fraction, respectively.

The form of the k-ε model shown in Table 3.3 is valid only for fully turbulent flows at high Reynolds numbers. However, close to solid walls, there are regions where the local Reynolds number becomes small such that viscous effects predominate over the turbulent effects. Therefore, the model equations do not accurately represent the turbulence in the near-wall region. The high-Reynolds number k-ε model avoids the need to integrate the model equations right through to the wall by making use of wall functions to describe the behaviour of the near-wall flows. These wall functions were developed by making use of the universal behaviour of near-wall flows. This method will be discussed later on in the chapter.

3.2.1 Control-Volume Method

In this thesis, the flow domain is solved for the dependent variable using the finite difference approach, specifically the Control-Volume method, to derive a set of algebraic equations that are solved using the SIMPLER algorithm due to Patanker and

Continuity equation

$$\frac{\partial(\rho u)}{\partial x}+\frac{\partial(\rho v)}{\partial y}=0$$

X-momentum equation

$$\frac{\partial(\rho uu)}{\partial x}+\frac{\partial(\rho vu)}{\partial y}=\frac{\partial}{\partial x}\left[(\mu_l+\mu_t)\frac{\partial u}{\partial x}\right]+\frac{\partial}{\partial y}\left[(\mu_l+\mu_t)\frac{\partial u}{\partial y}\right]+S_u$$

$$S_u=-\frac{\partial p}{\partial x}+\frac{\partial}{\partial x}\left[(\mu_l+\mu_t)\frac{\partial u}{\partial x}\right]+\frac{\partial}{\partial y}\left[(\mu_l+\mu_t)\frac{\partial v}{\partial x}\right]-\frac{\partial}{\partial x}\left[\frac{2}{3}(\mu_l+\mu_t)\left(\frac{\partial u}{\partial x}+\frac{\partial v}{\partial y}\right)\right]$$

Y-momentum equation

$$\frac{\partial(\rho uv)}{\partial x}+\frac{\partial(\rho vv)}{\partial y}=\frac{\partial}{\partial x}\left[(\mu_l+\mu_t)\frac{\partial v}{\partial x}\right]+\frac{\partial}{\partial y}\left[(\mu_l+\mu_t)\frac{\partial v}{\partial y}\right]+S_v$$

$$S_v=-\frac{\partial p}{\partial y}+\frac{\partial}{\partial y}\left[(\mu_l+\mu_t)\frac{\partial v}{\partial y}\right]+\frac{\partial}{\partial x}\left[(\mu_l+\mu_t)\frac{\partial u}{\partial y}\right]-\frac{\partial}{\partial y}\left[\frac{2}{3}(\mu_l+\mu_t)\left(\frac{\partial u}{\partial x}+\frac{\partial v}{\partial y}\right)\right]$$

Energy equation

$$\frac{\partial(\rho uH)}{\partial x}+\frac{\partial(\rho vH)}{\partial y}=\frac{\partial}{\partial x}\left[\left(\frac{\lambda}{C_P}+\frac{\mu_t}{\sigma_H}\right)\frac{\partial H}{\partial x}\right]+\frac{\partial}{\partial y}\left[\left(\frac{\lambda}{C_P}+\frac{\mu_t}{\sigma_H}\right)\frac{\partial H}{\partial y}\right]$$

Mass fraction equation

$$\frac{\partial(\rho uY_A)}{\partial x}+\frac{\partial(\rho vY_A)}{\partial y}=\frac{\partial}{\partial x}\left[\left(\rho D_{AB}+\frac{\mu_t}{\sigma_Y}\right)\frac{\partial Y_A}{\partial x}\right]+\frac{\partial}{\partial y}\left[\left(\rho D_{AB}+\frac{\mu_t}{\sigma_Y}\right)\frac{\partial Y_A}{\partial y}\right]$$

Turbulent kinetic energy equation

$$\frac{\partial(\rho uk)}{\partial x}+\frac{\partial(\rho vk)}{\partial y}=\frac{\partial}{\partial x}\left[\left(\mu_l+\frac{\mu_t}{\sigma_k}\right)\frac{\partial k}{\partial x}\right]+\frac{\partial}{\partial y}\left[\left(\mu_l+\frac{\mu_t}{\sigma_k}\right)\frac{\partial k}{\partial y}\right]+S_k$$

$$S_k=G-\rho\varepsilon$$

continued...

Table 3.3. Turbulent Flow Equations.

Turbulent dissipation rate equation

$$\frac{\partial(\rho u\varepsilon)}{\partial x}+\frac{\partial(\rho v\varepsilon)}{\partial y}=\frac{\partial}{\partial x}\left[\left(\mu_l+\frac{\mu_t}{\sigma_\varepsilon}\right)\frac{\partial\varepsilon}{\partial x}\right]+\frac{\partial}{\partial y}\left[\left(\mu_l+\frac{\mu_t}{\sigma_\varepsilon}\right)\frac{\partial\varepsilon}{\partial y}\right]+S_\varepsilon$$

$$S_\varepsilon=C_1\left(\frac{\rho\varepsilon}{k}\right)G-C_2\left(\frac{\rho\varepsilon^2}{k}\right)$$

Generation turbulent kinetic energy

$$G=(\mu_l+\mu_t)\left[2\left(\left(\frac{\partial u}{\partial x}\right)^2+\left(\frac{\partial v}{\partial y}\right)^2\right)+\left(\frac{\partial u}{\partial y}+\frac{\partial v}{\partial x}\right)^2-\frac{2}{3}\left(\frac{\partial u}{\partial x}+\frac{\partial v}{\partial y}\right)^2\right]-\frac{2}{3}\rho k\left(\frac{\partial u}{\partial x}+\frac{\partial v}{\partial y}\right)$$

Table 3.3. Turbulent Flow Equations.

Spalding [1972]. The following section is a brief account of the solution methods used in this thesis. More detail about these techniques can be found in Versteeg *et al.* [1992] and Patankar [1980].

The Control-Volume method involves integrating the partial differential equations over control volumes centered on grid points which cover the flow domain of interest. This yields a set of discretised conservation equations for every node within the flow domain. These equations represent the set of algebraic equations that need to be solved. Normally iterative numerical techniques are used to solve large equation sets. These methods start the solution process from a guessed distribution of the transport variable and perform successive updates until a converged solution is obtained. The SIMPLER algorithm is one such example of an iterative numerical method.

Discretising the Scalar-Transport Equation

This section illustrates the Control-Volume method for discretising the scalar-transport equations, although the same method is used to discretise the momentum equations. The scalar variables include vapour mass fraction (Y), enthalpy (H), turbulent kinetic energy (k), and turbulent dissipation (ε). The generalised steady state two-dimensional transport equation is

$$\frac{\partial(\rho u\phi)}{\partial x}+\frac{\partial(\rho v\phi)}{\partial y}=\frac{\partial}{\partial x}\left[\Gamma_\phi\frac{\partial\phi}{\partial x}\right]+\frac{\partial}{\partial y}\left[\Gamma_\phi\frac{\partial\phi}{\partial y}\right]+S_\phi \tag{3.29}$$

where ϕ is the scalar variable and S_ϕ is the scalar source term. The control volume shown in Figure 3.1 is considered. Integrating the transport equation over the control volume yields the following form:

$$\int\frac{\partial(\rho u\phi)}{\partial x}dV+\int\frac{\partial(\rho v\phi)}{\partial y}dV=\int\frac{\partial}{\partial x}\left[\Gamma_\phi\frac{\partial\phi}{\partial x}\right]dV+\int\frac{\partial}{\partial y}\left[\Gamma_\phi\frac{\partial\phi}{\partial y}\right]dV+\int S_\phi dV \tag{3.30}$$

When expanded, this becomes

$$(\rho uA\phi)_e-(\rho uA\phi)_e+(\rho uA\phi)_n-(\rho uA\phi)_s=\left(\Gamma A\frac{\partial\phi}{\partial x}\right)_e-\left(\Gamma A\frac{\partial\phi}{\partial x}\right)_w+\left(\Gamma A\frac{\partial\phi}{\partial y}\right)_n-\left(\Gamma A\frac{\partial\phi}{\partial y}\right)_s+\Delta V\bar{S}_\phi \tag{3.31}$$

Here A is the cross-sectional area of the control volume face, ΔV is the volume and $\bar{S}$ is the average value of source over the control volume. The continuity equation may be similarly integrated to give

$$(\rho uA)_e-(\rho uA)_w+(\rho uA)_n-(\rho uA)_s=0 \tag{3.32}$$

Two variables, F and D, are defined which represent the convective mass flux and diffusion conductance at the cell faces:

$$F=\rho uA$$
$$D=\frac{\Gamma}{\delta x}A \text{ or } D=\frac{\Gamma}{\delta y}A$$

The integrated transport and continuity equations may now be written

$$F_e\phi_e-F_w\phi_w+F_n\phi_n-F_s\phi_s=D_e(\phi_E-\phi_P)-D_w(\phi_P-\phi_W)+D_n(\phi_N-\phi_P)-D_s(\phi_P-\phi_S)+\Delta V\bar{S}_\phi \tag{3.33}$$

and

$$F_e-F_w+F_n-F_s=0 \tag{3.34}$$

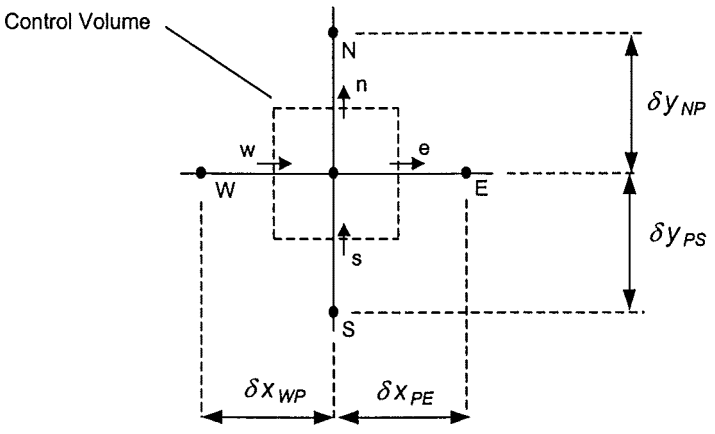

Figure 3.1. A control volume around node P.

The scalar variable ϕ must be evaluated at the east, west, north and south control volume faces. This may be evaluated using either a central differencing scheme or an upwind differencing scheme. Central differencing is more accurate at lower flows when diffusional transport dominates, whereas upwind differencing is more accurate in higher flows when convective transport dominates. The hybrid-differencing scheme is based on a combination of both central and upwind differencing schemes.

a) Central differencing scheme

The central differencing scheme uses a linear interpolation to compute the cell face values ϕ. The following approximations are made

$$\phi_e = \frac{\phi_E + \phi_P}{2},\ \phi_w = \frac{\phi_P + \phi_W}{2},\ \phi_n = \frac{\phi_N + \phi_P}{2},\ \phi_s = \frac{\phi_P + \phi_S}{2}$$

Substitution of these expressions into Equation (3.33) and rearrangement gives

$$\left[\left(D_w + \frac{F_w}{2}\right) + \left(D_e - \frac{F_e}{2}\right) + \left(D_s + \frac{F_s}{2}\right) + \left(D_n - \frac{F_n}{2}\right) + \left(F_e - F_w + F_n - F_s\right)\right]\phi_P =$$

$$\left(D_w + \frac{F_w}{2}\right)\phi_W + \left(D_e - \frac{F_e}{2}\right)\phi_E + \left(D_s + \frac{F_s}{2}\right)\phi_S + \left(D_n - \frac{F_n}{2}\right)\phi_N + \Delta V\bar{S}_\phi \tag{3.35}$$

The coefficients of the above equation can be identified as a_W, a_E, a_S, and a_N, and the source term can be represented in linearised form as

$$\Delta V\bar{S}_\phi = S_u + S_p\phi_P \tag{3.36}$$

Given the continuity equation (Equation 3.34), then the final form of the discretised equation becomes,

$$a_P\phi_P = a_W\phi_W + a_E\phi_E + a_S\phi_S + a_N\phi_N + S_u \tag{3.37}$$

where $a_P = a_W + a_E + a_S + a_N - S_P$

$$a_W = D_w + \frac{F_w}{2}$$

$$a_E = D_e - \frac{F_e}{2}$$

$$a_S = D_s + \frac{F_s}{2}$$

$$a_N = D_n - \frac{F_n}{2}$$

b) Upwind differencing scheme

The upwind differencing scheme takes into account the flow direction when determining the value ϕ at a cell face. The following approximations are made

$$\phi_w = \begin{cases} \phi_W & F_w > 0 \\ \phi_P & F_w < 0 \end{cases} \qquad \phi_e = \begin{cases} \phi_P & F_e > 0 \\ \phi_E & F_e < 0 \end{cases}$$

$$\phi_s = \begin{cases} \phi_S & F_s > 0 \\ \phi_P & F_s < 0 \end{cases} \qquad \phi_n = \begin{cases} \phi_P & F_n > 0 \\ \phi_N & F_n < 0 \end{cases}$$

Substituting these expressions into Equation (3.33), making use of the linearised source term given in Equation (3.36) and the continuity equation given in Equation (3.34), and finally rearranging gives

$$a_P\phi_P = a_W\phi_W + a_E\phi_E + a_S\phi_S + a_N\phi_N + S_u$$

where $a_P = a_W + a_E + a_S + a_N - S_P$

$$a_W = D_w + max(F_w, 0)$$
$$a_E = D_e + max(0, -F_e)$$
$$a_S = D_s + max(F_s, 0)$$
$$a_N = D_n + max(0, -F_n)$$

c) Hybrid differencing scheme

The hybrid-differencing scheme is a combination of both the central and upwind differencing schemes. It combines the advantages of upwind differencing when there is strong convection, with the greater accuracy of central differencing when diffusion dominates. Hybrid differencing has been widely used in commercial computational fluid dynamics (CFD) packages and has proved to be very useful for predicting practical flows. It uses piecewise formulae to evaluate the net flux through each control volume. The discretised equation is,

$$a_P\phi_P = a_W\phi_W + a_E\phi_E + a_S\phi_S + a_N\phi_N + S_u \tag{3.38}$$

which has coefficients defined by the following formulae:

$$a_P = a_W + a_E + a_S + a_N - S_P \tag{3.39}$$

$$a_W = max\left[F_w, \left(D_w + \frac{F_w}{2}\right), 0\right] \tag{3.40}$$

$$a_E = max\left[-F_e, \left(D_e - \frac{F_e}{2}\right), 0\right] \tag{3.41}$$

$$a_S = max\left[F_s, \left(D_s + \frac{F_s}{2}\right), 0\right] \tag{3.42}$$

Face	West	East	South	North
F	$(\rho u)_w A_w$	$(\rho u)_e A_e$	$(\rho u)_s A_s$	$(\rho u)_n A_n$
D	$\frac{\Gamma_w}{\delta x_{WP}} A_w$	$\frac{\Gamma_e}{\delta x_{PE}} A_e$	$\frac{\Gamma_s}{\delta y_{SP}} A_s$	$\frac{\Gamma_n}{\delta y_{PN}} A_n$

Table 3.4. Definitions for the convection and diffusion coefficients, F and D.

$$a_N = max\left[-F_n, \left(D_n - \frac{F_n}{2}\right), 0\right] \tag{3.43}$$

In the above expressions, the values of F and D are calculated with the expressions defined in Table 3.4.

Discretising the Momentum-Transport Equations

Transport equations for each velocity component are derived in a similar fashion to the scalar variable. A staggered grid for the velocity components is employed to avoid problems associated with a 'checker-board' pressure field (Patankar [1980]). Scalar variables such as pressure and enthalpy are evaluated at ordinary nodal points while the velocity components are calculated on staggered grids centred around the cell faces. The arrangement for a two-dimensional flow calculation is shown in Figure 3.2. The scalar variables are stored at nodes marked $(\bullet)$. The velocities are defined at the (scalar) cell faces between nodes and are indicated by arrows. Horizontal arrows indicate the locations for u-velocity nodes and vertical ones denote those for v-velocity nodes. The points defined previously as P, W, E, N, and S become (I,J), (I-1,J), (I+1,J), (I,J+1), and (I,J-1) for the scalar variables, and (i,J), (i-1,J), (i+1,J), (i,J+1), and (i,J-1) for the u-velocity component, and (I,j), (I-1,j), (I+1,j), (I,j+1), (I,j-1) for the v-velocity component.

Using the new notation shown in Figure 3.2, the discretised continuity, momentum and scalar equations become

$$\left[(\rho uA)_{i+1,J} - (\rho uA)_{i,J}\right] + \left[(\rho vA)_{I,j+1} - (\rho vA)_{I,j}\right] = 0 \tag{3.44}$$

$$a_{i,J} u_{i,J} = \sum (a_{nb} u_{nb})_u - (p_{I,J} - p_{I-1,J}) A_{i,J} + b_{i,J} \tag{3.45}$$

$$a_{I,j} v_{I,j} = \sum (a_{nb} v_{nb})_v - (p_{I,J} - p_{I,J-1}) A_{I,j} + b_{I,j} \tag{3.46}$$

$$a_{I,J} \phi_{I,J} = \sum (a_{nb} \phi_{nb})_\phi + b_{I,J} \tag{3.47}$$

where A is the cell face area, b is the source term, and the coefficients a are defined by Equations (3.39) to (3.43). The coefficients a contain combinations of the convective flux F and the diffusive conductance D (Table 3.4). Using the new notation, these coefficients become for a uniformly spaced grid:

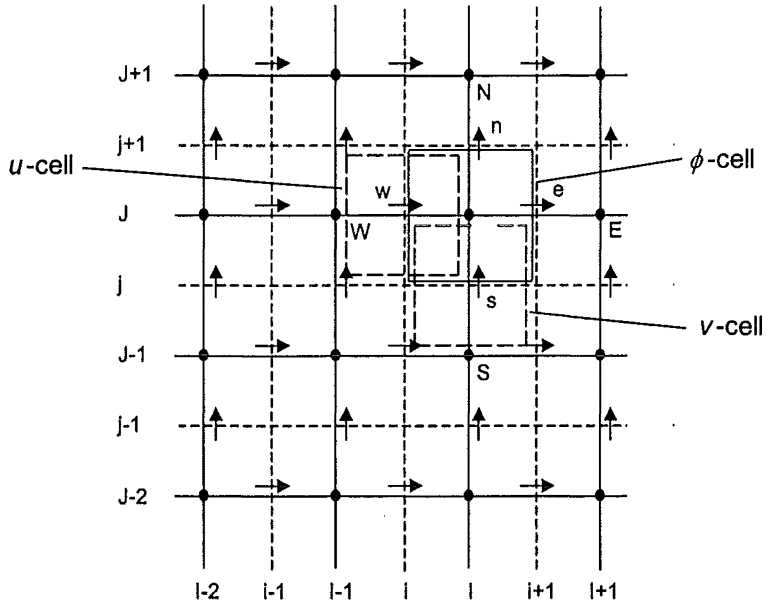

Figure 3.2. The grid arrangement for a two-dimensional flow calculation.

u-velocity equation

$$F_w = (\rho u)_w = \frac{F_{i,J} + F_{i-1,J}}{2} = \frac{1}{2}\left[\left(\frac{\rho_{I,J} + \rho_{I-1,J}}{2}\right)u_{i,J} + \left(\frac{\rho_{I-1,J} + \rho_{I-2,J}}{2}\right)u_{i-1,J}\right]$$

$$F_e = (\rho u)_e = \frac{F_{i+1,J} + F_{i,J}}{2} = \frac{1}{2}\left[\left(\frac{\rho_{I+1,J} + \rho_{I,J}}{2}\right)u_{i+1,J} + \left(\frac{\rho_{I,J} + \rho_{I-1,J}}{2}\right)u_{i,J}\right]$$

$$F_s = (\rho v)_s = \frac{F_{I,j} + F_{I-1,j}}{2} = \frac{1}{2}\left[\left(\frac{\rho_{I,J} + \rho_{I,J-1}}{2}\right)v_{I,j} + \left(\frac{\rho_{I-1,J} + \rho_{I-1,J-1}}{2}\right)v_{I-1,j}\right]$$

$$F_n = (\rho v)_n = \frac{F_{I,j+1} + F_{I-1,J+1}}{2} = \frac{1}{2}\left[\left(\frac{\rho_{I,J+1} + \rho_{I,J}}{2}\right)v_{I,j+1} + \left(\frac{\rho_{I-1,J+1} + \rho_{I-1,J}}{2}\right)v_{I-1,j+1}\right]$$

$$D_w = \frac{\Gamma_{I-1,J}}{x_i - x_{i-1}}$$

$$D_e = \frac{\Gamma_{I,J}}{x_{i+1} - x_i}$$

$$D_s = \frac{\Gamma_{I-1,J} + \Gamma_{I,J} + \Gamma_{I-1,J-1} + \Gamma_{I,J-1}}{4(y_J - y_{J-1})}$$

$$D_n = \frac{\Gamma_{I-1,J+1} + \Gamma_{I,J+1} + \Gamma_{I-1,J} + \Gamma_{I,J}}{4(y_{J+1} - y_J)}$$

v-velocity equation

$$F_w = (\rho u)_w = \frac{F_{i,j} + F_{i,J-1}}{2} = \frac{1}{2}\left[\left(\frac{\rho_{I,J} + \rho_{I-1,J}}{2}\right)u_{i,J} + \left(\frac{\rho_{I-1,J-1} + \rho_{I,J-1}}{2}\right)u_{i,J-1}\right]$$

$$F_e = (\rho u)_e = \frac{F_{i+1,J} + F_{i,J-1}}{2} = \frac{1}{2}\left[\left(\frac{\rho_{I+1,J} + \rho_{I,J}}{2}\right)u_{i+1,J} + \left(\frac{\rho_{I,J-1} + \rho_{I+1,J-1}}{2}\right)u_{i+1,J-1}\right]$$

$$F_s = (\rho v)_s = \frac{F_{I,j-1} + F_{I,j}}{2} = \frac{1}{2}\left[\left(\frac{\rho_{I,J-1} + \rho_{I,J-2}}{2}\right)v_{I,j-1} + \left(\frac{\rho_{I,J} + \rho_{I,J-1}}{2}\right)v_{I,j}\right]$$

$$F_n = (\rho v)_n = \frac{F_{I,j} + F_{I,J+1}}{2} = \frac{1}{2}\left[\left(\frac{\rho_{I,J} + \rho_{I,J-1}}{2}\right)v_{I,j} + \left(\frac{\rho_{I,J+1} + \rho_{I,J}}{2}\right)v_{I,J+1}\right]$$

$$D_w = \frac{\Gamma_{I-1,J-1} + \Gamma_{I,J-1} + \Gamma_{I-1,J} + \Gamma_{I,J}}{4(x_I - x_{I-1})}$$

$$D_n = \frac{\Gamma_{I,J-1} + \Gamma_{I+1,J-1} + \Gamma_{I,J} + \Gamma_{I+1,J}}{4(x_{I+1} - x_I)}$$

$$D_s = \frac{\Gamma_{I,J-1}}{y_j - y_{j-1}}$$

$$D_n = \frac{\Gamma_{I,J}}{y_{j+1} - y_j}$$

scalar equations

The values of ρ and Γ at the cell faces are linearly interpolated (averaged for a uniformly-spaced grid) between the scalar nodes when calculating the coefficients F and D. The velocities need not be interpolated since they are known at the cell faces of the scalar control volume.

3.2.2 SIMPLER algorithm for handling pressure-velocity coupling

One problem with solving the resultant set of discretised equations is that the pressure, which appears in the momentum equations, has no equation to be solved. Patankar *et al.* [1972] have overcome this problem by developing iterative solution strategies. One such strategy is the SIMPLER algorithm. In this algorithm, the discretised continuity equation is used to derive a discretised equation for pressure.

The discretised momentum equations are rearranged as

$$u_{i,J} = \frac{\sum a_{nb}u_{nb} + b_{i,J}}{a_{i,J}} + \frac{A_{i,J}}{a_{i,J}}(p_{I-1,J} - p_{I,J}) \tag{3.48}$$

$$v_{I,j} = \frac{\sum a_{nb}v_{nb} + b_{I,j}}{a_{I,j}} + \frac{A_{I,j}}{a_{I,j}}(p_{I,J-1} - p_{I,J}) \tag{3.49}$$

Pseudo-velocities are defined as

$$\hat{u}_{i,J} = \frac{\sum a_{nb} u^*_{nb} + b_{i,J}}{a_{i,J}} \tag{3.50}$$

$$\hat{v}_{I,j} = \frac{\sum a_{nb} v^*_{nb} + b_{I,j}}{a_{I,j}} \tag{3.51}$$

Thus,

$$u_{i,J} = \hat{u}_{i,J} + d_{i,J}\left(p_{I-1,J} - p_{I,J}\right) \tag{3.52}$$

$$v_{I,j} = \hat{v}_{I,j} + d_{I,j}\left(p_{I,J-1} - p_{I,J}\right) \tag{3.53}$$

The form for the coefficients d will depend on whether or not under-relaxation factors are used to help the solution to converge during the iterative process. This will be explained in more detail further on. The above expressions for the velocities $u_{i,J}$ and $v_{I,j}$ together with similar forms for $u_{i+1,J}$ and $v_{I,j+1}$ may be substituted into the discretised continuity equation (Equation 3.44) and rearranged to give the discretised pressure equation:

$$a_{I,J} p_{I,J} = a_{I+1,J} p_{I+1,J} + a_{I-1,J} p_{I-1,J} + a_{I,J+1} p_{I,J+1} + a_{I,J-1} p_{I,J-1} + b_{I,J} \tag{3.54}$$

where

$$a_{I,J} = a_{I+1,J} + a_{I-1,J} + a_{I,J+1} + a_{I,J-1} \tag{3.55}$$

$$a_{I+1,J} = (\rho dA)_{i+1,J} \tag{3.56}$$

$$a_{I-1,J} = (\rho dA)_{i,J} \tag{3.57}$$

$$a_{I,J+1} = (\rho dA)_{I,j+1} \tag{3.58}$$

$$a_{I,J-1} = (\rho dA)_{I,j} \tag{3.59}$$

$$b_{I,J} = (\rho \hat{u} A)_{i,J} - (\rho \hat{u} A)_{i+1,J} + (\rho \hat{v} A)_{I,j} - (\rho \hat{v} A)_{I,j+1} \tag{3.60}$$

To initiate the SIMPLER calculation process, the pressure field p is estimated from guessed values of the velocity components, u^* and v^*, using the pseudo-velocities concept. This new pressure field becomes the next best guess ($p^* = p$). The next best guess for the velocity components are now calculated by solving the momentum equations and using the next best guess for the pressure field. Correction variables (p', u', and v') are defined as the difference between the correct variables (p, u, and v) and the next best guessed variables (p^*, u^*, and v^*)

$$p = p^* + p'$$
$$u = u^* + u'$$
$$v = v^* + v'$$

At this point, equations for the correction variables (p', u', and v') are derived using the momentum and continuity equations, although this step is not detailed here. The correction equations are:

$$a_{I,J}p'_{I,J} = a_{I+1,J}p'_{I+1,J} + a_{I-1,J}p'_{I-1,J} + a_{I,J+1}p'_{I,J+1} + a_{I,J-1}p'_{I,J-1} + b'_{I,J} \tag{3.61}$$

$$u_{i,J} = u^*_{i,J} + d_{i,J}\left(p'_{I-1,J} - p'_{I,J}\right) \tag{3.62}$$

$$v_{I,j} = u^*_{I,j} + d_{I,j}\left(p'_{I,J-1} - p'_{I,J}\right) \tag{3.63}$$

The coefficients a are defined by Equations (3.55) to (3.59). The source term is defined by the equation

$$b'_{I,J} = \left(\rho u^* A\right)_{i,J} - \left(\rho u^* A\right)_{i+1,J} + \left(\rho v^* A\right)_{I,j} - \left(\rho v^* A\right)_{I,j+1} \tag{3.64}$$

The correction equations are solved so that the corrected velocity variables (u and v) can be determined.

The entire procedure described above is iterated until convergence is achieved. A summary of the SIMPLER algorithm is listed below:

1) Make an initial guess for the pressure (p^*), velocity (u^* and v^*) and scalar fields (ϕ^*)

2) Calculate the coefficients a and b of the u-momentum and v-momentum equations (Equations (3.39)-(3.43))

3) Calculate the pseudo-velocities. The equations that are solved are non-linear and prone to diverge even when a solution exists. The changes in the values of the dependant variables can be slowed down from iteration to iteration to handle the non-linearity of the equations by a process of under-relaxation. Under-relaxation factors are defined as follows:

$$\phi_{new} = \alpha_\phi \phi + (1-\alpha_\phi)\phi_{old}$$

where the subscripts *old* and *new* refer to the values of the dependant variables from the previous iteration and the current, respectively. This expression is substituted into the discretised transport equations. It can be shown that the pseudo velocities are defined by the following equation when under-relaxation is used:

$$\hat{u}_{i,J} = \frac{\sum a_{nb}u^*_{nb} + b_{i,J} + a_{i,J}(1-\alpha_u)u^*_{i,J}/\alpha_u}{a_{i,J}/\alpha_u}$$

$$\hat{v}_{I,j} = \frac{\sum a_{nb}v^*_{nb} + b_{I,j} + a_{I,j}(1-\alpha_v)v^*_{I,j}/\alpha_v}{a_{I,j}/\alpha_v}$$

4) Calculate the coefficients of the pressure equation. With under-relaxation, the d coefficients become

$$d_{i,J} = \frac{A_{i,J}\alpha_u}{a_{i,J}},\ d_{i+1,J} = \frac{A_{i+1,J}\alpha_u}{a_{i+1,J}},\ d_{I,j} = \frac{A_{I,j}\alpha_v}{a_{I,j}},\ d_{I,j+1} = \frac{A_{I,j+1}\alpha_v}{a_{I,j+1}}$$

5) Solve the pressure equation (Equation (3.54)).

6) Set $p^* = p$

7) Solve the discretised momentum equations. The coefficients a and b have already been calculated in Step 2.

$$\frac{a_{i,J}}{\alpha_u}u^*_{i,J} = \sum a_{nb}u^*_{nb} + \left(p^*_{I-1,J} - p^*_{I,J}\right)A_{i,J} + b_{i,J} + \left[\left(1-\alpha_u\right)\frac{a_{i,J}}{\alpha_u}\right]u^*_{i,J}$$

$$\frac{a_{I,j}}{\alpha_v}v^*_{I,j} = \sum a_{nb}v^*_{nb} + \left(p^*_{I,J-1} - p^*_{I,J}\right)A_{I,j} + b_{I,j} + \left[\left(1-\alpha_v\right)\frac{a_{I,j}}{\alpha_v}\right]v^*_{I,j}$$

8) Solve the pressure correction equation (Equation (3.61)) using the coefficients a of the pressure equation (determined in Step 4) but recalculating the source term b from Equation (3.64).

9) Correct the velocities using Equations (3.62) and (3.63).

10) Solve all other discretised transport equations

$$\frac{a_{I,J}}{\alpha_\phi}\phi_{I,J} = \sum\left(a_{nb}\phi^*_{nb}\right)_\phi + b_{I,J} + \left[\left(1-\alpha_\phi\right)\frac{a_{I,J}}{\alpha_\phi}\right]\phi^*_{I,J}$$

11) Test for convergence. Convergence is monitored by examining how perfectly the discretisation equations are satisfied by the current values of the dependant variables. For each grid point, a residual R can be calculated from

$$R = \sum\left(a_{nb}\phi^*_{nb}\right)_\phi + b - a_P\phi_P$$

Perfect convergence occurs when the sum of the residuals for every node in the flow domain $\sum|R|$ becomes equal to zero. Normally, convergence is defined as the point at which the sum of the residuals decreases below a certain small number. If the solution has not converged then the iterative process carries onwards returning to Step 2 and setting $p^* = p$, $u^* = u$, $v^* = v$, and $\phi^* = \phi$).

3.2.3 Boundary Conditions

Wall boundary condition

The no-slip condition (u=v=0) is used for the velocity components at the walls. This condition affects the form of the discretised transport equation. As an illustration, the scalar transport equation is derived for the nearest node from the south wall (Figure

3.3), although the same method is applied for the u-component equation. Special discretisation methods are not required for the v-component equation in a rectangular flow domain due to the layout of the staggered grid.

The value of ϕ at the south wall is ϕ_A. The generalised discretised scalar equation is

$$\left[\left(D_w+\frac{F_w}{2}\right)+\left(D_e-\frac{F_e}{2}\right)+\left(D_s+\frac{F_s}{2}\right)+\left(D_n-\frac{F_n}{2}\right)+\left(F_e-F_w+F_n-F_s\right)\right]\phi_P =$$

$$\left(D_w+\frac{F_w}{2}\right)\phi_W+\left(D_e-\frac{F_e}{2}\right)\phi_E+\left(D_s+\frac{F_s}{2}\right)\phi_S+\left(D_n-\frac{F_n}{2}\right)\phi_N+\Delta V\bar{S}_\phi \tag{3.65}$$

F_s is equal to zero because the velocity at the south wall is zero. Noting that $D_s = D_A = \Gamma A/\delta y_P$, and making use of the previously defined coefficients a, then the scalar equation becomes

$$a_P\phi_P = a_W\phi_W + a_E\phi_E + a_N\phi_N + D_A\phi_A + S_u \tag{3.66}$$

where $a_P = a_W + a_E + a_N - S'_P$

$$a_W = D_w + \frac{F_w}{2}$$

$$a_E = D_e - \frac{F_e}{2}$$

$$a_N = D_n - \frac{F_n}{2}$$

$$S'_P = -\left(F_e - F_w + F_n + D_A\right) + S_P$$

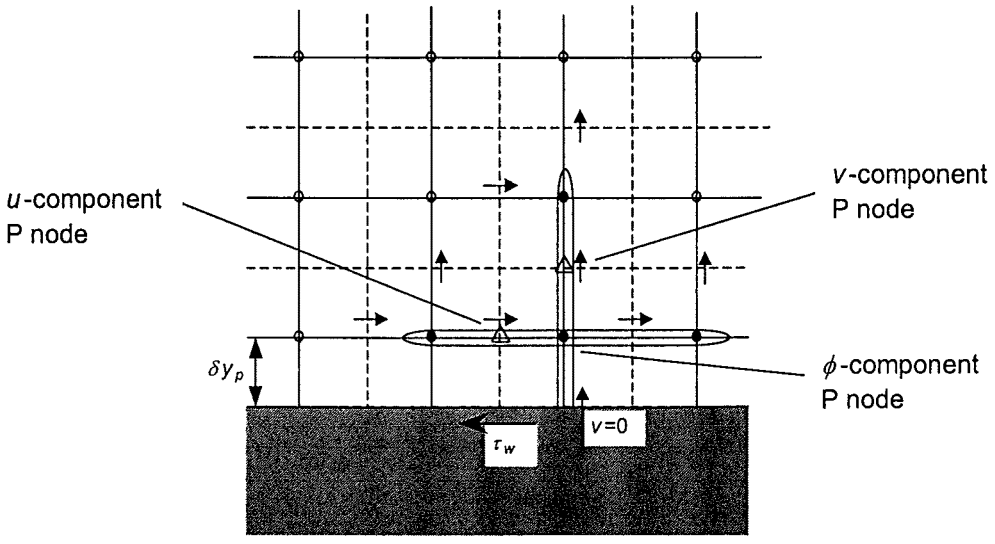

Figure 3.3. u-velocity, v-velocity and scalar cells at the wall boundary.

Similar equations can be derived for north, west, and east walls. The terms involving the coefficients D_A can be taken outside of the brackets to give the form $D_A(\phi_A - \phi_P)$, which is the wall-flux equation of the quantity ϕ. In laminar flows, when the turbulent viscosity μ_t is zero, it is easy to show that the momentum, heat, and mass fluxes from the surface become

$$\tau_A = \mu \frac{u_p}{\delta y_p} \qquad \left(D_A = \frac{\mu}{\delta y_p} A\right) \tag{3.67}$$

$$q_A = \frac{\lambda}{C_p} \frac{\left(H_A - H_p\right)}{\delta y_p} \qquad \left(D_A = \frac{\lambda}{C_p \delta y_p} A\right) \tag{3.68}$$

$$m_A = \rho D_{AB} \frac{\left(Y_A - Y_p\right)}{\delta y_p} \qquad \left(D_A = \frac{\rho D_{AB}}{\delta y_p} A\right) \tag{3.69}$$

The wall-flux equations take on different forms for turbulent flow conditions. The turbulent flow equations do not accurately represent the turbulence in the near wall region. The wall-function method (Launder *et al.* [1974]) avoids this problem by making use of the universal behaviour of near-wall flows. Two regions can be identified in the boundary layer of a turbulent flow: a viscous sub-layer near the wall where viscous stresses dominate over turbulent stresses, and a region outside the viscous sub-layer where both viscous and turbulent effects are important. In the viscous sub-layer, the dimensionless velocity increases proportionally with dimensionless distance from the wall. In the outer region, a logarithmic relationship exists between the dimensionless velocity and dimensionless distance.

The implementation of the wall boundary conditions starts by evaluating the dimensionless distance of the first node adjacent to the wall, y_P^+. The near wall flow is taken to be laminar if $y_P^+ \leq 11.225$ and turbulent if $y_P^+ > 11.225$. If the flow is known to be turbulent, then the nearest grid point to the wall must be located in the turbulent region of the boundary layer; that is, $y_P^+ > 11.225$. The value for the dimensionless velocity u^+ may be determined from the dimensionless distance using the wall function:

$$u^+ = \begin{cases} y^+ & y^+ \leq y_o^+ \\ \frac{1}{\kappa} ln\left(Ey^+\right) & y^+ > y_o^+ \end{cases} \tag{3.70}$$

where

$$y^+ = \frac{\rho C_\mu^{0.25} k_P^{\ 0.5}}{\mu_t} \Delta y_P \tag{3.71}$$

The shear stress at the wall may next be determined from the equation

$$\tau_w = -\frac{\rho C_\mu^{0.25} k_P^{\ 0.5}}{u^+} u_P \tag{3.72}$$

It can be shown that this equation reduces down to Equation (3.67) under laminar conditions. Comparison between Equation (3.67) and Equation (3.72) shows that the general form of the coefficient D_A that covers both laminar and turbulent flow conditions is given by the following formula

$$D_A = \frac{\rho C_\mu^{0.25} k_P^{0.5}}{u^+} A_P \tag{3.73}$$

A similar procedure is followed for the vapour mass fraction and heat equation wall treatments. The wall function for the turbulent heat transfer is

$$H^+ = \begin{cases} Pry^+ & y^+ \le y_H^+ \\ \dfrac{\sigma_H}{\kappa} ln\left(E_H y^+\right) & y^+ > y_H^+ \end{cases} \tag{3.74}$$

where

$$E_H = Eexp\left[9.0\kappa\left(\left(\frac{Pr}{\sigma_H}\right)^{0.75} - 1\right)\left(1 + 0.28exp\left(-0.007\frac{Pr}{\sigma_H}\right)\right)\right] \tag{3.75}$$

$$Pr = \frac{C_P \mu}{\lambda} \tag{3.76}$$

The sublayer thickness, y_H^+ can be determined numerically by finding the intersection of the linear profile and the log-law profile:

$$Pry^+ = \frac{\sigma_H}{\kappa} ln\left(E_H y^+\right) \tag{3.77}$$

The heat transfer from the wall is given by the following equation, which reduces down to Equation (3.68) under laminar conditions.

$$q_w = \frac{\rho C_\mu^{0.25} k_P^{0.5}}{H^+}\left(H_w - H_P\right) \tag{3.78}$$

Therefore,

$$D_A = \frac{\rho C_\mu^{0.25} k_P^{0.5}}{H^+} A_P \tag{3.79}$$

Similarly, for the vapour mass fraction wall treatment -

$$Y^+ = \begin{cases} Scy^+ & y^+ \le y_Y^+ \\ \dfrac{\sigma_Y}{\kappa} ln\left(E_Y y^+\right) & y^+ > y_Y^+ \end{cases} \tag{3.80}$$

where

$$E_Y = Eexp\left[9.0\kappa\left(\left(\frac{Sc}{\sigma_Y}\right)^{0.75} - 1\right)\left(1 + 0.28exp\left(-0.007\frac{Sc}{\sigma_Y}\right)\right)\right] \tag{3.81}$$

$$Sc = \frac{\mu}{\rho D_{AB}} \tag{3.82}$$

The sublayer thickness, y_Y^+ can be determined numerically by finding the intersection of the linear profile and the log-law profile:

$$Scy^+ = \frac{\sigma_Y}{\kappa} ln\left(E_Y y^+\right) \tag{3.83}$$

The vapour mass fraction transfer from the wall is given by the following equation, which reduces down to Equation (3.69) under laminar conditions:

$$m_w = \frac{\rho C_\mu^{0.25} k_P^{\ 0.5}}{Y^+}\left(Y_w - Y_P\right) \tag{3.84}$$

Therefore,

$$D_A = \frac{\rho C_\mu^{0.25} k_P^{0.5}}{Y^+} A_P \tag{3.85}$$

Wall treatment for k and ε Equations

A special treatment of the production terms in the *k*-equation for near-wall grid points is necessary in order to use only quantities interior to the flow (AEA Technology [1995]). The influence of the turbulent viscosity on the rapidly varying velocities is removed by redefining the generation term as follows:

$$G = G_{originallyevaluated} - \left(\mu_l + \mu_t\right)\left(\frac{\partial u}{\partial y}\right)^2 + \left|\tau_w \frac{u_P}{\Delta y_P}\right| \tag{3.86}$$

where

$$\tau_w \frac{u_P}{\Delta y_P} = \frac{\rho C_u^{0.25} k_P^{0.5} u_P}{u^+} \frac{u_P}{\Delta y_P} \tag{3.87}$$

The dissipation term becomes

$$-\rho\varepsilon = \left(-\frac{\rho^2 C_u k}{\mu_t}\right)k \tag{3.88}$$

where

$$\mu_t = -\frac{\tau_w}{\frac{\partial u}{\partial y}} = -\frac{\tau_w \Delta y_P}{u_P} \tag{3.89}$$

Rearranging Equation (3.72) gives

$$\frac{\tau_w}{u_P} = -\frac{\rho C_u^{0.25} k_P^{0.5}}{u^+} \tag{3.90}$$

Finally, substituting Equations (3.90) and (3.89) into Equation (3.88) gives

$$-\rho\varepsilon = \left(-\frac{\rho C_u^{0.75} k_P^{0.5} u^+}{\Delta y_P}\right) k_P \tag{3.91}$$

The k-equation is discretised as normal for the near-wall nodes, except that the diffusion term D_A is set equal to zero (Launder *et al.* [1974]). The term inside the bracket of Equation (3.91) multiplied by the volume ΔV of the control volume is equal to the source term S_p in the discretised k-equation for the near-wall nodes. The source term S_u is equal to Equation (3.86) multiplied by the volume ΔV of the control volume. At nodes away from the wall, S_p is equal to the term in the brackets of Equation (3.88) multiplied by the volume ΔV of the control volume; that is, no special treatment is done for nodes away from the wall. Likewise, the source term S_u is equal to $G_{originallyevaulated}$ multiplied by the volume ΔV of the control volume.

At the near wall nodes, no transport equation is solved for ε, which is given the value

$$\varepsilon = \frac{C_\mu^{0.75} k_p^{1.5}}{\kappa \Delta y_p} \tag{3.92}$$

The source term S_ε for nodes away from the wall is given by the following equation

$$\Delta V\left(C_1 \frac{\varepsilon}{k} G - C_2 \rho \frac{\varepsilon^2}{k}\right) \tag{3.93}$$

Using the definition for the turbulent viscosity (Equation (3.28)), this expression is rearranged to give

$$\frac{C_1 C_\mu \rho k}{\mu_t} G\Delta V + \left(-C_2 \rho \frac{\varepsilon}{k} \Delta V\right)\varepsilon \tag{3.94}$$

The source term S_p becomes equal to the term in the brackets of the second term of this equation. The source term S_u becomes equal to the first term.

Miscellaneous

The normal component of the velocity is set to zero at the wall (v=0), and the discretised v-momentum equation at the near-wall grid points is evaluated without modification. Since the wall velocity is known, it is unnecessary to perform a pressure correction at the wall. Therefore, in the pressure and pressure correction equations at near-wall grid points, the wall link is cut by setting the appropriate a value to zero (a_S=0 for the south wall) and taking $v_S^* = v_S$.

Inlet boundary condition

The distribution for all flow variables $(u, v, H, Y, k, \varepsilon)$ must be specified at the inlet boundary. The links to the nodes on or outside the inlet flow boundary remain active for u- and v-momentum equations and all scalar variables except for pressure (Figure 3.4). In the discretised pressure equation and pressure correction equation, the boundary-side a coefficient is set to zero and $u_W^* = u_W$ since the inlet velocities are known and therefore no pressure correction is needed.

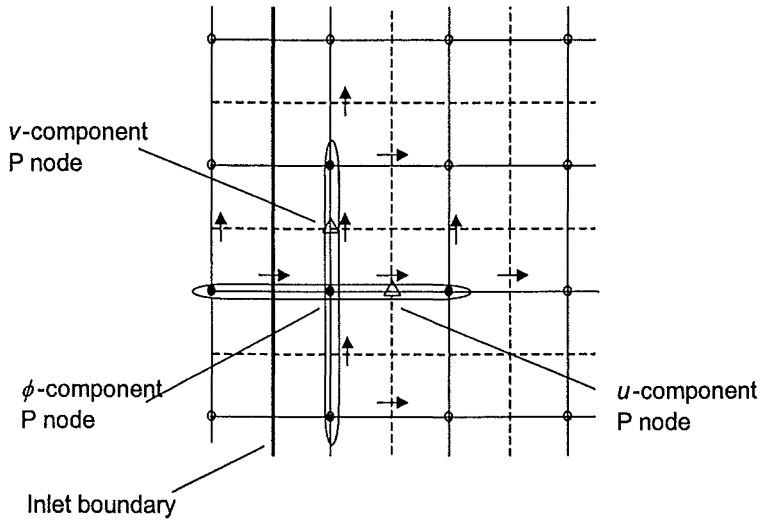

Figure 3.4. u-velocity, v-velocity and scalar cells at the inlet boundary.

Outlet boundary condition

The values of the flow variables just outside the outlet boundary are determined by extrapolation from the interior on the assumption of zero gradients at the outlet plane (Figure 3.5). This relies on the assumption that the location of the outlet is far away from geometric disturbances so that the flow reaches a fully developed state where no change occurs in the flow direction. For the v-momentum and scalar equations this implies setting

$$v_{NI,j} = v_{NI-1,j} \text{ and } \phi_{NI,J} = \phi_{NI-1,J} \tag{3.95}$$

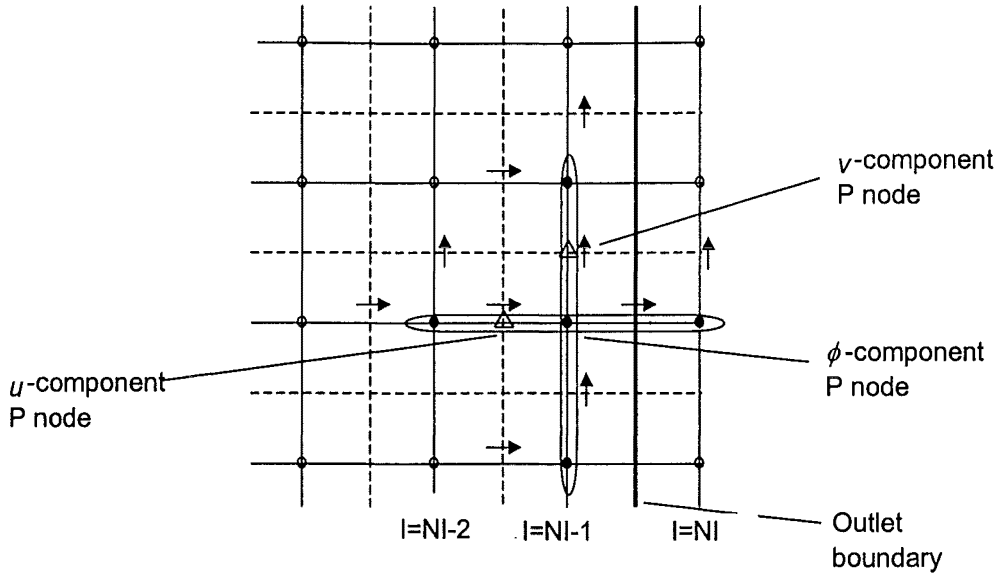

Figure 3.5. *u*-velocity, *v*-velocity and scalar cells at the outlet boundary.

To ensure that mass is conserved over the computational domain, the *u*-velocities just outside of the flow domain are weighted by the ratio of the inlet mass flux to the outlet mass flux which is the sum of the fluxes just inside the outlet boundary.

$$u_{NI,J} = u_{NI-1,J} \frac{M_{in}}{M_{out}} \tag{3.96}$$

where $M = \sum \rho u A$.

No pressure correction is done at the outlet, hence the pressure and pressure correction links to the outlet boundary side are suppressed by setting $a_E = 0$ and $u_E^* = u_E$.

3.2.4 Properties of the Vapour-Air Mixture

The thermal conductivity, viscosity, density, heat capacity and diffusivity used in the transport equations are functions of both temperature and mass fraction. The viscosity of the air-vapour mixture is calculated using the Wilke's approximation (Reid *et al.* [1977]).

$$\mu_m = \frac{y_1 \mu_1}{y_1 + y_2 \phi_{12}} + \frac{y_2 \mu_2}{y_2 + y_1 \phi_{21}} \tag{3.97}$$

where μ_m = viscosity of pure mixture (kg/ms)

μ_1, μ_2 = viscosities of pure components

y_1, y_2 = mole fractions

and $$\phi_{12} = \frac{\left[1+(\mu_1/\mu_2)^{0.5}(M_2/M_1)^{0.25}\right]^2}{\left(8[1+M_1/M_2]\right)^{0.5}} \tag{3.98}$$

$$\phi_{21} = \phi_{12}\frac{\mu_2}{\mu_1}\frac{M_1}{M_2} \tag{3.99}$$

where M_1, M_2 = molecular weights. The mole fraction of the vapour can be related to the mass fraction of vapour by the following relationship

$$y_v = \frac{Y_v M_a}{Y_v M_a + M_v(1-Y_v)} \tag{3.100}$$

The Mason-Saxena method (Reid *et al.* [1977]) is used to calculate the thermal conductivity from the ϕ_{ij} values used in the calculation of the viscosity.

$$\lambda_m = \frac{y_1\lambda_1}{y_1 + y_2\phi_{12}} + \frac{y_2\lambda_2}{y_2 + y_1\phi_{21}} \tag{3.101}$$

where λ_m = thermal conductivity of pure mixture (W/mK)

λ_1, λ_2 = thermal conductivities of pure components

It was assumed that the gas is weakly compressible and ideal, in which case density variations due to mass fraction changes are accounted for, but the effect of pressure changes are ignored. The density of the vapour-air mixture is given by

$$\rho = \frac{M_1}{Y_v(1-M_1/M_2)+M_1/M_2}\frac{P_{atm}}{RT} \tag{3.102}$$

where Y_v = mass fraction of vapour (kg/kg)

The diffusivity is the product of the binary diffusion coefficient of vapour in air (m^2/s), and the density of the mixture. The binary diffusion coefficient is calculated from the following correlation:

$$D_{AB} = \frac{10^{-7}T^{1.75}(1/M_1+1/M_2)^{0.5}}{P_{atm}\left(\alpha_1^{1/3}+\alpha_2^{1/3}\right)^2} \tag{3.103}$$

where $\alpha_1 = 20.1$ (air)

$\alpha_2 = 12.7$ (water)

All components are assumed to be thermally perfect; that is, their enthalpies are assumed to be functions of temperature only. The enthalpy of the fluid mixture is defined by the expression

$$H = \sum_{i=1}^{2} Y_i H_i = Y_v C_{Pv}(T)T + Y_a C_{Pa}(T)T - C_{Pa}(T_{ref})T_{ref} \tag{3.104}$$

for which T_{ref} is a reference temperature where the enthalpy is defined to be zero. Note that the following constraint exists on the mass fraction

$$Y_v + Y_a = 1 \tag{3.105}$$

The humidity of the air Y_G can be related to the mass fraction of vapour Y_v by the equation

$$Y_v = \frac{Y_G}{Y_G + 1} \tag{3.106}$$

The humidity of air Y_G can be taken from a Grosvenor chart given the dry and wet-bulb temperatures (Keey [1992]).

3.2.5 Summary of External Flow Model

Masmoudi *et al.* [1991] assumed that the characteristic time scales of the external turbulent flow were much smaller than the time scales of the transfers inside the porous body. Thus, they ignored the time derivative in the turbulent fluid flow equations. The time evolution for the external flow was viewed as a succession of steady state periods. The same approach was adopted in this chapter.

The simulation solved for seven variables: average horizontal velocity u, average vertical velocity v, enthalpy H (and hence temperature), vapour mass fraction Y (and hence humidity), turbulence kinetic energy k, turbulence dissipation ε, and static pressure P. The equations that are solved are the continuity equation, the momentum equation in the horizontal and vertical directions, two scalar equations for heat and concentration, and the k and ε equations which characterise the turbulence (Table 3.3). The static pressure was linked to the velocity by using a staggered grid and the SIMPLER algorithm due to Patakar *et al.* [1972]. The treatment of the convection and diffusion of any property followed the hybrid-differencing scheme described in Patankar [1980]. The high-Reynolds form of the k-ε model was applied (Launder *et al.* [1974]). In this model, wall function expressions for the turbulent boundary layers are used to determine the value of the dependant variable at the first node point from the wall. The iterative procedure was repeated until a converged solution was achieved which was indicated by the sum of the mass residuals for all the grid points being less than 0.05% of the total mass flux at the inlet to the flow domain.

Under-relaxation was employed to avoid divergence in the iterative solution. The following under-relaxation factors were used in the simulation: α_u =0.3, α_v =0.3, α_H =1.0, α_Y=1.0, α_k=0.7, α_ε=0.7.

The source terms shown in Table 3.3 were discretised using the prevailing values of the variables. Versteeg *et al.* [1995] describes this in more detail. The system of

algebraic equations that result from discretising the governing equations of fluid flow and heat transfer need to be solved for the dependant variables. These equations were solved using a simultaneous linear equation solver called the Tri-Diagonal Matrix Algorithm (TDMA) which was developed by Thomas [1949] and described in detail by Versteeg *et al.* [1995]. It was applied iteratively, in a line by line fashion, to solve the two-dimensional flow problem.

Several empirical constants are required in the turbulence models which have not previously been defined in this chapter. These are the Von Karmen constant (κ =0.4187), the constant in the turbulent wall model (E=9.793), the turbulent Prandtl number (σ_H =0.9), and the turbulent Schmidt number (σ_Y=0.9).

3.3 Timber Drying Equations

The two-dimensional form of the timber-drying model presented in the previous chapter is given below:

$$\frac{\partial}{\partial t}(\rho_s X)+\nabla\cdot\left(j_{wf}+j_{wv}\right)=0 \tag{3.107}$$

$$\frac{\partial}{\partial t}\left[\rho_s Cp(1+X)T\right]=\nabla\cdot(k\nabla T)-\nabla\cdot\left[\sum_i Cp_i j_{wi} T\right]-H\nabla\cdot\left(j_{wv}\right) \tag{3.108}$$

where $H=H_{vap}+T_{dew}\left(Cp_f-Cp_v\right)+H_{sorp}$. The flux equations j_w have been defined in the previous chapter, and assume the same form in this chapter.

Boundary Conditions

The external transport equations (Table 3.3) and the internal transport equations (Equations (3.107)-(3.108)) are coupled together by the boundary conditions at the interface between the two flow domains. The classical boundary conditions at the surface of the porous medium are the continuity of pressure and normal velocity across the surface, and the vanishing of the tangential velocity at the interface (no-slip condition). However, when a viscous fluid flows passed a porous medium, tangential stresses may move the fluid close below the surface. Masoudi *et al.* [1991] conducted a literature review on the boundary conditions at a porous medium interface and concluded that the layer at the surface which is affected by the external flow is very thin (of the order of the pore scale) so that the no-slip condition can be applied at the interface.

In the previous chapter it was shown that pressure gradients do not build up within *Pinus radiata* because it is relatively permeable. Furthermore, the pressure drop along the row of boards is very small (of the order of 10-100 Pa) and will not induce gaseous flows within the timber in the flow direction. Therefore, the gas phase pressure in the porous medium is considered to be uniform and constant. It was also shown in the previous chapter that the blowing effect at the surface of the timber board is negligible. Therefore, bulk-flow motion across the surface need not be considered in this chapter; that is, the normal velocity at the surface is set to zero.

The velocities, temperature, and vapour mass fraction at the interface are

$$u = v = 0 \tag{3.109}$$

$$T_{external} = T_{internal} \tag{3.110}$$

$$Y_v = \frac{M_v P_v}{M_A (P_{atm} - P_v) + M_v P_v} \tag{3.111}$$

There must exist continuity of fluxes at the interface. If it is assumed that there is a thin-dry layer at the timber surface that is below fibre-saturation point, then it follows that there are no liquid-water fluxes at the surface. Under these conditions, continuity of the flux densities can be written

$$\left(k \frac{\partial T}{\partial z} \right)_{internal} = (q_w)_{external} \tag{3.112}$$

$$(j_{wv})_{internal} = (m_w)_{external} \tag{3.113}$$

where q_w and m_w are defined by Equations (3.78) and (3.84), respectively.

The effects of surface roughness can be estimated by altering the values of the constants in the wall model (Equations (3.70), (3.74), (3.80)) as suggested by Jayatilleke [1969]. However, Kho [1993] and Langrish *et al.* [1993] showed both experimentally and theoretically that surface roughness has very little effect on the interfacial heat and mass-transfer coefficients. Therefore, in this chapter, the constants in the wall model are unaltered and it is assumed that the surface of the timber boards is smooth.

3.4 Simulations

Validation of the Flow Model

The numerical code 'Turb' that was developed to solve the turbulent flow equations was validated by comparing the results from 'Turb' with the predictions of a commercial computational fluid dynamics package called 'CFX' (AEA Technology [1995]). The airflow through a channel 1 m long and 0.025 m wide was modelled. Both the upper and lower walls of the channel were given a temperature of 70 °C and a vapour mass fraction of unity. The temperature and vapour mass fraction of the inlet air were 140 °C and 0.188 kg/kg, respectively. The inlet velocity was set to 15 m/s. The turbulence kinetic energy and dissipation at the inlet were set to 0.0001 m^2/s^2 and 0.0001 m^2/s^3, respectively. In both 'Turb' and 'CFX', the scalar grid had 200 evenly-spaced nodes along the length of the channel, and 10 evenly spaced nodes across the width of the channel. Thus, the flow domain consisted of 200x10 control volumes. Increasing the number of nodes along the length of the channel had very little effect on the flow solution.

Comparisons were made between the predictions of 'Turb' and 'CFX' for the distributions of the dependent variables across the width of the channel at two different locations along the length of the channel. The first position was located at 0.2 m from the inlet. The second position was located at the outlet. Comparisons

between the results of the two codes can be seen in Figure 3.6. Clearly, there is reasonable agreement in all dependant variables.

Solution Method

The method of solution is based on two computer codes. The first one solves the timber drying equations (Equations (3.107)-(3.108)) using a first-order differential equation solver called DVODE (Brown *et al.* [1989]) which simultaneously calculates the dependent variables at all nodes in the flow domain for each time step. The second numerical code solves the turbulent flow equations (Table 3.3) using the finite-difference method outlined above, in which an iterative method is used to calculate the flow field.

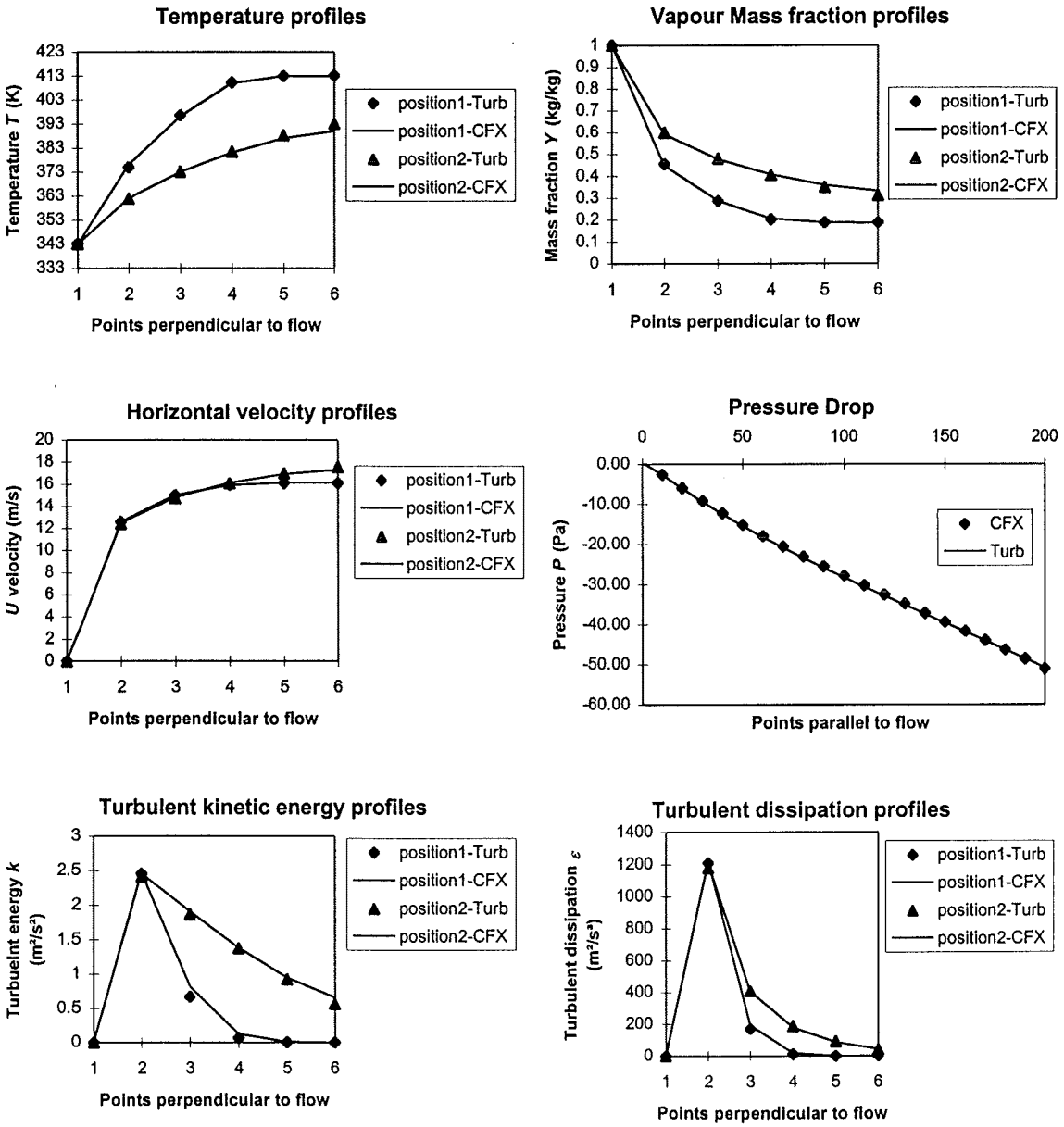

Figure 3.6. Comparison between results of the numerical codes 'Turb' and 'CFX'.

The first step in the solution algorithm is to calculate the external flow field. The following boundary conditions are required to solve the turbulent flow equations:

1) Surface temperature, which is given at time equal to zero, and which the timber drying equations determine at subsequent times.
2) Surface vapour mass fraction, which can be calculated from the surface moisture content and temperature given the sorption isotherm. The initial surface moisture content is given, and determined at subsequent times using the timber drying equations.
3) Inlet air velocity, humidity, and temperature into the fillet space (which is the flow domain of interest).

The surface heat and mass fluxes, which are necessary to solve the timber drying equations, are then determined using Equations (3.78) and (3.84). Thus, the timber drying equations can be solved which give the new temperatures and moisture-content distributions in the timber board at the new time step (including the surface moisture contents and temperatures). The method is then repeated for subsequent time steps until the moisture content reaches the desired moisture content.

Application

Figure 3.7 shows a simplified grid arrangement for the coupled flow domain. In the simulations, each board had 20 evenly-spaced nodes across the width, and 28 non-uniformly spaced nodes into the depth, with a greater proportion of the nodes concentrated near the surface of the timber board. The row of timber boards was 1 m in the airflow direction and each board was 20 mm thick and 100 mm wide; that is, 10 boards were butted against each other to form a row. It was assumed that no gaps separated the adjacent timber boards in a row and that every board had the same thickness so that the rows of boards formed a smooth continuous surface. Each board, however, remained a separate entity and therefore no flux of moisture occurred from one board to another. Furthermore, it was also assumed that the sides of the boards, which were butted against each other, were insulated to heat transfer. The centre-line of each timber board was defined as a symmetry plane which reduced the computational effort required since the number of nodes was effectively halved. The fillet space was 25 mm wide and had 11 nodes perpendicular to the flow and 200 nodes in the flow direction.

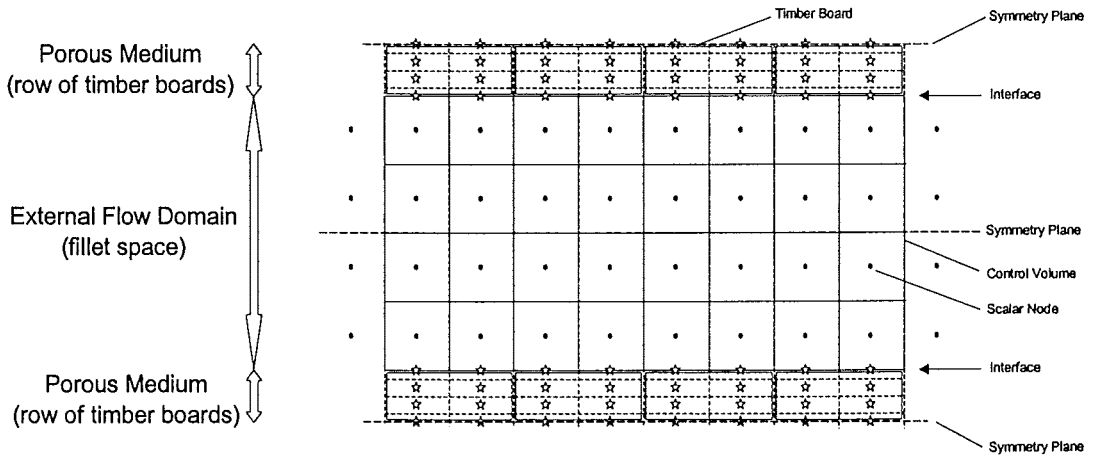

Figure 3.7. Grid system for the external and internal flow domains

The dry and wet-bulb temperatures of the air at the inlet to the fillet space were 140 °C and 70 °C, respectively. This corresponds to a vapour mass fraction of 0.188 kg/kg. The turbulence kinetic energy and dissipation at the inlet were set to 0.0001 m^2/s^2 and 0.0001 m^2/s^3, respectively. The wetting period and associated complications were avoided in the calculations by setting the initial temperature of the timber boards equal to the wet-bulb temperature (70 °C).

According to Launder *et al.* [1974], the high-Reynolds number turbulence model is applicable for channel flows at Reynolds numbers greater than 20000. Moreover, the wall-function method is only accurate when the near-wall grid point is sufficiently remote from the wall for the viscous effects to be entirely overwhelmed there by the turbulent effects. The dimensionless distance y^+ from the wall of the near-wall grid point must be at least equal to 30 in order to satisfy this criterion. The air velocity at the inlet to the fillet space was assumed to be even across the width of the fillet with a magnitude of 15 m/s. This air velocity corresponds to a Reynolds number, based on the hydraulic diameter of the fillet, of approximately 30000 and, therefore, the high-Reynolds number turbulence model is applicable at the velocity tested. Furthermore, 11 grid points traversed the width of the fillet, which was 0.025 m wide; thus, y^+ takes on a value of approximately 40 and therefore the wall-function method is applicable. The air velocity of 15 m/s is not entirely unrealistic for timber-drying kilns since modern industrial-scale kilns operate at air velocities of up to 12 m/s.

The time increment between iterations was set to 0.05 s. It was found that this time step was sufficiently small so that changes in the internal flow conditions between time steps were very slight. Therefore, the external flow transfers could be considered to be at steady state during each time step.

The drying of sapwood *Pinus radiata* timber boards was simulated. Each timber board was assumed to be isotropic with the following timber properties and initial conditions: K_{ls}=2.5x10^{-15} m^2, A=0.06, ξ=1.5 mm, ρ_s=438 kg/m^3, and X_i=1.42 kg/kg. The thin-zone moisture content was set at 0.124 kg/kg. These values are applicable to the timber board, dried at 140/65 °C, which was presented in Chapter 2.

The external heat and mass-transfer coefficients were calculated using the following formulae:

$$h = \frac{q_w}{\left(T_{centreline} - T_{surface}\right)} \tag{3.114}$$

$$K_o = \frac{m_w}{\left(Y_{centreline} - Y_{surface}\right)} \tag{3.115}$$

where q_w and m_w are defined by Equations (3.78) and (3.84), respectively, and $T_{centreline}$ and $Y_{centreline}$ are respectively the temperature and vapour mass fraction at the centre of the fillet.

Batch Drying model

Van Meel's batch drying equations are given by Equation (3.18). The definitions of the dimensionless numbers were modified slightly to account for the fact that, in the simulations, the surfaces of the timber boards were never saturated with water due to the presence of the thin-dry layer. That is, the surface moisture content was always less than the fibre-saturation moisture content. The saturation humidity Y_w was replaced with the surface humidity during the constant rate period Y_s, and the moisture flux from the surface $\dot{m}_{lv}$ was redefined as follows:

$$\dot{m}_{lv} = [f\beta(Y_s - Y_G)]a \tag{3.116}$$

where the mass-transfer coefficient based on humidity potential β is related to the mass-transfer coefficient K_o based on mass-fraction potential (Equation 3.115) by the following equation

$$\beta = \frac{K_o}{(Y_{centreline}+1)(Y_{surface}+1)} \tag{3.117}$$

With these changes, it can be shown that the dimensionless parameters (Equations (3.14-3.17)) become

$$\Pi = \frac{Y_s - Y_G}{Y_s - Y_G^o} \tag{3.118}$$

$$\xi = \frac{\beta a}{G}x \tag{3.119}$$

$$\theta = \frac{\beta a(Y_s - Y_G^o)}{(X_{cr} - X_e)\rho_s(1-\varepsilon)}t \tag{3.120}$$

The solution method for Van Meel's batch drying model will be discussed in the next chapter.

The presence of the thin-dry layer near the surface of the timber board prevents the accurate use of Van Meel's batch-drying model unless the surface humidity during the constant-rate period is known. This value can be determined by measurement or predicted by using a detailed model of the internal transport mechanisms within the timber, such as the model presented in the previous chapter and more rigorously in this chapter. In Chapter 4, a more simplified approach is taken. It is assumed that the surface of the timber board is above the fibre-saturation point during the constant-rate period. Thus, the surface humidity is equal to the saturation humidity Y_w at the given wet-bulb temperature. This assumption, which is unlikely to be valid for rough-sawn timber due to the inevitable presence of the thin-dry layer at the surface, will not affect the general trends observed.

3.5 Discussion

Moisture Content and Temperature fields

Figure 3.8 shows contour plots of the moisture-content fields (top) and temperature fields (bottom) inside the row of timber boards at various times during the drying schedule. The line described by y=0 represents the exposed surface of the row of timber boards, while the line described by y=0.01 is the centre-line (or symmetry plane) of the row of timber boards. Hot, humid air sweeps over the surface of the timber boards (y=0) from left to right. Each timber board is 0.1 m wide and 0.02 m thick, and there are 10 timber boards along the row. The discontinuities that are evident in the contour plots represent the edges of adjacent timber boards. These discontinuities exist because the heat and moisture fluxes across these interfaces have been set to zero; that is, it is assumed that these interfaces are insulated as a first approximation.

The evaporative front is made visible in the moisture-content contour plots (top) by lines that are closely spaced together, which indicate a region of a high moisture-content gradient. In the temperature-contour plots (bottom), the position of the evaporative front is indicated by the contour whose temperature is equal to 100 °C (the boiling point of water). Figure 3.8b shows that, in every timber board, the evaporative front has not moved from its initial position close to the exposed surface after one hour of drying. The evaporative front has begun to recede within the first two boards after 1.5 hours; however it is still stationary within the remaining boards (Figure 3.8c). After 2 hours, the evaporative front has begun receding within every board (Figure 3.8d). Figure 3.8e shows that, half-an-hour later, the evaporative front has reached the centre-line of every board along the row. Thus, the wet zone no longer exists and the timber boards are experiencing the second falling-rate period of the drying process, when moisture migrates by vapour and bound-moisture diffusion only. The boards are almost completely dried after 3 hours and are approaching the dry-bulb temperature (Figure 3.8f). Figure 3.8c shows clear leading-edge effects in which the transfer coefficients are enhanced at the leading edge resulting in the leading boards along the row drying out more quickly than the trailing boards.

Heat and Mass Transfer Coefficients

In practice, the variations in board-averaged transfer coefficients along a row of timber boards are superimposed onto the variations in local-transfer coefficients over each timber board. Variations in local-transfer coefficients over a single board are caused by the inevitable presence of gaps between adjacent boards which generate eddies with a subsequent enhancement of the local-transfer coefficients over the leading portion of each board (Kho [1993]). The local-transfer coefficients over a single board take on a peak value just beyond the leading edge and approach an asymptotic value towards the trailing edge. Similarly, the board-averaged transfer coefficients take on higher values over the first two or three boards along the row, while the board-averaged transfer coefficients onwards are virtually constant. The single-board transfer-coefficient variations are ignored in this investigation by assuming that no gaps exist between adjacent boards. This considerably simplifies the problem because predictions of the flow fields within the gaps are no longer required.

Figure 3.8(a) Drying time: 0.5 hrs

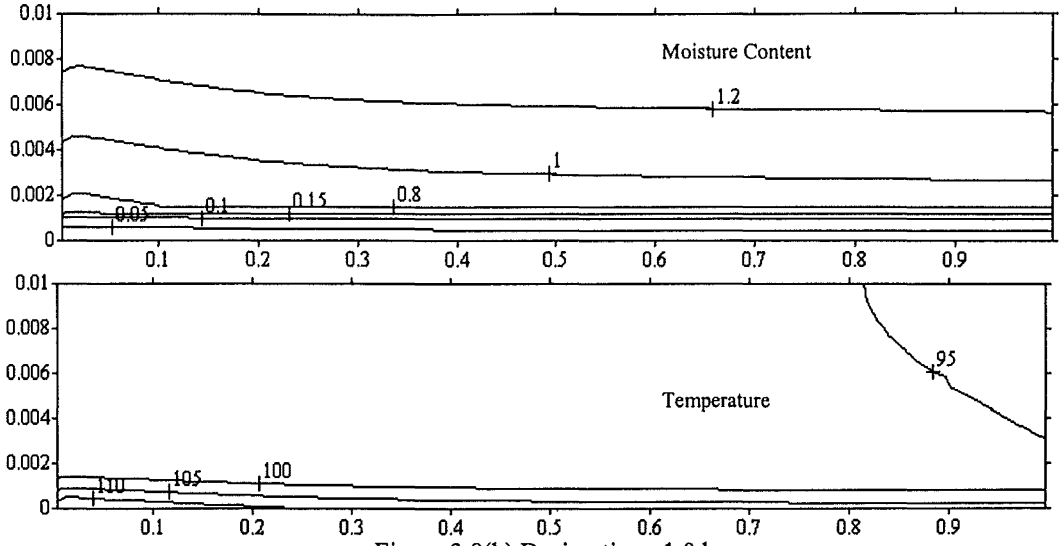

Figure 3.8(b) Drying time: 1.0 hrs

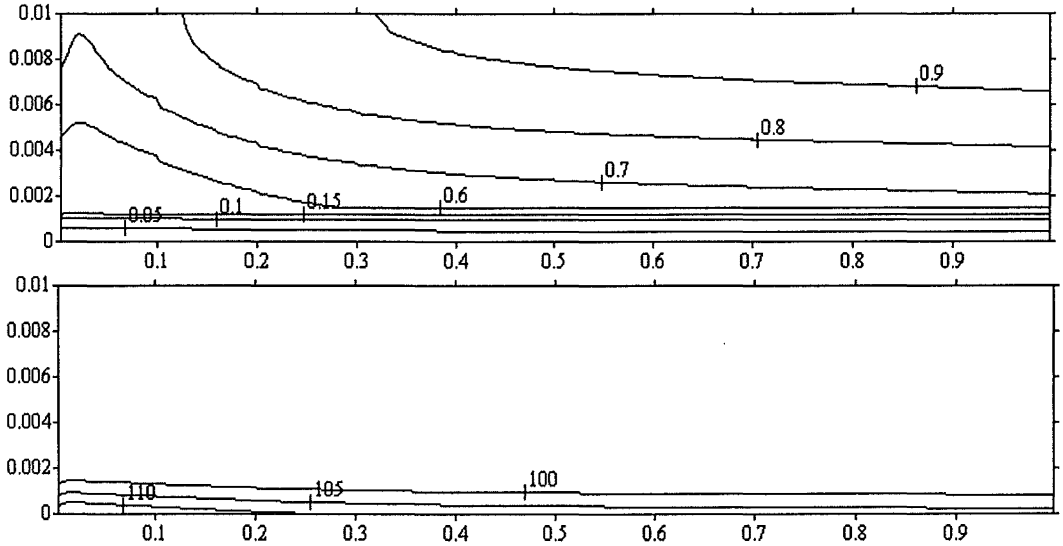

Figure 3.8(c) Drying time: 1.5 hrs

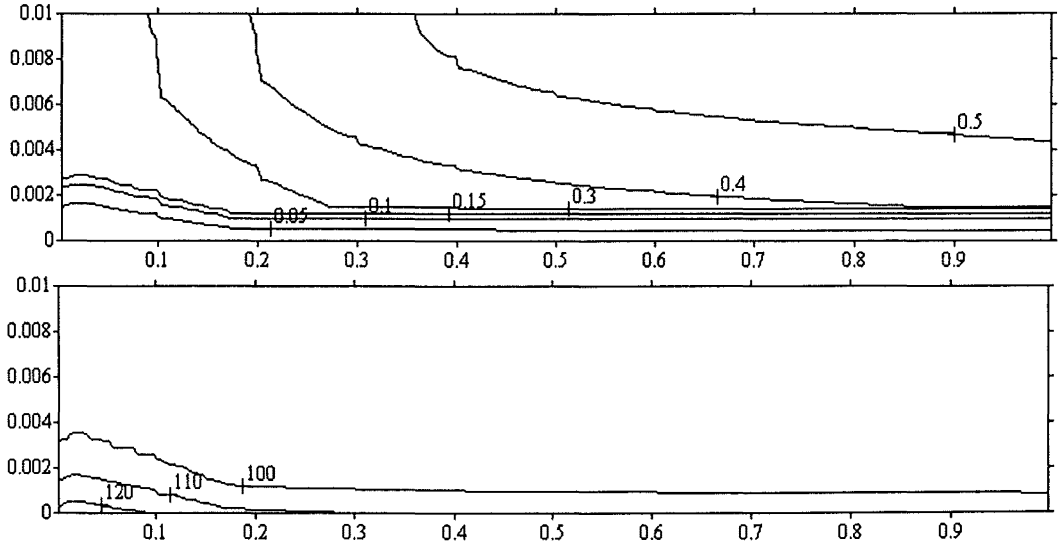

Continued...

Figure 3.8(d) Drying time: 2.0 hrs

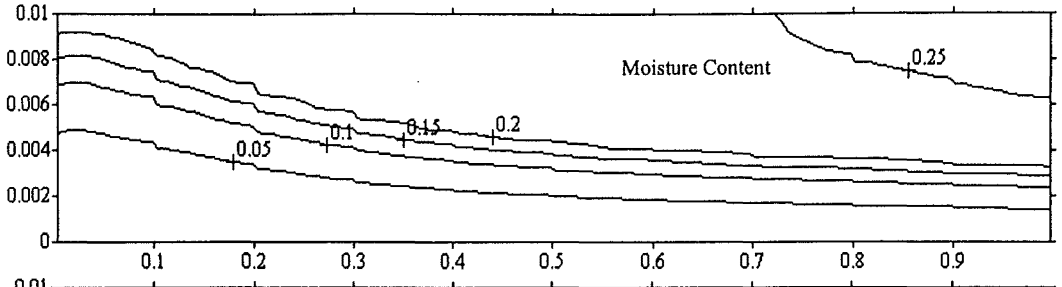

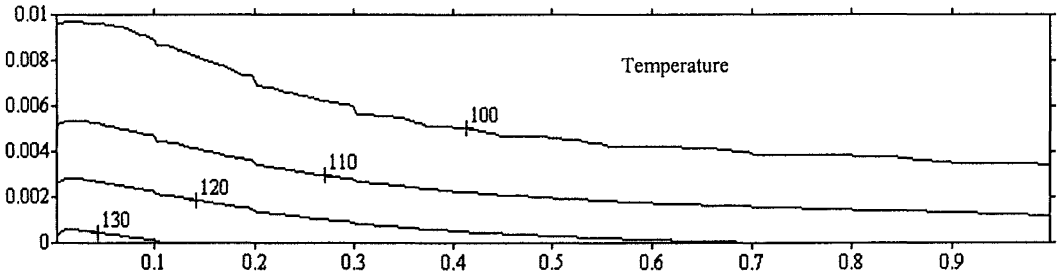

Figure 3.8(e) Drying time: 2.5 hrs

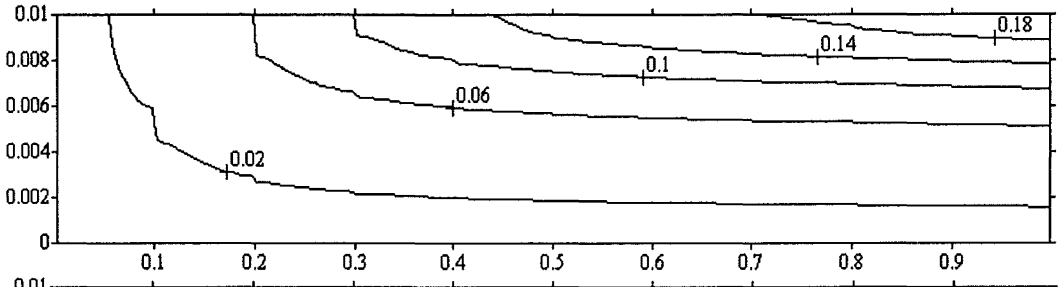

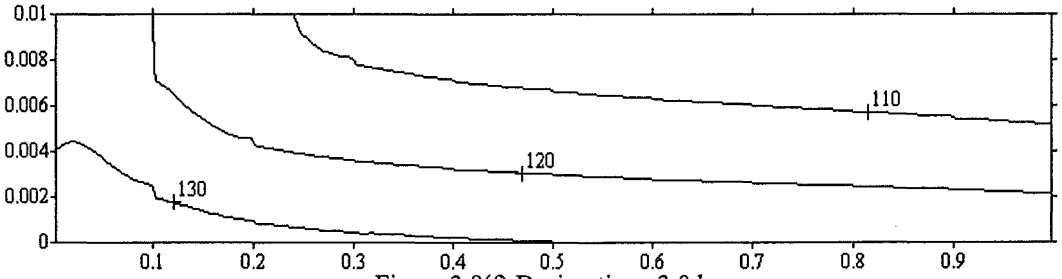

Figure 3.8(f) Drying time: 3.0 hrs

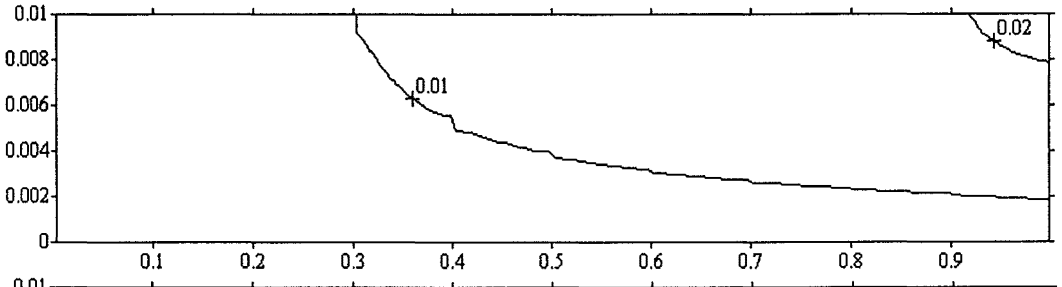

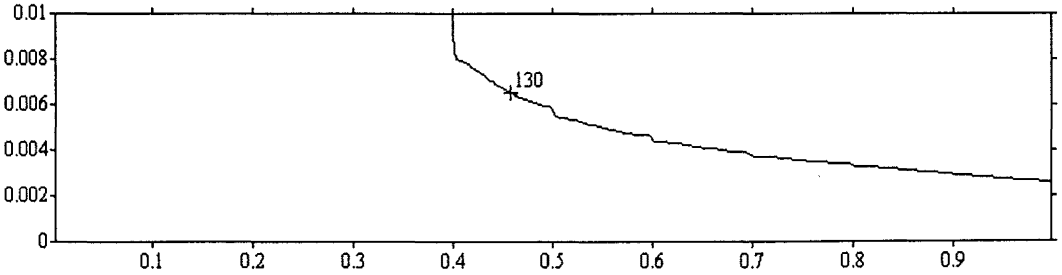

Figure 3.8. Contour plots showing the moisture content (kg/kg) and temperature fields (°C) inside the row of boards at various times; both x (width) and y (thickness) directions have units of metres: Drying conditions: 140/70 °C and 15 m/s.

Unfortunately, the predicted drying behaviour of each board will not be completely realistic, although the leading board should be modelled more accurately than the other boards. Local-transfer coefficient variations, which result from the sudden entrance to the stack, are modelled in the leading board by the sharp interface at the inlet to the fillet space.

The variations of the board-averaged transfer coefficients with respect to distance along the fillet space and drying time are shown in Figures 3.9 and 3.10, respectively. The board-averaged transfer coefficients are enhanced over the first two or three boards and take on nearly constant values from the fourth board onwards (Figure 3.9). There is a slight rise in the transfer coefficients towards the trailing edge of the row of boards. Belhamri *et al.* [1996] experimentally measured a similar rise in the transfer coefficients over a flat plate. They attributed this rise to the development of the flow from the leading edge of the flat plate as the transition from laminar to fully turbulent flow occurs. Figure 3.11 shows that the commercial CFD code called CFX predicts that the near-wall turbulence kinetic energy k rises near the trailing edge of the row of timber boards. It is this trend in k which is responsible for the increase in the transfer coefficients near the trailing edge of the row of boards.

The transfer coefficients are closely linked to the surface temperature and moisture content, which are in turn linked to the internal drying kinetics of the timber. This may explain why the transfer coefficients appear to vary with time in the later stages of the drying schedule (Figure 3.10). During the constant-rate period they remain almost constant because the surface temperature and moisture content are constant. However, once the evaporative plane begins to recede, the surface temperature approaches the dry-bulb temperature (140 °C) and the surface moisture content falls towards the equilibrium moisture content, which is below 1 %. These changes in the surface conditions as the timber boards dry out appear to affect the near-wall turbulence levels with a subsequent increase in the transfer coefficients.

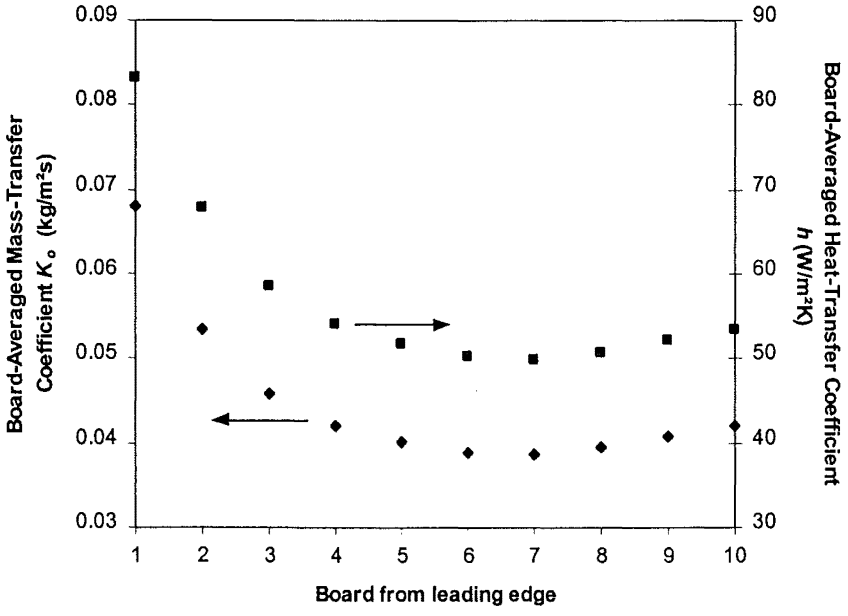

Figure 3.9. Variations of board-averaged heat and mass-transfer coefficients with board number (increasing in the airflow direction) during the constant-rate period.

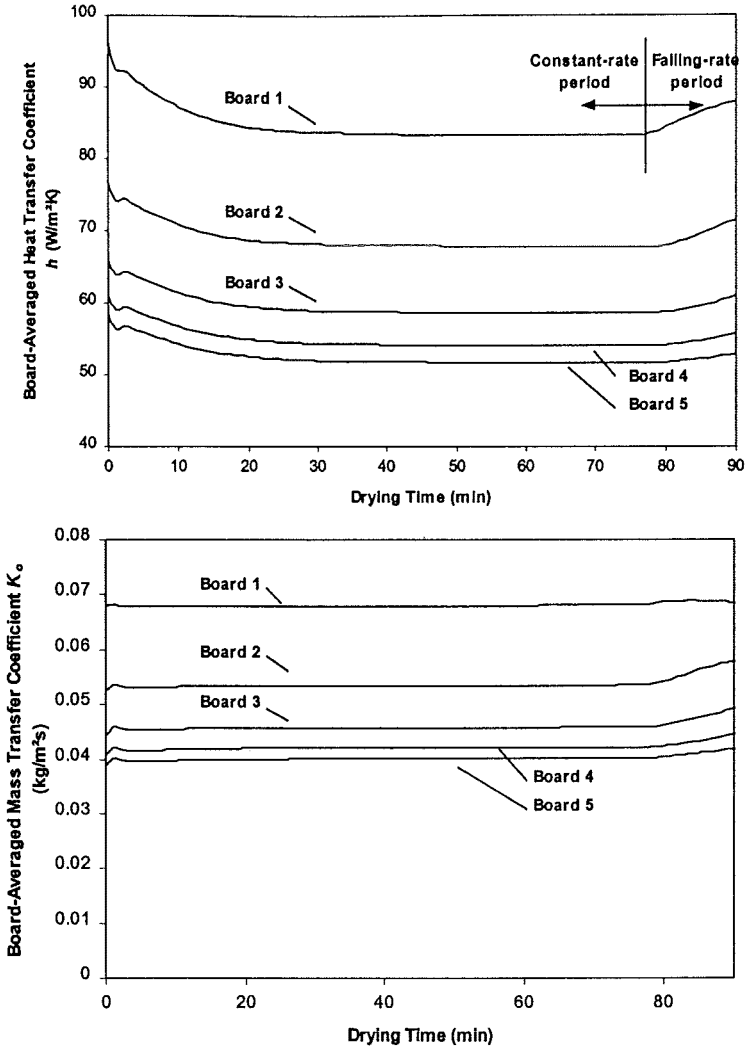

Figure 3.10. Variation of board-averaged heat and mass-transfer coefficients with respect to drying time.

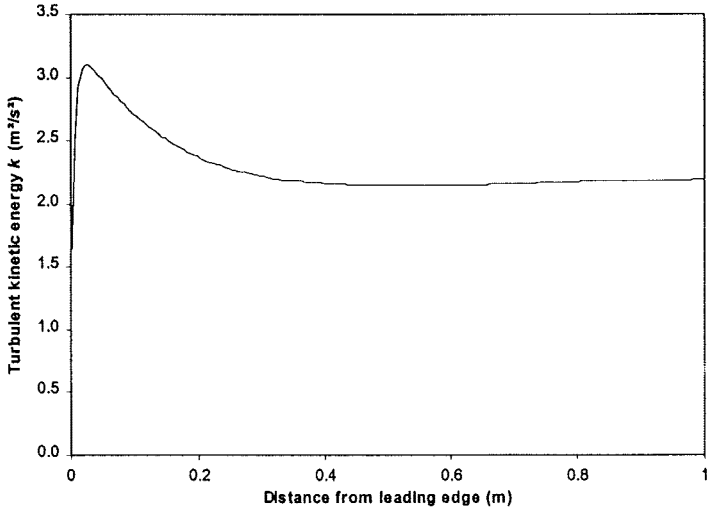

Figure 3.11. CFX predictions of the variation of the turbulent kinetic energy k with distance along the boards in the fillet space (the surface temperature and humidity were set to the values predicted by the rigorous drying model for the tenth board during the constant-rate period).

Critical Moisture Content

The critical moisture content X_{cr} is a transitional point that marks the board-averaged moisture content at which the constant-rate period ends and the first falling-rate period begins. More precisely, it represents the board-averaged moisture content at the time when the local evaporative front at some point within the timber board begins to recede from its initial position near the surface of the timber board. In practice, the local evaporative front is more likely to begin receding near the leading edge of each timber board where the local-transfer coefficients are enhanced due to the presence of the gaps which separate the boards.

Figure 3.12 shows plots of the relative drying rate versus board-averaged moisture content for the first four boards from the leading edge. These plots show that the critical moisture content X_{cr} takes on a higher value over the first two or three boards along the row, while the critical moisture content is virtually constant thereafter. This variation is a result of the enhanced transfer coefficients over the boards near the leading edge. In practice, it is expected that the variation in X_{cr} from board to board will be less severe than predicted in this chapter. As explained above, only the first board is realistically modelled for the local-transfer coefficient variations with respect to distance from the leading edge. For the remaining boards along the row, no account is taken of the sudden transition that occurs between adjacent boards which results in enhanced local-transfer coefficients over the leading edge of each board. In practice, the variations of the local-transfer coefficients over each board will cause these profiles to bear a greater resemblance to the profiles over the leading board, and therefore the variations in X_{cr} from board to board will take on a narrower range of values.

The concept of the characteristic drying curve, which is the basis of Van Meel's [1958] batch drying model, relies on the assumption that the critical point does not depend on the external drying conditions. Clearly, this assumption is incorrect for the first two or three boards from the leading edge, but is quite reasonable for the remaining boards. Another underlying assumption involved with the concept of the characteristic drying curve is that the characteristic drying curves for all timber boards

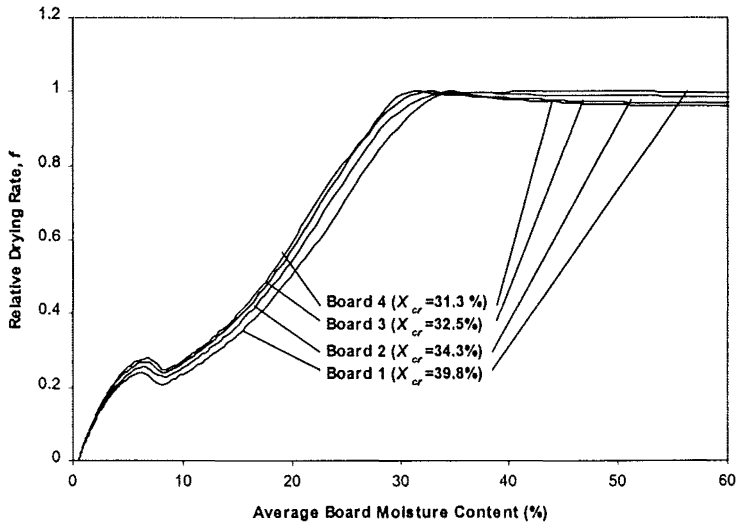

Figure 3.12. Characteristic Drying Curves for the leading four boards along the row.

within the stack are geometrically similar. Again, it is evident from Figure 3.12 that this assumption is not valid for the first two or three boards from the leading edge. Overall, the concept of the characteristic drying curve is invalid for only the first two or three boards from the leading edge. A typical timber stack contains at least 20 boards across the width. Therefore, Van Meel's batch drying equations, which applies the concept of the characteristic drying curve, should adequately model the moisture-content variations across most of the stack, provided that the enhanced transfer coefficients over the first two or three boards from the leading edge are taken into account in the calculations.

Figure 3.12 also shows that the constant-rate period is not exactly constant. Only the leading board experiences a constant-rate period with a relative drying rate of approximately unity. The remaining boards show a constant-rate period at higher moisture contents. However, as the critical point is approached, the drying rate increases and reaches a peak value at the critical moisture content. This increase in the drying rate is attributed to decreasing heat and mass-transfer driving forces over the upstream timber boards as they dry out, which results in enhanced drying rates over the downstream timber boards.

There is a clear kink in every characteristic drying curve during the falling-rate period (Figure 3.12). This kink, which is not realistic, is the direct consequence of setting the temperature gradients with respect to time equal to zero when the temperature in the wet zone reaches the boiling point of water. It was discussed in Chapter 2 that this restriction was necessary in order to limit the temperature in the wet zone to the boiling point of water since the transport equations would otherwise have no such restriction. Once the evaporative front reaches the centre-line of the board, it vanishes and the restriction on the temperature-time gradient also vanishes. This moment represents a discontinuity which is responsible for the kinks in the relative drying-rate curves (Figure 3.12), and the sharp increase in the centre-line temperature profiles of the predicted results shown in Figures 2.10 and 2.11 of Chapter 2. The experimental centre-line temperature profiles do not exhibit this behaviour. Although the relative drying-rate curve (Figure 3.12) appears to be heavily influenced by the restriction on the temperature-time gradient, Figures 2.10 and 2.11 show that the average moisture content profiles and temperature profiles are not seriously affected.

Moyne *et al.* [1985] and Perré *et al.* [1993] took a similar approach by limiting the surface temperature to the boiling point of water when the surface moisture content was above zero saturation in the case of a non-hygroscopic material, or above fibre saturation in the case of wood. This is essentially equivalent to setting the temperature gradient with respect to time equal to zero at the surface. These workers did not limit the temperature in the wet zone once the evaporative plane began to recede because they included convective gaseous flows in their models to account for the overpressures which may occur within less permeable timbers. Thus, in their models, the temperature of the wet zone could increase above the boiling point of water at atmospheric pressure.

Figure 3.13 shows the variation of the critical moisture content X_{cr} with distance from the leading edge for two different air velocities: 5 m/s and 15 m/s. The corresponding variations in the transfer coefficients with distance from the leading edge are shown in Figure 3.14. The high-Reynolds number turbulence model is not

applicable for an air velocity of 5 m/s since the corresponding Reynolds number is too low. Nevertheless, the turbulence model was used at this velocity to illustrate the point that the effective heat and mass-transfer coefficients have very little effect on the critical moisture content. In Chapter 4, it is implicitly assumed that the critical moisture content is independent of the air velocity. This is a reasonable assumption given that when the transfer coefficients are effectively halved by reducing the air velocity from 15 m/s to 5 m/s (Figure 3.14), the critical moisture content drops by only 4% at the leading edge of the row of boards and 2% at the trailing edge (Figure 3.13).

The effect of the thickness of the board on the critical moisture content is shown in Figure 3.15. The drying processes of both rows of boards, each with different board thicknesses, were simulated under the same external drying conditions and using the

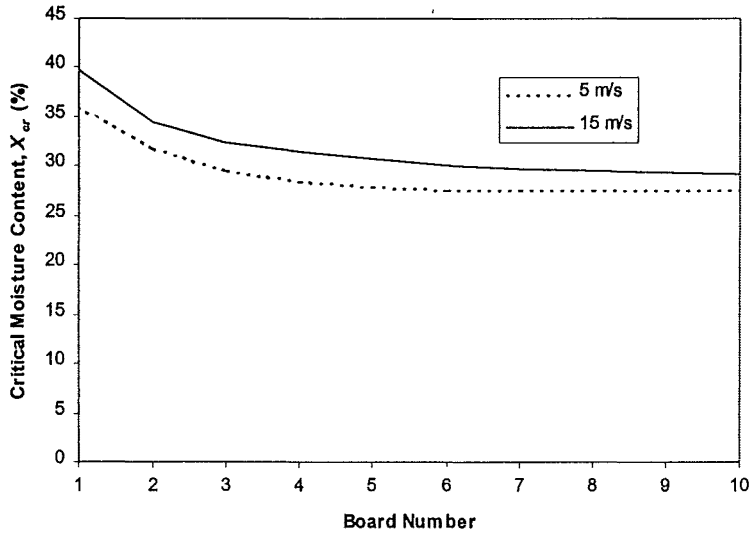

Figure 3.13. Variation of the critical moisture content with distance from the leading edge at two different fillet-space air velocities.

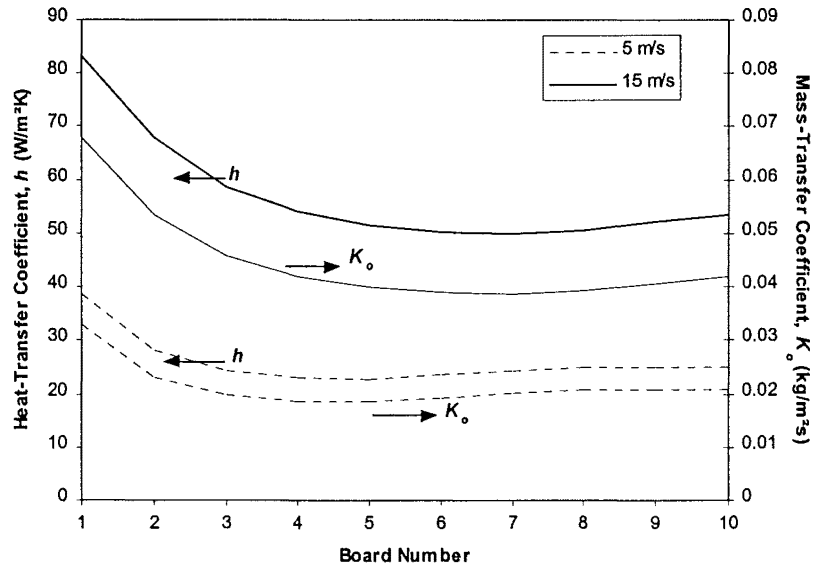

Figure 3.14. Variation of heat and mass transfer coefficients with distance from the leading edge during the constant-rate period at two different fillet-space air velocities.

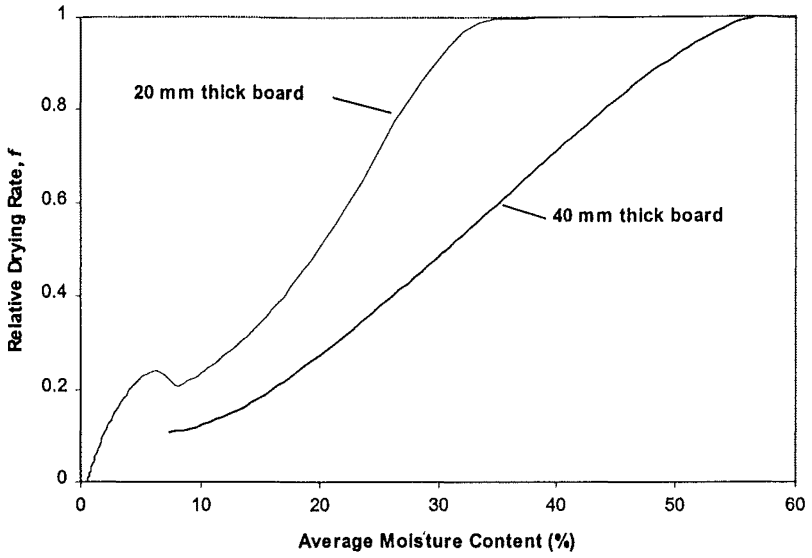

Figure 3.15. Characteristic Drying Curves for two boards of different thicknesses. Both boards are the leading boards along the row.

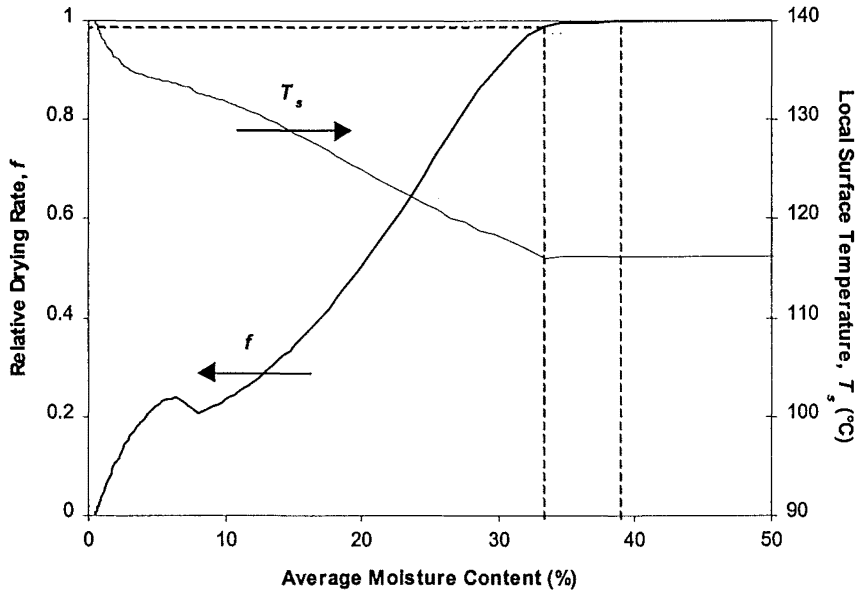

Figure 3.16. Characteristic Drying Curve and local surface-temperature (50 mm from the leading edge) plot for the 20 mm thick leading board.

same timber properties. The predicted critical moisture content of the 20 mm thick board is approximately 40 % while the predicted critical moisture content of the 40 mm thick board is approximately 60 %. Thus, the critical moisture content increases with board thickness. Krischer *et al.* [1978] have experimentally found similar trends for sand, wheat, and dye pigments. This demonstrates the importance of using a characteristic drying curve in Van Meel's batch drying model which is derived from drying-rate data for timber of the same thickness as the timber which is being simulated.

Figure 3.16 shows that a lag occurs between the critical moisture content and the board-averaged moisture content at which the local evaporative front, 50 mm from the

leading edge of the first board along the row, begins to recede. The characteristic drying curve of the first board along the row was presented because local transfer coefficient variations across the width of the board resulting from the sharp transition at the leading edge were taken into account in this case, whereas these variations were neglected in the remaining boards. The critical moisture content, when the evaporative plane at some point within the board begins to recede, is approximately 39 %, while the local evaporative plane 50 mm from the leading edge of the board begins to recede at an average moisture content of only 33 %. Clearly, the enhanced local-transfer coefficients at the leading edge of the board have caused the local evaporative plane at the leading edge to recede before the local evaporative plane 50 mm from the leading edge. The moisture-content contour plots shown in Figure 3.8c confirm this observation. This demonstrates the importance of accounting for the two dimensional drying behaviour of timber when mathematically deriving characteristic drying curves. A one-dimensional model should not be used to derive characteristic drying curves because the effects of varying local-transfer coefficients are not taken into account.

In Chapter 2 (Figure 2.8), the experimental data of Pang [1994] were presented that showed a moisture content lag, between the critical point and the moisture content at which the local evaporative plane began to recede, which was considerably greater than found in this chapter. The critical moisture content was approximately 100 % for the 50 mm thick board, while the local evaporative plane 60 mm from the leading edge of the board began to recede at an average moisture content of only 45 %. In Pang's experiments, a dummy board was placed in front of the drying specimen; however, no dummy board was placed behind it. Thus, air flowed over a third exposed surface which lead to heat transfer across this interface. Pang painted the third exposed surface to eliminate mass transfer through this surface. However, given that the drying process is predominantly heat transfer-controlled under high-temperature drying conditions, then this extra source of heat would certainly have contributed to the time and rate at which the evaporative plane receded within the board near the trailing edge. This would in turn have caused the board-averaged drying rate to drop significantly before the local evaporative plane 60 mm from the leading edge of the board began to recede.

Langrish [1998] points out that moisture-content profiles in stacked timber will be considerably less two-dimensional than those for the drying of single boards during laboratory testing. Therefore, precautions should be taken to simulate typical kiln stacking arrangements when conducting single-board tests in the laboratory. In addition, even though small gaps of approximately 1mm usually separate the remaining boards (Kho [1993]), the heat and moisture fluxes through the sides of the boards that are butted together will only be a small fraction of the fluxes through the exposed surfaces tangential to the airflow direction. Langrish [1998] states that, under laminar flow conditions, the fluxes through the sides of the timber boards are less than 1% of the fluxes through the broad faces exposed to the airflow, because there is no net airflow through the gaps that separate the boards. Nevertheless, enhanced transfer coefficients over the leading edge of each board and varying heat and moisture driving potentials in the airflow direction will ensure that the drying process remains two-dimensional. This is evident in the contour plots shown in Figure 3.8c, which show clear two-dimensional drying behaviour even though it is assumed that the leading and trailing edges of these boards are insulated.

Air Temperature and Humidity Variations

Figure 3.17 shows the variation in the air temperature and humidity with drying time and distance from the leading edge. During the first one-and-a-half hours, almost every board is undergoing the constant-rate period and therefore the temperature and humidity profiles do not change significantly. However, after two hours, the air temperature and humidity gradients with respect to distance along the fillet space begin to decrease as the average moisture contents of the boards approach the equilibrium moisture content and the temperature of the boards rises towards the inlet dry-bulb temperature.

The air temperature and humidity vary by about 8 °C and 0.009 kg/kg, respectively, across the stack during the constant-rate period (Figure 3.17). This corresponds to a change in the dry and wet-bub temperatures from 140/70 °C at the fillet-space inlet to 132/70.2 °C at the fillet-space outlet. Therefore, each timber board is drying under a different set of external conditions during the constant-rate period. Nevertheless, Figure 3.12 shows that the characteristic drying curves from the third board onwards are nearly unaffected by this variation in the external drying conditions. Thus, the assumption that the characteristic drying curves are independent of the external temperature and humidity is valid within the range of drying conditions tested.

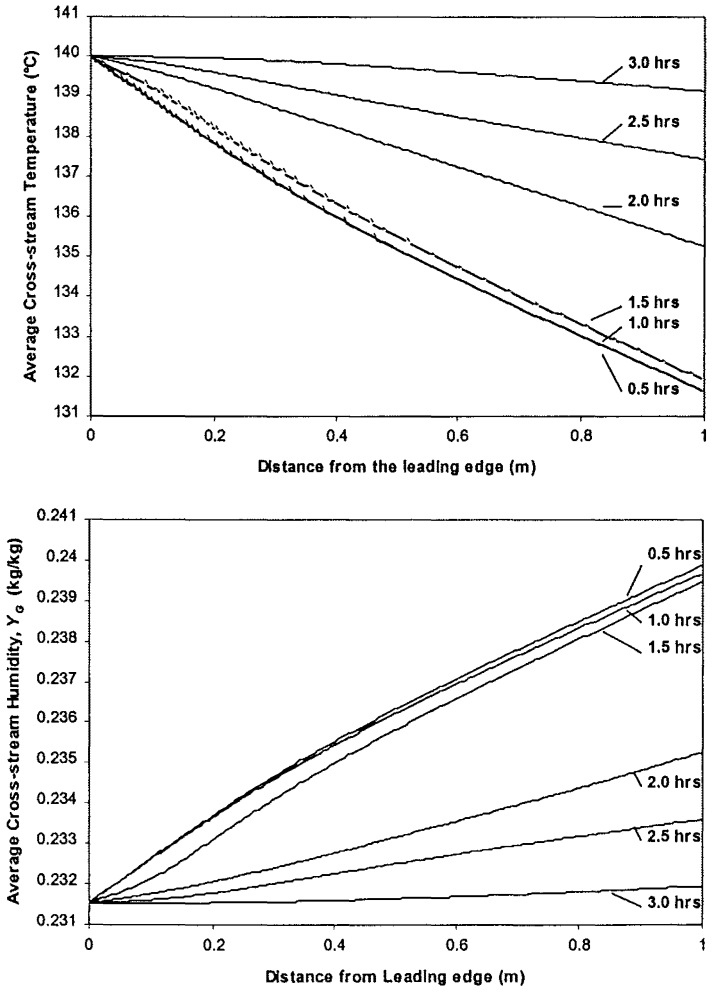

Figure 3.17. Variations in temperature and humidity with distance from the leading edge and drying time.

Validity of Van Meel's Batch Drying Model

Figure 3.18 compares the predictions of the rigorous batch-drying model (points) with Van Meel's batch-drying model (lines). The characteristic drying curve used in Van Meel's batch-drying model was taken from the predicted drying data produced by the rigorous drying model for the last timber board from the leading edge. Every facet of the drying process was represented in this characteristic drying curve, including the warm-up period and the 'kink' in the relative drying curve presented in Figure 3.12. The critical moisture content X_{cr} was set to 0.295 kg/kg and the surface humidity during the constant rate period Y_s was set to 0.2610 kg/kg, which was calculated from the temperature and the moisture content at the surface of the trailing timber board using the sorption isotherms (Equations (2.30)-(2.35)). The inlet mainstream humidity Y_G was given a value of 0.2315 kg/kg which corresponds to dry and wet-bulb temperatures of 140 and 70 °C, respectively. The mass-transfer coefficient β was given a value of 0.0257 kg/m²s which was calculated using Equation (3.116) and the average mass-transfer coefficient over the trailing boards during the constant rate period (K_o=0.04 kg/m²s) which was taken from the results of the rigorous drying model (Figure 3.14).

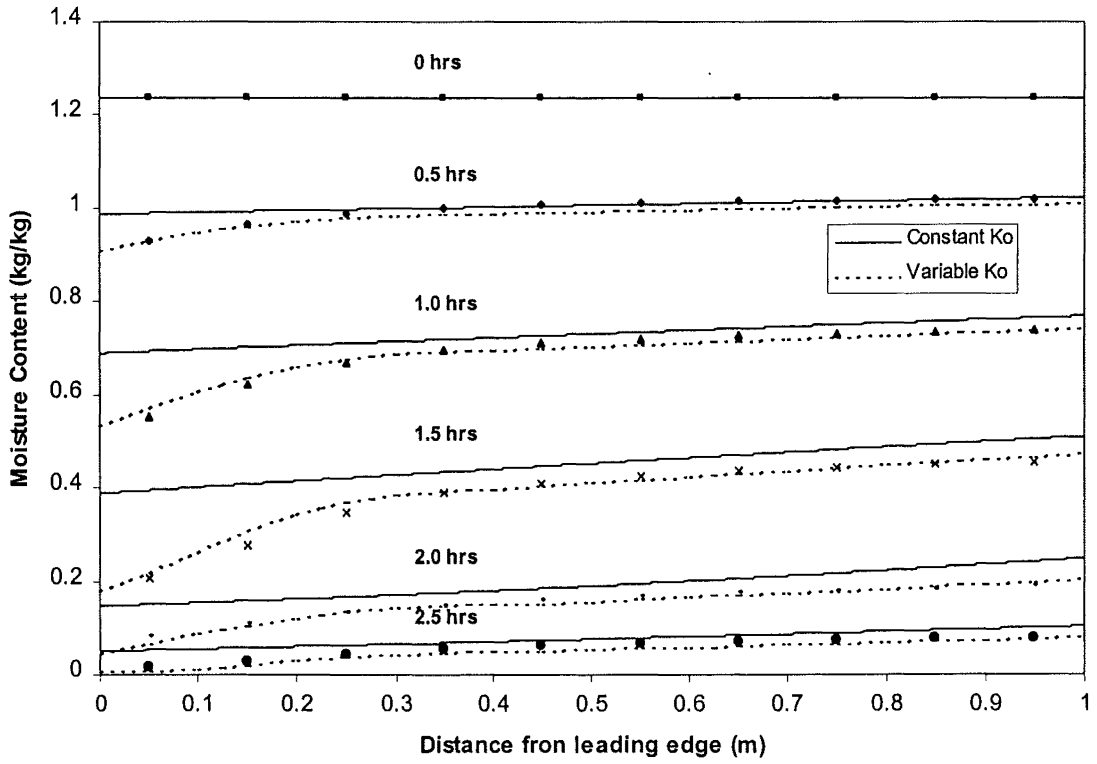

Figure 3.18. Comparison between the results of the rigorous batch-drying model and Van Meel's batch-drying model for the row of 100 mm wide x 20 mm thick boards with a 25 mm fillet gap.

Firstly, a comparison is made between the 'points' of the rigorous drying model and the 'lines' of Van Meel's model, for which a constant mass-transfer coefficient was assumed in the airflow direction. At 0.5 hrs, the results from the simple and rigorous drying models compare well with each other. However, after 0.5 hrs Van Meel's model begins to under-predict the drying rates for every board along the row. The under-predicted drying rates result, among other factors, from the incorrect assumptions involved with the concept of the characteristic drying curve, which have been explained above, and the enhanced average transfer coefficients over the leading boards which have not been taken into account in this particular application of Van Meel's model. The accuracy of the simple batch-drying model can be improved by accounting for the enhanced transfer coefficients over the leading boards along the row.

Ashworth [1977] has suggested a simple method to account for varying transfer coefficients. Another dimensionless number involving the variable transfer coefficient is defined as follows:

$$\sigma = \frac{\beta(x)}{\beta(L)} \tag{3.121}$$

where $\beta(x)$ is the local mass-transfer coefficient at a distance x from the leading edge, and L is the width of the stack. The dimensionless numbers for distance and time are then given by the following formulae:

$$\xi = \frac{\beta(L)a}{G}x \tag{3.122}$$

$$\theta = \frac{\beta(L)a\left(Y_s - Y_G^o\right)}{\left(X_{cr} - X_e\right)\rho_s\left(1-\varepsilon\right)}t \tag{3.123}$$

and the differential equations become

$$-\frac{\partial \Pi}{\partial \xi} = -\frac{\partial \Phi}{\partial \theta} = \sigma f \Pi \tag{3.124}$$

The dashed lines shown in Figure 3.18 show the improved solution which results when variable transfer coefficients are considered. In order to match this solution more closely with the solution of the rigorous drying model, the surface humidity during the constant-rate period was increased from 0.2610 kg/kg to 0.2626 kg/kg.

The sigma function σ defined by Equation (3.121), which corresponds to the mass-transfer coefficients shown in Figure 3.14, is plotted in Figure 3.19. However, this particular function was not used in the improved drying model. A sigma function σ corresponding to a narrower range of mass-transfer coefficients was chosen, as shown in Figure 3.19. This was necessary in order to correct for the fact that a constant surface humidity was chosen during the constant-rate period, whereas the rigorous drying model predicted that the surface humidity varied with distance from the leading edge (from 0.25 kg/kg at the leading edge up to 0.261 kg/kg at the trailing edge). These variations are also implied in the moisture-content contour plots shown in Figure 3.8a-b. Van Meel's model can only accurately model the drying kinetics

within the timber stack by accounting for variations in the surface humidity with distance from the leading edge during the constant-rate period. In the case of timber, the surface humidity does not necessarily correspond to the saturation humidity at the given wet-bulb temperature. In rough-sawn timber, a thin-dry layer exists at the surface and therefore the surface humidity during the constant-rate period will be closer to the mainstream humidity of the cross-circulating air. Figure 3.20 compares the solutions of the Van Meel's model when the saturation and actual surface humidities are used. Clearly, the solution is very sensitive to the magnitude of the surface humidity.

Variations of the surface humidity in the airflow direction will also have a large impact on the drying solution. Unfortunately, the variations in the surface humidity with distance during the constant-rate period are not easily determined. Therefore, in the next chapter, it is assumed that the surface moisture content during the constant-rate period is everywhere above the fibre saturation point so that the surface humidity becomes equal to the saturation humidity at the given wet-bulb temperature. This assumption will not affect the general trends observed.

3.5 Conclusions

The characteristic drying curve is nearly independent of the external air temperature and humidity over the range of drying conditions tested, although it is a weak function of the transfer coefficients. The dependence of the critical moisture content on the transfer coefficients results in higher values of the critical moisture content for the first two or three boards from the leading edge due to the enhanced transfer coefficients over these boards. The critical moisture content also increases with air velocity because there is a corresponding increase in the transfer coefficients, although it was shown that the rise in the critical moisture content is very slight even for a large increase in the transfer coefficients. Thus, the assumption that the characteristic drying curve is independent of the external conditions (air velocity, temperature and humidity) is reasonable over the range of conditions tested for the majority of the timber boards in a stack.

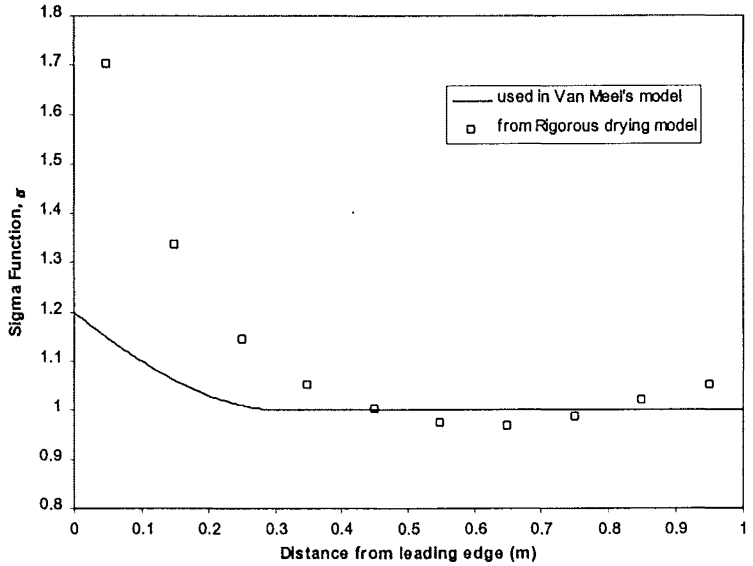

Figure 3.19. Variation of the sigma function σ (or relative mass-transfer coefficient) with distance from the leading edge.

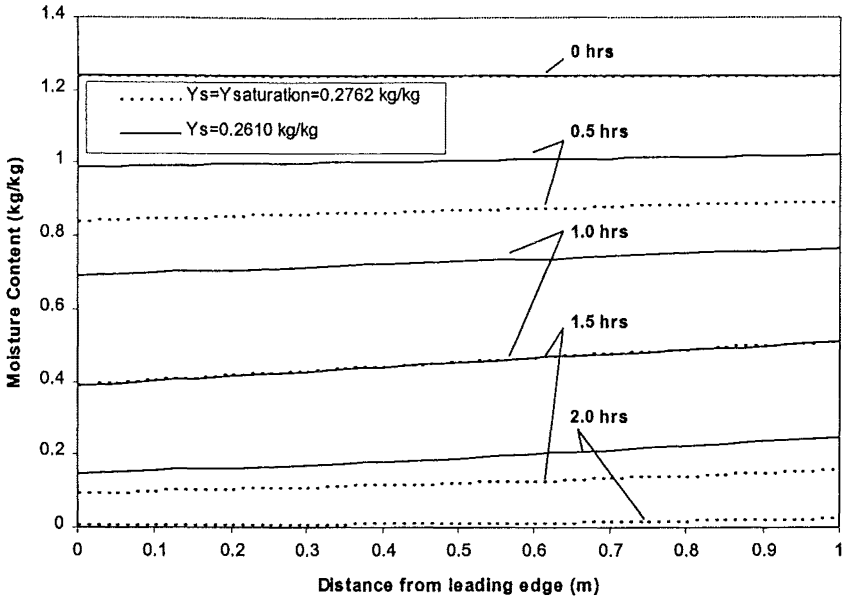

Figure 3.20. Comparison between the results of Van Meel's batch-drying model for two different constant-rate period surface humidities.

It is important when simulating kiln-wide timber drying using Van Meel's batch drying equations that the characteristic drying curve is derived from timber of the same thickness as the timber which is being simulated. It is also important when deriving the characteristic drying curve from a mathematical model, that a two-dimensional drying model is used since the two-dimensional drying behaviour of timber can influence the magnitude of the critical moisture content. In addition, the influence of kiln stacking arrangements should be considered when conducting single-board tests in the laboratory.

The results from Van Meel's model compares well with the results of the rigorous drying model especially when the variations in the mass-transfer coefficients with distance from the leading edge are considered. More accurate predictions are only possible by accounting for the variations of the characteristic drying curve with distance from the leading edge. Another difficulty with Van Meel's batch drying model is that it requires knowledge of the surface humidity during the constant-rate period. This does not necessarily correspond to the saturation humidity at the wet-bulb temperature. The thin-dry layer at the surface of the timber board ensures that the surface humidity is less than the saturation humidity even during the constant-rate period, which has classically been defined as the period when the surface moisture content is greater than the fibre-saturation point.

3.6 Symbols

a	exposed surface per unit volume of dryer, m^2/m^3
A	area, m^2
C_1, C_2, C_μ	constants in turbulence model
Cp	heat capacity, J/kgK
D	diffusion conductance at cell face

D_{AB}	diffusivity coefficient, m^2/s
E	constant in turbulence model (wall model)
f	relative drying rate
F	convective mass flux per unit area at cell face, kg/m^2s
G	air rate, kg/ms
	generation of turbulence kinetic energy, kg/ms^3
H	enthalpy, kJ/kg
j	flux, kg/m^2s
k	turbulence kinetic energy per unit mass, m^2/s^2
	thermal conductivity of wood, W/mK
k_p	turbulence kinetic energy per unit mass at near wall grid point, m^2/s^2
K_o	mass transfer coefficient based on mass-fraction potential, kg/m^2s
$\dot{m}$	phase change rate, kg/m^3s
m	mass flux, kg/m^2s
M	molecular mass, kg/mol
n	dimensionless parameter for flow
N_v	drying rate per unit exposed surface, kg/m^2s
NTU	dimensionless parameter for distance
P	static pressure, Pa
q	heat flux, J/m^2s
R	universal gas constant, 8.314 J/molK
S_ϕ	source term
t	time, s
T	temperature, K
u	horizontal component of velocity, m/s
v	vertical component of velocity, m/s
x	distance along kiln in air flow direction, m
X	moisture content, kg/kg
X_{cr}	critical moisture content, kg/kg
X_e	equilibrium moisture content, kg/kg
y	distance up height of stack or fillet, m
y_v	mol fraction of vapour component
Y_A	mass fraction of component A, kg/kg
Y_W	saturation humidity, kg/kg
Y_G	dry-bulb humidity, kg/kg
V	volume, m^3
Z	streamed length, m

Greek

α	under-relaxation factor
β	mass transfer coefficient based on humidity potential, kg/m^2s
ε	voidage of the stack in a kiln
	dissipation rate of turbulence kinetic energy, m^2/s^3
Φ	normalised free moisture content
	scalar variable

ϕ	humidity potential coefficient general variable
Γ_ϕ	diffusion coefficient
κ	von Karman constant
λ	thermal conductivity of air-vapour mixture, W/mK
μ_l	laminar viscosity, kg/ms
μ_t	turbulent viscosity, kg/ms
Π	normalised humidity potential
θ	dimensionless parameter representing the extent of drying
ρ_l	density of liquid water (kiln volume basis), kg/m^3
ρ_v	density of water vapour (kiln volume basis), kg/m^3
ρ_s	density of wood, kg/m^3
ρ_G	density of air, kg/m^3
σ	constant in turbulence model turbulent Prandtl or Schmidt number
τ	time, s
τ_w	wall shear stress, N/m^2
ξ	dimensionless parameter representing distance (*NTU*)
	relative humidity of air
	general variable

Dimensionless numbers

H^+	dimensionless enthalpy
Sc	Schmidt number
Pr	Prandtl number
u^+	dimensionless velocity
y^+	dimensionless distance
Y^+	dimensionless mass fraction

3.7 References

AEA Technology, 1995, *CFX 4.1: Flow Solver User Guide*, Computational Fluid Dynamics Services, Harwell Laboratory, Oxfordshire, UK.

ASCE Task Committee on Turbulence Models in Hydraulic Computations, 1988, Journal of Hydraulic Engineering, Vol 114, No 9.

Belhamri, A., Fohr, J.P., 1996, Heat and mass transfer along a wetted porous plate in an air stream, AIChE Journal, 42(7):1833-1843.

Jayatilleke, C.L.V., 1969, The influence of surface roughness on the resistance of a laminar sub-layer to momentum and heat transfer, In U. Grigull and E. Hahne (eds), *Progress in Heat and Mass Transfer*, 1, Pergamon Press, NY, 193-330.

Keey, R.B., 1978, *Introduction to Industrial Drying Operations*, Permamon Press, Oxford, UK.

Keey, R.B., 1992, *Drying of Loose and Particulate Materials*. Hemisphere Publishing Corporation, New York.

Kho, P.C.S., 1993, Mass transfer coefficients from in-line slabs, Phd thesis, Department of Chemical and Process Engineering, University of Canterbury, New Zealand.

Krischer, O., Kast, W., 1978, Die wissenschaftlichen Grundlagen der Trocknungstechnik (The Scientific Fundamentals of Drying Technology), 3rd ed., Springer-Verlag, Berlin, New York.

Langrish, T.A.G., Keey, R.B., Kho, P.C.S., Walker, J.C.F., 1993, Time-dependent flow in arrays of timber boards: flow visualisation, mass-transfer measurements and numerical simulation, Chemical Engineering Science, 48 (12):2211-2223.

Langrish, T.A.G., 1998, The significance of the gaps between boards in determining the moisture-content profiles in the drying of hardwood timber, Industrial Drying Symposium, Greece.

Launder, B.E., Spalding, D.B., 1974, The numerical computation of turbulent flows, *Computer Methods in Applied Mechanics and Engineering*, 3:269-289.

Moyne, C., Degiovanni, A., 1985, Drying '85 edited by Mujumdar, A.S., Hemisphere Publishing Corporation, New York, 109-115.

Pang, S., 1994, High-temperature drying of Pinus radiata boards in a batch kiln. PhD Thesis, University of Canterbury, New Zealand.

Patankar, S.V., 1980, *Numerical Heat Transfer and Fluid Flow*, Hemisphere Publishing Corporation, Taylor- Francis Group, New York

Patankar, S.V., and Spalding, D.B., 1972, A calculation procedure for heat, mass and momentum transfer in three-dimensional parabolic flows, *Int. J. Heat Mass Transfer*, 15:1787.

Perré, P., Moser, M., Martin, M., 1993, Advances in transport phenomena during convective drying with superheated steam or moist air, *Int J Heat and Mass Transfer*, 38 (11):2725-2746.

Reid, R.C., Prausnitz, J.M., Sherwood, T.K., 1977, *The properties of gases and liquids*, 3rd edition, McGraw-Hill Book Company. New York.

Rodi, W., 1980, *Turbulence models and their application in hydraulics- a state of the art review*, International Association for Hydraulic Research, Delft, The Netherlands.

Thomas, L.H., 1949, Elliptic Problems In linear Difference Equations over a Network, *Watson Sci. Comput. Lab. Report*, Columbia University, New York.

Van Meel, D.A., 1958, Adiabatic convection batch drying with recirculation of air, *Chem. Eng. Sci.*, 9:36-44.

Versteeg, H.K., Malalasekera, W., 1995, *An introduction to computational fluid dynaimcs: the finite volume method*, Longman Group Ltd.

CHAPTER FOUR

LUMPED-PARAMETER MODEL

4.1 Introduction

In Chapter 2, a mathematical model was developed to simulate the high-temperature drying of softwood boards. The model was applied to both sapwood and heartwood boards to predict the one-dimensional temperature and moisture profiles within a single board during drying. In the model, the moisture and heat fluxes at the surface of the timber board were expressed as products of concentration or temperature difference driving forces, and external mass or heat-transfer coefficients, respectively. Chapter 3 extended this approach by using the two-dimensional form of the mathematical model developed in Chapter 2, and simulating the external flow using the Navier-Stokes equations, a turbulence model, and scalar equations for enthalpy and humidity. Continuity of fluxes and the no-slip condition were stipulated at the surface of the timber boards. The resultant set of equations formed an extremely rigorous drying model which was found to be computationally too slow for the purpose of analysing commercial kiln behaviour.

A simplified method is required to model the kiln behaviour with sufficient accuracy for the evaluation or improvement of kiln design and operation. In this Chapter, a simplified batch-drying method developed by Van Meel [1958] is employed, which depends upon lumped-parameter models of the moist timber. This method was investigated in the previous chapter to determine its accuracy. It was found that the model accurately predicts moisture content variations across the stack except at the leading edge where the concept of the characteristic drying curve breaks down.

4.2 Moisture-Content Variation

Board timber is dried to make it more suitable for use as a building material. Correctly-dried wood results in an improvement in its dimensional stability, increased tensile and compressive strengths, and a reduction in its degradation by micro-organisms. From an economic viewpoint, it is important to dry timber rapidly and efficiently with minimal degrade. The use of kilns to meet these criteria is preferred whenever possible over the traditional method of outdoor air-seasoning due to a greater control of the process variables.

Kilns for drying *Pinus radiata* operate across a range of temperatures. High-temperature kilns operate at dry-bulb temperatures above 100 °C, whereas conventional kilns operate at lower temperatures (between 70 and 90 °C). The advantages of using a high-temperature kiln are quicker drying times, and a lower

fibre-saturation point. On the other hand, conventional kilns are less likely to cause wood degradation. Conventional kilns will be the focus of this chapter, although the analysis is applicable to kiln operations above 100 °C.

Consider the kiln shown in Figure 4.1. The drying medium, air, is in direct contact with the surfaces of the boards to be dried. These boards are assembled in horizontal rows with each row separated by a number of regularly-spaced stickers to form a stack. The stack should be high enough and long enough to minimise free areas within the kiln through which the air can bypass the wood. In practice, quite modest gaps offer a large flow area with low resistance compared to the stack flow area, and the amount of air bypassing can be quite considerable. Riley [1986] has observed that air bypass around a stack can be up to 100%, even in a fully loaded kiln: that is, as much air is moving around the stacks as is moving through the stacks. The proper use of baffles and curtains can reduce the bypass fraction, but some loss around the stack is unavoidable.

The rate at which air is circulated within a kiln is very important, particularly at higher kiln temperatures when the external convection in the kiln becomes increasingly rate-determining. The higher the velocity of the air, the greater the rate of heat transfer by convection and the rate of water-vapour removal. As air gains moisture, its ability to take up further moisture decreases.

Moisture variation in stacked wood is inevitable because, as air travels through a stack, the gas becomes more humid. Therefore, the driving force for moisture evaporation diminishes so that wood at the air-outlet face of the stack is not dried so rapidly as wood at the air-inlet face. This effect can be minimised with the use of airflow reversals. Periodically reversing the direction of the air flow ensures that both sides of the kiln are exposed to the driest air at some point during the schedule, thus reducing the moisture-content difference across the kiln in the stream-wise direction. Airflow reversals are accomplished by the use of bidirectional fans whose rotational direction can be switched over.

Non-uniform drying rates are intensified to a minor degree by entrance effects at the inlet to each fillet space. Entrance effects cause the board-averaged heat and mass-transfer coefficients to take on higher values over the first two or three boards, while the coefficients thereafter are virtually constant (Kho [1993]). Airflow reversals also mitigate the effect of varying transfer coefficients. However, such considerations are ignored in this investigation; the transfer coefficients are assumed to be constant along each row of timber boards since only a few boards at the leading edge of the stack are affected by the entrance effect.

The number of airflow reversals and the time interval between reversals will play a large role in effecting the moisture-content distribution in the timber boards throughout the kiln by the end of drying. The kiln operator must decide when and how often these reversals should take place for optimum results. Studies by computer simulation to determine appropriate flow-reversal times have been done by Ashworth

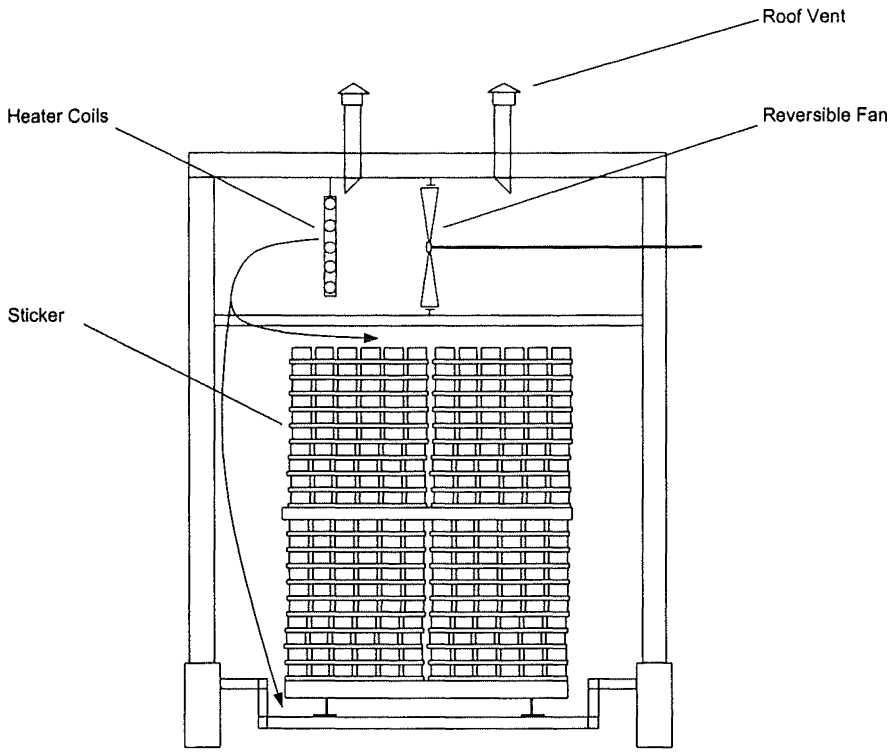

Figure 4.1. A kiln, holding a stack of stickered timber, showing some of the possible paths for bypass of air around the stack.

[1977], Pang [1994], and Pang *et al.* [1995]. They have found that only a few reversals are needed to reduce significantly the variability of moisture content in timber boards. The recommendation of Pang and co-workers was that a single reversal after four hours would be adequate for drying *Pinus radiata* boards under high-temperature conditions. However, these workers did not optimise the reversal time, and they neglected to determine the effect of this variable on the drying time. Commercially, reversal periods vary from at least once during drying to once every two hours with periodic reversals every 4 hours being the commonest policy (Riley [1984]).

Maldistribution of airflow through a kiln also causes moisture-content variations throughout a stack. Flow maldistribution can result from incorrectly placed fans and baffles within the kiln, and improperly stacked timber. It is important when handling boards of uneven length to sort the lengths of timber to ensure a square-faced stack. This will reduce flow maldistribution and, in turn, result in a smaller moisture-content variation and related effects. Flow maldistribution also results from the recirculation zone, located close to the uppermost timber boards, which is generated by the sharp right-angled bend from the ceiling space where the fans are located into the inlet plenum chamber (Kröll [1978]). This recirculation zone is responsible for retarding the flow of air through the uppermost fillet spaces - and can result in reverse flow under certain conditions - and results in an increasing flow in the lower fillet spaces. The effect of flow reversals in the possible mitigation of the effects of flow maldistribution has not been investigated previously.

Kiln Schedules

Optimum drying conditions can be achieved by manipulating the air speed, temperature, and relative humidity within the kiln. A kiln schedule is a combination of these aspects controlled so as to maximise the drying rate while minimising timber degrade, improving the uniformity of drying over the stack, and reducing the energy consumption of the process. Ashworth [1977] and Pang [1994] have found an efficient and economical method to investigate various aspects of a kiln schedule by using a lumped-parameter approach. The batch-drying behaviour of a stack of timber boards, which is undergoing a particular kiln schedule, is predicted by solving the expressions that result from coupling the mass conservation and rate equations, and assuming a lumped-parameter model for the solid drying kinetics first proposed by Van Meel [1958]. In this way, different kiln schedules may be tested and the best solutions used in kiln operation.

In the lumped-parameter approach, the drying rate of a single board over a range of high-temperature conditions is presented as a single drying curve by the choice of non-dimensional parameters for the drying rate and the moisture content of the board. This normalisation produces a characteristic drying curve, which has been used by Ashworth [1977,1979] and Pang [1994] as a basis for analysing kiln behaviour, and by Keey [1978,1992] more generally in the understanding of drying operations. Lumped-parameter models are unable to predict the internal drying kinetics of the timber and, therefore, cannot be used to determine temperature and relative humidity conditions which minimise timber degrade. However, they are useful for optimising airflow conditions that improve the uniformity of drying rates across the timber stack, and reduce energy consumption. Thus, kiln schedules may be determined which mitigate the effects of progressive humidification of air through the stack and airflow maldistribution across the stack, and minimise drying times and fan-power requirements. The aim of this chapter is to optimise a kiln schedule which minimises non-uniform drying of stacked timber boards, and reduces the energy requirements of the process.

The energy intensive process of drying wood requires about 40 to 70% of the total amount of energy used in processing sawn timber from log to final product (Rosen [1981]). Thus, any savings of energy in drying would have considerable impact on the overall needs of the timber industry. A cost-saving kiln schedule has been proposed in which the airflow through a kiln is reduced after the timber stack reaches the fibre-saturation point. The theory is that the drying speed of the timber will not be adversely affected by a reduction in the air flowrate towards the end of drying (Culpepper [1990]). Culpepper states that reducing the airflow at the fibre saturation point reduces fan energy costs by 40 to 50%. The effect of this policy on drying green sapwood will also be investigated in this chapter.

4.3 Scope

Part 1 of this chapter is concerned with the determination of process conditions in the conventional (lower temperature) kiln drying of *Pinus radiata* boards, and the effects of air by-pass, flowrate, flow reversals, and flow maldistribution on these process

conditions. More specifically, the frequency and number of reversals which achieve the most uniform drying of *Pinus radiata* will be sought. These optimum reversal conditions will be compared to flowrate increases to determine their effectiveness in reducing moisture content variation caused by flow maldistribution, flow bypass, and a decreasing evaporative driving force as the air progresses though a stack. In Part 2, flow maldistribution in kilns will be investigated more closely to elucidate some of the findings of Part 1. Finally, Part 3 examines the use of Hi-Lo kiln drying strategies for process improvement.

The concepts involved in this investigation are based on the work done by Pang [1994] on the high-temperature drying of *Pinus radiata* boards in a batch kiln. The model is also applicable to high-temperature behaviour, with appropriate changes in boundary conditions. Thus, the general conclusions about the impact of air bypass, progressive humidification, airflow maldistribution, and Hi-Lo kiln drying schedules will be applicable to both conventional and high-temperature kiln operations.

4.4 Part 1: Kiln-wide Model

A well-insulated kiln is considered so that moisture and heat losses due to condensation on the walls are negligible. The average timber-board transfer coefficients are assumed to be constant along each row of timber boards, although such variations can easily be accounted for as shown in the previous chapter. Green moisture-content, permeability, and density variations between timber boards are ignored. Variations in the equilibrium moisture content of the timber with gas relative humidity will be encountered in a real kiln; however, these variations are also neglected in this analysis. Ashworth [1977] found that the errors which arise from ignoring variable equilibrium moisture contents are small when simulating softwood drying. Furthermore, timber-shrinkage effects are ignored since Ashworth [1977] found that they are negligible insofar as they impact on the board-to-board moisture-content profiles. Finally, it is assumed that the surface of the timber board is above fibre saturation during the constant-rate period so that the surface humidity is equal to the saturation humidity at the given wet-bulb temperature. In Chapter 2, it was shown that a thin-dry layer, which is below the fibre-saturation point, exists at the surface of a rough-sawn timber board. Thus, in practice, the surface of a timber board is unlikely to be greater than the fibre-saturation point during the constant-rate period. However, the assumption that the surface is greater than fibre saturation will not affect the general trends observed.

4.4.1 Theory

Timber Drying Simulation

Moisture-content profiles across the width of the boards with respect to time and path length may be determined from Van Meel's set of equations which relates moisture content and drying rate to drying time and location in a dryer. These equations assume uniform airflow and neglect variations in moisture content in the boards normal to the swept surface.

A moisture balance over a differential volume yields

$$\frac{\partial \Phi}{\partial \theta} = \frac{\partial \Pi}{\partial \xi} \tag{4.1}$$

so that the local rate of drying ($\partial \Phi / \partial \theta$) is equal to the rate of air humidification with distance ($\partial \Pi / \partial \xi$) across the kiln.

The rate equation can be written as

$$-\frac{\partial \Phi}{\partial \theta} = \Pi f \tag{4.2}$$

in which the rate of drying is directly proportional to the humidity potential Π and the function $f = f(\Phi)$.

The dimensionless parameters in these equations are defined as follows:

a) The normalised humidity potential Π is given by the humidity difference relative to that at the air inlet,

$$\Pi = \frac{Y_S - Y_G}{(Y_S - Y_G)_o} \tag{4.3}$$

b) The normalised moisture content Φ is the relative free moisture content at any location (moisture content variations normal to the board surface are neglected),

$$\Phi = \frac{X - X_e}{X_{cr} - X_e} \tag{4.4}$$

where X_{cr} is the critical moisture content and X_e is the equilibrium value.

c) The relative drying time θ is related to the actual drying time τ,

$$\theta = \frac{K_o \phi a}{\rho_s (1 - \varepsilon)(X_{cr} - X_e)} \tau \tag{4.5}$$

Keey [1978] shows that θ represents the extent of drying to be undertaken, taking into account the capacity of the kiln.

d) The relative distance across the kiln ξ is related to the distance z in the air flow direction,

$$\xi = \frac{K_0 \phi a}{G} z \tag{4.6}$$

Where z is equivalent to the width of the kiln in the air flow direction, then the relative distance becomes the total Number of Transfer Units, or *NTU*, which is a measure of the extensiveness of the kiln.

e) The characteristic drying curve relates the normalised moisture content Φ to the relative drying rate f. It enables one to predict the drying behaviour of a board from limited experimental data taken under one set of conditions with material of the same thickness (Keey [1978]). The drying-rate expression may be written as

$$f = f(\Phi) \tag{4.7}$$

where the function $f(\Phi)$ is found from the drying curve obtained under constant drying conditions.

If the characteristic drying curve of the timber to be dried is known, and the appropriate boundary conditions are specified, then kiln-wide variations of moisture content, humidity potential, and drying rate can be determined by solving Van Meel's equations (Keey [1994]).

Kiln Simulation: determining the boundary conditions, NTU and θ

The influence of air maldistribution can be determined by modelling an actual stack as a set of stacks in parallel, each being cross-circulated at a different but uniform air velocity. It is apparent from Equation (4.6) that the *NTU* for each sub-stack will depend on the airflow through that sub-stack. The simulation of the drying process in a sub-stack is a matter of determining the *NTU* corresponding to the flow through the sub-stack, and then solving Van Meel's equations with this value as a boundary condition on ξ. Similarly, the time allowed for drying may be calculated and used as a boundary condition on θ.

If a reference *NTU* is assumed which corresponds to a certain air velocity (u_1, NTU_1) then a relationship can be developed such that the *NTU* at a different air velocity (u_2, NTU_2) can be calculated from this reference value. The derivation for such an equation follows.

An average mass-transfer coefficient may be obtained which applies across the entire row of boards. This value can be calculated from the equation (Kho [1993]),

$$Sh_Z = A\, Re_Z^{\,n}\, Sc^{1/3} \tag{4.8}$$

where

$$Re_Z = \frac{Zu}{\nu_A}$$ = Reynolds Number based on a streamed length, Z.

$$Sc = \frac{\nu_A}{D_{NA}} \quad = \text{Schmidt Number.}$$

$$Sh_Z = \frac{K_0 Z}{D_{NA}} \quad = \text{Sherwood Number based on a streamed length, } Z\text{, and a distance-averaged mass-transfer coefficient, } K_o.$$

in which n = 1/2 for laminar flow
= 3/4 for turbulent flow

If the dimensions of each zone are the same, and the changes in thermodynamic properties of the air through the dryer considered negligible, then one can make a mathematical comparison between the mass-transfer coefficients for each air velocity by dividing the mass-transfer equation for one velocity by the mass-transfer equation for another velocity. Whence,

$$\frac{K_{01}}{K_{02}} = \left(\frac{u_1}{u_2}\right)^n \tag{4.9}$$

In Equation (4.6), G is the mass air rate over a unit cross-section between the boards (kg/m²s); that is,

$$G = \varepsilon u \rho_G \tag{4.10}$$

where u is the incident velocity at the air-inlet face of the stack and ε is the fractional free space in the stack.

Combining Equations (4.6) and (4.10) leads to the expression

$$NTU = \frac{AK_0}{u} \tag{4.11}$$

in which A is a lumped constant.

On comparing two zones with different flows, (u_1, NTU_1) and (u_2, NTU_2), we find

$$\frac{NTU_2}{NTU_1} = \frac{K_{02}}{K_{01}} \frac{u_1}{u_2} \tag{4.12}$$

Substitution of Equation (4.9) into Equation (4.12) yields

$$\frac{NTU_2}{NTU_1} = \left(\frac{u_2}{u_1}\right)^{n-1} \tag{4.13}$$

A similar derivation applies for the relative drying time:

$$\frac{\theta_2}{\theta_1} = \left(\frac{u_2}{u_1}\right)^n \frac{\tau_2}{\tau_1} \tag{4.14}$$

Thus, the *NTU* and θ values corresponding to a certain air velocity may be calculated from a reference velocity with known *NTU* and θ values.

A relationship can be derived to relate the *NTU* of a kiln with no bypass to the *NTU* of a kiln with bypass of air around the timber stacks. Two flow paths are possible for air in a kiln with bypass; flow through the stack Q_1, and flow around the stack Q_2. In a similar kiln which is baffled to prevent bypass and with equal cross-sectional stack area, only one flow path exists; air must flow through the timber stack. Should the fan in both kilns provide the same volumetric flow, then the following expression applies:

$$Q_0 = Q_1 + Q_2 \tag{4.15}$$

where Q_0 is the flow through the stack in a kiln with no bypass.

The bypass ratio is defined as

$$b = \frac{Q_2}{Q_1} \tag{4.16}$$

Substitution of Equation (4.16) into Equation (4.15) yields

$$Q_0 = Q_1(1+b) \tag{4.17}$$

or equivalently,

$$u_0 A_0 = u_1 A_1 (1+b) \tag{4.18}$$

where u_0 and u_1 are the average air velocities through stacks with cross-sectional areas of A_0 and A_1, respectively.

The area of the stacks in both kilns are the same. Therefore, Equation (4.18) reduces to

$$\frac{u_1}{u_0} = \frac{1}{1+b} \tag{4.19}$$

Substituting this expression into Equation (4.13) and (4.14) gives

$$\frac{NTU_1}{NTU_0} = \left(\frac{1}{1+b}\right)^{n-1} \tag{4.20}$$

$$\frac{\theta_1}{\theta_0} = \left(\frac{1}{1+b}\right)^n \frac{\tau_1}{\tau_0} \tag{4.21}$$

Thus, the NTU and θ values in a stack for a kiln with bypass may be calculated from the NTU and θ values in a stack for a kiln with no bypass if the bypass ratio is known.

4.4.2 Process Description and Specifications

The investigation is broken into two sections. In the first section, the effect of airflow reversals on the drying process of timber is considered. A simplified kiln with neither flow maldistribution nor bypass is simulated. In the second section, two existing kilns, kiln A and kiln B, are investigated for which their respective flow maldistributions are known from kiln audits of the actual air velocity distribution at the inlet face of the stack. Information concerning the flow through and around the stacks in kiln A is known. This kiln will be used to investigate the effect of air-bypass, flow reversals, and flow maldistribution on the kiln-wide moisture content distribution. Flow data were collected at three fan speeds in kiln B. These fan speeds correspond to average flowrates through the stacks of 4.1, 5.0, and 5.4 m/s when the fans are operating in forward-circulation mode. Thus, useful information can be found about the effects of air velocity and the stack flow distribution on the kiln-wide moisture content differences.

The initial moisture content varies significantly between the heartwood and sapwood of *Pinus radiata*. Sapwood is the outer portion of the tree trunk which is used for the transport of nutrients, whereas heartwood is the older wood no longer capable of this function and in which resins have been deposited. Typically, the sapwood of freshly felled *Pinus radiata* has a moisture content of approximately 1.4 kg/kg, and may be higher, but heartwood has only a moisture content of 0.4 kg/kg (Walker [1993]). These moisture contents may be converted to their normalised forms using Equation (4.4). From Pang [1994], the critical moisture contents, when convection ceases to control exclusively the drying of heartwood and sapwood are 0.4 kg/kg and 0.94 kg/kg, respectively. The measured value for the critical moisture content of 0.94 kg/kg for a 50 mm thick sapwood board is consistent with the simulations detailed in Chapter 3 which predict critical moisture contents of 0.4 kg/kg and 0.6 kg/kg for a 20 mm and 40 mm thick board, respectively. The equilibrium moisture contents under the kiln conditions specified in Table 4.1 are 0.047 kg/kg for heartwood and 0.05 kg/kg for sapwood (Kininmonth [1991]). Thus, the normalised initial moisture content of heartwood and sapwood are approximately 1 for heartwood and 1.5 for sapwood.

The boundary conditions used in the simulation of the kilns depend on which variable is chosen to be the limiting one. In Section 1, the final moisture content of the timber is the limiting variable. The drying process in the kiln is simulated by solving Van Meel's equations until the moisture content of the timber falls below a specified point. In this case, the drying simulation is stopped when the wettest moisture content within the board falls below 0.1 kg/kg. For heartwood this corresponds to Φ=0.150, and for sapwood Φ=0.056. In Section 2, the kiln-drying time is the limiting variable. Kilns A

Heartwood

Moisture content of the wettest timber in the stack, X (kg/kg)	Dry-bulb temperature (°C)	Wet-bulb temperature (°C)	Relative humidity of air, ψ	Moisture content of timber, Φ	Humidity potential of air, Π
0.4	75	60	0.49	1.000	1.360
0.2	80	60	0.39	0.433	1.805

Sapwood

Moisture content of the wettest timber in the stack, X (kg/kg)	Dry-bulb temperature (°C)	Wet-bulb temperature (°C)	Relative humidity of air, ψ	Moisture content of timber, Φ	Humidity potential of air, Π
1.4	71	60	0.58	≈1.5	1.000
0.5	75	60	0.49	0.506	1.360
0.2	80	60	0.39	0.169	1.805

Table 4.1. Typical kiln schedules for conventional kiln drying of *Pinus radiata* for heartwood and sapwood (Walker [1993]).

and B are simulated by breaking the stacks into sub-stacks each having a constant air velocity. The drying time in each sub-stack must be equal to the drying time allowed for the entire kiln: that is,

$$\tau_1 = \tau_2 = ... = \tau_r = \tau_{overall}$$

The dimensionless overall drying time, $\theta_{overall}$, is set to the time for drying when a hypothetical kiln with no maldistribution and no bypass is operated at an arbitrary *NTU* corresponding to the average flow through the existing kiln. The overall drying time can be determined by solving Van Meel's equations until the moisture content of the timber falls below the point specified above. The dimensionless drying time for each sub-stack may be found from the overall dimensionless drying time using Equation (4.14). The overall dimensionless drying times for a kiln with and without bypass will differ because bypass has the effect of decreasing the extensiveness of drying. Equation (4.21) is used to relate these overall dimensionless drying times θ assuming that the drying time τ in each case is the same. When simulating kilns A and B, Van Meel's equations are solved until the drying time falls below the calculated value.

Keey [1992] states that the *NTU* for most batch-drying units is about unity. It is assumed that the kilns in both sections have an *NTU* of unity which corresponds to the average air velocity through the kiln. In Section 2, the *NTU* of each sub-stack may be found from the average air velocity through the kiln using Equation (4.13). When considering bypass in kiln A, an *NTU* of unity is used corresponding to an overall air flowrate which is essentially the sum of the bypass and average flow through the stack. The *NTU*, which corresponds to the average flow through the stack, may be calculated from the overall *NTU* and the bypass ratio using Equation (4.20). In the

case of kiln B, an *NTU* of unity is used for the average air velocity corresponding to the lowest fan speed. At higher fan speeds, the *NTU* are calculated from the lowest average air velocity using Equation (4.13). The overall dimensionless drying time for the kiln is set to the drying time for a hypothetical kiln with no maldistribution and no bypass which is operating at the *NTU* value corresponding to the new fan speed. The dimensionless drying time can be determined by solving Van Meel's equations until the moisture content of the timber falls below the desired moisture content. By assuming a drying time for the kiln at the lowest fan speed, τ, the dimensionless drying times at higher fan speeds can be translated into actual drying times using Equation (4.14).

The relative humidity of the inlet air is adjusted downwards stepwise during the kiln-drying schedule to counter a diminishing drying rate. This can be done by raising the wet-bulb and dry-bulb temperature of the inlet air during the drying cycle when the moisture content falls below certain defined levels. Table 4.1 shows a typical kiln schedule for heartwood and sapwood, described by Walker [1993], which will be used in the kiln simulation. When the moisture content reaches specified points, the humidity potential of the inlet air is increased. In the case of sapwood, two increases in humidity potential occur when the moisture content of the timber is reduced to 0.5 kg/kg and 0.2 kg/kg, respectively. However, for heartwood only one increase occurs when its moisture content reaches 0.2 kg/kg because it starts from a lower moisture content than sapwood.

Flow reversals are simulated by simply specifying the humidity potential of the inlet air at the opposite side of the kiln, and calculating the moisture content and humidity changes backward towards the original air inlet: that is,

$$(\Pi)_{\zeta=0} = (\Pi)_{\zeta=NTU} \tag{4.22}$$

Equations (4.23) and (4.24) below describe the characteristic drying curves used in the simulation which were fitted to experimental data collected by Pang [1994] for heartwood and sapwood, respectively.

$$f = -1.6516\Phi^4 + 3.8651\Phi^3 - 2.7106\Phi^2 + 1.4978\Phi \tag{4.23}$$

$$\begin{aligned} f &= 1 && \Phi \geq 1 \\ f &= -0.6766\Phi^3 + 0.2\Phi^2 + 1.4713\Phi && \Phi < 1 \end{aligned} \tag{4.24}$$

These expressions have been obtained to represent the drying over a range of high-temperature conditions. It is assumed that the *f*-function is only slightly dependant upon temperature, and Equations (4.23) and (4.24) apply to the conditions simulated in the analysis.

Numerical Solution

A simple Euler-based explicit finite-difference scheme was used to calculate the moisture-content profiles throughout the timber stack. Equation (4.1) was discretised

as follows:

$$\frac{\partial \Phi}{\partial \theta} = \frac{\partial \Pi}{\partial \xi} \approx \frac{\Delta \Pi}{\Delta \xi} \tag{4.25}$$

which can be rearranged to give

$$\Pi_{i+1,j} = \Pi_{i,j} + \left.\frac{\partial \Phi}{\partial \theta}\right|_{i,j} \Delta \xi \tag{4.26}$$

The numbering of the nodes of the grid layout is ..., *i-1*, *i*, *i+1*,... in the 'distance' direction, and ..., *j-1*, *j*, *j+1*,... in the 'time' direction. Equation (4.2) was discretised in a similar fashion. Thus,

$$\Phi_{i,j+1} = \Phi_{i,j} + \left.\frac{\partial \Phi}{\partial \theta}\right|_{i,j} \Delta \theta \tag{4.27}$$

The gradient of moisture content with respect to time was given by the equation

$$\left.\frac{\partial \Phi}{\partial \theta}\right|_{i,j} = -f_{i,j} \Pi_{i,j} \tag{4.28}$$

where

$$f_{i,j} = f\left(\Phi_{i,j}\right) \tag{4.29}$$

The new values of humidity potential or moisture content can be calculated from the previous values by forward marching in distance or time, respectively. The humidity potential at the leading edge of the stack $\Pi_{0,j}$ is a boundary condition which takes on the values specified in Table 4.1. The initial moisture content of the timber in the stack $\Phi_{i,0}$ is constant.

The accuracy of the solution depends upon the step sizes chosen. The step sizes for distance ($\Delta \xi$) and time ($\Delta \theta$) required to attain accuracy in the simulations were determined by decreasing these quantities until the change between successive solutions was negligibly small. The resultant step sizes were then halved.

4.4.3 Results

Section 1: Airflow Reversals

Figure 4.2 shows the moisture-content profiles for heartwood obtained by solving Van Meel's equations with a single flow reversal incorporated at $\theta = 0.4$.

At the end of drying the moisture content Φ at a given point in the kiln will be

slightly different from the specified end-value Φ_f. A useful measure of the closeness of the final moisture content to the desired value is the ratio

$$m(\Phi) = \left[\frac{\Phi - \Phi_f}{\Phi_0 - \Phi_f} \right]$$

where Φ_0 is the initial moisture content. We will call this ratio the final moisture-content approach or *FMCA*. Over any given row of boards, there will be a range of values of $m(\Phi)$, and the average approach $\bar{m}$ over a row of boards is given by

$$\bar{m} = \frac{1}{n} \sum_{i=1}^{n} m(\Phi_i)$$

As the final moisture-content approach tends towards zero, the boards being dried approach the desired dryness. A negative final moisture-content approach $\bar{m}$ implies that, on average, the moisture contents across a row of timber boards have fallen below the desired value. Figures 4.3 and 4.4 show how the final moisture-content approach is affected by the number of reversals used and their period, for both heartwood and sapwood respectively.

A measure of the spread of values of $m(\Phi)$ across any row of boards is the standard deviation:

$$\sigma = \sqrt{\frac{\sum_{i=1}^{n} \left(m(\Phi_i) - \bar{m}(\Phi) \right)^2}{n-1}}$$

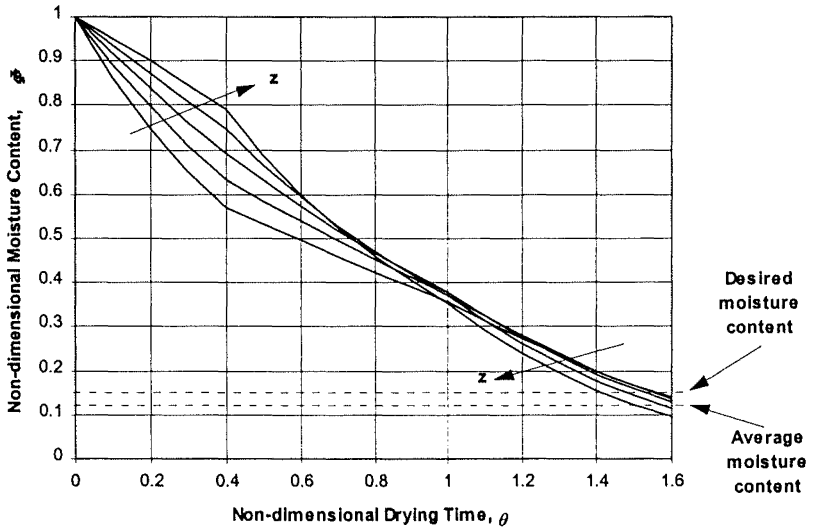

Figure 4.2. Moisture-content variations across a row of timber boards as a function of time, θ, with a single air-flow reversal at $\Delta\theta_r = 0.4$.

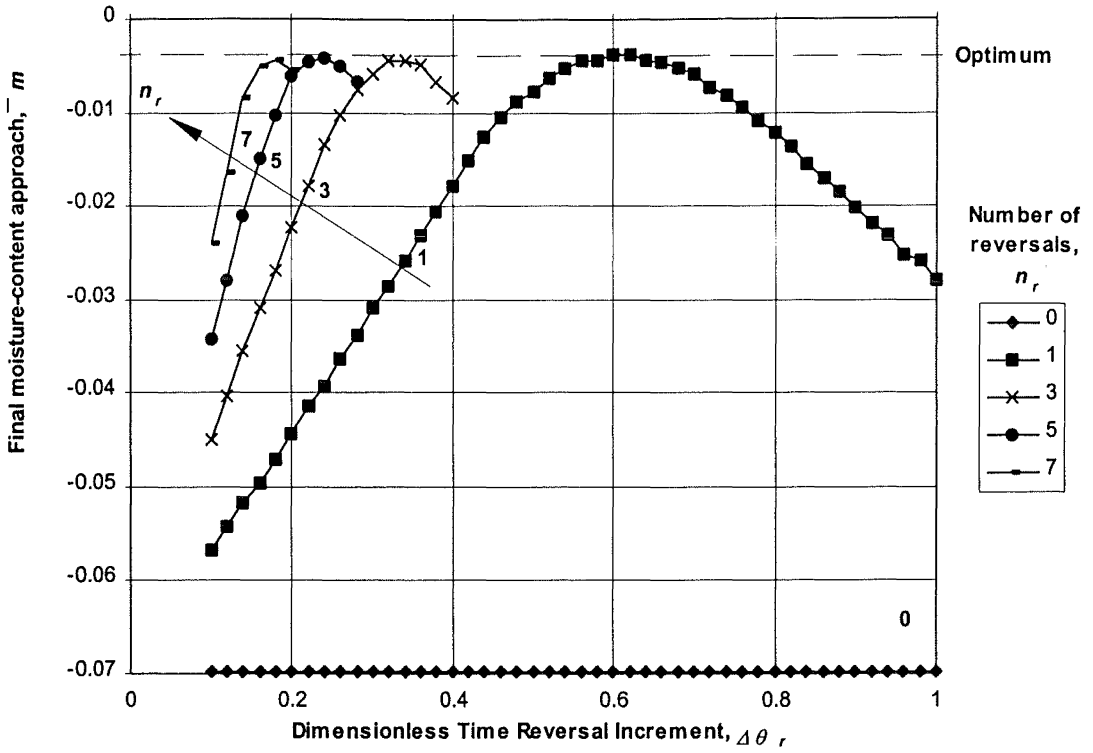

Figure 4.3. Final moisture-content approach of heartwood timber, $\bar{m}$, versus the reversal time period, $\Delta\theta_r$ for an increasing number of reversals, n_r.

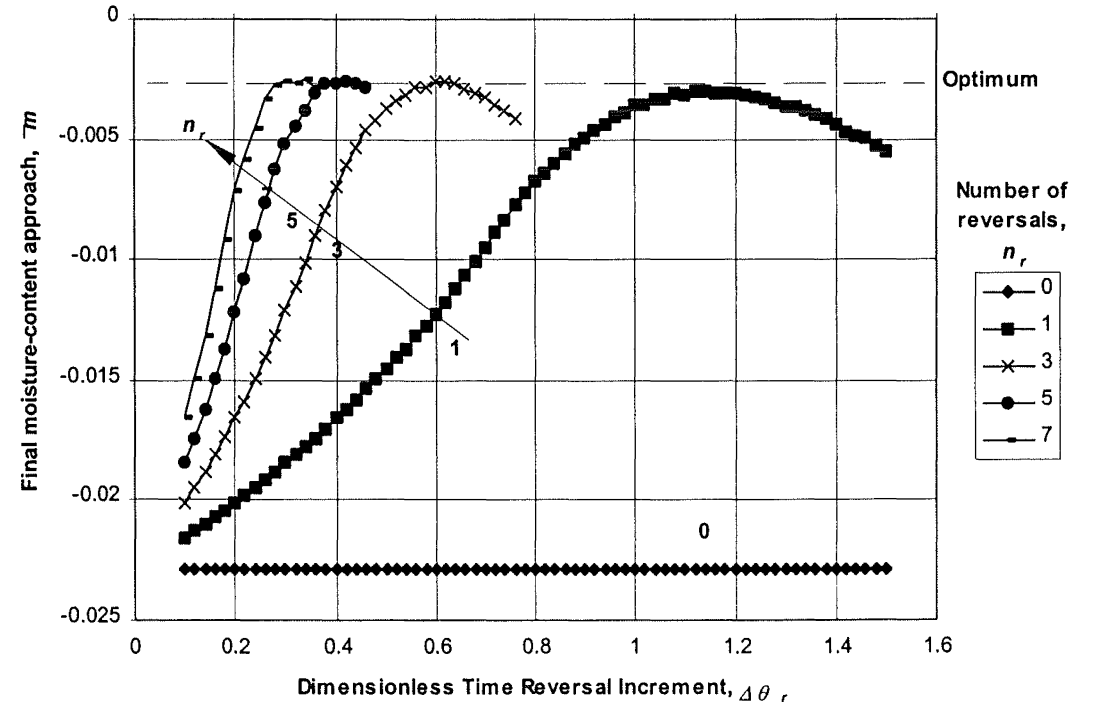

Figure 4.4. Final moisture-content approach of sapwood timber, $\bar{m}$, versus the reversal time period, $\Delta\theta_r$ for an increasing number of reversals, n_r.

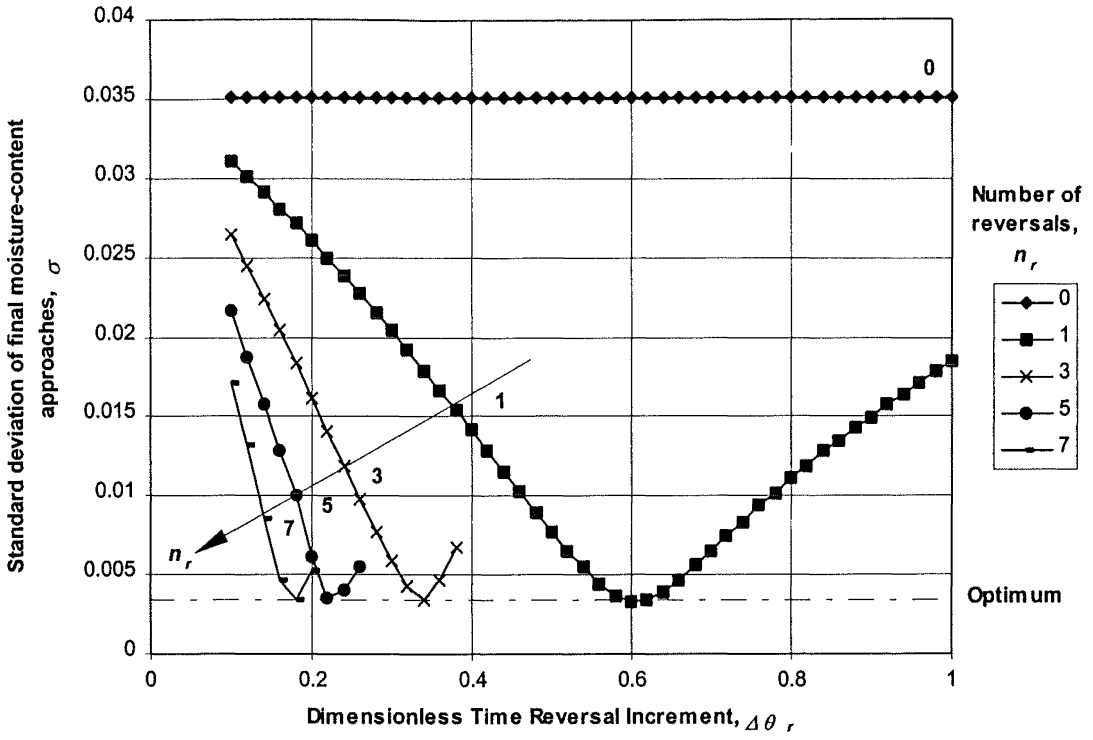

Figure 4.5. Standard deviation of the final moisture-content approaches of heartwood timber, σ, versus the reversal time period, $\Delta\theta_r$ for an increasing number of reversals, n_r.

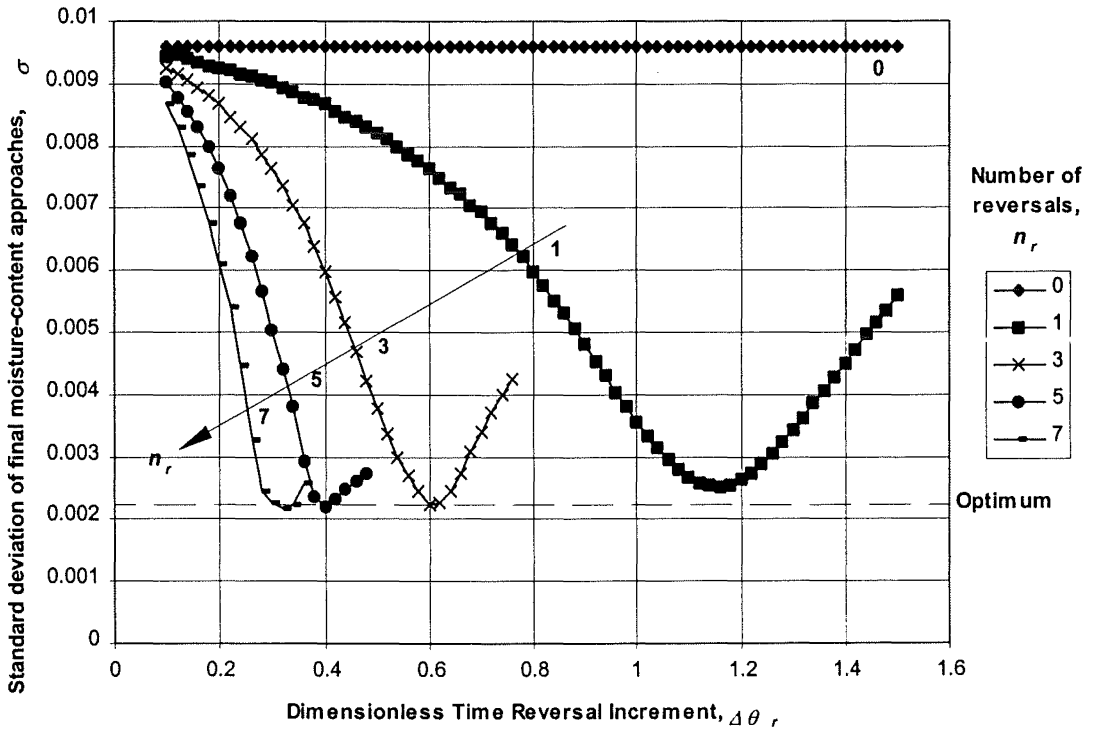

Figure 4.6. Standard deviation of the final moisture-contents approaches of sapwood timber, σ, versus the reversal time period, $\Delta\theta_r$ for an increasing number of reversals, n_r.

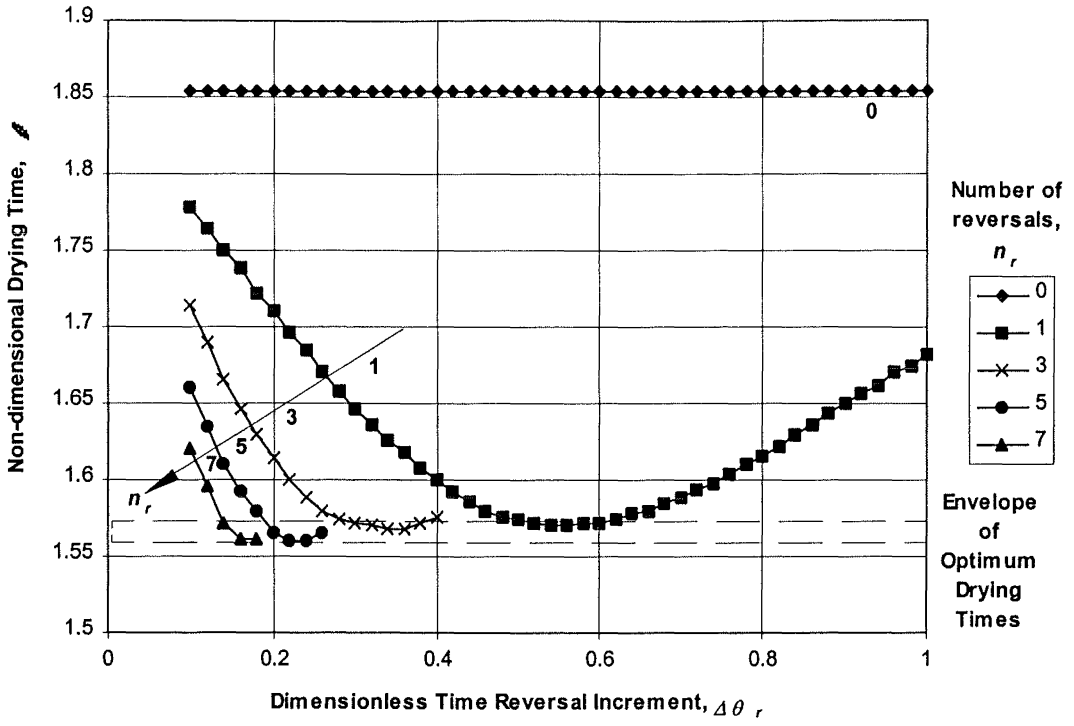

Figure 4.7. Drying time of heartwood timber, θ, versus the reversal time period, $\Delta\theta_r$ for an increasing number of reversals, n_r.

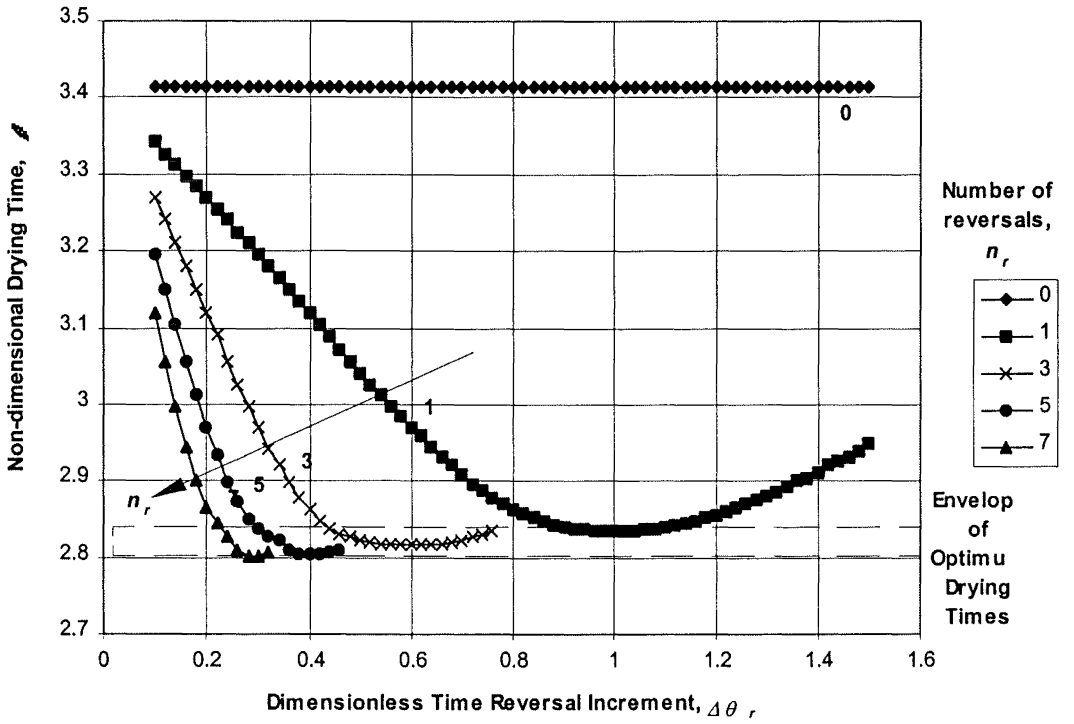

Figure 4.8. Drying time of sapwood timber, θ, versus the reversal time period, $\Delta\theta_r$ for an increasing number of reversals, n_r.

The smaller the standard deviation, the more uniform are the moisture contents across the row. Figures 4.5 and 4.6 show how this value is affected by the number of reversals used and their period, for heartwood and sapwood respectively.

As the reversal period and number is changed, the drying time required to reach the specified dryness correspondingly changes. The effect of reversals on the drying time is shown in Figures 4.7 and 4.8, for heartwood and sapwood respectively.

Section 2: Kiln Audits

Besides the variation of moisture contents across any row in the stack, there are differences between rows. The former variations are caused by the humidification of the air as it passes through the stack, whereas the differences between rows (or sub-stacks) result from the airflow maldistribution over the stack.

The kiln audits indicate the extent of the air maldistribution in the tested kilns. The extent of the differences in moisture content between rows (or sub-stacks) is given by the mean and standard deviation of the individual values for each row, or sub-stack:

$$\overline{M} = \frac{1}{r}\sum_{j=1}^{r}\overline{m}_j$$

and

$$\overline{S} = \frac{1}{r}\sum_{j=1}^{r}\sigma_j$$

for r sub-stacks. As the mean of the final moisture-content approaches $\overline{M}$ tends toward zero, the closer is the timber to being dried to the desired point on a kiln-wide basis. As the mean of the standard deviations $\overline{S}$ tends towards zero, the more uniformly dried is the timber in the airflow direction; however, over the entire kiln, there may or may not be a large distribution of moisture contents, depending upon the air maldistribution. Therefore, a third measure of the uniformity of drying is the standard deviation of moisture contents taken over the whole kiln:

$$\sigma_k = \sqrt{\frac{\sum_{j=1}^{r}\left(\overline{m}_j - \overline{M}\right)^2}{r-1}}$$

The lower the standard deviation, σ_k, the more uniform are the moisture contents over the entire kiln.

Table 4.2 shows the moisture statistics of kiln A at the end of drying. The first two columns show the effect of flow reversals on the uniformity of drying. The last two columns demonstrate the effect of flow bypass and reversals on the uniformity of drying.

Wood type	Heartwood	Heartwood	Heartwood	Heartwood
Average air velocity through stack, u (m/s)	6.9	6.9	3.5	3.5
Number of transfer units (stack), *NTU*	1	1	1.19	1.19
%Bypass, b	NA	NA	100	100
Relative drying time, θ	1.86	1.58	1.11	0.94
Drying time, τ (hr)	72	61	72	72
Number of reversals, n_r	0	1	0	1
Reversal increment, $\Delta\theta_r$	0	0.6	0	0.6
Kiln-wide mean of *FMCA*, $\overline{M}$	-0.067	-0.001	0.252	0.336
Kiln-wide standard deviation of *FMCA*, σ_k	0.034	0.042	0.048	0.044
Maximum *FMCA*, $\overline{m}_{max}$	0.071	0.152	0.412	0.480
Minimum *FMCA*, $\overline{m}_{min}$	-0.133	-0.091	0.136	0.224
Kiln-wide mean of variability of *FMCA*, $\overline{S}$	0.036	0.004	0.089	0.040

Wood type	Sapwood	Sapwood	Sapwood	Sapwood
Average air velocity through stack, u (m/s)	6.9	6.9	3.5	3.5
Number of transfer units (stack), *NTU*	1	1	1.19	1.19
%Bypass, b	NA	NA	100	100
Relative drying time, θ	3.43	2.86	2.04	1.7
Drying time, τ (hr)	72	61	72	72
Number of reversals, n_r	0	1	0	1
Reversal increment, $\Delta\theta_r$	0	1.15	0	1.15
Kiln-wide mean of *FMCA*, $\overline{M}$	-0.021	0.001	0.240	0.340
Kiln-wide standard deviation of *FMCA*, σ_k	0.011	0.019	0.056	0.055
Maximum *FMCA*, $\overline{m}_{max}$	0.042	0.093	0.432	0.518
Minimum *FMCA*, $\overline{m}_{min}$	-0.035	-0.028	0.112	0.207
Kiln-wide mean of variability of *FMCA*, $\overline{S}$	0.011	0.003	0.139	0.067

Table 4.2. Moisture-content statistics at the end of the drying schedule for Kiln A. Data courtesy Haslett [NZFRI], *pers. comm.*

Wood type	Heartwood	Heartwood	Heartwood	Heartwood
Average air velocity through stack, u (m/s)	4.1	4.1	5.0	5.4
Number of transfer units (stack), *NTU*	1	1	0.95	0.93
%Bypass, b	NA	NA	NA	NA
Relative drying time, θ	1.86	1.58	1.83	1.81
Drying time, τ (hr)	72	61	61	57
Number of reversals, n_r	0	1	0	0
Reversal increment, $\Delta\theta_r$	0	0.6	0	0
Kiln-wide mean of *FMCA*, $\overline{M}$	-0.066	0.001	-0.065	-0.061
Kiln-wide standard deviation of *FMCA*, σ_k	0.039	0.047	0.035	0.035
Maximum *FMCA*, $\overline{m}_{max}$	0.063	0.141	0.038	0.004
Minimum *FMCA*, $\overline{m}_{min}$	-0.136	-0.092	-0.120	-0.123
Kiln-wide mean of variability of *FMCA*, $\overline{S}$	0.037	0.004	0.035	0.035

Wood type	Sapwood	Sapwood	Sapwood	Sapwood
Average air velocity through stack, u (m/s)	4.1	4.1	5.0	5.4
Number of transfer units (stack), *NTU*	1	1	0.95	0.93
%Bypass, b	NA	NA	NA	NA
Relative drying time, θ	3.43	2.86	3.35	3.32
Drying time, τ (hr)	72	61	61	57
Number of reversals, n_r	0	1	0	0
Reversal increment, $\Delta\theta_r$	0	1.15	0	0
Kiln-wide mean of *FMCA*, $\overline{M}$	-0.020	0.002	-0.020	-0.019
Kiln-wide standard deviation of *FMCA*, σ_k	0.013	0.021	0.011	0.010
Maximum *FMCA*, $\overline{m}_{max}$	0.036	0.085	0.021	0.002
Minimum *FMCA*, $\overline{m}_{min}$	-0.036	-0.029	-0.033	-0.034
Kiln-wide mean of variability of *FMCA*, $\overline{S}$	0.012	0.004	0.011	0.011

Table 4.3. Moisture-content statistics at the end of the drying schedule for Kiln B with varying kiln-wide flow distributions as the fan speed is changed. Data courtesy Haslett [NZFRI], *pers. comm.*

Table 4.3 show the moisture statistics for kiln B at the end of drying with columns 1, 3 and 4 showing how these statistics vary with increasing fan speed. The second column shows the effect of flow reversals on the moisture content. Thus, direct comparisons can be made between the effects of flow increases and the effect of introducing flow reversals on the moisture content distribution through the kiln.

A turbulent flow regime has been assumed in the channels comprising the sub-stacks. However, computational fluid dynamic studies of a timber stack show that the flow in a channel is neither fully developed laminar nor turbulent motion. The pressure drop is somewhat higher than that estimated for fully turbulent flow [Langrish, *pers. comm.*]. Therefore, the effect of airflow variations between channels which make up the sub-stacks, shown in Tables 4.2 and 4.3, is indicative only of the impact of airflow maldistributions.

4.4.4 Discussion

Section 1: Airflow reversals

The drying simulation in this section ends when the wettest timber along the air-flow path falls below the desired dryness. Therefore, the timber in the stack will be slightly overdried which is indicated by a negative value for $\bar{m}$, the final moisture-content approach (Figures 4.3 and 4.4). On the moisture-content profiles (Figure 4.2), timber is overdried when its moisture content falls below the desired moisture-content line. The difference between the desired moisture content and average moisture content is the final moisture-content approach, $\bar{m}$. The variation of moisture contents around $\bar{m}$ is given by the standard deviation of final moisture-content approaches, σ.

There does appear to be a common limiting moisture-content difference which a policy of flow reversals can achieve (Figures 4.3 and 4.4). This minimum final moisture content approach $\bar{m}$, takes a value of -0.004 for heartwood and -0.003 for sapwood, and is found at progressively shorter time intervals for flow reversals as the number of individual flow switches is increased. Note that when no flow reversals are used, the expected $\bar{m}$ values are -0.070 for heartwood and -0.023 for sapwood. Thus, in this section, flow reversals work to reduce $\bar{m}$ towards the desired dryness; however this value can never be reached. The $\bar{m}$ values correspond to an increase in moisture content from 0.08 kg/kg to 0.10 kg/kg for heartwood, and from 0.07 kg/kg to 0.10 kg/kg for sapwood when the optimum flow reversal conditions are used.

The standard deviation plots, Figures 4.5 and 4.6, confirm these trends in that there exists an optimum σ, or standard deviation of final moisture-content approaches, to suggest a limit to the narrowness of the spread of moisture contents that can be achieved across a row of timber boards. These optimum conditions correspond exactly to those seen on the final moisture-content approach plots (Figures 4.3 and 4.4). Thus, a flow-reversal increment can be chosen which will result in timber boards that are as uniformly dried and as close to the desired dryness as possible. In this situation, the moisture-content profiles shown in Figure 4.2 would almost converge on one point,

and the average moisture content would be very close to the desired moisture-content line. Note that there is for heartwood and sapwood respectively, about a 90% and 75% reduction in σ compared to no reversals when the optimum flow reversal conditions are used.

The optimum exists because of a cross-over in moisture content reduction, when the position of the wettest timber across a row of boards moves away from timber at either side of the stack. The moisture-content profiles with time thus cross-over each other as an increased driving force enhances the local drying rate at the places where the timber is wettest. Figure 4.2 illustrates cross-over of the moisture-content profiles. Should the reversal occur too soon, then a cross-over can become so pronounced such that there is a complete inversion of the moisture-content profile. This is the case in Figure 4.2 when a single reversal is incorporated at $\theta = 0.4$. If the reversal increment is too large, then no cross-over occurs. At the optimum, the moisture-content profiles converge towards the limiting conditions discussed above.

One might expect that more flow reversals will result in a reduction in the time required for drying because both sides of the kiln are subject to the hottest air more often. Figures 4.7 and 4.8 for heartwood and sapwood, respectively, show that this is indeed true. However, the optimum drying time decreases insignificantly with increasing reversal number, n_r. Therefore, it is only necessary to reverse the airflow once for optimum results. When one flow reversal is used (n_r is unity), the optimum flow-reversal time ($\Delta\theta_r$) increment is approximately 0.60 for heartwood, and 1.15 for sapwood. For both the heartwood and sapwood of *Pinus radiata*, the optimum reversal time should be used at approximately one-third of the no-reversal drying time provided that the initial kiln-wide moisture-content differences do not build to critical values with the likelihood of degrade. Reversals are more effective in the earlier stages of drying when large moisture-content differences have arisen across the kiln. This would explain the relatively small optimum flow-reversal increment compared to the overall no-reversal drying time, when n_r is zero, of approximately 1.86 for heartwood and 3.43 for sapwood.

Pang *et al.* [1995] have found similar results. In their study, they compared experimental data to a receding evaporative plane model which predicted temperature and moisture content profiles within a single board of *Pinus radiata* as a function of time. The model was then used to derive a characteristic drying curve for a kiln-wide analysis. First, they showed that the discrepancies between the experimental data and their drying model were small. Then they used their kiln-wide model to investigate the effect of flow reversals on the drying of sapwood. The predictions of the drying model suggested that in a 24-hour schedule, either two flow reversals every eight hours, or a single airflow reversal after four hours was a minimum requirement for the average moisture contents along the length of the stack in the airflow direction to vary by less than 0.2 kg/kg for sapwood at any time during drying. The calculations imply that, when airflow reversals are not used, moisture-content differences of up to 0.4 kg/kg can occur with sapwood.

The time fraction, which compares the reversal drying time to the no-reversal drying time, is the same for both θ and τ provided that the flowrate through the kiln is the

same whether the fan is operated in forward or reverse circulation mode. By assuming a drying time τ which corresponds to the no-reversal dimensionless drying time θ, then the dimensionless drying times for the flow reversal cases may be translated to actual drying times using this time fraction. The reduction in the drying time when the optimum flow reversal conditions are applied is approximately 15% and 17% for heartwood and sapwood, respectively. A kiln drying time of 72 hours has been assumed which is derived from the recommended schedule given by Kininmonth [1974] for closely similar working conditions. When the optimum flow reversal conditions are used, this drying time can be reduced to approximately 61 hours for both heartwood and sapwood, which should result in significant energy savings.

Section 2: Kiln Audits

A drying time of 72 hours has been assumed for the kiln with no air bypass and which is operated without flow reversals (Table 4.2). The dimensionless drying times for a kiln operated under different conditions may be converted to real times using this drying time. The kiln with 100% bypass is operated for the same drying time as the kiln without bypass to investigate the effect of bypass on the moisture content distribution through the kiln. However, the kiln with a flow reversal incorporated is operated for a shorter time (61 hours) because the moisture content of the timber falls to the desired moisture content in less time (Table 4.2). A fan speed increase will also reduce the drying time required to reach the desired moisture content, as shown by a decrease from 72 to 57 hours when the flowrate is increased from 4.1 to 5.4 m/s (Table 4.3).

It has been shown that the introduction of flow reversals results in an increase in $\overline{m}$, and a reduced σ for a kiln with uniform flow. Thus, the spread of moisture contents across a row of boards is narrower and the moisture contents closer to the desired dryness. These same trends are observed for kiln A with non-uniform flow when the optimum flow reversal conditions were used with an optimal reversal time increment $(\Delta\theta_r)$ of 0.60 for heartwood and 1.15 for sapwood. Firstly, there is a general upward shift in the moisture content on introducing reversals, as shown by the increase in $\overline{M}$, $\overline{m}_{max}$ and $\overline{m}_{min}$ (compare columns 1 and 2 in Table 4.2). Secondly, the distribution of moisture contents across the rows of timber boards is reduced, as indicated by the decrease in $\overline{S}$, from 0.036 to 0.004 for heartwood, and 0.011 to 0.003 for sapwood.

The introduction of flow reversals results in sub-stacks that were originally overdried to become less overdried, as shown by the increase in $\overline{m}_{min}$ from -0.133 to -0.091 for heartwood. However, the sub-stacks that were originally underdried become more severely underdried, as can be seen by the increase in $\overline{m}_{max}$ from 0.071 to 0.152 for heartwood. Similar trends are observed for sapwood. Therefore, reversals are beneficial for sub-stacks that are overdried, but detrimental for underdried sub-stacks. Thus, the use of reversals is not the final solution to the problem of non-uniform drying and is useless to compensate for airflow maldistribution. Steps must be taken to produce more uniform flow through the stacks, for example, by attention to stacking arrangements and baffling.

On introducing flow reversals, there is an increase in σ_k, the kiln-wide standard deviation of $\overline{m}$ values, from 0.034 to 0.042 for heartwood, and from 0.011 to 0.019 for sapwood. Thus, on a kiln-wide basis the spread of local moisture contents increases when flow reversals are used even though the spread of moisture contents across the row of timber boards in the air-flow direction are reduced. Again, this illustrates that flow reversals are not useful for reducing kiln-wide differences in moisture content in a kiln with non-uniform flow. However, such reversals may be used to dry timber more uniformly along the airflow path.

Table 4.2 also shows the effect of bypass on the moisture content distribution in the timber boards. The timber boards become more severely underdried because bypass has the effect of decreasing the extensiveness of drying on the basis of both time θ and streamed-length Z. When no bypass occurs, $\overline{M}$ is -0.067 for heartwood and -0.021 for sapwood. $\overline{M}$ increases to 0.252 and 0.240 for heartwood and sapwood, respectively with 100% bypass. These final moisture-content approaches correspond to a moisture content of 0.18 kg/kg for heartwood and 0.41 kg/kg for sapwood. Considering that the desired final moisture content is 0.1 kg/kg, then on average, both heartwood and sapwood timber is dried only 75% as much as it would with no bypass, for the same drying time and with 100% air bypass. The maximum moisture-content approaches $\overline{m}_{max}$ show that in some areas within the kiln, timber is dried only 58% as much as it would with no bypass. Reversals make the situation worse by further increasing the moisture content of the timber in the sub-stacks (compare the values of $\overline{M}$ for column 3 when no reversals are used, and column 4 with one reversal incorporated; 0.252 and 0.336 for heartwood, and 0.240 and 0.340 for sapwood). It can be seen that the penalties for bypass are severe and significant increases in fan power would be necessary to reach the required level of timber dryness within the scheduled time.

Kiln B was used to investigate the effect of air flowrate on the moisture content. Comparisons between the timber moisture statistics for the three flowrates used in the kiln show three results (Table 4.3). Firstly, there is a very small change in $\overline{M}$, which range from -0.066 to -0.061 for heartwood, and from -0.020 to -0.019 for sapwood, for the corresponding flow range from 4.1 to 5.4 m/s. Thus, merely increasing the air flowrate cannot be used to dry the timber closer to the desired value on a kiln-wide basis. Secondly, there is a decrease in the variation of moisture contents across the rows of boards $\overline{S}$ with increasing flowrate, but not to the extent that the introduction of reversals provide. The value of $\overline{S}$ for heartwood is reduced from 0.037 to 0.004 when flow reversals are used, compared to a reduction from 0.037 to only 0.035 when the flow is increased from 4.1 to 5.4 m/s. Thus, reversals have a larger impact on the variation of moisture contents across a row of timber boards than flowrate increases over the tested range. Thirdly, there is a general reduction in σ_k from 0.039 to 0.035 for heartwood on increasing the air velocity from 4.1 to 5.4 m/s. There is also a narrowing in the range of moisture contents which is shown by a decrease in $\overline{m}_{max}$ from 0.063 to 0.004, and an increase in $\overline{m}_{min}$ from -0.136 to -0.123, with an increase

in air velocity from 4.1 to 5.4 m/s. Therefore, increasing the air flowrate has the effect of reducing the kiln-wide differences in moisture content.

Table 4.3 shows that the drying time is reduced from 72 hours to 57 hours when the flowrate is increased from 4.1 to 5.4 m/s, for both heartwood and sapwood. A single reversal in a kiln with a fan speed corresponding to an average stack velocity of 4.1 m/s results in a reduction in drying time to only 61 hours, for both heartwood and sapwood. This is the same reduction in drying time achieved when the air velocity is increased from 4.1 to 5.0 m/s.

4.5 Part 2: Detailed Investigation into Flow Maldistribution

In Part 1, it was shown that when the air flowrate through a kiln is increased, the moisture-content variation expected at the end of drying decreases. This trend is investigated more closely in this section. In addition, limited data from industry is presented which supports these findings.

4.5.1 Impact of Flow Maldistribution

Moisture variation across a stack of timber is inevitable at the end of a kiln schedule. Some timber in the stack may have reached or passed the desired final moisture content whilst others may need further drying. Part 1 showed that final moisture-content variation is caused by the progressive humidification of the air as it passes through the stack, and non-uniformity of flow at the inlet face of the stack. Differences in the initial moisture content and drying properties from board to board also cause moisture-content variations, although these considerations are outside of the scope of this chapter. If a timber board is exposed to different air velocities at each surface, then the subsequent variability in within-board moisture contents can result in differential shrinkage of the timber, with the possibility of subsequent warping if the associated stresses build up to critical levels (Bester [1982] and Rosen [1987]). A similar problem may occur in structures built from timber boards with differences in dried moisture contents. Thus, timber should be dried with minimal moisture variation and as close to the desired final moisture content as possible.

One method of reducing final moisture-content variations is to 'equalise' the timber. With this technique, the wet-bulb depression is reduced until the equilibrium moisture content of the timber is increased to the desired final moisture content. The drier boards will then tend to become wetter while at the same time allowing the wetter ones to continue drying. Equalising, however, is a slow process and the operator cannot afford to equalise for long. The New Zealand Forest Service Information Series [1974] suggests that equalising for the last 24 hours of a run in a conventional kiln can be beneficial in reducing moisture variation. *Pinus radiata* dried at 80 °C dry-bulb temperature and 60 °C wet-bulb temperature can take up to 72 hours to dry. Therefore, a kiln operator can expect to lose an entire kiln load for every three kiln loads dried should an equalising period be included in the drying schedule.

Figure 4.9 show plots of the moisture-content distribution of timber boards in a stack dried at three different average between-board velocities. These data were generated from known air velocity distributions at the inlet face of an actual stack, and are presented in numerical format in Part 1 (Table 4.3). The plots show that the range of

final moisture contents narrows as the velocity through the stack is increased, even though the range of velocities at the inlet face of the stack increases slightly. When the average between-board air velocity is 4.1 m/s, the moisture-content distribution ranges from 6 to 23 % (Figure 4.9a). The moisture-content distribution reduces to a range of 6 to 19% when the air velocity is increased to 5.0 m/s (Figure 4.9b), and from 6 to 14% at an even higher air velocity of 5.4 m/s (Figure 4.9c). Clearly, increasing the airflow rate presents a method for reducing moisture content variation without resorting to the time-consuming process of equalising.

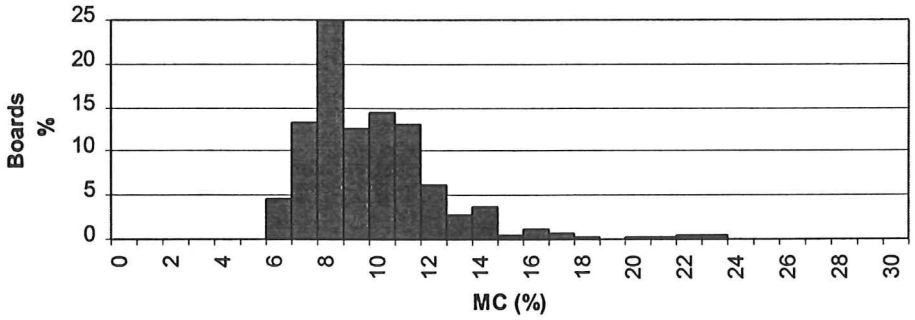

(a) air velocity 4.1 m/s, range 2.5 m/s

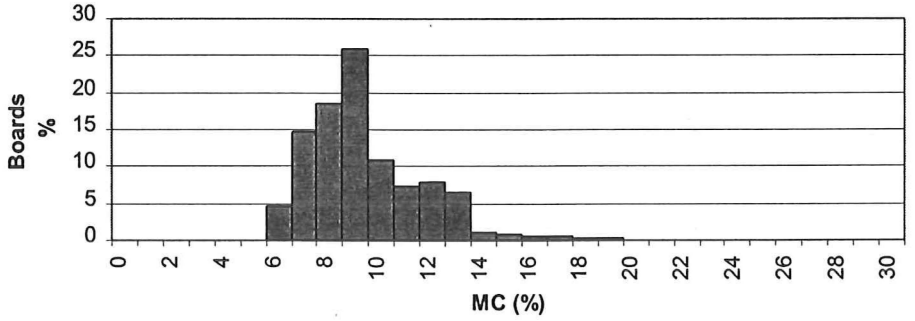

(b) air velocity 5.0 m/s, range 2.5 m/s

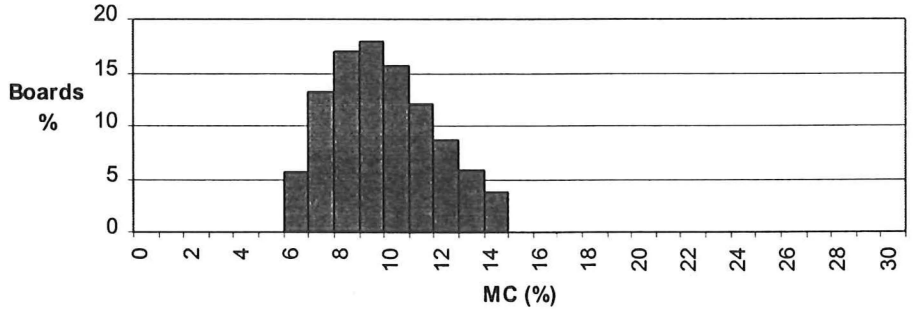

(c) air velocity 5.4 m/s, range 2.7 m/s

Figure 4.9. Frequency data for the final moisture-content distribution of stack of timber dried at various average between-board air velocities.

Final moisture-content frequency plots for sapwood *Pinus radiata* stacked timber dried in the conventional kilns at Waipa were provided by Worsfold from the Forestry Corporation of New Zealand Limited, *pers. comm.* (Figure 4.10, 4.11 and 4.12). The boards were 50mm thick and were dried at 80 °C dry-bulb and 60 °C wet-bulb temperature. These graphs suggest similar trends calculated using Van Meel's batch drying equations; that is, when the average stack flow rate is increased, the kiln-wide moisture variation is reduced. Figure 4.10 shows that when the average between board air velocity is 3 m/s, the moisture-content distribution ranges from 2 to 24%. When the air velocity is increased to 4 m/s, the moisture-content distribution narrows to range from 1 to 17% (Figure 4.11). The moisture-content range narrows even further to range from 4% to 15% when the air velocity is increased to 5 m/s (Figure 4.12). Note that these frequency plots are only suggestive of the indicated trends since they were taken from a number of different kilns and in an uncontrolled manner. The next section attempts to substantiate these limited observations theoretically.

4.5.2 Theory

The analysis is simplified by assuming first-order drying kinetics for the timber. This implies that the following equation describes the characteristic drying behaviour of the timber boards:

$$f = \Phi \tag{4.30}$$

This is a reasonable approximation to the drying behaviour of heartwood timber, and implies that the moisture-diffusion coefficient is independent of moisture content (Keey, *priv. comm.*)

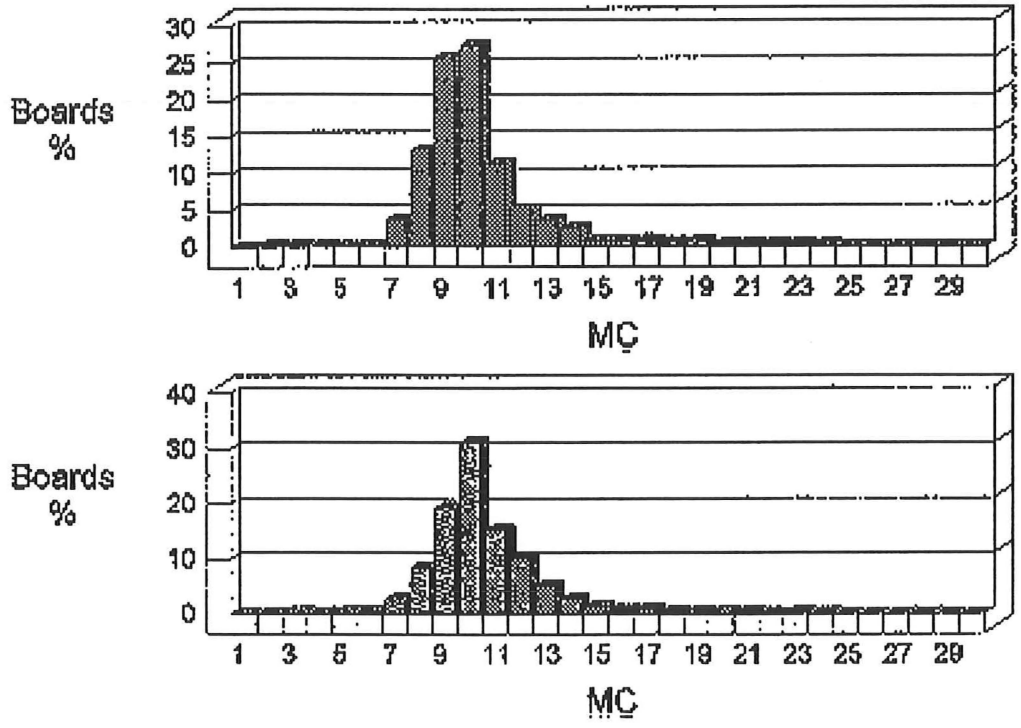

Figure 4.10. Frequency plots for the final moisture content distributions of two separately dried loads of stacked sapwood timber boards, dried at 80/60°C with an average between-boards air velocity of 3 m/s.

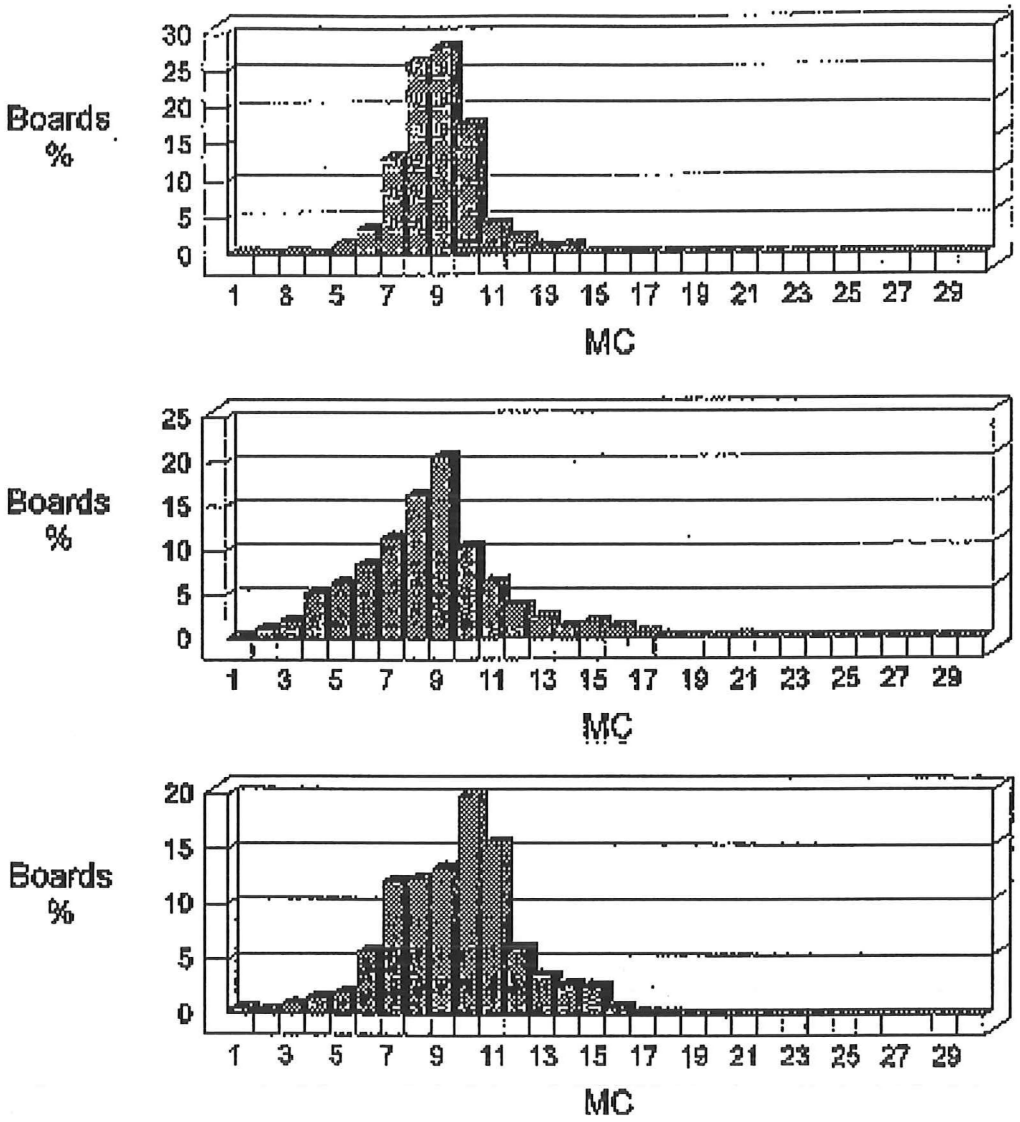

Figure 4.11. Frequency plots for the final moisture content distributions of three separately dried loads of stacked sapwood timber boards dried at 80/60°C with an average between-board air velocity of 4 m/s.

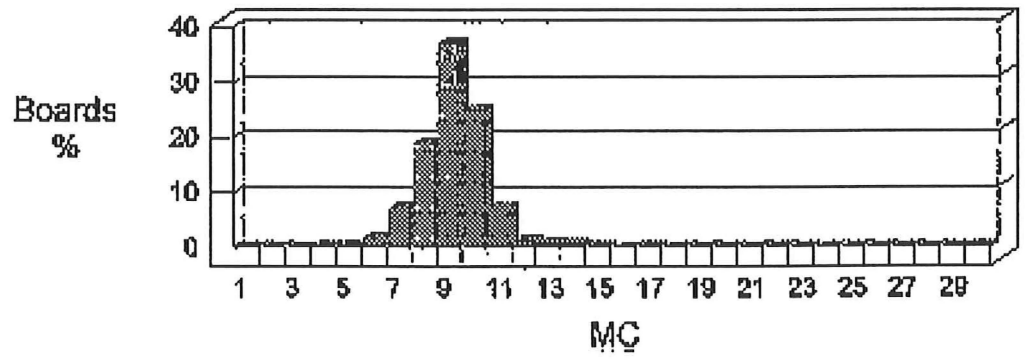

Figure 4.12. Frequency plot for the final moisture content distribution of a load of sapwood timber dried at 80/60°C with an average between-board air velocity of 5 m/s.

The analytical solution to the batch-drying equations becomes (Keey [1978]):

$$\Phi = \frac{\Phi_o}{\Phi_o\left[exp(\theta + 1 - \Phi_o) - 1\right]exp(-\Phi_o \xi) + 1} \tag{4.31}$$

where Φ_o is the initial dimensionless moisture content, ξ is the relative distance across the width of the stack, and θ is the relative drying time.

The maximum value of relative distance ξ is equal to the total number of transfer units NTU across the width of the stack. When Φ_o and NTU are known, then the variations in dimensionless moisture content with relative time θ and relative distance across the width of the stack ξ may be determined.

In Part 1, it was shown that NTU is a function of air velocity by the following equation:

$$\frac{NTU_2}{NTU_1} = \left(\frac{u_2}{u_1}\right)^{n-1} \tag{4.32}$$

Thus, the NTU_2 at a particular air velocity u_2 may be determined from a known reference NTU_1 and air velocity u_1. NTU_1 is given a value of unity when the between-board air velocity is 4 m/s.

In this investigation, heartwood timber boards were dried from an initial moisture content of 0.4 kg/kg down to a final moisture content of 0.1 kg/kg. The drying conditions were 80 °C dry-bulb temperature and 60 °C wet-bulb temperature giving an equilibrium moisture content for the timber of 0.047 kg/kg. Equation (4.4) shows that Φ_o is equal to unity, and the final dimensionless moisture content Φ_f is equal to 0.15 for a critical moisture content X_{cr} for heartwood of 0.4 kg/kg.

The relative drying times θ, at different air velocities, required to reduce the average moisture content of the heartwood boards from Φ_o down to Φ_f were determined from Equation (4.31). In Part 1 it was shown that the following equation could be used to calculate the actual drying time τ_2 for a particular air velocity u_2 given the reference values (u_1, τ_1) and the relative drying times, θ_1 and θ_2:

$$\frac{\theta_2}{\theta_1} = \left(\frac{u_2}{u_1}\right)^n \frac{\tau_2}{\tau_1} \tag{4.33}$$

The actual time τ required to dry the heartwood timber boards from 0.4 kg/kg to 0.1 kg/kg at 4 m/s was assumed to be 72 hours.

Figure 4.13 shows the graphs of average moisture content along a row of boards versus drying time for various air velocities. These drying curves were determined

using the analytical solution (Equation (4.31)), and calculating the *NTU* for a particular air velocity from Equation (4.32).

4.5.3 Discussion

The flow maldistribution in the actual stack (Figure 4.9) had a range of 2.5 m/s when the air velocity was 4.1 m/s, a range of 2.5 m/s when the air velocity was increased to 5.0 m/s, and a range of 2.7 m/s when the air velocity was increased further to 5.4 m/s. Thus, the range in the distribution of velocities increased only slightly when the air velocity was increased. Figure 4.13 shows the range of final moisture contents which can be expected in a stack with average between-board air velocities of 3, 5, and 7 m/s and a constant range in the distribution of velocities of 2 m/s. As the average between-board air velocity is increased, the range of final moisture contents decreases, provided that the range of the flow maldistribution remains constant. This trend was also observed in the industrial data (Figures 4.10-4.12) and in the kiln simulations (Figure 4.9). Figure 4.13 also shows that the uppermost moisture content decreases by a larger amount than the increase in the lowermost moisture content as the air velocity is increased. Thus, the wettest timber boards are affected more significantly by an increase in the air velocity than the drier timber boards, which is the same trend that was observed in the industrial data (Figures 4.10-4.12) and in the kiln simulations (Figure 4.9).

The range in final moisture contents decreases as the air velocity is increased because the drying curves become closer together at higher air velocities since the drying rate is increasingly controlled by the internal drying kinetics of the timber and less dependant on the external flow resistance. Therefore, moisture content variations in dried timber could be reduced to a significant extent by increasing the airflow rate sufficiently. Increasing the airflow rate may have a detrimental effect on the quality of the timber since the drying rates are intensified. Moreover, the power requirements of the fan will be increased. However, there is a commercial trend towards using higher kiln velocities which suggests that the quality of the timber is not seriously affected by the increase in drying rates, and that the disadvantage of higher fan costs is outweighed by an increase in the annual throughput of dried timber.

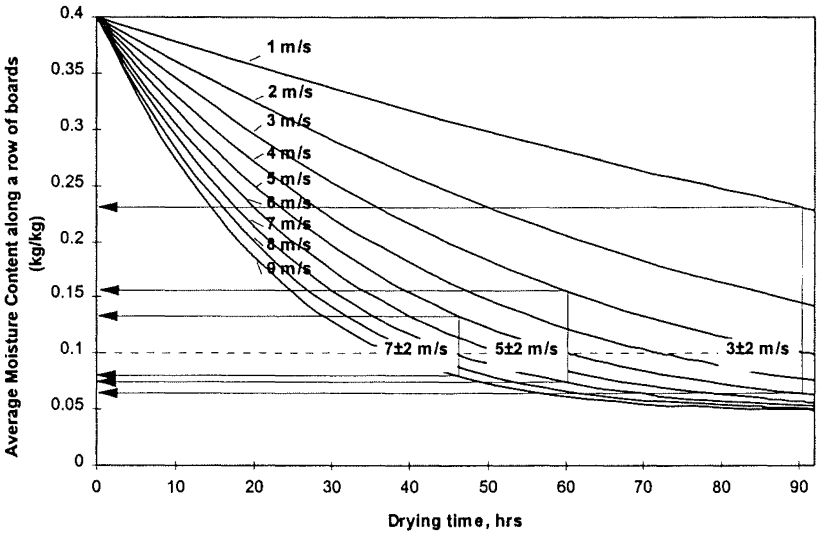

Figure 4.13. Drying curves for various airflow velocities.

4.6 Part 3: Hi-Lo Kiln-Drying Strategies

In Parts 1 and 2, a kiln schedule was optimised to reduce final moisture-content variations resulting from progressive humidification of air through the stack and flow maldistribution across the inlet face of the stack. In this section, Hi-Lo schedules, which aim at minimising the energy usage of a kiln, are investigated. This will complete this study into methods of controlling airflow conditions so as to improve the uniformity of drying rates across the timber stack and reduce energy consumption.

4.6.1 External and Internal Resistances

The drying curve of sapwood can be divided into three periods: a constant rate period followed by two falling rate periods (Figure 4.14). In the first period, there exists an evaporative plane near the surface of the wood at which water evaporates. Liquid water flows from the interior towards the surface through the capillary structure of the cell cavities. The drying rate is relatively constant during this period and externally controlled by the rate of heat transfer to the wood surface.

In the second period, the evaporative plane recedes into the wood as drying proceeds. The influence of internal resistance to moisture vapour transport gradually dominates over the external resistance and the drying rate falls. The evaporative plane divides the wood into two parts: a wet zone within the core, and a dry zone in the outer portion. The moisture content within the dry zone is below the fibre saturation point and moisture migrates by bound-water diffusion through the cell walls and vapour diffusion across the cell cavities. The moisture content within the wet zone is above fibre saturation, and moisture migrates in a similar fashion to the moisture flow in the first period. Thus, the fibre-saturation moisture content is a transitional point, located at the evaporative front, where free moisture has evaporated and bound-moisture diffusion begins.

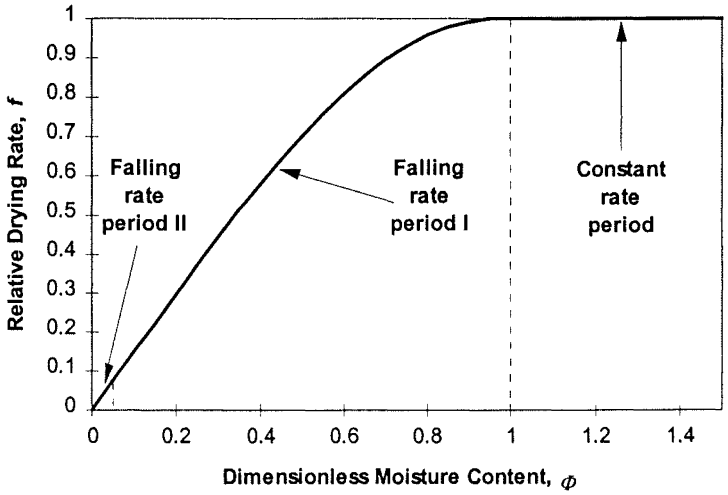

Figure 4.14. Characteristic Drying Curve for *Pinus radiata* sapwood: the green moisture content is 140%, the equilibrium moisture content is 5%, and the first and second critical moisture contents are 94% and 9.3%, respectively (Pang [1994]).

The third period begins when the evaporative plane has reached the centre of the board. Bound-water diffusion controls at this point and the drying rate falls rapidly.

Internal resistance gradually eclipses the external resistance to moisture flow during the second drying period. In the Hi-Low strategy, the airflow is reduced at the fibre-saturation moisture content; however, such a sharp transitional point does not exist. The fibre saturation point travels behind the evaporative plane as it gradually moves towards the centre of the board. This period may last up to 60% of the conventional kiln drying time (Pang [1994]).

The purpose of this section is to determine when the airflow through a kiln should be reduced. According to Culpepper [1990], should the fan speed be changed too soon, then there will be an increase in cost due to an extended drying time. However, should the fan speed be changed too late then the full benefit in fan-energy savings will be lost.

4.6.2 Process Description and Specifications

Kiln Description

The kiln being considered has a timber capacity of 35 m^3. The timber boards are 50 mm thick with 20 mm sticker spacings between boards, and the dimensions of the stack are 4.8 m long, 4 m high, and 2.5 m wide. The timber to be dried is sapwood *Pinus radiata*. The kiln is operated at 80 °C dry-bulb temperature and 60 °C wet-bulb temperature. The airflow direction is reversed every 8 hours, which is typical of industrial-scale conventional kilns. When the air speed through the stack is 4 m/s, it is assumed that the timber load will take 61.2 hours to dry from 140% to 10% moisture content. Half the amount of air that passes through the stack is assumed to bypass the stack. This is a realistic bypass ratio according to Riley [1986].

Process Conditions

An *NTU* of unity is assumed which corresponds to an air velocity of 4 m/s. Keey [1992] states that this is a typical value for most batch-drying units. Equations (4.13) and (4.14) are used to determine the boundary conditions on ξ and to convert the dimensionless drying times θ to actual drying times τ. The exponent n in Equation (4.8) was given a value of 0.75 (Kho [1993]). Equation (4.24) describes the characteristic drying curve for sapwood *Pinus radiata*, which was fitted to experimental data collected by Pang [1994].

Timber Production Costs

The basic density, which is a measure of dry wood substance per unit volume of green timber, of sapwood is 430 kg/m^3 (Kininmonth [1991]). Assuming that 1.67 kg of steam is required per 1 kg of water evaporated (60% efficiency) and that steam at 70 °C is produced from water at 20 °C, then the heating requirement is about 2550 MJ per unit volume of greenwood. The cost of natural gas is $9.25/GJ: thus, the heating cost is $23.6/$m^3$.

The power requirements for operating the fans in a kiln is equal to the total air flowrate through the kiln multiplied by the pressure drop. Pressure drop-air velocity relationships across a stack have been developed by Langrish [1996] using a Computational Fluid Dynamics program to model the airflow pattern inside the kiln. The following curve was fitted to Langrish's results which applies for the stack configuration being investigated:

$$\Delta P = 3.036u^{2.05} \tag{4.34}$$

The price of electricity is approximately \$0.12/kWhr. Thus, the cost function, assuming a 50% fan efficiency, is

$$C = \$0.00413u^{3.05}\tau \,/\, ki\ln load \tag{4.35}$$

Usually 3% of the capital cost is allowed for maintenance. Assuming a capital cost of \$150000 for a conventional kiln (operating below 100 °C), the annual maintenance cost is \$4500. Annual operator costs are estimated at \$10000. The sticker cost which include labour costs for filleting and defilleting, and material costs is \$15 per unit volume greenwood.

4.6.3 Results

An economic analysis was carried out for various Hi-Low strategies with the 'high' velocity at 4 m/s and the 'low' velocity ranging from 1 m/s to 3 m/s. The Hi-Low change-over times were varied to find the optimum Hi-Low strategy. The normal procedure when using the Hi-Low strategy is to lower the air velocity when the average stack moisture content reaches the fibre-saturation point. For *Pinus radiata*, the fibre-saturation point is at a moisture content of 30% at ambient conditions (Kininmonth [1991]). In these simulations, the average moisture content of the stack reaches the fibre-saturation moisture content in approximately 38.6 hours when the air velocity is 4 m/s. Figure 4.15 shows the expected drying times for various Hi-Low strategies.

The annual loss in profit is defined as the difference in profit between a kiln that is operated at a constant velocity of 4 m/s throughout the drying schedule and the kiln that uses a Hi-Low strategy. The profit is based on the current market price for the kiln drying of timber of \$65 per unit green volume. The calculated annual loss in profit for various Hi-Low strategies is given in Figure 4.16.

4.6.4 Discussion

When the air velocity is reduced at the so-called fibre saturation moisture content of the stack, there is an increase in the drying time (Figure 4.15). A significant increase in the drying time also occurs when the air velocity is reduced at any time after the fibre-saturation point has been reached. Thus, the external conditions at average-stack

moisture contents less than the fibre saturation point still affect the drying rate of the timber.

An optimum change-over time may exist at which the annual loss in throughput due to an increased drying time balances the fan energy savings made by reducing the air velocity. The optimum change-over time is at 61.2 hours, which is the drying time when the air velocity is fixed at 4 m/s (Figure 4.16). This indicates that a fixed-speed strategy produces a greater annual profit than any Hi-Low strategies.

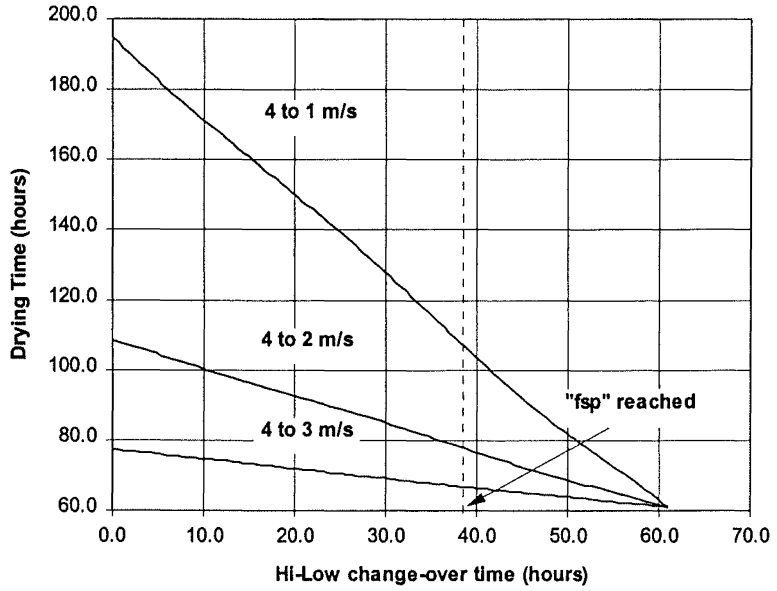

Figure 4.15. Expected drying times when using the Hi-Low strategy for a range of 'low' velocities and varying change-over times.

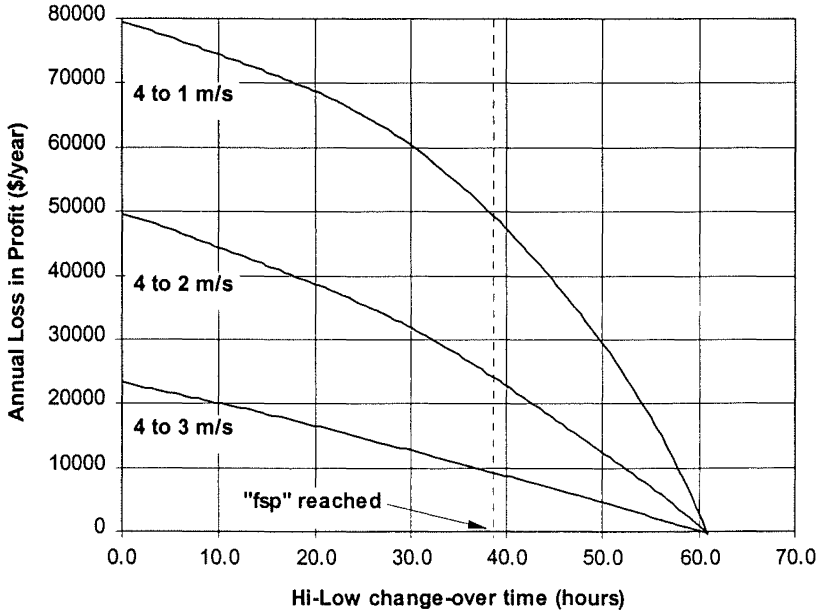

Figure 4.16. Expected annual loss in profit ($/year) when using the Hi-Low strategy for a range of 'low' velocities and varying change-over times.

Halving the air velocity at the fibre saturation point is a typical Hi-Low strategy used in industry. The annual fan costs will be reduced from $3397 to $1890 when the air velocity is halved at the fibre saturation point, which is a 44% saving. This value lies within the range of expected fan energy savings stated by Culpepper [1990] of 40 to 50%. However, the cost due to the loss in annual throughput far outweighs the fan energy savings made such that there is an expected loss in the annual profit of $24000.

4.7 Conclusions

The effect of flow reversals, flowrate and flow bypass on the timber moisture-content distribution within in a kiln was investigated. It was found that only one flow reversal is necessary to kiln-dry timber close to a uniform moisture content in the minimum drying time. In drying *Pinus radiata* boards, the fans should be reversed at approximately one-third of the no-reversal drying time. The application of this optimum flow reversal conditions will result in a decrease in the drying time by 15% and 17% and an increase in the uniformity of moisture by 90% and 75%, for heartwood and sapwood respectively.

On average, timber in a kiln with 100% bypass will be dried only 75% as much as it would with no bypass for the same drying time. Reversals make the situation worse by further increasing the amount of drying required to reach the desired dryness.

The application of the optimum flow reversal conditions in a kiln with flow maldistribution will result in an improved uniformity in timber moistness in the air-flow direction and a shortened drying time. On a kiln-wide basis, flowrate increases improve the uniformity of timber moistness, whereas reversals have the opposite effect of widening the moisture distribution. However, reversals improve moisture variations across a row of timber boards in the airflow direction more significantly than flowrate increases. A single airflow reversal at the optimum reversal conditions used in a kiln operated with an average stack velocity of 4.1 m/s is more effective in shortening the kiln-drying schedule than increasing average stack velocities up to 5 m/s.

Hi-Low strategies, in which the air velocity through the stack is reduced at some point during the schedule, were compared with the fixed-speed strategy. The expected loss in annual profits was plotted against the change-over time at which the air velocity is reduced. The results show that a fixed-speed strategy will produce a greater annual profit than a Hi-Low strategy.

4.8 Symbols

a	exposed surface per unit volume of dryer, m^2/m^3
A	constant
	cross-sectional area, m^2
b	ratio of airflow bypassing the stack to the airflow through the stack
C	fan cost, $/kiln load
D_{NA}	diffusivity coefficient, kg/ms

f	relative drying rate
$FMCA$	final moisture-content approach
G	air rate, kg/m²s
K_o	average mass-transfer coefficient, kg/m²s
$\bar{m}$	average final moisture-content approach in the stream-wise direction
$\bar{m}_{min}$	kiln-wide minimum average final moisture-content approach
$\bar{m}_{max}$	kiln-wide maximum average final moisture-content approach
$\bar{M}$	kiln-wide mean of average final moisture-content approaches
n	dimensionless parameter for flow
	number of integration points in the stream-wise direction
n_r	number of flow reversals
NTU	dimensionless parameter for distance
ΔP	pressure drop, Pa
Q	flowrate, m³/s
r	number of sub-stacks
$\bar{S}$	kiln-wide mean of the standard deviations of final moisture-content approaches
u	air velocity, m/s
X	moisture content, kg/kg
X_{cr}	critical moisture content, kg/kg
X_e	equilibrium moisture content, kg/kg
Y_S	wet-bulb humidity, kg/kg
Y_G	dry-bulb humidity, kg/kg
z	distance along kiln in air flow direction, m
Z	streamed length, m
ε	voidage of the stack in a kiln
Φ	normalised free moisture content
ϕ	humidity potential coefficient
ν_A	viscosity of air, kg/ms
Π	normalised humidity potential
θ	dimensionless parameter representing the extent of drying
$\Delta\theta_r$	flow-reversal period
ρ_s	basic density of wood, kg/m³
ρ_G	density of air, kg/m³
σ	standard deviation of final moisture-content approaches
σ_k	kiln-wide standard deviation of the mean final moisture-content approaches
τ	time, s
ξ	dimensionless parameter representing distance (NTU)
	relative humidity of air

4.9 References

Ashworth, J.C., 1977, *The Mathematical Simulation of Batch Drying of Softwood Timber.* Ph.D. Thesis, Department of Chemical Engineering, University of Canterbury.

Ashworth, J.C., Keey, R.B., 1979, *The kiln seasoning of softwood timber boards*, Chem. Eng. No 347/8, 593-8, 607.

Culpepper, L.G., 1990, *High Temperature Drying: Enhancing Kiln Operation*, Miller Freeman Publications.

Keey, R.B., 1978, *Introduction to Industrial Drying Operations*, Permamon Press, Oxford, UK.

Keey, R.B., 1992, *Drying of Loose and Particulate Materials.* Hemisphere Publishing Corporation, New York.

Keey, R.B., Pang, S., 1994, *The high-temperature drying of softwood boards: a kiln-wide model*, Transactions IChemE Series A, Vol 72, 741-753.

Kininmonth, J.A., Williams, D.H., 1974, *Kiln Schedules for New Zealand Timbers.* NZ Forest Service Information Series No 69.

Kininmonth, J.A., Whitemann, L.J., 1991, *Properties and uses of New Zealand Radiata Pine.* Volume 1. New Zealand Ministry of Forestry.

Kröll, K., 1978, Trockner und Trocknungsverfahren, 2nd edition, Springer-Verlag, Berlin, Heidelberg, New York.

Langrish, T.A.G., 1996, *The effects of air bypassing in timber kilns on fan power consumption*, 24th Australian and New Zealand Chemical Engineering Conference (CHEMECA '96), Sydney, 103-108.

Pang, S., 1994, *High Temperature Drying of Pinus Radiata in a Batch Kiln.* Ph.D. Thesis, Department of Chemical Engineering, University of Canterbury.

Pang, S., Keey, R.B., Walker, J.C.F., Langrish, T.A.G., 1994, *Airflow reversals in high-temperature kiln drying of Pinus Radiata boards. 2: drying of a stack of boards*, New Zealand Journal of Forestry Science, Vol 24 (1), 104-119.

Pang, S., Keey, R.B., Langrish, T.A.G., 1995, *Modelling the temperature profiles within boards during the high-temperature drying of Pinus Radiata timber: the influence of airflow reversals*, International Journal of Heat and Mass Transfer, Vol 38 (2), 189-205.

Riley, S., 1984, *Air flow in Timber Dryers.* Timber Drying News, New Zealand Forest Research Institute, Vol 7.

Riley, S., 1986, *Bypass air in timber Driers*. Timber Drying News, New Zealand Forest Research Institute, Vol 13.

Rosen, H.N., 1981, *Drying Processes for the year 2000,* Proc. XVII IUFRO World Congress, Japan.

Van Meel, D.A., 1958, *Adiabatic Convection Batch Drying with Recirculation of Air*, Chem. Eng. Sci. Vol 9, 36-44.

Walker , J.C.F., 1993, *Primary Wood Processing Principles and Practice*, London, New York, Chapman and Hall.

CHAPTER FIVE

HYDRAULIC KILN

The kinetics of batch drying was analysed in Chapter 4 by considering simplified transfer equations of convection from the timber surface into the passing airstream. The kiln-wide drying behaviour of stacked timber boards was simulated by incorporating into the model known airflow maldistributions from kiln audits. Airflow maldistribution was shown to contribute significantly to uneven drying of timber in a stack. A sufficient increase in the fan speed mitigates to a certain extent the effect of flow maldistribution. Further improvements in the uniformity of dried timber are possible by reducing the extent of flow maldistribution across the timber stack. In this chapter, a hydraulic model will be utilised to study flow maldistribution in kilns. Different design alternatives for reducing flow maldistribution across a timber stack will be investigated, such as changing the geometry of the plenum chambers on either side of the stack and incorporating guides to promote a more uniform flow.

5.1 Flow Maldistribution

Most board timber (lumber) is dried in stacks placed in box-like chambers known as kilns. Overhead fans circulate air through the stack, and it has been assumed that a uniformly stacked pile of timber will ensure a uniform air distribution across the whole cross-section. In the previous chapter, kiln audits were reported which show that the air velocity over the inlet face of the stack can be non-uniform. Such maldistribution is not unexpected. For example, Kröll [1978] presents data of such a non-uniform velocity profile in a drying chamber of similar design to a timber kiln in which the mean air velocity was 2.52 m/s and the coefficient of variation 0.67. Indeed, there was a reverse flow in the uppermost air channel.

It is important to reduce the variation in moisture contents of the boards within a stack at the end of drying to maintain wood quality and meet trade specifications. Clearly, one prerequisite is that the air be uniformly distributed. To determine the possible extent of air maldistribution in kilns of current design, it was decided to study the flow maldistribution in a model kiln over a range of flow conditions.

A typical timber kiln is shown in Figure 1.1 (Chapter 1). The airflow path consists of the ceiling space, in which the circulation fans are located, and two plenum chambers on either side of the stack of timber boards. The stacked timber boards are assembled in horizontal rows, with each row separated by a number of regularly spaced fillets. Hot air is able to circulate through the fillet spaces between the boards so that the transfer of heat and moisture between the timber boards and air may be facilitated.

One contribution to flow maldistribution is the imbalance which exists between the inertial and frictional forces along the length of the plenum chamber. As air flows down the inlet plenum chamber, its velocity decreases because air flows into the fillet

spaces. According to Bernoulli's equation, a reduction in the velocity corresponds to an increase in the pressure. This is the inertial effect which forces more fluid through the fillet spaces at the bottom of the plenum chamber. Frictional forces act in opposition to the inertial forces in the inlet plenum chamber and therefore cause a reduction in the pressure. The frictional effects in the inlet plenum chamber tend to force more fluid through the fillet spaces near the top of the stack. In the outlet plenum chamber, frictional and inertial effects act in the same direction, and are added together instead of opposing each other as in the inlet plenum chamber. There is a tendency for the pressure variations due to the inertial effect in one plenum chamber to counteract those in the other plenum chamber. However, when the frictional effects outweigh the inertial effects, then the relative magnitudes of these forces within the inlet and outlet plenum chambers determine to a certain extent the severity of the airflow maldistribution down the stack.

Superimposed on the combined effect of the inertial and frictional forces is the effect of any vortex in the inlet plenum chamber which would be caused by the sharp right-angled turn from the ceiling space into the inlet plenum chamber.

Arnaud *et al.* [1991] have studied the influence of the important geometrical ratios on the velocity distribution across a stack of timber. They concluded that flow maldistribution may be reduced by designing the kiln so that the ratio of the plenum-space width to the ceiling-space height above the stack be at least equal to unity. According to these workers, if this condition is not met, then the turn from the ceiling space into the plenum chamber, together with the reduction in the cross-sectional area, will produce significant velocity gradients across the width of the plenum chamber (normal to the direction of flow). The velocity gradient across the width of the plenum chamber has a significant effect on the uniformity of flow across the stack.

When the ratio of the plenum-chamber width to the ceiling-space height is increased significantly, the air velocities along both plenum chambers in the airflow direction can be reduced to very small values. Thus, the pressure variations along both plenum chambers in the airflow direction become insignificant and, in effect, the plenum chamber acts as an infinite reservoir. The resultant flow will be distributed uniformly among the fillet spaces, provided any eddies formed in the inlet plenum chamber are eliminated by introducing flow guides or baffles. A similar solution is to increase the width of the timber stack until the pressure drop across the stack far exceeds the pressure variations along the plenum chambers in the airflow direction; thus, the plenum chambers approach the infinite reservoir solution. Likewise, the fillet space width can be decreased by reducing the thickness of the fillets. This reduction has the effect of increasing the average velocity through the stack, thus increasing the pressure drop across the timber stack (which is once again the infinite reservoir solution). When the fillet space width is decreased, the effective porosity of the timber stack is reduced, which would have the added advantage that more timber can be put into the kiln. However, the disadvantage of these solutions is that there may be practical limitations on fan power, and an increase in the pressure drop across the timber stack is accompanied by a considerable increase in the power requirements of the fan.

Werner [1958] and Sturany [1952] have demonstrated that a uniform air-velocity distribution can be attained by streamlining the plenum chambers and using curved

flow guides. Kröll [1978] presents similar solutions (also presented in Charm [1963]) involving the use of streamlining techniques and flow guides, which also include placing screens in front of the timber stack to increase the pressure drop over the stack so that the plenum chamber approaches the infinite reservoir solution. However, many of these solutions are not practical in kilns for drying timber. Typical industrial-scale plenum chambers are 18 m long, 6 m high, and 1.5 m wide. Streamlining this space or attempting to install an 18 m long curved flow guide within the plenum chamber would be a difficult and expensive task. The simpler alternative of varying the geometric ratios of a 'box'-shaped kiln is preferable to incorporating such sophisticated designs. Nevertheless, flow guides for improving the uniformity of flow across a timber stack may still be useful if they are both simple to construct and easy to install.

In this investigation, direct flow visualisation through a transparent kiln model was employed in which water took the place of air. The advantage of this approach is that it allows the simultaneous observation of the whole flow field in minute detail without the obstruction of instruments for measuring the flow. Moreover, the use of water instead of air provides similarity at much lower velocities which facilitates observation and recording of the flow details. The flows along each fillet space were measured by tracing hydrogen bubbles along the length of the fillet spaces. These bubbles were generated by electrolysing the flowing water using a fine platinum wire electrode which passed through each fillet space normal to the direction of flow.

5.2 Similarity

Valid comparisons between a hydraulic model and the prototype can be made provided that the two systems are both geometrically and dynamically similar. However, perfect geometric similarity proved impractical in the design and construction of the hydraulic kiln. Thus, the flow distributions down the height of the stack, which are obtained from the hydraulic kiln, will differ from those that can be expected from the prototype. Nevertheless, the characteristic shape of these flow distributions, and the general trends observed will be similar. In addition, the data obtained from the hydraulic kiln are useful for the possible verification of Computational Fluid Dynamics (CFD) methods for analysing flow behaviour in kilns. More realistic industrial-scale kiln configurations can be investigated quickly and efficiently using a CFD analysis.

Geometric Similarity

The first requirement in the design of a hydraulic model is that the model be geometrically similar to the prototype. Thus, the ratio of any length in the model to the corresponding length in the timber drying kiln must be everywhere the same. However, perfect geometric similarity was not practical in the design of the hydraulic kiln. The model was constructed almost entirely from Perspex to allow visual observation of the flow fields. Perspex is almost smooth and wood is relatively rough in comparison, even when this roughness is scaled down for the hydraulic kiln. Therefore, surface roughness in the model and the prototype could not be made geometrically similar. This has an effect on the pressure drop through the stack, which in turn effects the distribution of flow down the height of the stack.

A timber stack is comprised of rows of boards stacked above each other. In the hydraulic kiln, a perspex plate replaced each row of timber boards. This is again a violation of the geometric similarity condition. Kho [1993] has shown that eddies are generated in the spaces separating the boards in a particular row. Therefore, pressure losses can be expected as kinetic energy is dissipated as heat in these eddies. The pressure losses which result from surface roughness and eddies can be accounted for in the hydraulic kiln by increasing the length of the Perspex boards, or installing an orifice plate or a similar pressure reduction device between the Perspex boards.

Langrish *et al.* [1996] calculated the pressure drop across a stack of timber using CFD methods. They verified these calculations by comparing their results with the experimental data of Wu [1989]. The dimensionless pressure drop across the timber stack ($\Delta P / \rho u^2$) was 2.7 when the fillets were 20 mm wide, the stack 2.4 m wide, the between board air velocity equal to 5 m/s, and the air temperature equal to 300K. The equivalent length of the Perspex plates in the hydraulic kiln required to achieve the same dimensionless pressure drop is 1.8 m. This length was not practical for the design of the hydraulic kiln. In addition, data for the characteristics of an orifice plate of rectangular cross-section are not readily available in the literature. Therefore, no pressure reduction devices were installed in the hydraulic kiln, and the Perspex boards were given shorter lengths of 0.46 m. Thus, the flow distributions down the height of the stack, which are obtained from the hydraulic kiln, will differ from those of the prototype due to differences in the dimensionless pressure drop across the stack. However, the characteristic shape of the distribution will be similar, and the general trends observed will not change.

In kilns for drying timber, the boards may be 50mm thick and separated by stickers which are 25 mm wide. Thus, the porosity of the stack is 0.33. This porosity was put to use in the hydraulic kiln design. In an industrial kiln, thirty to fifty rows of timber boards are usually stacked above one another. However, only thirteen plates were installed in the hydraulic kiln so that the fillet spaces were wide enough to facilitate velocity measurements using flow visualisation techniques, and to minimise complications in the construction of the model.

Strict geometric similarity was observed in the stack height, plenum chamber width and ceiling-space height. Thus, similar flow patterns between the model and the original apparatus can be expected outside of the stack provided that the dynamic similarity condition holds. Kilns are normally designed on the basis that the important geometric ratios are equal to unity. For example, the ratio of the width of the plenum chamber to the sum of the fillet-space widths, and the ratio of the plenum-chamber width to the ceiling-space height are both normally set equal to unity. In the hydraulic kiln, the plenum-chamber width could be varied so that the ratio of the plenum chamber width to the sum of the fillet-space widths was adjustable between values of 0.4 and 1.4. The ceiling-space height was not variable. When the ratio of the width of the plenum chamber to the sum of the fillet space widths was unity, then the ratio of the plenum-chamber width to the ceiling-space height was also unity.

The depth of a typical kiln for drying timber is usually considerably greater than the other dimensions of the plenum chamber. Therefore, the flow in a typical kiln is approximately two-dimensional, provided that the heating coils dampen the swirling motion induced by the fans. However, there was an economic constraint on the size of

the circulation pump that could be used, and a physical constraint on the head of water being supplied to the hydraulic kiln (approximately 4m). Therefore, there was a limit on the maximum flowrate possible, and consequently, a limit on the depth of the hydraulic kiln. The ratio of the fillet space widths to the depth of the hydraulic kiln was fixed at unity. This ratio will produce flows in the third dimension. However, in the Chapter 6, it will be shown that the depth of the kiln only indirectly affects the flow maldistribution down the height of the timber stack.

Dynamic Similarity

The second requirement in the design of the hydraulic kiln was that the water flow be dynamically similar to airflow in a typical timber-drying kiln. Dynamic similarity occurs when the ratios of forces in the model are equal to the ratios of the forces in the original apparatus. These forces may be caused by factors such as viscosity, gravity, surface tension, and compressibility. When similarity is achieved, the flow pattern will be similar in both the model and the original apparatus because the forces acting on corresponding particles in the two flows have the same relative magnitudes.

Dynamic similarity implies that the dimensionless groups such as the Reynolds number (viscous effect of the fluid), Froude number (gravity effect due to free surfaces), Weber number (surface tension effect of the fluid) and Mach number (compressibility effect of the fluid), have the same magnitudes in the model and the original apparatus. Kilns for drying timber are closed systems with relatively low flows; therefore, gravity and surface tension effects are non-existent since there are no free surfaces, and compressibility effects are negligible. Heat transfer effects are ignored as a first approximation even though heat transfer occurs between the stacked timber boards and the cross-circulating air. Only Reynolds number is considered in the dynamic similarity analysis.

The Reynolds number may also be unimportant in a kiln which has been streamlined to prevent boundary-layer separation, and which has high air circulation rates so that the influence of viscosity on the flow patterns becomes small, and the boundary layer at the wall is very thin. The possibility that the Reynolds number is unimportant is relevant in the next chapter when potential flow theory is used to determine the flow patterns through streamlined passages. However, the sharp-right angled bend in typical timber-drying kilns causes severe boundary layer separation. The dynamic similarity condition must be obeyed in this case because viscous effects become important in the separation zone. The dynamic similarity condition is mathematically expressed as

$$\left(\frac{Du}{\nu}\right)_{model} = \left(\frac{Du}{\nu}\right)_{prototype}$$

This formula allows the flow rate to be adjusted to suit the reduction in scale of the model and the change in viscosity of the working fluid. Thus, provided the Reynolds numbers are identical in each case, then the characteristics of the flow in a given system can be determined from observation of the corresponding characteristics in a model.

Applicability of the Similarity Condition

Dynamic and geometric similarity outside of the stack in the hydraulic kiln will ensure that the flow patterns in the ceiling space and plenum chambers will be similar qualitatively to the corresponding flow patterns in an industrial-scale kiln. However, the lack of geometric similarity within the stack, and the consequential underestimation of the dimensionless pressure drop across the stack, will result in accentuated flow maldistributions down the height of the stack in the hydraulic kiln. The effect of underestimating the pressure drop across the stack will be investigated in Part 2 of Chapter 6.

5.3 Experimental

Apparatus

The apparatus used in the water model study was a continuous flow, closed-circuit system with circulation provided by a centrifugal pump of 270 l/min rated capacity at 30 kPa gauge. Water was pumped from a large tank at ground level to an elevated tank approximately 4m above ground level, whose purpose was to provide a constant head of water to the hydraulic kiln (Figure 5.1). The water level inside the elevated tank was kept constant by an overflow which drained down to the large tank at ground level. The second outlet from the elevated tank directed the water flow, via a connecting pipe, to the hydraulic kiln. The flow through the hydraulic kiln was controlled by a valve placed on the outlet pipe of the kiln which drained the water into the ground level tank. The ground level tank was sized so that all of the water within the system could by contained within it when the apparatus was not in operation.

Both the ground level and elevated tanks had free liquid surfaces. A baffle arrangement was required within these tanks to prevent vortex motion of the flow which tended to entrain excessive amounts of air into the system. A removable gauze screen was inserted over the second outlet from the elevated tank for preventing the circulation of dust and other small particles which accidentally entered the system. Lids on both tanks also helped to minimise the introduction of foreign particles into the system.

The hydraulic kiln was made completely of Perspex which allowed photo, video, and visual observations of the flow. Baffles and guides could be installed within the hydraulic kiln by means of removable end plates on either side of the kiln. The widths of the inlet and outlet plenum chambers were adjustable. Due to the limitations involved in the hydraulic kiln design, the flow of water entered the kiln perpendicular to the direction which air normally flows in the ceiling space of a commercial box-shaped kiln. Therefore a flow straightener was employed to redirect the flow and to eliminate any swirling flows. A gauze screen was placed on the trailing edge of the flow straightener so that the intensity of turbulence was controlled. The equivalent average between-board air speeds ranged from 0 to 8 m/s at 400 K. This range of air

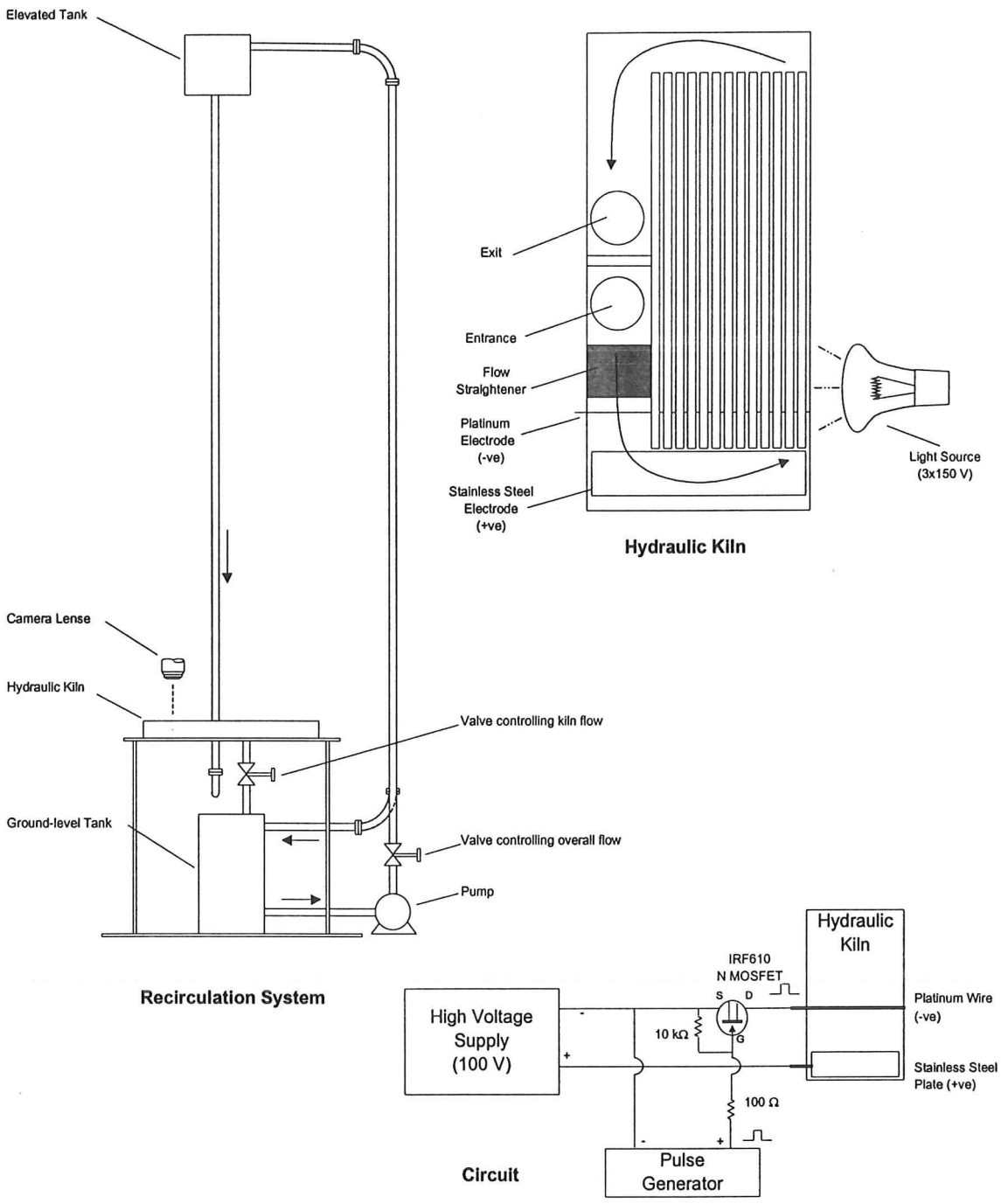

Figure 5.1. Schematic of the hydraulic kiln and recirculation system, and a circuit diagram for generating pulses of hydrogen bubbles on the platinum wire.

velocities covers the range used in industry for the high-temperature kiln drying of softwood boards.

When operating at the higher circulation rates, the water undergoes significant pressure changes which causes the release of cavitation-induced gas bubbles. The result is the introduction into the hydraulic kiln of a dispersion of fine bubbles which have close to zero buoyancy. The motion of the water through the hydraulic kiln is thus made apparent by these bubbles which follow the stream. These bubbles are not

able to rise to the free surfaces in the elevated and ground level tanks when the flowrates are high and therefore they remain within the circulation system. This is a convenient method by which the flow through the hydraulic kiln can be visualised qualitatively.

The velocities of the bubbles produced by cavitation at high flow rates were difficult to measure because they tended to be obscured by other bubbles from either above or below, making it difficult to distinguish one bubble from another. Furthermore, the quantity of bubbles per unit volume was very high which exacerbated this problem. Therefore, flow measurements could not be made at the higher flow settings. Cavitation-induced bubbles were eliminated when the flowrate was reduced sufficiently. A different tracer was required at these lower flow rates in order to measure the flow.

The hydrogen-bubble technique for tracer production was chosen due to its flexibility and ease of application. Hydrogen bubbles were formed on a fine platinum wire which was the cathode of a d-c circuit for electrolysing water. The anode was a stainless steel plate on which oxygen evolved, which was placed close to the platinum wire cathode. When a voltage was applied over these electrodes, hydrogen bubbles were produced on the platinum wire which were then swept from the cathode by the flowing water in the form of a continuous sheet. The bubbles were video-taped using a Sony Handycam camera, which operated at 24 frames per second, and the velocities were extracted by measuring the distances travelled by individual bubbles over a frame. The hydrogen-bubble method is explained in detail by Shraub *et al.* [1965].

Platinum wire 0.075 mm in diameter was stretched over the height of the hydraulic kiln so that it passed through every fillet space, and was normal to the mean flow direction in the fillet spaces. It was positioned 50 mm from the leading edge of the boards to minimise the entrance effects on the velocity distribution across each channel. An applied voltage over the electrodes of 100 V was found to be sufficient for producing an adequate number of bubbles. The quantity of bubbles generated on the wire was increased further by adding 0.15 g/l of sodium sulphate (Na_2SO_4) which improved the conductivity of the water (Shraub *et al.* [1965]).

The illumination of the gas bubbles at high and low circulation rates was achieved by means of three 150 W tungsten filament lamps. This light was projected through one side of the model so that the viewing direction was normal to the plane of the beam. A dark background was used, which sharpened the contrast of the bubbles, and all incident light other than that produced by the lamps was minimised.

Shraub *et al.* [1965] discusses the 'time-line' method for measuring the fluid velocity in which the voltage across the electrodes is pulsed with a known duration. The pulsing action generates blocks of hydrogen bubbles which follow the flow direction. The local velocities may be determined by measuring the length of these bubble blocks and dividing by the duration of the pulse. A pulse generator was included in the electrical circuit so that the average velocity across each channel could be measured using the 'time-line' method (Figure 5.1). However, the pulse generator did not have sharp enough on-off characteristics and therefore the length of each bubble block was difficult to determine. Thus, individual bubbles were tracked for flow measurement purposes.

A number of bubbles were tracked per channel so that the uncertainty in the flow measurement could be determined. Therefore, the severest errors were contained within this uncertainty. The greatest contribution to the error was caused by the boundary layer near the walls. Bubbles within the boundary layer travelled more slowly than bubbles outside of the boundary layer. The effect of the boundary layer on the flow measurement was minimised by tracking bubbles near the centre of the channel. Thus, the maximum velocities were measured in each channel. However, due to the high turbulence levels within the channel, many bubbles diffused across the width of the channel and entered into the boundary layer for a short time, before bouncing off the wall and moving back into the mainstream. This was unavoidable in the range of flowrates tested, and sometimes it was necessary to track one of these bubbles if no other bubble was available. Another similar source of error was caused by the bubble acceleration from a speed of zero at the platimum wire to the free stream velocity downstream of the wire. These sources of error were minimised by eliminating consecutive points in which there was a clear deceleration or acceleration of the bubble. A linear curve was then fitted by least squares to the remaining points, and the gradient of this curve was equal to the free-stream velocity.

The uncertainty in each measurement is defined by the expression

$$error = \pm t_{0.025,n-1} \frac{s}{\sqrt{n}}$$

where s is the standard deviation of the velocity distribution, n is the number of bubbles measured, and t is the distribution statistic (Montgomery [1991]). A number of bubbles were measured for each velocity measurement until the relative uncertainty fell to approximately 5% or less.

5.4 Discussion

Plenum-chamber Width

The flow patterns in the hydraulic kiln for various ratios r of the plenum space width to the sum of the fillet space widths are shown in Figure 5.2. For a large ratio (r=1.385), a large vortex is created near the upper boards in the inlet plenum chamber. The vortex zone extends about one ceiling space height past the bend in the plenum chamber, significantly constricting the mainstream cross section. Furthermore, the velocity field past the bend normal to the direction of flow is highly asymmetrical since the flow is deflected towards the outer wall. The vortex zone, and accordingly the non-uniform velocity field, decreases gradually with distance from the turn, however, its presence impacts on the entire flow distribution across the stack. As the space ratio r becomes smaller, the vortex shrinks in size.

The vortex zone which arises upon separation of flow from the outer wall of the right-angled bend is insignificant and does not affect the flow distribution across the stack. A similar vortex can be seen more clearly near the outward wall at the bottom of the hydraulic kiln (Figure 5.2).

Figure 5.3 shows the expected velocity profiles across the stack for different equivalent average air flow velocities of 1.0 to 4.2 m/s. The greatest non-uniformity of flow occurs in the top half of the stack near the major vortex zone, with the flow through the uppermost fillet spaces being considerably reduced. The upper-middle fillet spaces experience the highest flows due to the centrifugal forces induced in the 90-degree turn which tend to increase the velocity of the flow nearest to the centre of rotation. Thus, the higher velocity streams enter the upper-middle fillet spaces, and the lower velocity streams are directed toward the lower fillet spaces. This distribution of velocities normal to the direction of flow down the inlet plenum chamber will occur even if the major vortex zone was eliminated by using flow guides and baffles, because it results from the centrifugal forces generated in the right-angled bend.

The velocity gradient tapers to zero from the upper-middle fillet spaces to the lowest fillet space at the bottom of the hydraulic kiln which shows that the effect of the vortex zone diminishes in this direction. This also suggests that the combined inertial and frictional effects are negligible compared with the effect of the vortex in the plenum space configuration tested, because otherwise more significant gradients in the velocity profile near the lower fillet spaces would be apparent. Most timber drying kilns in industry are designed on the basis that all significant geometric ratios are close to unity. For example, the ratio of the plenum chamber width to the sum of the fillet space widths is close to unity, and the ratio of the plenum chamber width to the ceiling-space height is close to unity. Given that these ratios were set in the configuration used to produce Figure 5.3, then it is clear that inertial and frictional effects are unlikely to significantly affect flow uniformity in existing kiln designs. Therefore, only the vortex need be targeted when reducing flow maldistribution across a stack of timber boards in existing kiln designs. Inertial and frictional forces are negligible because when a geometric ratio of unity is applied to the major dimensions in a kiln, the plenum chamber is close to the infinite reservoir solution.

Inertial and frictional effects within the plenum chambers become less prominent when the pressure drop over the stack increases for a given flow rate and, therefore, the velocity profile across the stack becomes more uniform. Thus, underestimating the dimensionless pressure drop over the stack in the hydraulic kiln will result in accentuated velocity profiles especially in the lower half of the stack where the effect of the vortex zone is diminished and inertial and frictional effects are important. More uniform profiles can be expected in an industrial timber kiln. Therefore, the conclusion drawn in the previous paragraph, that inertial and frictional effects are unlikely to significantly affect flow uniformity in existing kiln designs, is justifiable even though geometric similarity does not exist between the stack in the hydraulic kiln and a timber stack in an industrial kiln.

When the average flowrate through the hydraulic kiln is increased, the general shape of the flow maldistribution is not affected; however, the profile becomes more peaky in the upper-middle fillet spaces; that is, the flow maldistribution worsens (Figure 5.3). The flowrate in the fifth fillet space from the top is about 1.8 times higher than the flow through the upper-most fillet space when applying a hydraulic velocity equivalent to an average air velocity of 4.2 m/s. Such difference in flowrates within industrial kilns would result in considerable variations in drying rates between rows of boards with subsequent variations in final moisture contents of the dried boards.

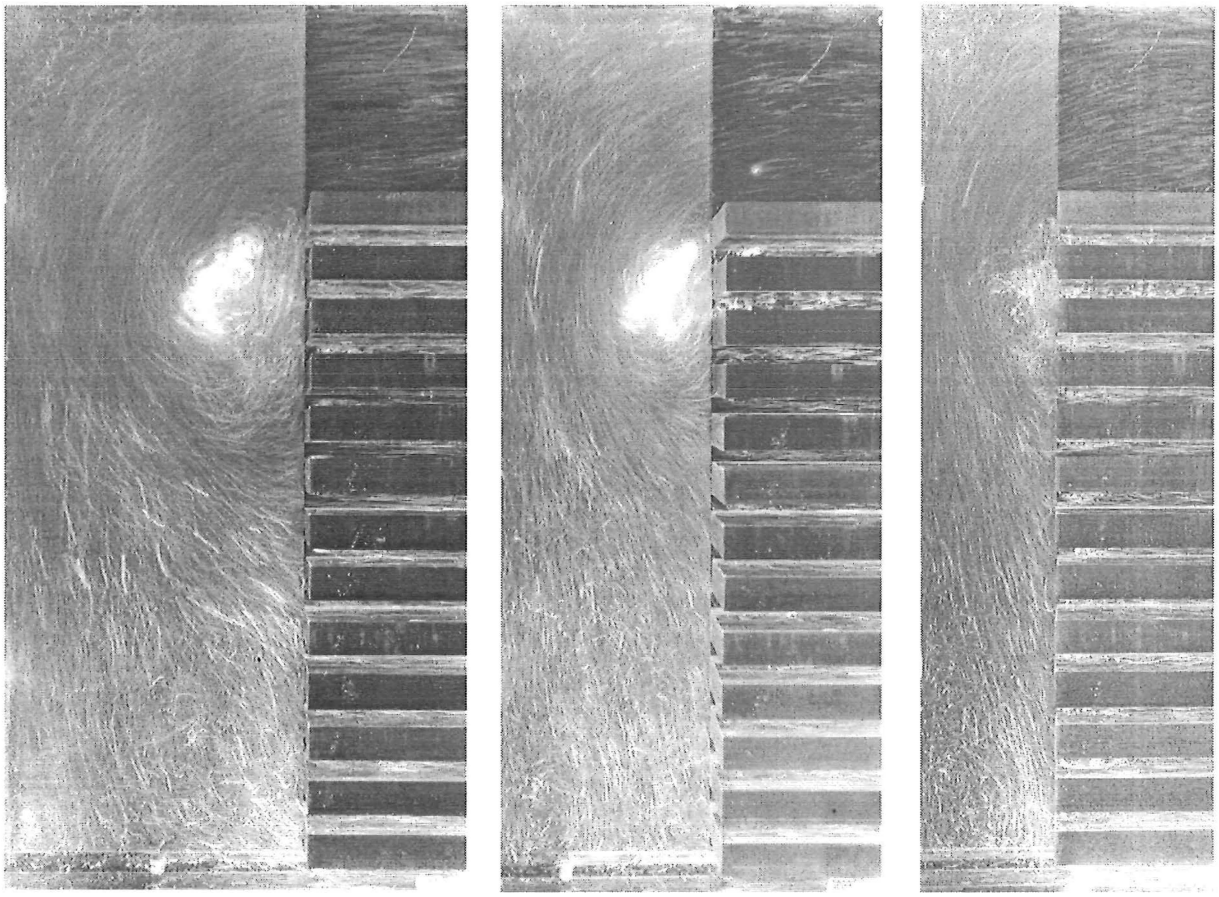

(a) r=1.385 (b) r=1.0 (c) r=0.615

Figure 5.2. Flow patterns in the hydraulic kiln for various ratios r of the plenum space width to the sum of the fillet space widths: equivalent average between-board air speed is 8 m/s at 400 K.

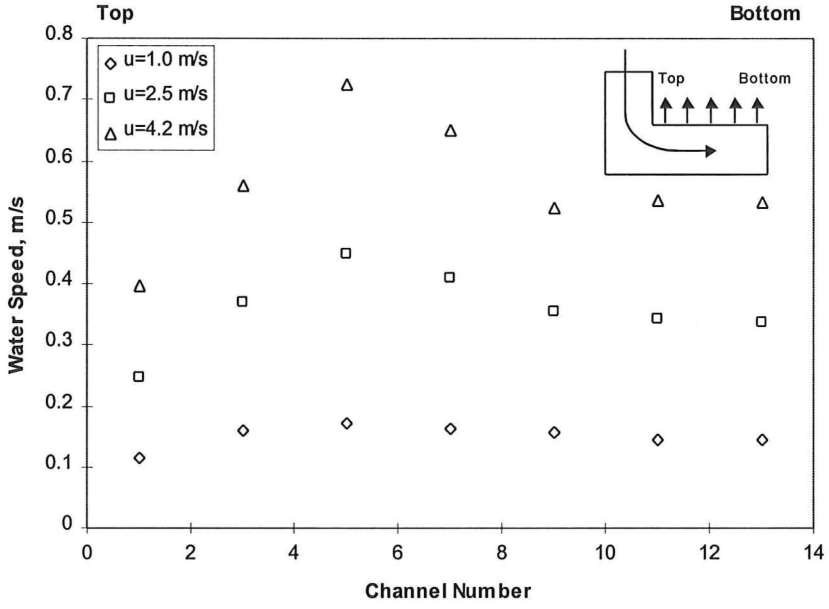

Figure 5.3. The effect of flowrate on the flow distribution across the stack (equivalent average between-board air speed calculated at 400 K): ratio of plenum-chamber width to sum of fillet space widths is unity (r=1).

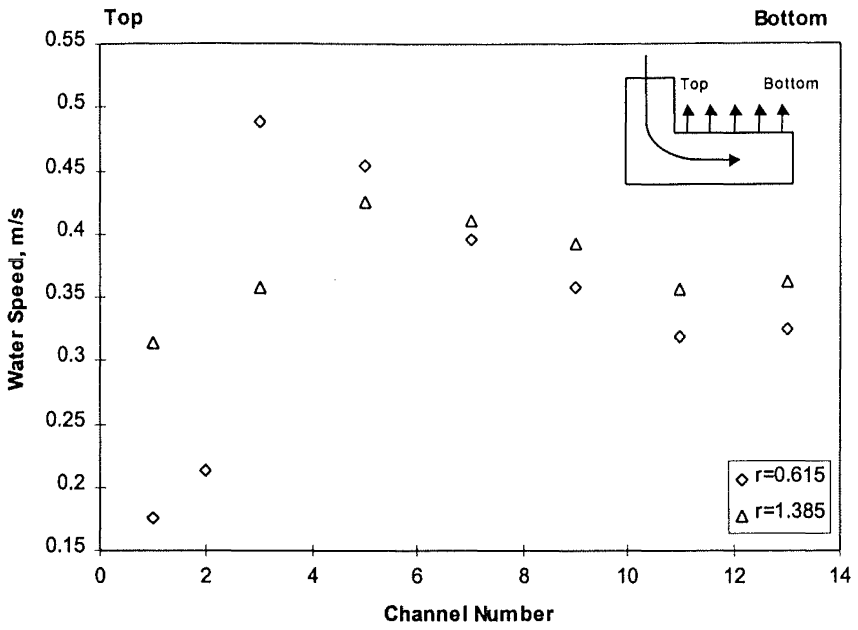

Figure 5.4. The effect of ratio *r* of plenum chamber width to sum of fillet-space widths on the flow distribution across the stack: equivalent average between-board air speed is 2.5 m/s at 400K.

When the equivalent air velocity is 1 m/s, this ratio of maximum and minimum between-board velocities is approximately 1.5. However, the advantage of more uniform flow distributions at lower average flowrates is offset by longer drying times.

The higher the ratio of the plenum-space width to the ceiling-space height, the greater the 'diffuser' effect and, consequently, the larger the separation zone. When the flow discharged from the right-angled bend is constricted, as in Figure 5.2c, the size of the separation zone shrinks and the velocity distribution across the width of the plenum chamber becomes more uniform. However, the strength of the vortex increases because higher flowrates are generated by the reduction in cross section, and therefore the flows through the uppermost fillet spaces become severely restricted, which results in even greater flows through the upper-middle fillet spaces. Furthermore, frictional effects become more prominent as the plenum-chamber width is reduced, which results in higher velocities in the upper-middle fillet spaces.

Figure 5.4 demonstrates the effect of the ratio of the width of the plenum space to the sum of the fillet-space widths on the flow maldistribution across the stack. Clearly, the narrower the plenum space, the more significant the flow maldistribution. This confirms the conclusions of Arnaud *et al.* [1991] that the ratio of the width of the plenum chamber to the sum of the widths of the fillet spaces should be at least equal to unity in order to minimise flow maldistribution. However, it is apparent from Figure 5.2 that the flow maldistribution cannot be entirely eliminated by increasing the width of the plenum space without some effort to remove the vortex zone, perhaps by installing flow guides and streamlining the right-angled bend.

If the length from the inner corner of the right-angled bend to the first fillet-space could be increased, then the vortex zone would move away from the stack, and therefore the effect of the vortex on the flow maldistribution across the stack would be

reduced somewhat. Figure 5.2 indicates that the vortex zone is approximately one ceiling-space height long which would be the minimum height required for this 'entrance length' into the plenum chamber. Figure 5.2 also shows that the width of the vortex zone diminishes as the width of the plenum chamber is reduced, and therefore the uniformity of flow across the plenum-chamber width improves. If the vortex zone could be moved away from the stack by introducing an entrance length, then it may be beneficial to set the ratio of the plenum-chamber width to the ceiling-space height to a value less than unity, so that the vortex zone would be reduced in size. This is likely to mitigate the effect of the vortex on the flow uniformity across the stack.

Reducing the width of the plenum chamber may also cause the inertial and frictional forces to become relevant which could have a detrimental affect on the flow uniformity. It should be pointed out that no matter how wide the plenum chambers, the inertial forces on one side of the stack will tend to counteract the inertial forces on the other side of the stack so long as the widths of the plenum chambers are equal. Assuming that the flow across the plenum width is evenly distributed, then flow uniformity across the stack is only affected significantly when the frictional forces become important, for example, when the plenum-chamber width is reduced notably which would result in higher velocities and, consequently, greater frictional effects. Figure 5.4 shows that a narrow plenum-chamber width results in steeper gradients in the velocity profile at the lower half of the stack, where the vortex zone has only a minor influence on the flow distribution, and the velocity profile across the width of the plenum chamber has become more uniform.

Flow Partitioner

The 'outer' streams, which are farthest away from the inlet face of the stack, have lower average velocities than the 'inner' streams due to the centrifugal forces induced in the right-angled bend which tend to reduce the magnitude of the fluid velocity away from the centre of curvature. The slower outer-streams are directed towards the lower portions of the stack, while the faster inner-streams flow towards the upper portions of the stack. A flow partitioner half of the stack height in length was placed within the plenum chamber (Figure 5.5). The partitioner was intended to prevent the faster streams from entering the upper-middle fillet spaces (channels 3 to 7), to significantly reduce the size of the vortex zone so that it affected considerably fewer or preferably none of the fillet space velocities, and to improve the uniformity of flow across the width of the plenum chamber.

Figure 5.5 shows that the vortex still exists when the flow partitioner is used, although the width of the vortex zone has shrunk. The effect of the partitioner on the distribution of flow across the stack can be seen in Figure 5.6. The flow distribution becomes more uniform from the fifth fillet space downwards; however, the flow through the uppermost fillet spaces becomes severely restricted. Introducing the flow partitioner appears to impress the vortex zone onto the side of the stack thereby restricting even further the flow into the fillet spaces adjacent to the vortex.

The even profile from the fifth fillet space downwards suggests that the non-uniformity in the velocity profile across the width of the plenum chamber is reduced significantly by the flow partitioner. Only Channel 3 is affected by the faster streams that are generated in the right-angled bend. However, it is clear that the flow

partitioner is useless to reduce flow maldistribution across the stack while the vortex has an influence over the flow patterns. Increasing the flow rate intensifies the strength of the vortex so that the flow is even more restricted in the uppermost fillets (Figure 5.7).

Ramp

A ramp was positioned in the ceiling space in order to move the vortex zone away from the stack so that the flows in the uppermost fillets were not restricted. Figure 5.8 shows that the vortex zone is significantly reduced in intensity; however, it has increased in size to encompass about two-thirds of the width of the plenum chamber, and three-quarters of the height of the stack. The ramp effectively constricts the flow in the ceiling space and, therefore, increases its velocity at the constriction. The consequential increase in momentum at the constriction ensures that the fluid is able to sustain its original direction along the ceiling space for longer than in the case when no ramp exists; therefore, the vortex zone is significantly larger. The high velocity stream near the outer wall persists down the height of the plenum chamber, and only begins to diverge about three-quarters of the way down.

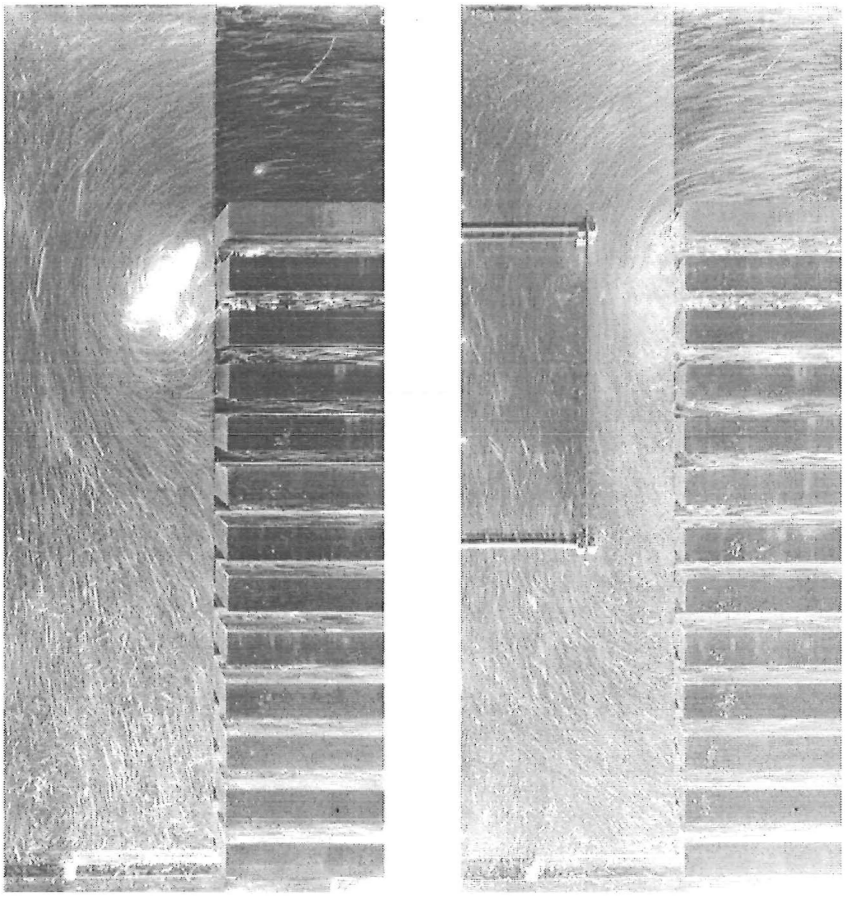

(a) no curtain

(b) curtains in inlet and outlet plenum chambers

Figure 5.5. Flow patterns in the hydraulic kiln with ratio of plenum space width to the sum of the fillet space widths with equal to unity: equivalent average between-board air speed is 8 m/s at 400 K.

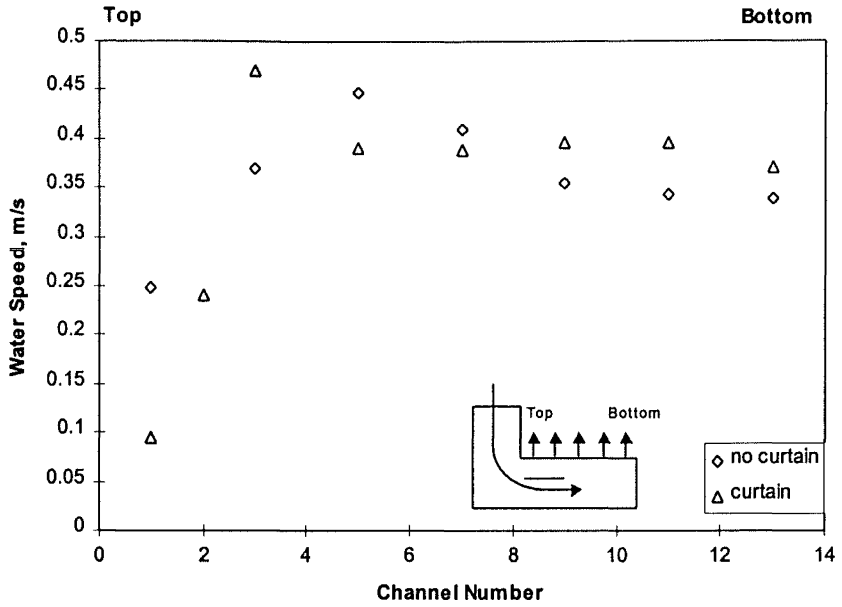

Figure 5.6. The effect of a curtain placed in the inlet and outlet plenum chambers on the flow distribution across the stack: equivalent average between-board air speed is 2.5 m/s at 400K; ratio of plenum-chamber width to sum of fillet space widths is unity (r=1).

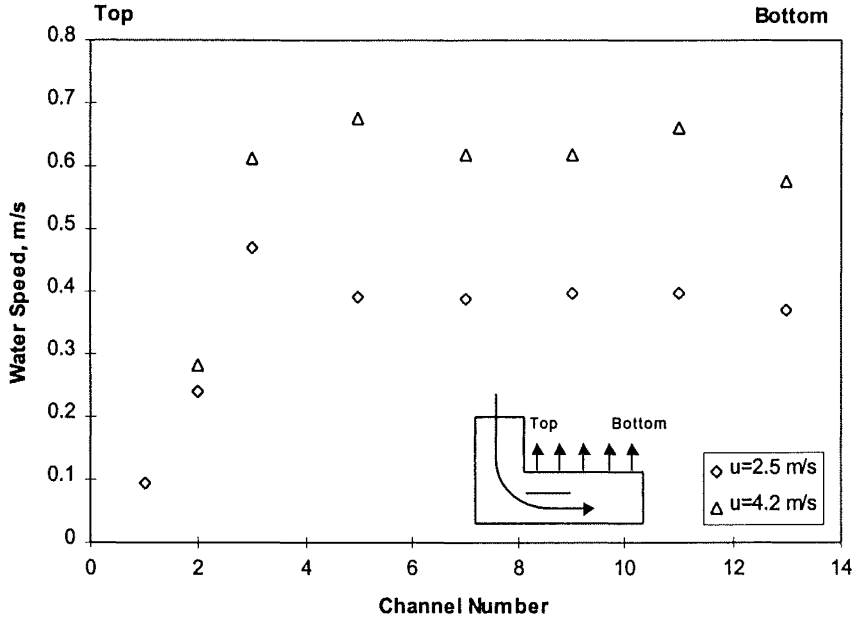

Figure 5.7. The effect of flowrate on the flow distribution across the stack (equivalent average between-board air speed calculated at 400 K): curtains placed in inlet and outlet plenum chamber; ratio of plenum-chamber width to sum of fillet space widths is unity (r=1).

Figure 5.9 shows that the flow maldistribution across the stack worsens with the use of the ramp. The flow through the uppermost fillets is reduced even further, and the velocity in the lower fillets in increased. There appears to be two distinct zones in the stack affected by different flow phenomena (Figure 5.10). The flow in the top half of the stack is influenced by the vortex zone, whereas the flow in the bottom half of the stack is influenced by the high velocity stream which is generated by the ramp, and which follows a path along the outside wall of the plenum chamber. Increasing the average flow rate accentuates the general shape of the flow distribution across the stack. The velocity distribution across the upper half of the stack is affected to a minor degree by an increase in the flow rate. However, the velocity through the lower portion of the stack is increased significantly because the increased flows bypass the upper half of the stack and are funnelled into the lower fillets.

Rounding the sharp corner of the ramp will help to reduce the degree of flow separation to a certain extent. However, the constriction effect on the flow, which causes an increase in the velocity and momentum of the fluid, and the oblique angle of the ramp will encourage the fluid to follow its original course along the ceiling space such that flow separation is unavoidable.

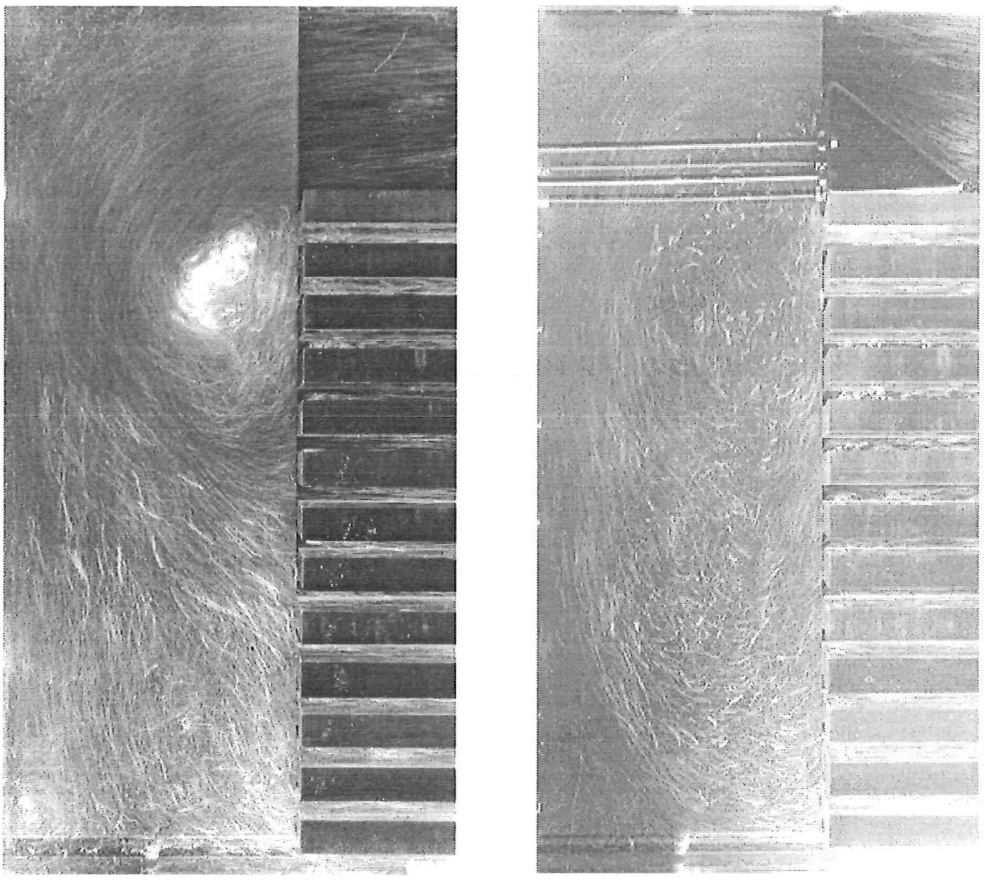

(a) no ramp (b) ramp

Figure 5.8. Flow patterns in the hydraulic kiln with ratio of plenum space width to the sum of the fillet space widths with equal to 1.385: equivalent average between-board air speed is 8 m/s at 400 K.

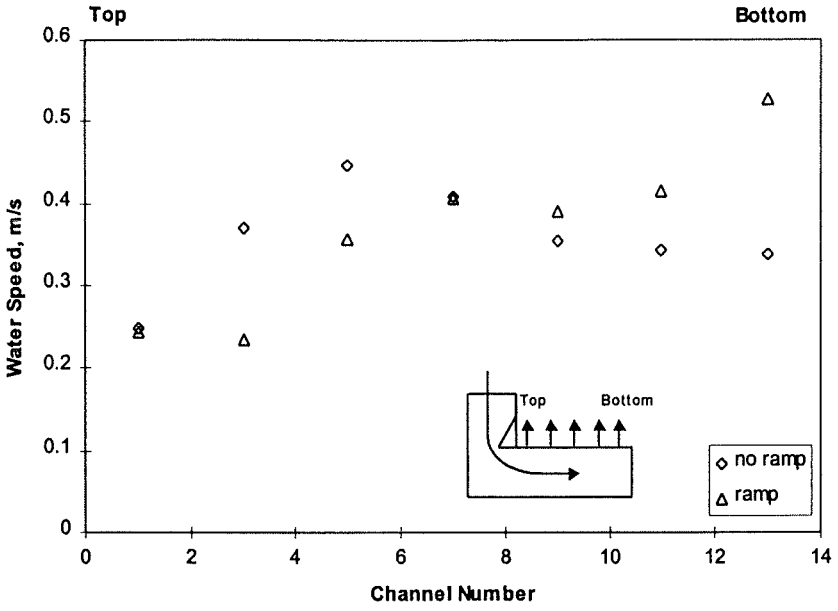

Figure 5.9. The effect of a ramp placed in the inlet ceiling space on the flow distribution across the stack: equivalent average between-board air speed is 2.5 m/s at 400K; ratio of plenum-chamber width to sum of fillet space widths is 1.385.

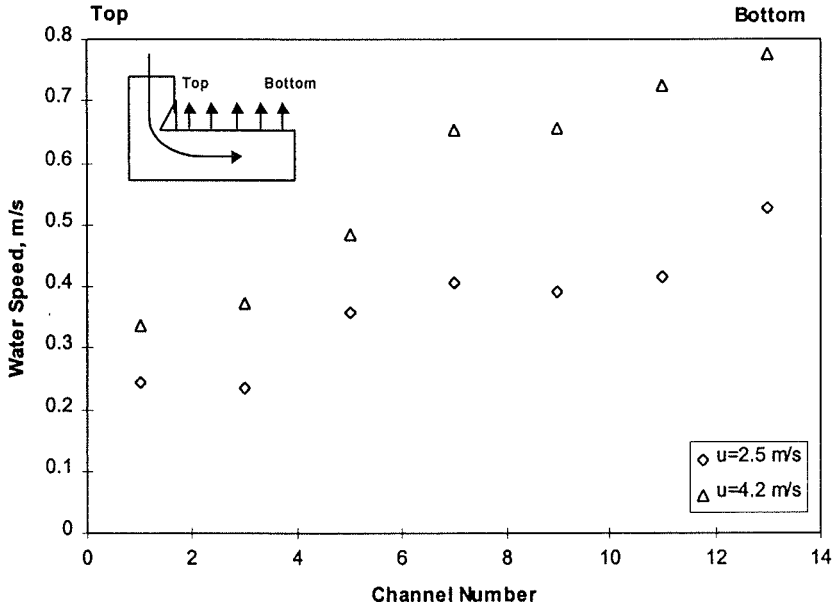

Figure 5.10. The effect of flowrate on the flow distribution across the stack (equivalent average between-board air speed calculated at 400 K): ramp placed in inlet ceiling space; ratio of plenum-chamber width to sum of fillet space widths is 1.385.

Curvature

Idelchik [1993] demonstrated that smoothing a sharp right-angled bend by rounding the inner corner significantly reduces the extent of flow separation and, consequently, improves the uniformity in the velocity distribution across the channel width downstream of the bend. In a timber kiln, a smoother transition from the ceiling space into the inlet plenum chamber should result in a more uniform velocity profile down the height of the stack. Round-sections were placed in the inlet ceiling space of the hydraulic kiln in an attempt to reduce the extent of flow separation at the right-angled bend (Figure 5.11). In each configuration shown in Figure 5.11, the width of the plenum chamber was set equal to the height of the ceiling space at the apex of the round-section. Thus, flow separation resulting from the 'diffuser' effect, in which the flow diverges as the cross-section through the transition increases, was avoided.

Separation of flow at the wall continues to persist when the sharp right-angled bend is smoothed with the addition of a small round-section (Figure 5.11a). The ratio c of the radius of the round-section to the maximum height of the ceiling space is too small to eliminate the vortex zone. Thus, an across-stack velocity distribution similar to the case in which no round-section is present can be expected. The vortex zone does not appear when the ratio c is increased to 0.2 (Figure 5.11b); however, flow separation still occurs, and the separation point is located at an angle of about 130° from the horizontal axis. The resultant separation zone, which has significantly lower flows than the mainstream, feeds directly into the uppermost fillet space thus reducing the flow though this fillet. The second fillet from the top is unaffected by the separation zone and, therefore, the flow through this fillet will not be reduced.

When the ratio c of the radius of the round-section to the maximum height of the ceiling space is increased to 0.3, then the extent of flow separation is reduced even further. The separation point is close to 180° from the horizontal axis, and the separation zone is less than half the width of the separation zone that occurs when the ratio c is 0.2. However, the separation zone continues to supply the uppermost fillet space with fluid. Therefore, a reduced flow will ensue through this fillet space, although the restriction in flow should not be as severe.

Figure 5.12 shows that rounding the corner of the right-angled bend has the effect of moving the peak velocity towards the uppermost fillet space and narrowing the distribution of flow down the height of the stack. The peak velocity is moved from the fifth fillet space to at least the third fillet space, and the ratio of the maximum velocity to the minimum velocity reduces from 1.8 to 1.3 when the right-angled bend is rounded.

Figure 5.13 shows the effect of the radius of the round-section on the distribution of flow across the stack. As the radius is increased, the flow distribution becomes less peaky and more even. The vortex zone is removed once the ratio c is greater than or equal to 0.2. However, the flow continues to separate at the corner, which reduces the velocity in the uppermost fillet space. The restriction becomes less pronounced as the radius of the round-section is increased. The trend shown in Figure 5.13 suggests that even when the radius of the round-section is increased sufficiently to completely eliminate flow separation, a distribution of velocities will still exist across the stack,

with the highest flow in the uppermost fillet space, and the lowest flow in the bottom fillet space. Frictional effects down the height of the plenum chamber are responsible for such an occurrence in the flow distribution. Uniform velocity profiles can only be achieved when the width of the plenum chamber (and correspondingly the height of the ceiling space) and the radius of the round-section are increased sufficiently.

In order to eliminate the diffuser effect in the right-angled bend, the ratio of the intake cross section (at the apex of the round-section) to the discharge cross section (or the width of the plenum chamber) remained constant at unity as the radius of the round-section increased. However, this resulted in the reduction of the ratio r of the plenum-chamber width to the sum of the fillet space widths. The ratio r decreased from 0.9 to 0.7 as the ratio c increased from 0.1 to 0.3. It has been shown above that the ratio r of

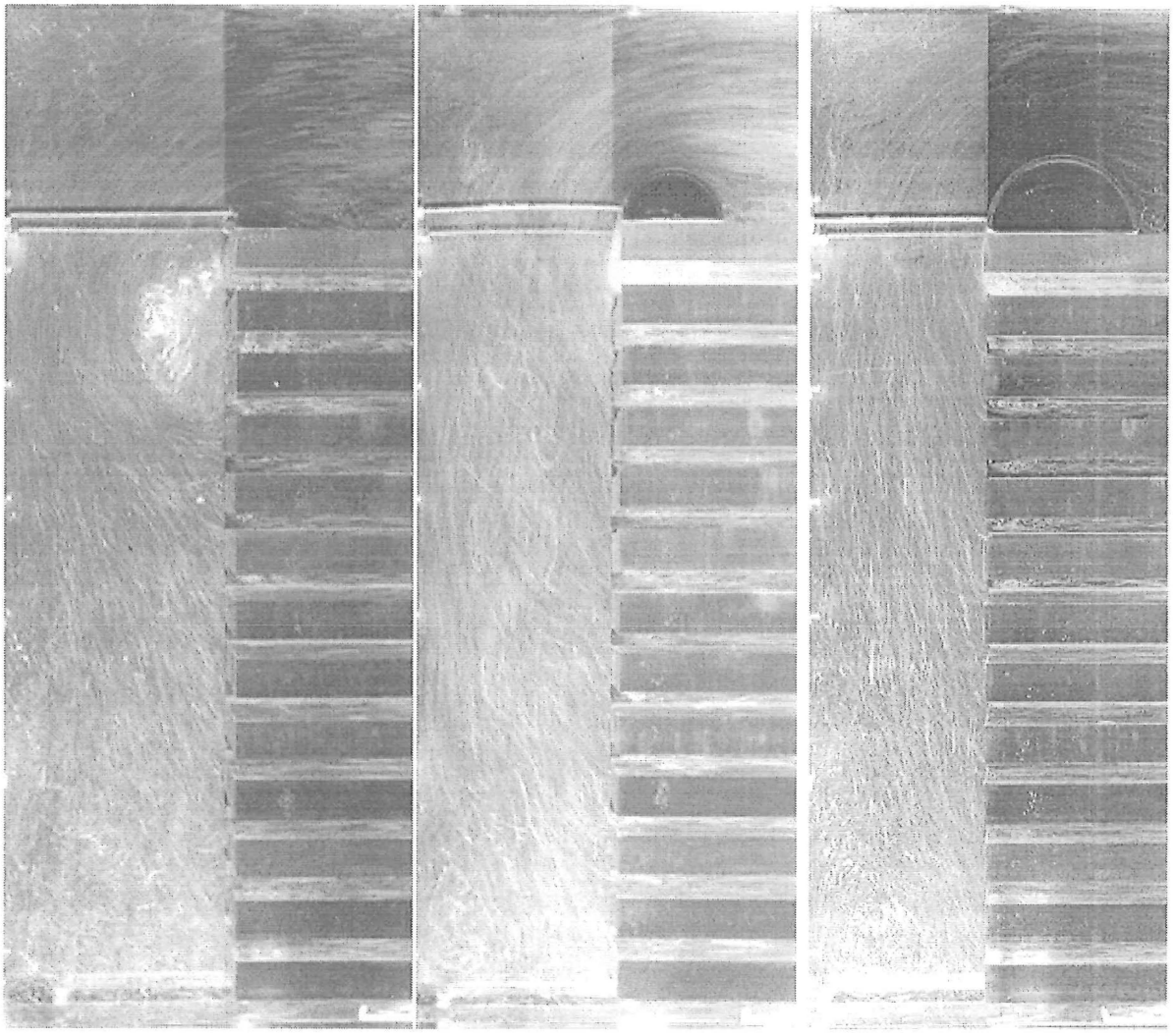

(a) c=0.1 (b) c=0.2 (c) c=0.3

Figure 5.11. Flow patterns in the hydraulic kiln for various ratios c of the radius of the curvature to the maximum height of the ceiling space: ratio of the width of the plenum chamber to the height of the ceiling space at the apex of the curvature equal to unity; equivalent average between-board air speed is 8 m/s at 400 K.

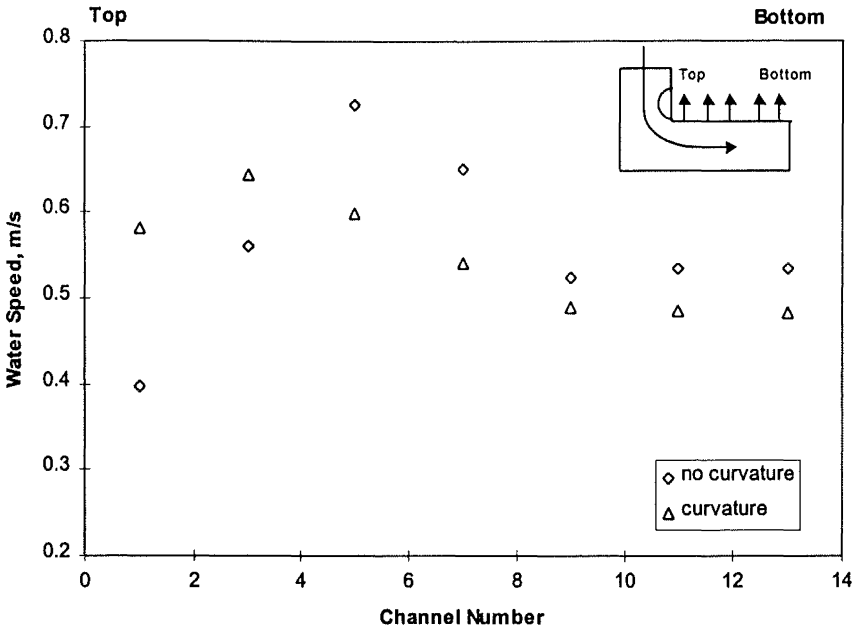

Figure 5.12. The effect of curvature in the inlet ceiling space on the flow distribution across the stack: equivalent average between-board air speed is 4.2 m/s at 400K; ratios *c* of the radius of the curvature to the maximum height of the ceiling space is 0.3; ratio of the width of the plenum chamber to the height of the ceiling space at the apex of the curvature equal to unity; ratio of plenum-chamber width to sum of fillet space widths is unity in the case with no curvature.

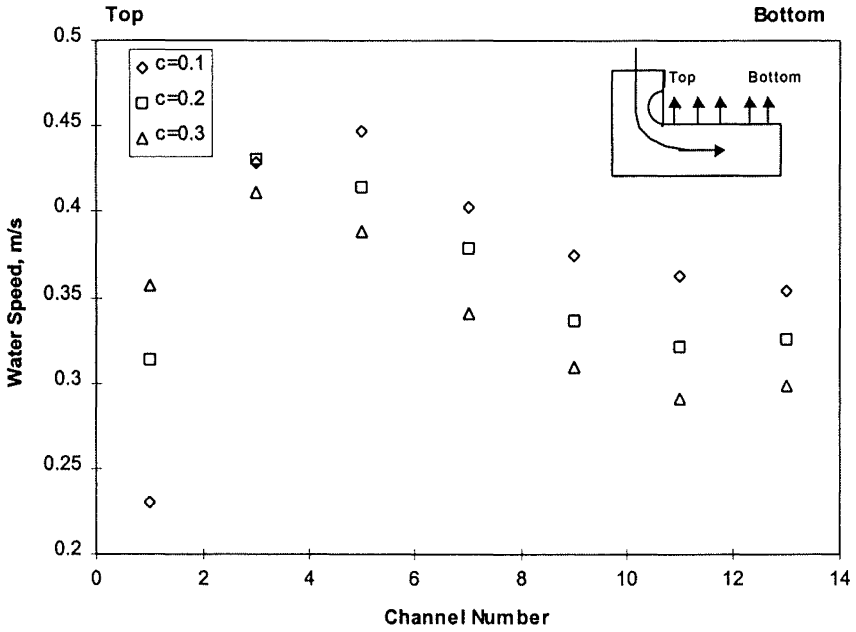

Figure 5.13. The effect of the ratio of the radius of the curvature to the maximum height of the ceiling space on the flow distribution across the stack: ratio of the width of the plenum chamber to the height of the ceiling space at the apex of the curvature equal to unity; equivalent average between-board air speed is 2.5 m/s at 400K.

the plenum-chamber width to the sum of the fillet space widths must be at least equal to unity for frictional and inertial effects to become negligible. The reduction of the ratio r below unity may explain why there appears to be no improvement in the uniformity of the velocity profile from the fifth fillet space downwards, even though the round-section increases in radius thus mitigating the influence of the separation zone. Clearly, the separation zone has the most significant affect on the top quarter on the stack, while the frictional and inertial effects down the height of the plenum chamber influence the remaining portion of the stack. Frictional and inertial effects can be mitigated by increasing the width of the plenum chamber so that the ratio r is at least equal to unity.

Figure 5.14 shows the effect of increasing the average velocity through the stack on the flow distribution across the stack when the ratio c of the radius of the round-section to the maximum height of the ceiling space is 0.3. The peak in the distribution becomes slightly more prominent as the flow rate is increased. Otherwise, there does not appear to be a significant difference between the profiles which suggests that flow maldistribution is not strongly affected by the flow rate when the vortex zone is eliminated. Figure 5.3 shows that when the round-section is not used, then there is a clear accentuation of the distribution of velocities as the flow rate is increased. The strength of the vortex zone generated by a sharp right-angled bend is strongly affected by the flow rate; thus, flow maldistribution across the stack is likewise affected by the flow rate. Introducing the round-section reduces the influence of the flow rate on the velocity distributions across the stack.

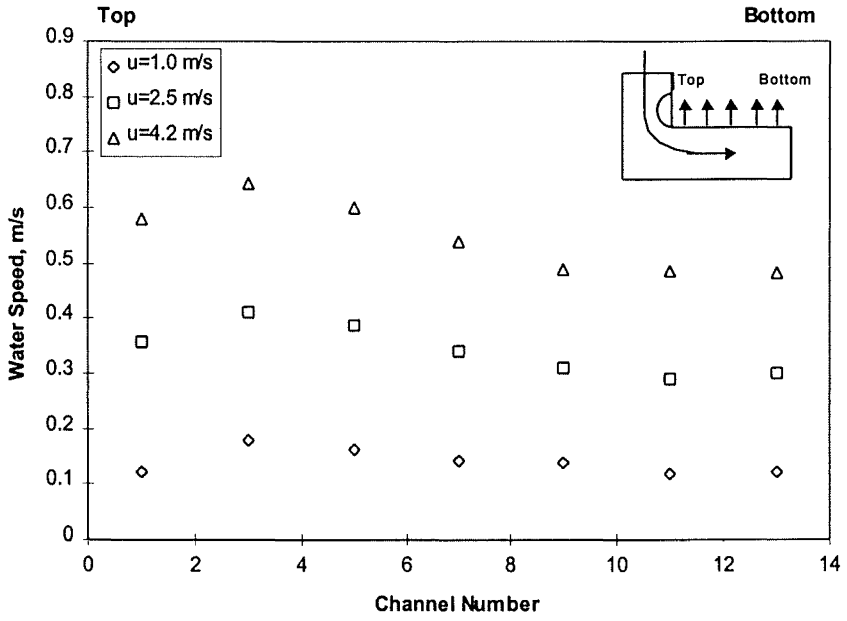

Figure 5.14. The effect of flowrate on the flow distribution across the stack (equivalent average between-board air speed calculated at 400 K): ratios c of the radius of the curvature to the maximum height of the ceiling space is 0.3; ratio of the width of the plenum chamber to the height of the ceiling space at the apex of the curvature equal to unity.

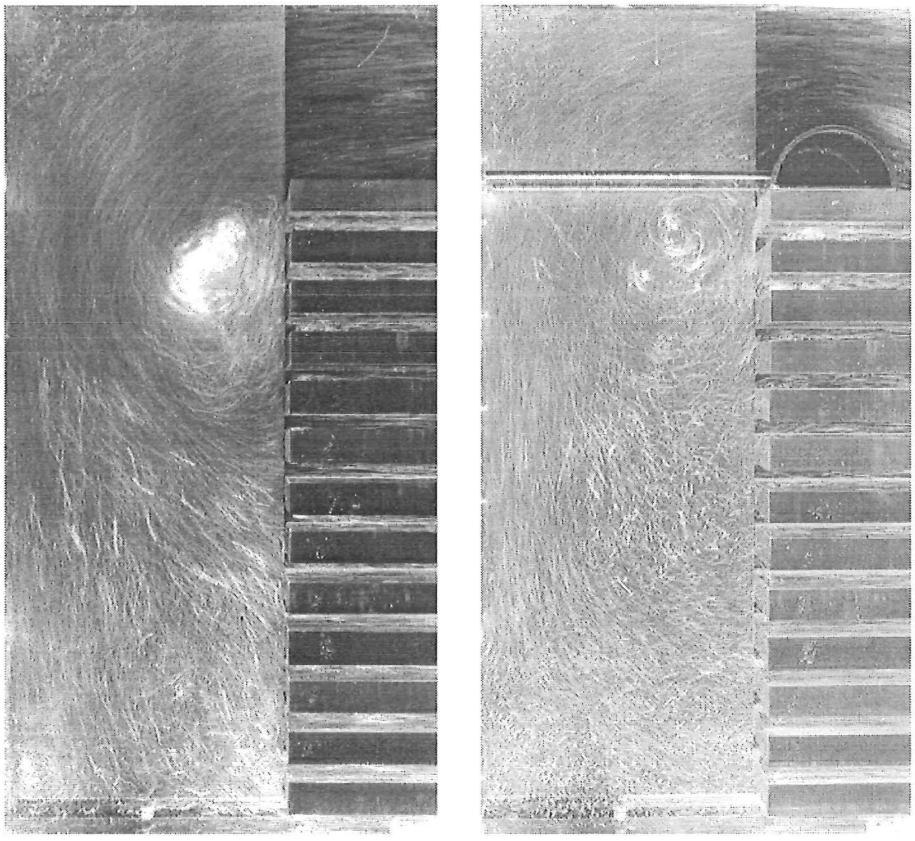

(a) no curvature (b) curvature

Figure 5.15. Flow patterns in the hydraulic kiln with ratio of plenum space width to the sum of the fillet space widths with equal to 1.385: equivalent average between-board air speed is 8 m/s at 400 K.

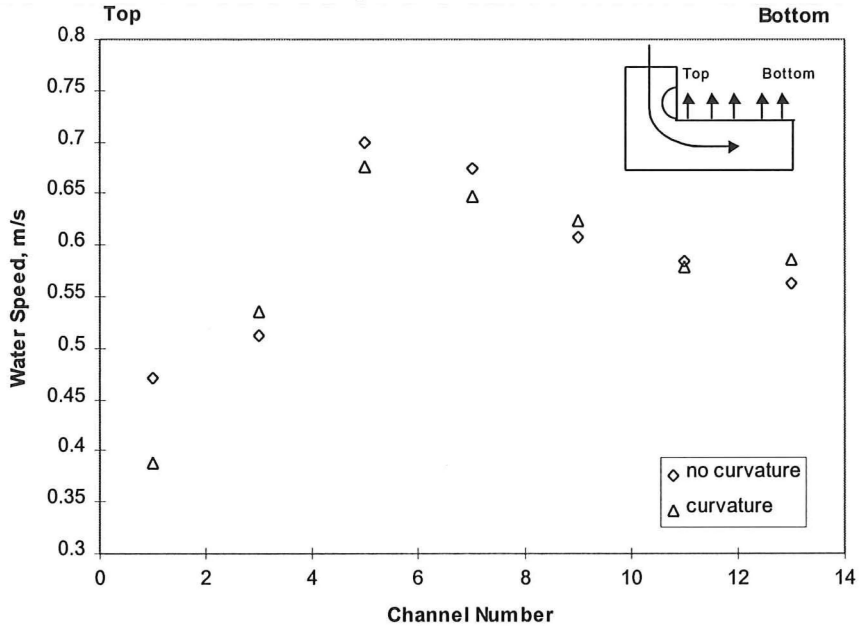

Figure 5.16. The effect of curvature in the inlet ceiling space on the flow distribution across the stack: equivalent average between-board air speed is 4.2 m/s at 400K; ratio of plenum-chamber width to sum of fillet space widths is 1.385.

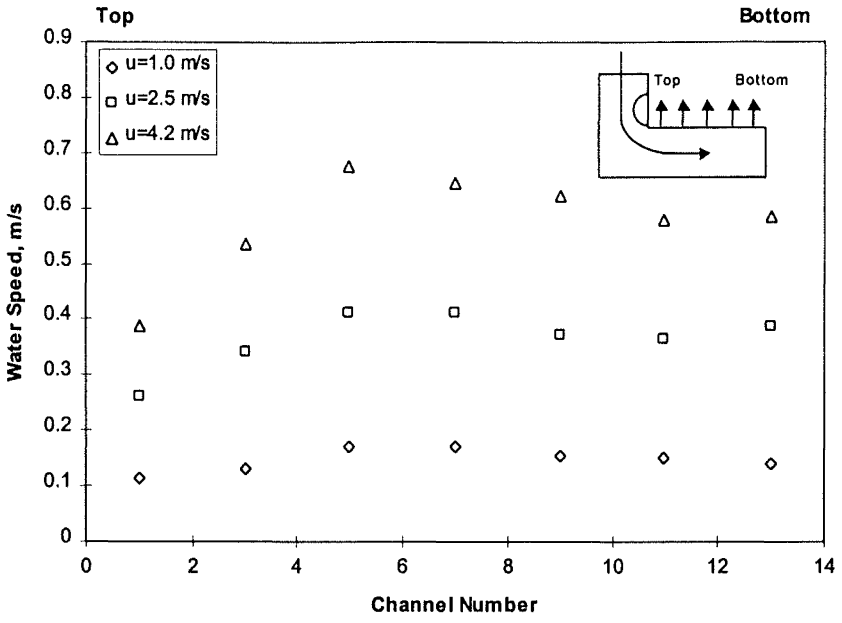

Figure 5.17. The effect of flowrate on the flow distribution across the stack (equivalent average between-board air speed calculated at 400 K): curvature placed in inlet ceiling space; ratio of plenum-chamber width to sum of fillet space widths is 1.385.

Figure 5.15 shows that the vortex zone is not eliminated when the ratio of the width of the plenum chamber to the height of the ceiling space at the apex is greater than unity. The higher the ratio of the discharge to intake widths, the greater the diffuser effect, and consequently the larger the separation zone. Thus, the velocity distribution across the width of the plenum chamber downstream of the turn is a function of the degree of expansion of the right-angled bend. Rounding the section has very little influence on the severity of flow maldistribution across the stack when an expansion in the cross-section occurs. In fact, the flow maldistribution appears to worsen when the corner is rounded (Figure 5.16). The round-section reduces the height of the ceiling space, which increases the flow rate at the constriction. The fluid is able to resist a change in direction for longer as it travels along the ceiling space due to the increase in momentum which is induced by the constriction. Thus, the size of the vortex zone increases and the flow through the uppermost fillets is reduced.

Figure 5.17 demonstrates the advantage to be gained from increasing the width of the plenum chamber so that the ratio r is at least equal to unity. In Figure 5.17, r was set to 1.385. A comparison between these velocity profiles and the velocity profiles presented in Figure 5.3, in which r was set to unity, shows that the gradient in the velocity profile at the bottom half of the stack is not as steep when r is 1.385. Inertial and frictional effects become less significant when the width of the plenum chamber is increased sufficiently.

General Observations

Many of the photographs show clear streamlines through the ceiling space and plenum chamber, which suggests that the fluid motion is mostly two-dimensional in nature. Some of the photographs show flow patterns near the bottom of the plenum

chamber that are more difficult to follow. In these photographs, the streamlines, which can be clearly seen near the top of the plenum chamber, lose their identity as they approach the bottom of the plenum chamber, and it appears as if the flow direction becomes random. This implies that the level of turbulence has increased and therefore motion in the third dimension has become significant. In fact, three-dimensional motion was observed through the end plates of the hydraulic kiln. A weak vortex could be seen near the bottom of the plenum chamber, which was generated by fluid being deflected back up the plenum chamber after hitting the floor. Three-dimensional fluid motion near the bottom of the plenum chamber is unlikely to significantly affect the flow distribution across the stack since the velocity in this area is very low.

5.5 Conclusions

The presence of the vortex within the inlet plenum chamber has a major effect on the flow maldistribution across the stack. No plenum chamber configuration can completely eliminate the effect of this vortex which forces more fluid through the upper-middle boards and severely retards the flow through the uppermost boards. Streamlining techniques, involving the use of curved-sections in the ceiling space, may be used to remove the vortex thereby improving the flow uniformity across the stack, although the vortex can be moved away from the stack by introducing an entrance length into the plenum chamber.

It has been shown that two conditions must be met in order to eliminate the vortex zone using round-sections in the ceiling space. Firstly, the radius of a round-section must be at least equal to one-fifth of the height of the ceiling space. Secondly, the width of the plenum chamber must be less than or equal to the height of the ceiling space height at the apex of the round-section. The magnitude of the flow rate has very little effect on the uniformity of flow across the stack provided the vortex zone has been eliminated. The analysis shows that inertial and frictional effects are unlikely to contribute significantly to flow maldistribution in a kiln in which the plenum chamber width is greater than or equal to the sum of the fillet space widths.

5.6 References

Arnaud, G., Fohr, J.P., Garnier, J.P., Ricolleau, C., 1991, Study of the air flow in a wood drier, *Drying Technology*, 9 (1):183-200.

Charm, S.E., 1963, The fundamentals of food engineering, The AVI Publishing Company, Inc., Westport, Connecticut.

Idelchik, I.E., 1991, Fluid dynamics of industrial equipment: flow distribution design methods, Hemisphere Publishing Corporation, New York.

Kröll, K., 1978, Trockner und Trocknungsverfahren, 2nd edition, Springer-Verlag, Berlin, Heidelberg, New York.

Langrish, T.A.G., Keey, R.B., 1996, The effects of air bypassing in timber kilns on fan power consumption, 24th Australian and New Zealand Chemical Engineering Conference (CHEMECA '96), Sydney, 103-108.

Montgomery, D.G., 1991, Design and analysis of experiments, 3rd edition, John Wiley & Sons, New York.

Shraub, F.A., Kline, S.J., Henry, J., Runstadler, P.W., Littell, A., 1965, Use of hydrogen bubbles for quantitative determination of time-dependant velocity fields in low speed water flows, *ASME J. Basic Eng*, 87:429-444.

Sturany H., 1952, Questions of flow in the drying of wood, *Holz als Roh-und Werkstoff*, 10 (5): 201-207.

Werner, H., 1958, Methods of air and heat distribution in convective dryers, *Chem. Ing. Techn.*, 44 (8): 570-576.

Wu, Q., 1989, An investigation of some problems in drying of Tasmanian Eucalypt timbers, M. Eng. Sci. Thesis, University of Tasmania at Hobart.

CHAPTER SIX

THEORETICAL MODELS OF FLOW

The experimental investigation of the previous chapter illustrated the effect of asymmetric velocity profiles across the width of the inlet plenum chamber, and frictional and inertial effects down the height of the plenum chamber, on the uniformity of flow across the stack. The geometric ratios of the important spatial dimensions in the kiln were explored in an attempt to improve significantly the uniformity of flow across the stack of boards. In addition, distribution devices were employed to reduce the extent of boundary-layer separation at the corner of the right-angled bend.

In this chapter, theoretical methods will be used to confirm some of the conclusions drawn in the previous chapter, and to develop further criteria for improving the non-uniformity of flow across the stack. In Part 1, potential-flow solutions through streamlined right-angled bends and contractions will be investigated, and recommendations on the entrance length to the inlet plenum chamber will be made. In Part 2, a one-dimensional flow model of a kiln will be used to determine the width of the plenum chamber that reduces flow maldistribution across the timber stack.

6.1 Part 1: Potential-Flow Solutions

Uniformity of airflow is an important consideration in the drying of stacked timber boards in kilns because it governs the homogeneity of drying across the stack. Flow maldistribution across the stack leads to variations in drying rates between timber boards and, therefore, different times for drying these boards to the desired moisture content. Consequently, a stack of dried timber boards may acquire a distribution of final moisture contents, which can result in differential shrinkage of the timbers while they are in use.

In the previous chapter, it was shown that a significant contribution to flow maldistribution across a stack of boards is the vortex generated by the sharp right-angled bend from the ceiling space into the inlet plenum chamber. The vortex is located close to the uppermost boards of the stack and is approximately one ceiling-space height in length, and varies in width depending on the width of the plenum chamber. Fluid flow into the uppermost fillets is severely retarded by the blocking action of the vortex, and consequently, the flow through the upper-middle fillets is increased. The most effective method for controlling the vortex zone is to smooth sufficiently the sharp edges off the right-angled bend. This will reduce the severity of flow separation at the corners of the bend with a subsequent improvement in the velocity distribution across the plenum-chamber width downstream of the bend.

Even if the vortex is eliminated, the centrifugal forces experienced by the fluid as it turns 90 degrees in the right-angled bend, are likely to cause non-uniformity of flow over the width of the plenum chamber with subsequent flow maldistribution across the stack. An entrance length may be beneficial, between the right-angled bend and the top of the timber stack, to allow the flow to become uniformly distributed across the width of the plenum chamber. Estimation of this entrance length requires knowledge of the flow fields in the right-angled bend.

Potential flow theory may be used to find analytical expressions for the flow fields in simple polygonal flow domains. This theory is based on the assumption that the fluid is inviscid so that it experiences no shearing stress, and fluid particles in contact with the walls slip tangentially along the walls without resistance. In a real fluid, shearing stresses are always present and the fluid particles in contact with the walls adhere to it and have no tangential motion along it. However, potential flow theory may be used with reasonable accuracy to determine flow fields around streamlined objects and in converging passages especially when the Reynolds number is reasonably high (Valentine [1959]).

Assumptions

A number of assumptions must be specified before potential flow theory can be used to approximate the flow patterns in a kiln. One important assumption is that no boundary-layer separation occurs at the boundaries of the flow domain. The unknown form of the zones of separation, which can involve large vortices in the worst case, prevents the use of potential flow theory to approximate flows in which boundary-layer separation occurs. Boundary-layer separation can be avoided when the following conditions are satisfied:

a) The shape of the flow boundaries must be such that the streamlines converge in the direction of flow. Diverging streamlines generate adverse pressure gradients with subsequent boundary-layer separation.

b) The corners at abrupt changes in cross-section and direction must be rounded (or streamlined) sufficiently to eliminate boundary-layer separation.

These conditions echo the results found in Chapter 5; it was shown that the separation zone is reduced to a negligible thickness when the right-angled bend is rounded sufficiently, and the width of the plenum chamber is less than or equal to the height of the ceiling space.

Another important assumption is that the viscosity of the fluid is relatively low so that the flow in the mainstream (outside of the boundary layer) is irrotational, or inviscid. Air and water, which are the fluids used in kiln drying and the hydraulic model described in the previous chapter, have relatively low viscosities. Valentine [1959] reports that these fluids can be approximated as irrotational in the mainstream.

The mainstream flow pattern is determined primarily by the boundary-layer form. Therefore, it is also important that the Reynolds number is relatively high so that the boundary layer at the wall has a very small thickness. Thus, the presence of the

boundary layers will not change significantly the geometry of the flow domain in which irrotational flow occurs from the flow domain defined by the solid boundaries. Fortunately, the Reynolds number in the ceiling space and plenum chamber of an industrial-scale kiln is relatively high due to the low viscosity of the working fluid and the high air speeds generated by the fans.

The assumption that no flow separation occurs is fairly severe and is only valid in streamlined, convergent passages. However, it is impractical to construct a right-angled bend with solid boundaries that follow exactly the streamlines calculated using potential flow theory. The round-section presented in the previous chapter is a more realistic design. Furthermore, there is no guarantee that flow separation will not occur when two streamlines, calculated from potential flow theory, are used as the solid boundaries of a streamlined right-angled bend. The extent of flow separation can be significantly reduced when the boundaries of the right-angled bend are smoothed sufficiently. However, a certain degree of flow separation is unavoidable because right-angled bends, by the nature of their geometry, must diverge (and converge) along the passage. Nevertheless, the potential flow solutions may be used to provide criteria for the minimum entrance length required for improving the uniformity of flow across the width of the plenum chamber. Right-angled bends, in which boundary-layer separation occurs, will require longer entrance lengths to mitigate the effects of the separation zones.

Scope

It is the aim of Part 1 to find analytical expressions for streamlines around a sharp right-angled bend using potential flow theory. The velocity distribution across the width of the plenum chamber can then be calculated at various points downstream of the right-angled bend, and therefore a plenum chamber entrance length can be designed.

Since, by definition, there is no flow across a streamline, one can substitute a solid surface for any given streamline without a change in the flow pattern. Therefore, if streamlines through a right-angled bend can be determined, then the corner can be streamlined, using the criterion for the minimum radius of curvature found in the previous chapter, to promote uniform flow and eliminate the vortices near the inner and outer walls. Thus, the secondary purpose of this section is to present equations for streamlines (determined analytically) which could be used to make up the solid boundaries of a smoother right-angled bend. Some current kiln designs use a contraction along the ceiling space from the fan to the right-angled bend. Thus, streamlines are also presented for flow through a suddenly contracting channel so that contoured contractions may be designed. It is realised that such streamlined transitions would be difficult to put into practice. However, these complex transitions could be used as the basis of more easily manufactured transitions involving straight-line segments.

6.1.1 Theory

Potential-Flow Theory

The following section summarises the concepts and mathematics involved in potential flow theory which Milne-Thomson [1960], Vallentine [1959], Plapp [1968] and Hildebrand [1976] discuss in detail.

The velocity field of an ideal flow, or equivalently a potential flow, is completely determined by two important kinematic considerations - the fluid is non-divergent or incompressible, and the fluid has no vorticity or is irrotational (or inviscid). The term divergent implies that the velocity distribution tends to separate parcels of particles at a point. Mathematically, divergence is expressed as the dot product of the velocity vector and the gradient operator. If the fluid is incompressible, then the divergence becomes zero unless there is a source of fluid at that point:

$$divV = \nabla.V = 0 \qquad \text{(incompressible flow)}$$

Vorticity characterises the tendency of parcels of particles that make up the fluid to rotate about their centres. It is associated with the rotation of the parcel and not with the rotation of the flow field. Therefore, it is possible to have a curving flow with a velocity distribution such that parcels will move along the curved path, but will not rotate. Mathematically, vorticity is expressed as the cross-product of the velocity vector and the gradient operator, or equivalently, vorticity is the curl of the velocity vector. Only when the vorticity is zero at all points in a domain is the flow field called irrotational (or inviscid):

$$curlV = \nabla \times V = 0 \qquad \text{(irrotational flow)}$$

In potential flow theory, the 'potential' is a scalar field variable which when differentiated yields the velocity field. Thus, when the scalar potential field is known, the velocity field is also known. If φ is the scalar potential function, then the velocity vector in two dimensions may be written

$$V = V_x i + V_y j = \frac{\partial \varphi}{\partial x} i + \frac{\partial \varphi}{\partial y} j = \nabla \varphi \qquad (6.1)$$

The divergence and curl of the velocity vector are defined by the following expressions

$$\nabla.V = divV = \left(\frac{\partial \varphi}{\partial x} i + \frac{\partial \varphi}{\partial y} j\right).\left(\frac{\partial}{\partial x} i + \frac{\partial}{\partial y} j\right) = \frac{\partial^2 \varphi}{\partial x^2} + \frac{\partial^2 \varphi}{\partial y^2} \qquad (6.2)$$

$$\nabla \times V = curlV = \begin{vmatrix} \frac{\partial}{\partial x} & \frac{\partial}{\partial y} \\ \frac{\partial \varphi}{\partial x} & \frac{\partial \varphi}{\partial y} \end{vmatrix} = \frac{\partial^2 \varphi}{\partial x \partial y} - \frac{\partial^2 \varphi}{\partial y \partial x} = 0 \qquad (6.3)$$

It is assumed that the flow through the domains dealt with in this paper is irrotational and therefore, the curl of the velocity vector is zero. Equation (6.3) shows that assuming irrotational flow implies that a scalar potential field exists such that $V = \nabla\varphi$ (Equation (6.1)). Therefore, from Equation (6.2) and assuming that the flow is incompressible, the following expression may be derived:

$$\frac{\partial^2\varphi}{\partial x^2} + \frac{\partial^2\varphi}{\partial y^2} = 0 \qquad (6.4)$$

This equation is known as Laplace's equation. Thus, it has been shown that if a flow is assumed to be irrotational and incompressible, then the velocity vector is the gradient of the scalar function φ, called the velocity potential, and that φ satisfies Laplace's equation.

The solution of Equation (6.4), which satisfies the appropriate boundary conditions of the region considered, yield equipotential lines given by equations of the form

$$\varphi(x,y) = c$$

as c takes on successive constant values.

There exists another potential function for determining the velocities, called the stream function ψ. This is a function that also yields the velocity field under differentiation but is independent of the potential function φ. Solution of Laplace's equation for the stream function gives streamlines of the form

$$\psi(x,y) = d$$

which are normal to the equipotential lines. Different values for the coefficient d define different streamlines. Streamlines are a powerful graphical representation of the two-dimensional flow field. For example, one property of streamline flow patterns is that the streamline spacing varies inversely with the velocity, so that relatively narrow spacings indicate relatively high velocities. Thus, streamlines converging in the direction of flow indicate an increase in velocity with respect to distance. Another property of streamlines is that they are tangential to the velocity vector at all points and, therefore, there are no components of velocity normal to streamlines; that is, there can be no flow across the streamlines. Consequently, a solid boundary can replace a streamline without any change in the flow pattern provided the flow is irrotational.

Conformal Mapping

It is possible to solve boundary-value problems for Laplace's equation (Equation (6.4)) with the aid of a technique known as conformal mapping. This approach involves solving a simpler related problem in a certain complex plane (w-plane), and then transforming the solution back to the complex plane where the actual flow field is required (z-plane). In this mapping, a point in the z-plane which has real and imaginary parts (x and y) of the independent variable z, corresponds to a point in the

w-plane which has real and imaginary parts (u and v) of the dependant variable w. The relationship between the two planes is $w = f(z)$ where $w = u + iv$ and $z = x + iy$.

A unique solution is normally required of solutions to physical problems and therefore the mapping between the planes must be one-to-one. Mapping one-to-one implies that two distinct points in the z-plane are never mapped to the same point in the w-plane. Therefore, u and v are single-valued functions of x and y. As well as the requirement that the mapping be one-to-one, the relative angles and shape must be preserved in the mapping; that is, the mapping must be conformal.

Many boundary-value problems that arise in practice require the solution of Laplace's equation in a region bounded by a simple polygon: for example, ideal flow around a right-angled bend. The Schwarz-Christoffel transformation can be used to transform polygonal boundaries in the z-plane to the real axis in the w-plane, with the interior of the polygon mapping conformally and one-to-one to the upper half of the w-plane. This same mapping relation will transform the points along the equipotential lines and streamlines in the z-plane to their corresponding points in the w-plane. If a solution of Laplace's equation, which takes on these values, can be found in the w-plane, this solution can be transformed back into x-y coordinates to give the solution of the original problem.

The potential and stream functions may be expressed in the following form called the complex potential

$$\Phi(z) = \varphi(x,y) + \psi(x,y)i \tag{6.5}$$

The equipotential lines and streamlines corresponding to a flow in the z-plane will be mapped onto a corresponding configuration in the w-plane using the given transformation. The fact that the mapping is conformal and one-to-one implies that the following Cauchy-Riemann equations are applicable:

$$\frac{\partial u}{\partial x} = \frac{\partial v}{\partial y} \tag{6.6}$$

$$\frac{\partial u}{\partial y} = -\frac{\partial v}{\partial x} \tag{6.7}$$

where u and v are field variables and x and y are orthogonal distances.

Equation (6.1) shows that

$$V_x = \frac{\partial \varphi}{\partial x} \text{ and } V_y = \frac{\partial \varphi}{\partial y}$$

Therefore, the Cauchy-Riemann equations give

$$\frac{\partial \psi}{\partial x} = -\frac{\partial \varphi}{\partial y} = -V_y \text{ and } \frac{\partial \psi}{\partial y} = \frac{\partial \varphi}{\partial x} = V_x$$

such that

$$\frac{d\Phi}{dz} = V_x - iV_y \tag{6.8}$$

This equation is known as the complex velocity and may be used to find the x and y component velocities once the streamlines or equipotential lines have been determined. The speed at a point within the flow domain is then given by the equation

$$|V| = \sqrt{V_x^2 + V_y^2} \tag{6.9}$$

Boundary Conditions

The following examples are useful elementary potential flows, which will be used to define the boundary conditions on flow around a right-angled bend and through a sudden contraction:

a) The potential

$$\Phi = Uz \tag{6.10}$$

with U either real or imaginary depending on the whether the flow is in the x direction or y direction, corresponds to the complex velocity

$$\frac{d\Phi}{dz} = \frac{\partial\varphi}{\partial x} + i\frac{\partial\psi}{\partial x} = V_x - iV_y \tag{6.11}$$

where $V_x = U$ and $V_y = 0$, or $V_x = 0$ and $V_y = U$. This equation represents uniform flow with magnitude U in either the positive or negative x direction, or the positive or negative y direction.

b) A point source or sink is given by the equation

$$\Phi = \pm\frac{m}{\theta}\log z \tag{6.12}$$

where m is the strength of the source or sink, and θ is the angle over which the source acts. The positive sign is used for a source, and the negative sign for a sink.

6.1.2 Mathematical Formulation

The two-dimensional, steady, irrotational flow of an incompressible fluid is considered through two differently shaped domains: a sudden contraction and a sharp right-angled bend. Fluid is forced along the ceiling space of a timber kiln by the fans, and may pass through a contraction before flowing through the right-angled bend and into the plenum chamber. It is assumed that a flow straightener is positioned soon after the fan so that three-dimensional swirling flows, which are produced by the fans, are eliminated. Thus, flows through the sudden contraction and the right-angled bend are essentially two dimensional in nature. This is a reasonable assumption since, in practice, the heating elements, which are located close to the fans in some kilns, act as flow straighteners. Furthermore, the length of a typical kiln is greater then the width of the plenum chamber or height of the ceiling space by a factor of at least 5.

The contraction and right-angled bend are considered separately in the analysis. The flow at a point far upstream of the sudden contraction is required to be uniform with constant speed U. The channel width at this point is h. The channel width at a point far downstream of the sudden contraction and far upstream of the sharp right-angled bend is k, and the velocity at this point must satisfy continuity. The channel width far downstream of the sharp right-angled bend is m and the velocity at this point must also satisfy continuity.

It is assumed that the kiln is symmetrical on the plane at which the overhead-centred fan is located. Thus, when the fans are reversed, the new flow patterns will mirror the old flow patterns.

Sudden change in the width of a channel

Consider the limit of the polygon shown in Figure 6.1 as points A and B are stretched to positive and negative infinity, respectively. A sudden contraction is formed by this limit. The velocity at A_∞ is U, and the velocity at B_∞ must by continuity be Uh/k.

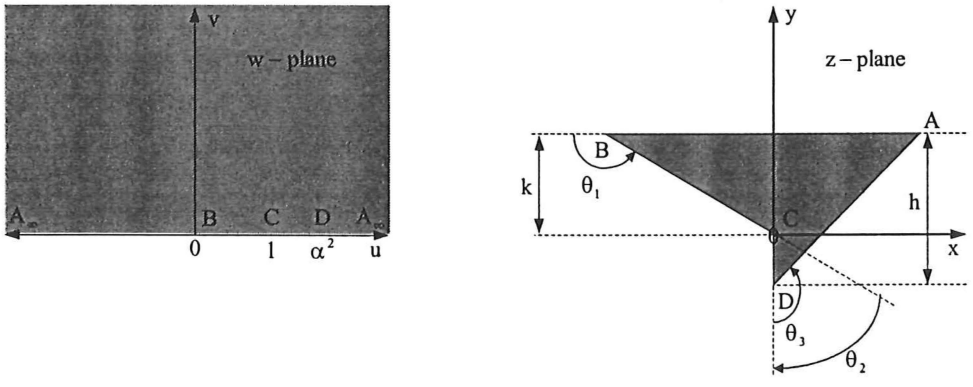

Figure 6.1. Mapping between the w and z-planes.

The Schwarz-Christoffel transformation may be used to map the polygonal boundary in the z-plane to points on the real axis in the w-plane. Starting from point B and moving counter-clockwise

$$\frac{dz}{dw} = K(w)^{-\frac{\theta_1}{\pi}}(w-1)^{-\frac{\theta_2}{\pi}}(w-\alpha)^{-\frac{\theta_3}{\pi}} \tag{6.13}$$

In the limit as point B is stretched to $-\infty$, and point A is stretched to $+\infty$, $\theta_1 \to \pi$, $\theta_2 \to -\pi/2$, and $\theta_3 \to \pi/2$. Therefore,

$$\frac{dz}{dw} = K\frac{1}{w}\sqrt{\frac{w-1}{w-\alpha}} \tag{6.14}$$

There is a source of output Uh at A_∞, and a sink of input Uh at B_∞ in the z-plane. Therefore, in the w-plane, there exists a sink at the origin which takes in a volume of Uh over an angle of π. The sink has strength Uh/π and is given the potential (Equation (6.12))

$$\Phi = -\frac{Uh}{\pi}\log w \tag{6.15}$$

which can be differentiated to give

$$\frac{d\Phi}{dw} = -\frac{Uh}{\pi w} \tag{6.16}$$

Hence, combining Equations (6.14) and (6.16) gives

$$\frac{d\Phi}{dz} = -\frac{Uh}{\pi K}\sqrt{\frac{w-\alpha}{w-1}} \tag{6.17}$$

The constants K and α may be determined from potential flow theory in the following manner.

a) At $A_\infty (w=\infty)$ $V_x = -U$ and $V_y = 0$. Equation (6.8) gives

$$U = \frac{Uh}{\pi K}\sqrt{\frac{\infty-\alpha}{\infty-1}}$$

and therefore

$$K = \frac{h}{\pi} \tag{6.18}$$

b) At $B_\infty (w=0)$ $V_x = -\frac{Uh}{k}$ and $V_y = 0$. Equation (6.8) gives,

$$\frac{Uh}{k} = \frac{Uh}{\pi K}\sqrt{\frac{0-\alpha}{0-1}}$$

thus,

$$\alpha = \frac{h^2}{k^2} \tag{6.19}$$

To obtain the relationship between z and w, Equation (6.14) must be integrated. The integration may be simplified by writing

$$t = \sqrt{\frac{w-1}{w-\alpha}} \tag{6.20}$$

which on rearrangement gives

$$w = \frac{\alpha t^2 - 1}{t^2 - 1} \tag{6.21}$$

and on differentiation yields

$$\frac{dw}{dt} = 2t\frac{(1-\alpha)}{(t^2-1)^2} \tag{6.22}$$

Substituting Equations (6.20), (6.21), and (6.22) into Equation (6.14), and rearranging and integrating gives,

$$z = F(t) = \frac{2h}{\pi}\left[\tanh^{-1} t - \frac{k}{h}\tanh^{-1}\frac{h}{k}t\right] + L \tag{6.23}$$

where L is the integration constant. If w=1 is taken to correspond to z=0, then t=0 and therefore L=0. Thus,

$$z = F(w) = \frac{2h}{\pi}\left[\tanh^{-1}\sqrt{\frac{w-1}{w-a}} - \frac{k}{h}\tanh^{-1}\frac{h}{k}\sqrt{\frac{w-1}{w-a}}\right] \tag{6.24}$$

The solution of the flow problem lies in separating the real and imaginary parts of Equation (6.24).

Firstly, the square-root term is considered. In the w-plane, the following complex equations can be formed (Figure 6.2):

$$\sqrt{w-1} = \sqrt{r_2}e^{\frac{i\theta_2}{2}}$$

$$\sqrt{w-a} = \sqrt{r_1}e^{\frac{i\theta_1}{2}}$$

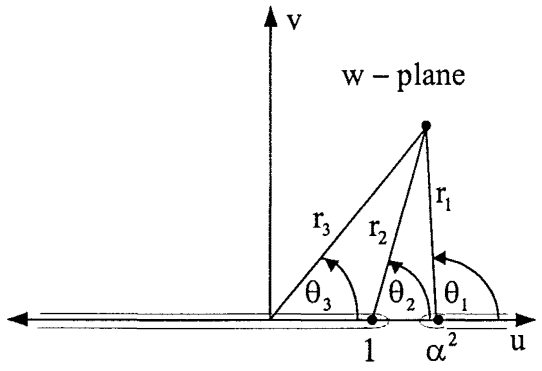

Figure 6.2. The *w*-plane.

Therefore,

$$\sqrt{\frac{w-1}{w-a}} = \sqrt{\frac{r_2}{r_1}} e^{\frac{(\theta_2-\theta_1)i}{2}} \tag{6.25}$$

The following identities are useful when separating the imaginary and real parts from Equation (6.24) (Hildebrand [1976]):

$$e^{iz} = \cos z + i \sin z$$

$$\tanh^{-1} z = \frac{1}{2} Log \frac{1+z}{1-z}$$

$$\tan^{-1} z = \frac{1}{2i} Log \frac{i-z}{i+z}$$

$$Logz = \log|z| + i\theta$$

Substituting Equation (6.25) into Equation (6.24), and making use of the above identities, and with some rearrangement it can be shown that

$$x = \frac{h}{2\pi} \log \left[\frac{1 + 2\sqrt{\frac{r_2}{r_1}} \cos\left(\frac{\theta_2 - \theta_1}{2}\right) + \frac{r_2}{r_1}}{1 - 2\sqrt{\frac{r_2}{r_1}} \cos\left(\frac{\theta_2 - \theta_1}{2}\right) + \frac{r_2}{r_1}} \right] - \frac{k}{2\pi} \log \left[\frac{1 + 2\frac{h}{k}\sqrt{\frac{r_2}{r_1}} \cos\left(\frac{\theta_2 - \theta_1}{2}\right) + \frac{h^2}{k^2}\frac{r_2}{r_1}}{1 - 2\frac{h}{k}\sqrt{\frac{r_2}{r_1}} \cos\left(\frac{\theta_2 - \theta_1}{2}\right) + \frac{h^2}{k^2}\frac{r_2}{r_1}} \right] \tag{6.26}$$

$$y = \frac{h}{\pi}\left[tan^{-1}\left(\frac{sin\left(\frac{\theta_2 - \theta_1}{2}\right)}{cos\left(\frac{\theta_2 - \theta_1}{2}\right) + \sqrt{\frac{r_1}{r_2}}} \right) - tan^{-1}\left(\frac{sin\left(\frac{\theta_2 - \theta_1}{2}\right)}{cos\left(\frac{\theta_2 - \theta_1}{2}\right) - \sqrt{\frac{r_1}{r_2}}} \right) \right]$$

$$-\frac{k}{\pi}\left[tan^{-1}\left(\frac{sin\left(\frac{\theta_2 - \theta_1}{2}\right)}{cos\left(\frac{\theta_2 - \theta_1}{2}\right) + \frac{k}{h}\sqrt{\frac{r_1}{r_2}}} \right) - tan^{-1}\left(\frac{sin\left(\frac{\theta_2 - \theta_1}{2}\right)}{cos\left(\frac{\theta_2 - \theta_1}{2}\right) - \frac{k}{h}\sqrt{\frac{r_1}{r_2}}} \right) \right] \tag{6.27}$$

The cosine rule can be used to evaluate r_1 and r_2 (Figure 6.2); that is,

$$r_1^2 = r_3^2 + \alpha^2 - 2\alpha r_3 \cos\theta_3$$

$$r_2^2 = r_3^2 + 1 - 2r_3 \cos\theta_3$$

and therefore

$$\sqrt{\frac{r_2}{r_1}} = \left[\frac{r_3^2 + 1 - 2r_3 \cos\theta_3}{r_3^2 + \alpha^2 - 2\alpha r_3 \cos\theta_3} \right]^{1/4} \tag{6.28}$$

The angles θ_1 and θ_2 can be calculated using the following expressions

$$\theta_2 = \begin{cases} tan^{-1}\left(\frac{r_3 \sin\theta_3}{r_3 \cos\theta_3 - 1} \right) & x > 1 \\ \pi - tan^{-1}\left(\frac{r_3 \sin\theta_3}{1 - r_3 \cos\theta_3} \right) & x < 1 \end{cases} \tag{6.29}$$

$$\theta_1 = \begin{cases} tan^{-1}\left(\frac{r_3 \sin\theta_3}{r_3 \cos\theta_3 - \alpha} \right) & x > \alpha \\ \pi - tan^{-1}\left(\frac{r_3 \sin\theta_3}{\alpha - r_3 \cos\theta_3} \right) & x < \alpha \end{cases} \tag{6.30}$$

The complex potential given by Equation (6.15) may be used to calculate r_3 and θ_3 from a given set of equipotential and streamline values.

$$w = e^{(\varphi + i\psi)\frac{\pi}{Uh}} = e^{\beta}\cos\gamma + ie^{\beta}\sin\gamma$$

where $\beta = \frac{\varphi\pi}{Uh}$ and $\gamma = \frac{\psi\pi}{Uh}$.

Therefore,

$$r_3 = \sqrt{\left(e^{\beta}\cos\gamma\right)^2 + \left(e^{\beta}\sin\gamma\right)^2} = e^{\beta} \tag{6.31}$$

$$\tan\theta_3 = \frac{e^{\beta}\sin\gamma}{e^{\beta}\cos\gamma} = \tan\gamma \tag{6.32}$$

giving $\theta_3 = \gamma$.

The speed at any point is calculated from the complex velocity (Equations (6.8) and (6.17))

$$\frac{\partial\Phi}{\partial z} = -U\sqrt{\frac{w-\alpha}{w-1}} = V_x - iV_y$$

$$= -U\sqrt{\frac{r_1}{r_2}}e^{i\frac{(\theta_1-\theta_2)}{2}}$$

$$= -U\sqrt{\frac{r_1}{r_2}}\left(\cos\left(\frac{\theta_1-\theta_2}{2}\right) + i\sin\left(\frac{\theta_1-\theta_2}{2}\right)\right)$$

The x and y component velocities may be found by using the imaginary and real parts of this equation. Finally,

$$|V| = \sqrt{V_x^2 + V_y^2} = U\sqrt{\frac{r_1}{r_2}} \tag{6.33}$$

Sharp right-angled bend

A similar procedure is followed to find the analytical expressions for the equipotential lines and streamlines of a sharp right-angled bend. Consider the limit of the polygon shown in Figure 6.3 as point A is stretched to positive infinity, and point C is stretched to negative infinity on the imaginary axis; a sharp right-angled bend is formed by this limit. The velocity at A_∞ is V, and the velocity at C_∞ must by continuity be *(Vk/m)i*.

The Schwarz-Christoffel transformation may be used to map the polygonal boundary in the z-plane to points on the real axis in the w-plane. Starting from point D and moving clockwise

$$\frac{dz}{dw} = K\left(w-\alpha^2\right)^{-\frac{\theta_n}{\pi}}\left(w\right)^{-\frac{\theta_1}{\pi}}\left(w+1\right)^{-\frac{\theta_3}{\pi}} \tag{6.34}$$

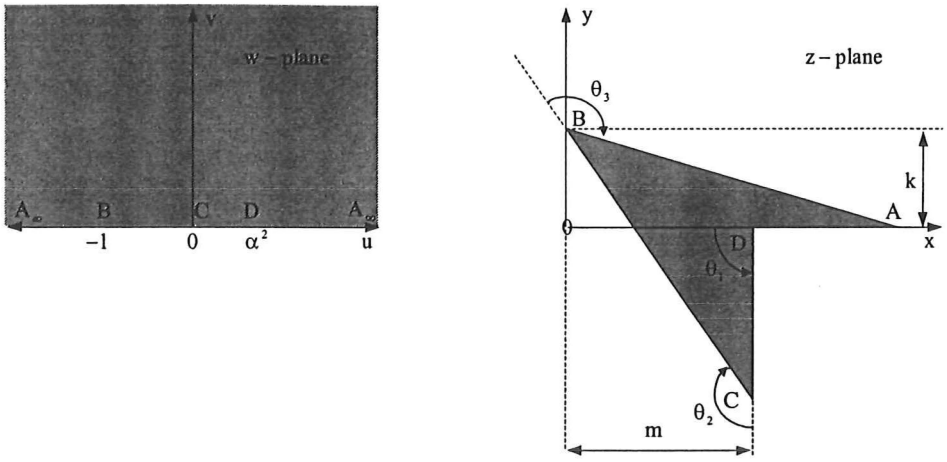

Figure 6.3. Mapping between the *w* and *z*-planes

In the limit as point *C* is stretched to $-\infty i$, and point *A* is stretched to $+\infty$, $\theta_1 \to -\frac{\pi}{2}$, $\theta_2 \to \pi$, and $\theta_3 \to \pi/2$. Therefore,

$$\frac{dz}{dw} = \frac{K}{w}\sqrt{\frac{w-\alpha^2}{w+1}} \tag{6.35}$$

There is a source of output Vk at A_∞ and a sink of input Vk at C_∞ in the *z*-plane. Therefore, in the *w*-plane, there exists a sink at the origin which takes in a volume of Vk over an angle of π. The sink has strength Vk/π and is therefore given the potential

$$\Phi = -\frac{Vk}{\pi} log\, w \tag{6.36}$$

which can be differentiated to give

$$\frac{d\Phi}{dw} = -\frac{Vk}{\pi w} \tag{6.37}$$

Hence, combining Equations (6.35) and (6.37) gives

$$\frac{d\Phi}{dz} = -\frac{Vk}{\pi K}\sqrt{\frac{w+1}{w-\alpha^2}} \tag{6.38}$$

The constants *K* and α may be determined from potential flow theory.

a) At $A_\infty (w=\infty)$ $V_x = -V$ and $V_y = 0$. Equation (6.8) gives

$$V = \frac{Vk}{\pi K}\sqrt{\frac{\infty+1}{\infty-\alpha^2}}$$

and therefore

$$K = \frac{k}{\pi} \tag{6.39}$$

b) At $C_\infty (w=0)$ $V_y = -\left(\frac{Vk}{m}\right)$ and $V_x = 0$. Equation (6.8) gives,

$$\frac{Vk}{m} i = -\frac{Vk}{\pi K}\sqrt{\frac{0+1}{0-\alpha^2}}$$

thus,

$$\alpha = \frac{m}{k} \tag{6.40}$$

To obtain the relationship between z and w, Equation (6.35) must be integrated. The integration may be simplified by writing

$$t = \sqrt{\frac{w-\alpha^2}{w+1}} \tag{6.41}$$

which on rearrangement gives

$$w = \frac{\alpha^2 + t^2}{1-t^2} \tag{6.42}$$

and on differentiation yields

$$\frac{dw}{dt} = 2t\frac{\left(1+\alpha^2\right)}{\left(1-t^2\right)^2} \tag{6.43}$$

Substituting Equations (6.41), (6.42), and (6.43) into Equation (6.35), and integrating gives,

$$z = F(t) = \frac{2k}{\pi}\left[\tanh^{-1} t - \frac{m}{k}\tan^{-1}\frac{k}{m}t\right] + L \tag{6.44}$$

where L is the integration constant. If $w = \alpha^2$ is taken to correspond to $z=m$, then $t=0$ and therefore $L=m$. Thus

$$z = F(w) = \frac{2k}{\pi}\left[\tanh^{-1}\sqrt{\frac{w-m^2/k^2}{w+1}} - \frac{m}{k}\tan^{-1}\frac{k}{m}\sqrt{\frac{w-m^2/k^2}{w+1}}\right] + m \tag{6.45}$$

The solution of the flow problem lies in separating the real and imaginery parts of Equation (6.46).

Firstly, the square root term is considered. In the *w*-plane, the following complex equations can be formed (Figure 6.4):

$$\sqrt{w-\alpha^2} = \sqrt{r_1}e^{\frac{i\theta_1}{2}}$$

$$\sqrt{w+1} = \sqrt{r_2}e^{\frac{i\theta_2}{2}}$$

Therefore,

$$\sqrt{\frac{w-\alpha^2}{w+1}} = \sqrt{\frac{r_1}{r_2}}e^{\frac{(\theta_1-\theta_2)i}{2}} \tag{6.46}$$

Substituting Equation (6.46) into Equation (6.45), and making use of the identities, and with some rearrangment it can be shown that

$$x = \frac{k}{2\pi}log\left|\frac{1+2\sqrt{\frac{r_1}{r_2}}cos\left(\frac{\theta_1-\theta_2}{2}\right)+\frac{r_1}{r_2}}{1-2\sqrt{\frac{r_1}{r_2}}cos\left(\frac{\theta_1-\theta_2}{2}\right)+\frac{r_1}{r_2}}\right| + \frac{m}{\pi}tan^{-1}\left(\frac{sin\left(\frac{\theta_1-\theta_2}{2}\right)+\frac{m}{k}\sqrt{\frac{r_2}{r_1}}}{cos\left(\frac{\theta_1-\theta_2}{2}\right)}\right)$$

$$-\frac{m}{\pi}tan^{-1}\left(\frac{sin\left(\frac{\theta_1-\theta_2}{2}\right)-\frac{m}{k}\sqrt{\frac{r_2}{r_1}}}{cos\left(\frac{\theta_1-\theta_2}{2}\right)}\right)+m$$

(6.47)

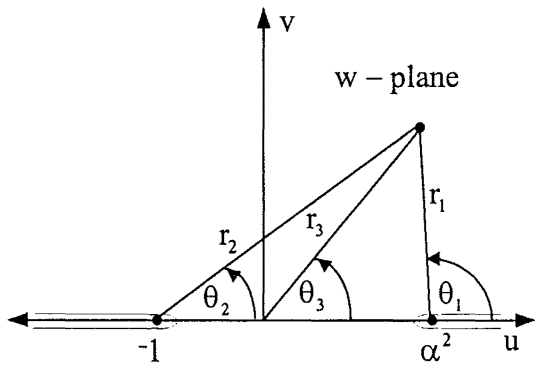

Figure 6.4. The *w*-plane.

$$y = \frac{m}{2\pi} log \left| \frac{1 - 2\frac{k}{m}\sqrt{\frac{r_1}{r_2}} sin\left(\frac{\theta_1 - \theta_2}{2}\right) + \frac{k^2}{m^2}\frac{r_1}{r_2}}{1 + 2\frac{k}{m}\sqrt{\frac{r_1}{r_2}} cos\left(\frac{\theta_1 - \theta_2}{2}\right) + \frac{k^2}{m^2}\frac{r_1}{r_2}} \right| + \frac{k}{\pi} tan^{-1}\left(\frac{sin\left(\frac{\theta_1 - \theta_2}{2}\right)}{cos\left(\frac{\theta_1 - \theta_2}{2}\right) + \sqrt{\frac{r_2}{r_1}}} \right)$$

$$- \frac{k}{\pi} tan^{-1}\left(\frac{sin\left(\frac{\theta_1 - \theta_2}{2}\right)}{cos\left(\frac{\theta_1 - \theta_2}{2}\right) - \sqrt{\frac{r_2}{r_1}}} \right) \tag{6.48}$$

The cosine rule can be used to evaluate r_1 and r_2 (Figure 6.4); that is,

$$r_1^2 = r_3^2 + \alpha^2 - 2\alpha r_3 \cos\theta_3$$

$$r_2^2 = r_3^2 + 1 + 2r_3 \cos\theta_3$$

and therefore

$$\sqrt{\frac{r_1}{r_2}} = \left[\frac{r_3^2 + \alpha^2 - 2r_3\alpha\cos\theta_3}{r_3^2 + 1 + 2r_3\cos\theta_3} \right]^{1/4} \tag{6.49}$$

The angles θ_1 and θ_2 should be calculated using the following equations

$$\theta_2 = \begin{cases} tan^{-1}\left(\frac{r_3 \sin\theta_3}{r_3\cos\theta_3 + 1}\right) & x > -1 \\ \pi + tan^{-1}\left(\frac{r_3\sin\theta_3}{1 + r_3\cos\theta_3}\right) & x < -1 \end{cases} \tag{6.50}$$

$$\theta_1 = \begin{cases} tan^{-1}\left(\frac{r_3 \sin\theta_3}{r_3\cos\theta_3 - \alpha}\right) & x > \alpha \\ \pi - tan^{-1}\left(\frac{r_3\sin\theta_3}{\alpha - r_3\cos\theta_3}\right) & x < \alpha \end{cases} \tag{6.51}$$

The complex potential given by Equation (6.36) may be used to calculate r_3 and θ_3 from a given equipotential or streamline value.

$$w = e^{(\varphi + i\psi)\frac{\pi}{Vk}} = e^{\beta}\cos\gamma + ie^{\beta}\sin\gamma$$

where $\beta = \frac{\varphi\pi}{Vk}$ and $\gamma = \frac{\psi\pi}{Vk}$.

Therefore,

$$r_3 = \sqrt{\left(e^{\beta}\cos\gamma\right)^2 + \left(e^{\beta}\sin\gamma\right)^2} = e^{\beta} \tag{6.52}$$

$$\tan\theta_3 = \frac{e^{\beta}\sin\gamma}{e^{\beta}\cos\gamma} = \tan\gamma \tag{6.53}$$

giving $\theta_3 = \gamma$

The speed at any point is calculated from the complex velocity

$$\frac{\partial\Phi}{\partial z} = -V\sqrt{\frac{w+1}{w-\alpha^2}} = V_x - iV_y$$

$$= -V\sqrt{\frac{r_2}{r_1}}e^{i\frac{(\theta_2-\theta_1)}{2}}$$

$$= -V\sqrt{\frac{r_2}{r_1}}\left(cos\left(\frac{\theta_2-\theta_1}{2}\right)+i\,sin\left(\frac{\theta_2-\theta_1}{2}\right)\right)$$

Therefore,

$$|V| = \sqrt{V_x^2 + V_y^2} = V\sqrt{\frac{r_2}{r_1}} \tag{6.54}$$

6.1.3 Results

Equipotential lines may be calculated by assuming a series of constant values for γ, which is related to the stream function by the equation

$$\gamma = \frac{\psi\pi}{Uh}$$

while varying β, which is related to the equipotential function by the equation

$$\beta = \frac{\varphi\pi}{Uh}$$

Conversely, streamlines maybe calculated by assuming a series of constant values for the equipotential function while varying the streamline function.

The coordinates (*x*,*y*) on the *z*-plane corresponding to these equipotential and stream function values may be determined from Equations (6.26)-(6.32) in the case of the sudden contraction and Equations (6.47)-(6.53) in the case of the right-angled bend. The *arctan* terms in Equations (6.26)-(6.27) and Equations (6.47)-(6.48) describe the angle θ in the logarithmic identity

$$Logz = log|z| + i\theta$$

Most calculators and computer software calculate *arctan* in the range $-\pi < \theta < \pi$. Discontinuous streamlines and equipotential lines will result if θ is restricted in this manner since θ may take on values outside this range. The value π should be added or subtracted, depending on the trend of θ, from the *arctan* value in cases where discontinuous streamlines and equipotential lines are produced.

The speeds at each (x,y) coordinate may be calculated from Equations (6.33) and (6.54) for the sudden contraction and right-angled bend, respectively.

Figures 6.5 and 6.6 show the streamlines and equipotential lines of potential flow through a sudden contraction and right-angled bend, respectively, for different inlet and outlet dimensions. The dimensions used to produce these graphs are typical of industrial-scale kilns.

The percent variation in velocities across a particular equipotential line is defined by the equation

$$\sigma = \frac{|V|(\gamma = 0) - |V|(\gamma = \pi)}{\overline{V}} \tag{6.55}$$

where $\overline{V}$ is the average velocity across the equipotential line. Table 6.1 shows the variation in velocities σ across equipotential lines located at various distances from the inner corner of the right-angled bend for a range of configurations of the right-angled bend. Thus, the entrance length (distance from the inner corner of the bend to the top of the timber stack) may be determined given the minimum required variation in velocities, σ_{min}. The flow rate through most of these configurations is same. However, the flow rate through the last configuration was increased to demonstrate its effect on the entrance lengths. The flow fields corresponding to the configurations of columns 1 and 2 in Table 6.1 are shown in Figures 6.6a and 6.6b, respectively.

6.1.4 Discussion

Figures 6.5 and 6.6 show the flow fields in a sudden contraction and a right-angled bend, respectively. The velocity distributions far upstream and far downstream of these flow domains are assumed to be constant across the widths of the channels. This assumption was necessary for specifying uniform flow distributions at the boundaries of each flow domain. Incorporating such 'dead legs' upstream and downstream of the contraction and right-angled bend is not practical for kiln design. However, these entrance and exit lengths can be truncated to practical dimensions without seriously affecting the flow patterns.

The first column of Table 6.1 shows that the variable σ drops to 3.7% at a distance of 0.99 m from the inner corner of the right-angled bend with entrance and exit widths both equal to 1.0 m. Thus, an entrance length (from the inner corner of the right-angled bend to the top of the timber stack) equal to the width of the plenum chamber m is required to reduce the velocity distribution σ across the equipotential line below 5%. The remaining columns of Table 6.1 show that this entrance length is

independent of the height of the ceiling space, width of the plenum chamber, and velocity of the fluid. For example, the third column shows that when the plenum-chamber width is 1.0 m and the ceiling-space height is 2.0 m, σ drops below 5% at a distance of 0.93 m from the inner corner, which is close in magnitude to the plenum-chamber width. A comparison between columns 2 and 5 indicates that the streamlines and equipotential lines are independent of the average velocity, which is expected since that the fluid is assumed to be irrotational. If the limit on σ is relaxed to 10%, then the entrance length is reduced to about two-thirds of the plenum chamber width. A shorter entrance length results in a smaller, more compact kiln. However, this advantage is offset by an increase in the flow maldistribution across the stack, which can cause significant final moisture content variations throughout the stack of dried timber boards.

Introducing an entrance length in the plenum chamber will create a dead-space in the kiln which has a volume equal to the entrance length multiplied by the width of the timber stack multiplied by the length of the timber stack. Reducing the width of the plenum chamber will shorten the entrance length thus reducing the volume of the dead space. However, it was shown in the previous section that inertial and frictional effects in the plenum chamber become important as the plenum-chamber width is reduced, which can result in flow non-uniformity across the stack even though a symmetrical velocity distribution exists across the plenum chamber. Kröll [1978] states that the plenum-chamber width should be at least equal to the sum of the fillet space widths to mitigate the effect of inertial and frictional forces.

If the right-angled bend is not streamlined, then flow separation will occur at the corner which will generate a vortex zone close to the inlet face of the stack and near the uppermost boards. In this case, the entrance length required to mitigate the effect of unsymmetrical flow across the plenum chamber will need to be increased even further. Idelchik [1991] states that the effect of the vortex zone on the flow field across the channel will extend from the bend to a distance down the channel of at least 8 hydraulic diameters. In the previous chapter it was shown that the vortex zone is approximately one ceiling-space height long which would be the minimum height required for the 'entrance length' into the plenum chamber.

The following assumption were made in using potential flow theory to calculate the flow fields in the right-angled bend and sudden contraction:

a) The corners were rounded sufficiently so that they became streamlined and therefore no boundary layer separation occurred at the flow boundaries.
b) The plenum chamber width was less than the ceiling space height to avoid divergence of the streamlines.
c) The Reynolds number was relatively high so that the flow was irrotational in the mainstream and the boundary layer hugged the walls very closely.
d) The flow far upstream and downstream of the contraction or bend was two-dimensional and uniform across the height of the ceiling space.

All but one of these assumptions is reasonable. Boundary-layer separation is unavoidable in the right-angled bend since the streamlines diverge as they approach

the corner (Figure 6.6). The unknown form of the separation zone precludes a precise analysis of the flow field using potential flow theory. However, in the previous chapter it was demonstrated that adequately smoothing the sharp corners of the right-angled bend resulted in separation zones that were negligibly thin compared with the dimensions of the right-angled bend. In this case, potential flow theory might be used with moderate accuracy to determine the flow fields.

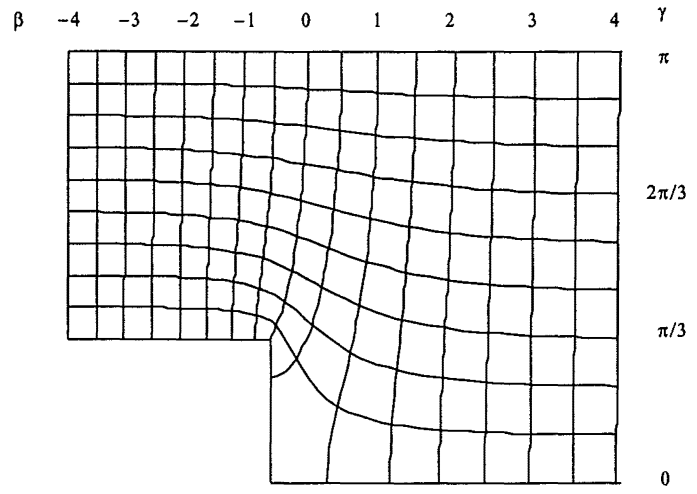

(a)

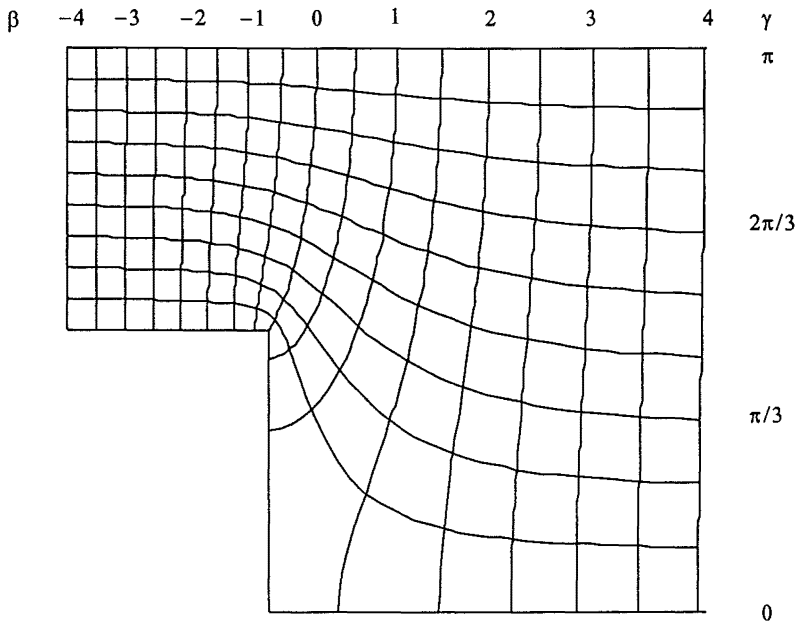

(b)

Figure 6.5. Irrotational flow through a sudden contraction: a) h=1.5 m, k=1.0 m, b) h=2.0 m, k=1.0 m.

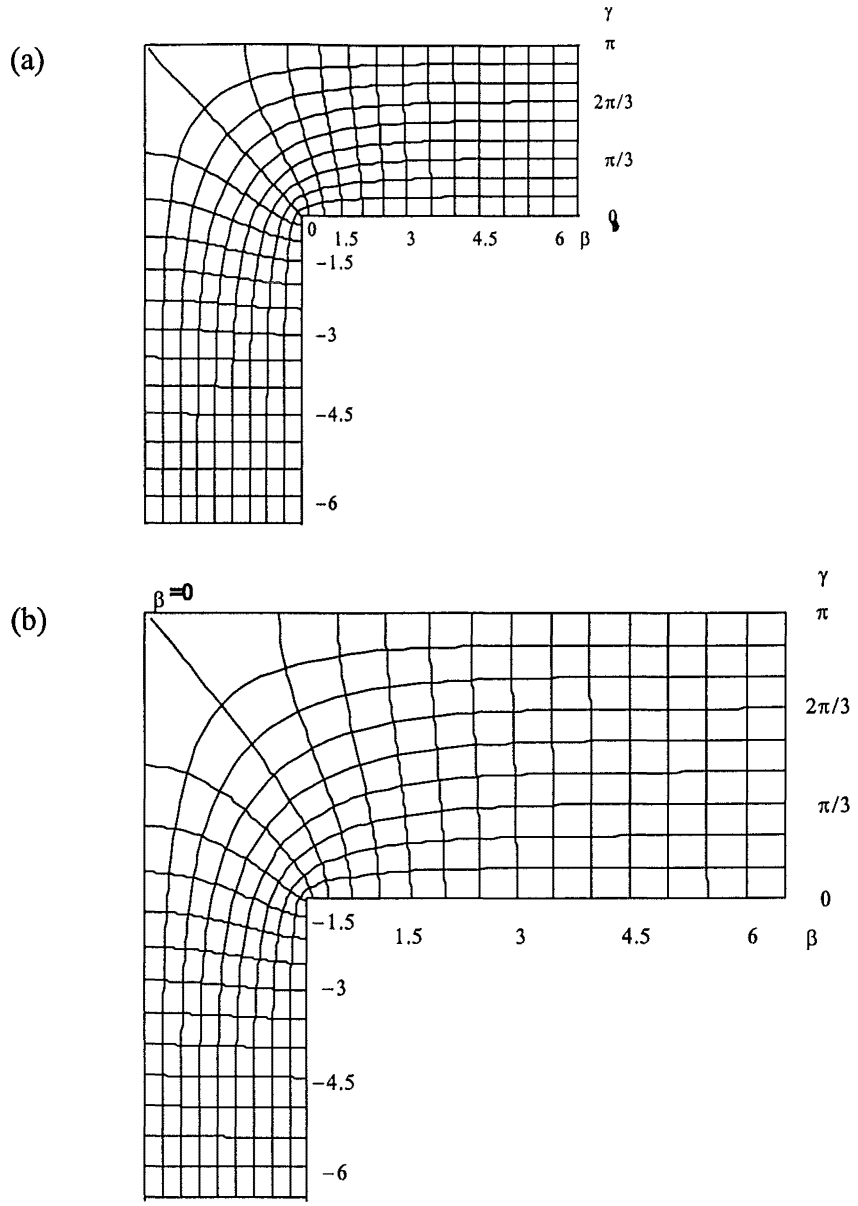

Figure 6.6. Irrotational flow through a right-angled bend: a) k=1.0 m, m=1.0 m b) k=1.5 m, m=1.0 m.

k (m)		1		1.5		2		2		1.5	
m (m)		1		1		1		2		1	
V (m/s)		5		3.333		2.5		2.5		5	
β	σ (%)	L (m)	σ (%)	L (m)	σ (%)	L (m)	σ (%)	L (m)	σ (%)	L (m)	
-3	10	0.68	16.3	0.46	25.5	0.29	10	1.35	16.3	0.46	
-3.5	6	0.83	9.8	0.62	15.2	0.45	6	1.67	9.8	0.62	
-4	3.7	0.99	6	0.78	9.2	0.61	3.7	1.99	6	0.78	
-4.5	2.2	1.15	3.6	0.94	5.6	0.77	2.2	2.31	3.6	0.94	
-5	1.3	1.31	2.2	1.1	3.4	0.93	1.3	2.62	2.2	1.1	

Table 6.1. Variation in velocities σ across equipotential lines located at various distances L from the inner corner of the right-angled bend for different configurations of the right-angled bend.

6.2 Manifold Analysis

The uniformity of flow across stacked timber in a kiln is governed to a certain extent by the variations in fluid pressure inside the plenum chambers on either side of the stack. These variations in pressure result from wall friction, and loss or gain of fluid momentum due to turning, contraction, and expansion effects at the entrance to and exit from the fillets. A uniform flow distribution across the stack is attained only when the plenum chambers act as infinite reservoirs. This condition is approached when the plenum chambers become very wide or when the resistance across the timber stack becomes very large (Pigford *et al.* [1983]). Placing screens over the inlet and outlet faces of the stack can increase the resistance across the stack. However, large timber-stack resistances result in an increase in total pressure loss through the kiln with a subsequent increase in the fan power requirement. Therefore, the most effective method for reducing flow maldistribution caused by friction losses and momentum changes is to increase the width of the plenum chambers.

How wide should the plenum chambers be in order to reduce within acceptable limits the flow maldistribution across the stack? A common rule of thumb used for kiln design is that the ratio of the plenum chamber width to the sum of the widths of the fillets be at least equal to unity. However, given the variation in sizes of timber stacks dried in industrial-scale kilns, and the differences in loading techniques, it is likely that this minimum ratio will vary from one kiln to another. In this section, a method is presented for designing the plenum chamber of a kiln that minimises the non-uniformity of flow across the stack. This method requires accurate prediction of the flow distribution across the stack given the flow rate and the geometry of the stack and plenum chambers. Thus, the model may be used to investigate different design options so that minimum plenum-chamber widths can be found for different kiln configurations.

If sidewall effects are neglected, the flow of air through the stack may be regarded as one-dimensional. Thus, the flow distribution down the stack may be computed from a one-dimensional equation of fluid motion, if enough information is available on the pressure changes that occur near the points at which the airflow divides, as in the inlet plenum chamber, or recombine, as in the outlet plenum chamber. Eddies are generated by such changes in cross-section of the boundaries and direction of the fluid and, therefore, friction losses occur as kinetic energy is dissipated as heat in eddies. The flow patterns near the dividing and recombining streams are very complex. Nevertheless, an accurate one-dimensional approach may be taken by absorbing the effects of friction losses in the transitions and at the walls into empirical coefficients. These coefficients must be evaluated experimentally before kiln-wide flow distributions can be determined.

Workers such as Keller [1949], Bajura *et al.* [1976], and Pigford *et al.* [1983] have derived one-dimensional equations of fluid motion in a manifold system. These equations rely on the assumptions that the fluid is incompressible, and the velocity distribution at the entrance to the manifold is uniform and fully developed. The first assumption is valid for airflow in kilns; however, the second assumption may be in error. In most industrial kilns, the fluid must turn by 90 degrees from the ceiling

space, where the fan is located, into the inlet plenum chamber. In Chapter 5 it was shown that sharp right-angled bends generate vortices which cause severe distortion of the velocity profile downstream of the bend. However, in this chapter it is assumed that the right-angled bend, from the ceiling space into the inlet plenum chamber, is sufficiently rounded to prevent boundary-layer separation at the corner. It is also assumed that a sufficient entrance length exists between the right-angled bend and the top of the stack so that the velocity distribution becomes fully developed and uniform when it reaches the top of the stack. Actual kilns may not meet these criteria, so that the estimated velocity distribution represents the best possible, and more maldistribution is likely in practice.

6.2.1 Theory

A momentum balance on a small volume element in the inlet plenum chamber yields the equation

$$\frac{\partial P_1}{\partial y_1} + \frac{2\rho v_1}{\alpha_1}\frac{\partial v_1}{\partial y_1} + \frac{2f_1\rho}{D_{H1}}v_1^2 = 0 \qquad (6.56)$$

where α_1 is a momentum correction factor to account for the rearrangement of air between the boundary layer and the main stream as the branch point is traversed, f_1 is the Fanning friction factor which is a function of the Reynolds number, and D_{H1} is the hydraulic diameter of the inlet plenum chamber. In this equation, y_1 is positive in the direction pointing towards the bottom of the inlet plenum chamber, and the flow direction is defined as being positive in the positive y_1 direction.

The analogous momentum balance on a control volume in the outlet plenum chamber is

$$\frac{\partial P_2}{\partial y_2} + \frac{2\rho v_2}{\alpha_2}\frac{\partial v_2}{\partial y_2} - \frac{2f_2\rho}{D_{H2}}v_2^2 = 0 \qquad (6.57)$$

In this equation, y_2 is positive in the direction pointing towards the bottom of the outlet plenum chamber; however, the fluid flows in the opposite direction and, therefore, the flow direction is defined as being positive in the negative y_2 direction. Thus, the sign of the friction factor term is negative in Equation (6.57).

By continuity, the fluid speed at any point down the inlet plenum chamber is equal to the fluid speed at that same distance down the outlet plenum chamber. Moreover, it is assumed that the inlet and outlet plenum chamber areas are constant and equal. Therefore,

$$y = y_1 = y_2$$
$$D_H = D_{H1} = D_{H2}$$
$$v = v_1 = v_2$$

$$f = f_1 = f_2$$

The continuity condition and the difference between Equations (6.57) and (6.56) gives the overall momentum balance across a plane located at any given point down the timber stack. Thus,

$$\frac{\partial(P_2 - P_1)}{\partial y} + 2\rho v\left(\frac{1}{\alpha_2} - \frac{1}{\alpha_1}\right)\frac{\partial v}{\partial y} - \frac{2(2f)\rho}{D_H}v^2 = 0 \tag{6.58}$$

Once the pressure drop across the stack is known $(P_2 - P_1)$, then Equation (6.58) can be used to determine the velocity profiles along the plenum chambers. The velocity profile across the stack can then be calculated by conducting a continuity balance over the control volume in the inlet or outlet plenum chambers:

$$A\partial v = -u\partial A' \tag{6.59}$$

where A is the cross-sectional area of the inlet or outlet plenum chamber, v is the average velocity in the plenum chamber, A' is the lateral area of the branching point, and u is the average velocity of the fluid moving through the surface A'. This equation may be rewritten

$$A\partial v = -uw\varepsilon\partial y \tag{6.60}$$

where w is the depth of the plenum chamber, and ε is the ratio of the area available for fluid flow through the stack to the total cross-sectional area of the inlet (or outlet) face of the stack. Thus, the fluid velocity along a fillet space at any point down the timber stack is

$$u = -\frac{A}{w\varepsilon}\frac{\partial v}{\partial y} \tag{6.61}$$

The pressure drop across the stack is given by Bernoulli's equation

$$P_2 - P_1 = -\left(K_1 + \frac{4f_c L_c}{D_{Hc}} + K_2\right)\rho\frac{u^2}{2} \tag{6.62}$$

which includes a term for the loss in head due to contraction as the fluid enters the fillet from the inlet plenum chamber (K_1), a term for the frictional losses across the width of the stack, and a term for the loss in head due to expansion as the fluid moves from the fillet into the outlet plenum chamber (K_2). Equation (6.61) can be substituted into the derivative of Equation (6.62) with respect to distance y to give

$$\frac{\partial(P_2 - P_1)}{\partial y} = -\frac{\rho}{2}\left(\frac{A}{w\varepsilon}\right)^2\left[\frac{\partial H}{\partial y}\left(-\frac{\partial v}{\partial y}\right)^2 + 2H\frac{\partial v}{\partial y}\frac{\partial^2 v}{\partial y^2}\right] \tag{6.63}$$

where H is the sum of the terms within the brackets of Equation (6.62). In this section, the friction factor is assumed to take the form

$$f = \frac{b}{Re^n} \tag{6.64}$$

where the Reynolds number in the plenum chamber is given by $Re = \frac{D_H v}{\nu}$, and the Reynolds number in the fillet space is given by $Re = \frac{D_{Hc} u}{\nu}$.

In Equation (6.64), the coefficients b and n may take on a different set of values in the plenum chambers than in the fillets since the walls will have different roughness coefficients due to the smooth aluminium of the plenum wall and the rough-sawn surface of lumber in the fillet space. Equation (6.63) and (6.64) can be substituted into Equation (6.58) to give the final form of the overall momentum balance

$$\left(\beta(-F')^{1-n_c}\left(1-\frac{2}{n_c}\right)+\gamma F'\right)F''-\Pi F F'+\theta F^{2-n}=0 \tag{6.65}$$

where

$$\beta = \frac{2n_c L_c b_c \upsilon^{n_c}}{(D_{Hc})^{n_c+1}}\left(\frac{A}{w\varepsilon}\right)^{2-n_c}$$

$$\gamma = (K_1 + K_2)\left(\frac{A}{w\varepsilon}\right)^2$$

$$\Pi = 2\left(\frac{1}{\alpha_2}-\frac{1}{\alpha_1}\right)$$

and $$\theta = \frac{4b\upsilon^n}{D_H^{n+1}}$$

Equation (6.65) is non-linear and therefore must be solved numerically to give the velocity profile down the plenum chambers. This can be achieved by decomposing Equation (6.65) into two first-order equations, and solving the resultant equations using a standard ordinary differential equations solver. The first-order differential equations are

$$\frac{dx_1}{dy} = x_2 \tag{6.66}$$

$$\frac{dx_2}{dy} = \frac{\Pi x_1 x_2 + \theta x_1^{2-n}}{\beta\left(-x_2^{1-n_c}\right)\left(1-\frac{2}{n_c}\right)+\gamma x_2} \tag{6.67}$$

where

$$x_1 = F \tag{6.68}$$

$$x_2 = F' \tag{6.69}$$

The boundary conditions are

$$x_1(L) = 0 \tag{6.70}$$

$$x_1(0) = v_o \tag{6.71}$$

Substituting Equation (6.69) into Equation (6.60) gives the equation for the fillet space velocity profile down the stack.

$$u = -\frac{A}{w\varepsilon} x_2 \tag{6.72}$$

The ratio of the cross-sectional area of the inlet or outlet plenum chamber to the depth of the plenum chamber (A/w) is equivalent to the plenum-chamber width. Thus, the depth of the plenum chamber w appears solely in the hydraulic diameter of the Fanning friction factor equation (Equation (6.64)). In the fillet spaces of the hydraulic kiln described in Chapter 5, w is larger than the fillet-space width by a factor of 13. It can be shown that the hydraulic diameter becomes independent of the depth of the kiln (w) when w becomes very large. In the plenum chambers of the hydraulic kiln, the kiln depth w is close to the widths of the plenum chambers and, therefore, affects the magnitude of the hydraulic diameter. However, it will be shown later that wall friction in the plenum chambers has an insignificant effect on the flow distribution across the stack when the ratio of the width of the plenum chamber to the sum of the fillet space widths is unity. As this ratio is reduced, the hydraulic diameter becomes increasingly less dependent on the depth of the kiln. Thus, the depth of the plenum chamber only weakly effects the velocity distribution across the stack in the hydraulic kiln. This is even more applicable in industrial-scale timber kilns where the length of the kiln, or equivalently the depth of the plenum chamber w, is very large compared with the other dimensions of the stack.

6.2.2 Results

Equations (6.66) and (6.67) were solved numerically using a standard ordinary differential equation solver, and the Shooting Method (Conte and de Boor [1980]) to estimate the gradient in velocity at the entrance to the inlet plenum chamber.

The coefficients required to solve Equations (6.66) and (6.67) are the wall-friction coefficients, b and n, the contraction and expansion coefficients, K_1 and K_2, and the overall momentum correction factor Π. Pigford *et al.* [1983] found experimental values for the contraction and expansion coefficients of pipe manifolds with circular cross-section of approximately 0.4 and 1.0, respectively. An expansion coefficient K_2 of unity can be determined from the Borda-Carnot head loss equation if it is assumed that the flow area increases abruptly to infinity at the expansion (Massey [1983]). The Borda-Carnot head loss equation is applicable for any cross-sectional shape of the branch. Therefore, a value of unity for K_2 is reasonable when considering flow from a fillet space (rectangular cross-section) into the outlet plenum chamber. Due to the lack of experimental data available in the literature, a contraction coefficient for circular cross-sectional branches of 0.4 is assumed even though the fillets in a kiln are rectangular in shape. It will be shown later that this coefficient has only a minor effect on the flow distributions across the timber stack.

Bajura *et al.* [1976] found experimentally a value of 1.55 for the momentum correction factor Π in pipe manifolds with circular cross-section. In this thesis, the momentum correction factor, applicable to flows in manifolds of rectangular cross-section, was estimated by adjusting Π until the mathematical model fitted various experimental data found in Chapter 5, in which the flow rates of water through the fillets of a hydraulic model of a kiln was measured.

In the previous chapter, attempts were made to eliminate boundary-layer separation at the right-angled bend of the hydraulic kiln by introducing a round-section in the ceiling space. The radius of the round-section was equal to 0.3 times the maximum height of the ceiling space, and close to half of the width of the plenum chamber. This radius was nearly twice the minimum radius recommended by Idelchik [1991] for eliminating boundary-layer separation in right-angled pipe bends. Nevertheless, the velocity profile across the plenum width was skewed slightly due to the centrifugal forces generated in the right-angled bend, and the presence of a very narrow zone of boundary-layer separation persisting downstream of the turn. Any complications of the actual entrance velocity profile were removed from the experimental data by analysing only that portion of the plenum chamber downstream from bend where the velocity profile had adjusted to a fully developed condition.

The friction coefficients b $(=b_c)$ and n $(=n_c)$ in Equation (6.64) were given values of 0.0791 and 0.25, respectively, which are the coefficients of the Blasius equation for the friction factor in smooth pipes (Dow *et al.* [1950]). The smooth-pipe correlation is applicable for flow in the Perspex hydraulic model. A constant friction factor (f=0.02) was used when investigating flow through an industrial-scale kiln. This value was extracted from data presented by Langrish *et al.* [1996] of pressure drops across a stack of timber over a range of fillet-space velocities. Their data was calculated using computational fluid dynamics (CFD) methods and was verified by comparison with the experimental data of Wu [1989].

Figure 6.7 compares the experimental velocity distribution, measured in the previous chapter (Figure 5.14), with the velocity distribution calculated using the one-

dimensional model. The profile shown in Figure 5.14 was truncated to remove the entrance effects into the inlet plenum chamber. The momentum correction factor Π was found to be 2.0. Figure 6.8 shows how various terms in the mathematical model affect the velocity distributions in the hydraulic kiln. Figure 6.9 demonstrates the effect of the ratio of the plenum-chamber width to the sum of the widths of the fillets on the velocity distribution across the stack in actual timber kiln.

The following dimensions, which are typical of industrial-scale single-tracked kilns, were used to produce the data presented in Figures 6.9: depth of kiln 12 m; height of stack 3.5 m; width of stack 2.4 m; fillet width 0.02 m; board thickness 0.05 m. The average between-board air velocity was 5 m/s and the air temperature was assumed to be 300 K.

Figure 6.10 shows the effect of stack width on the flow maldistribution across the stack. Single-track kilns have stacks approximately 2.4 m in width. Doubled-track kilns have stacks which are approximately 4.8 m in width. Another term equal to (K_1+K_2) was included in the brackets of Equation (6.62) when the velocity distributions in the double-track kiln was calculated. This term accounted for contraction and expansion of the flow as it crossed from the first track to the second.

One prerequisite for achieving similar flow distributions across the stack in the hydraulic model presented in the previous chapter and a timber stack in an industrial-scale kiln is that the dimensionless pressure drop ($\Delta P / \rho u^2$) over both stacks must be equal. A dimensionless pressure drop of 2.7 can be expected across a timber stack with fillets 20 mm wide, a stack 2.4 m wide, a between-board air velocity of 5 m/s, and an air temperature of 300K (Chapter 5). Due to design limitations, which are discussed in Chapter 5, pressure similarity across the stack in the hydraulic kiln could not be achieved. Figure 6.11 compares the flow distribution that can be expected in a hydraulic kiln in which the pressure similarity condition is obeyed, with the flow distribution in the existing hydraulic kiln. The dimensionless pressure drop is defined by the following expression:

$$P_d = \frac{\Delta P}{\rho u^2} = \frac{2 f_c L_c}{D_{Hc}} \tag{6.73}$$

Contraction and expansion losses are not included in this definition for the dimensionless pressure drop over the stack.

6.2.3 Discussion

Figure 6.7 shows that the agreement between the one-dimensional model and the experimental data is good. Clearly, the coefficients used in the model accurately account for the complex flow patterns that occur at the entrance and exit to the fillet spaces.

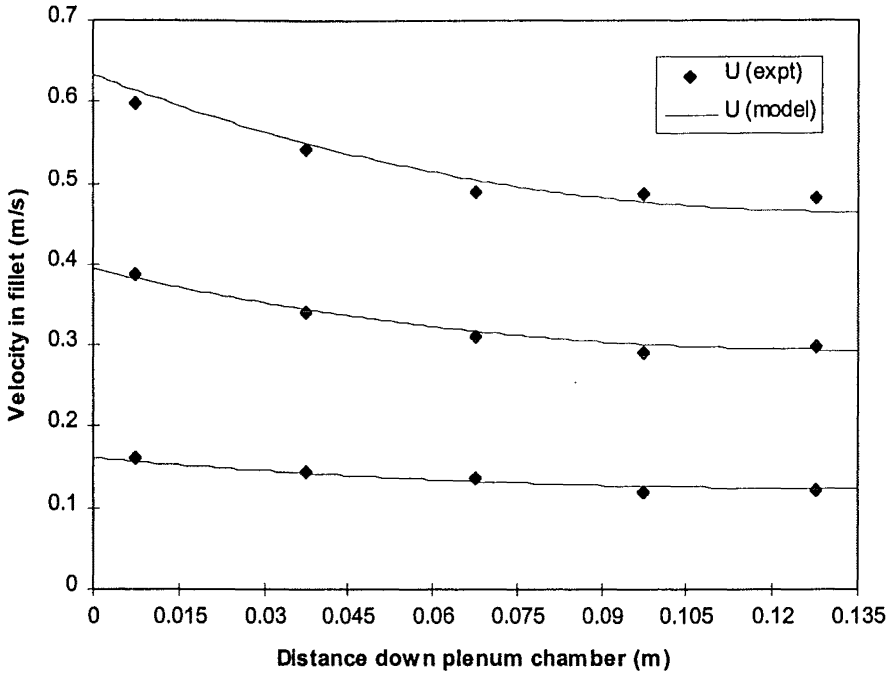

Figure 6.7. Comparison of the theoretical velocity distribution across the stack with experimental data from the hydraulic kiln of Chapter 5.

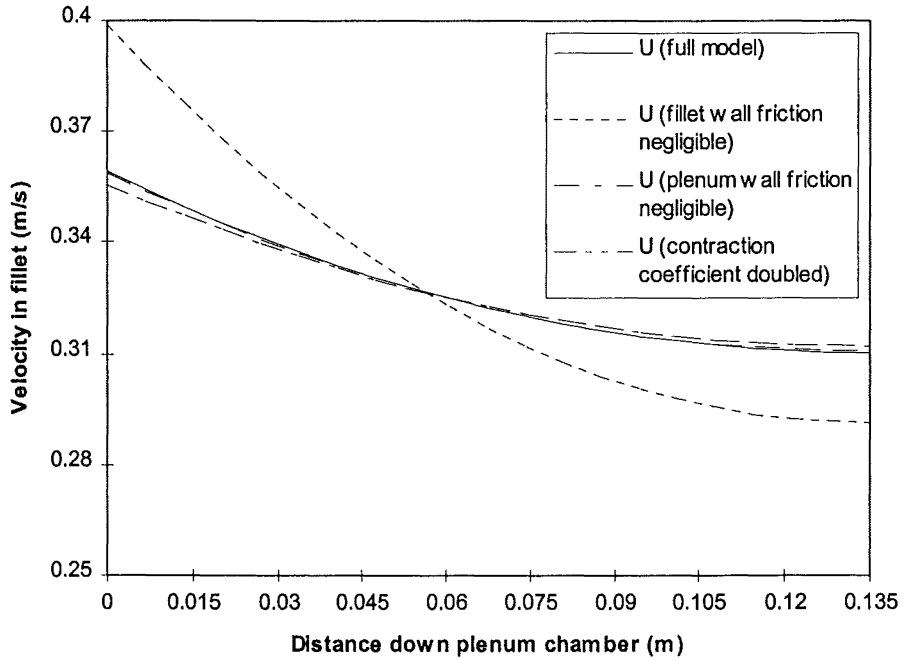

Figure 6.8. Theoretical flow across the stack in the hydraulic kiln: the influence of different terms in the one-dimensional model; ratio of plenum-chamber width to sum of fillet-space widths A_r is unity.

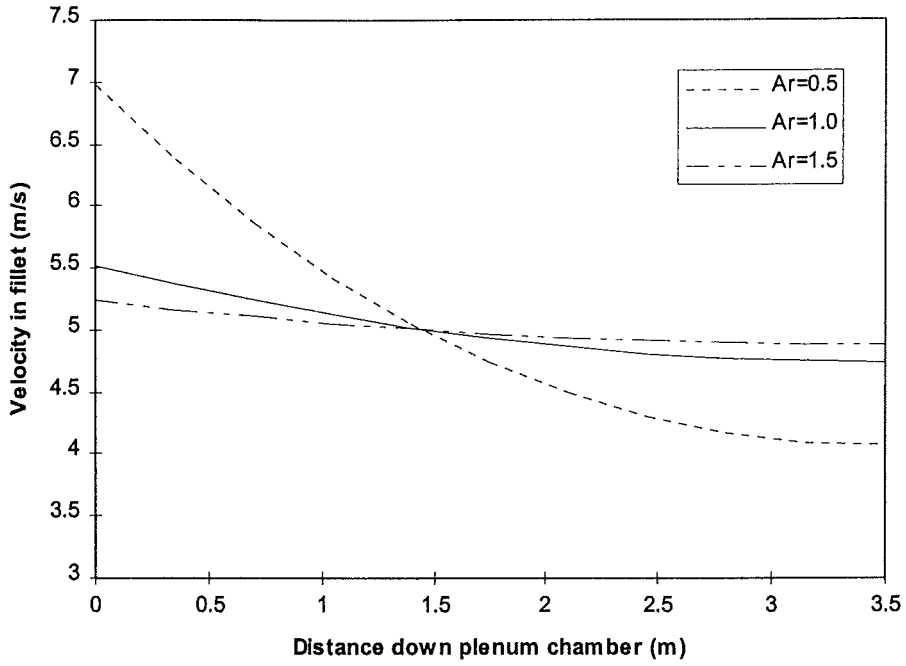

Figure 6.9. Theoretical flow across a stack of timber in a single-track kiln: the influence of A_r, the ratio of the plenum chamber width to the sum of the widths of the fillets, on the flow distribution across the stack

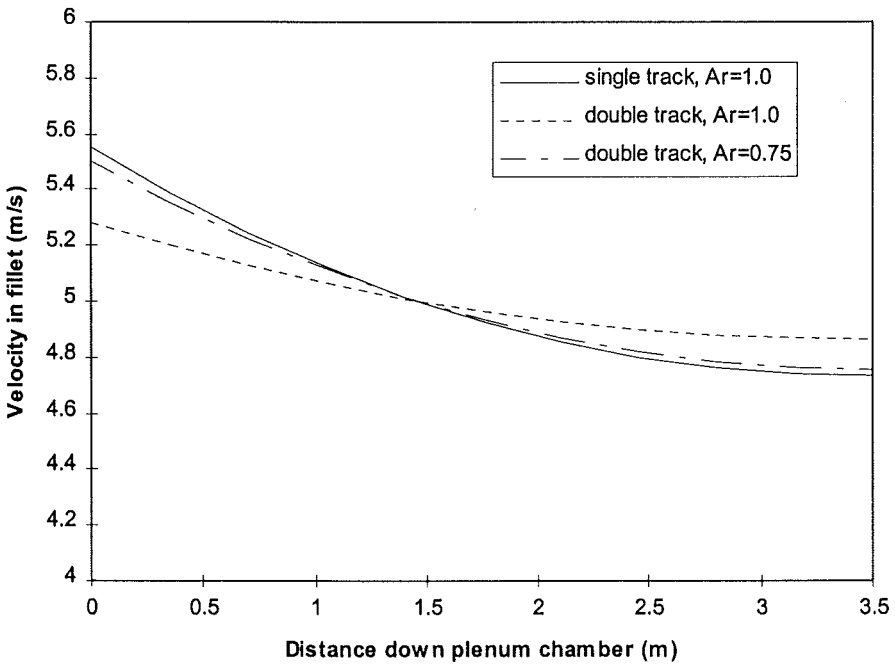

Figure 6.10. Comparison between the theoretical flow across stacks of timber in single and double-track kilns.

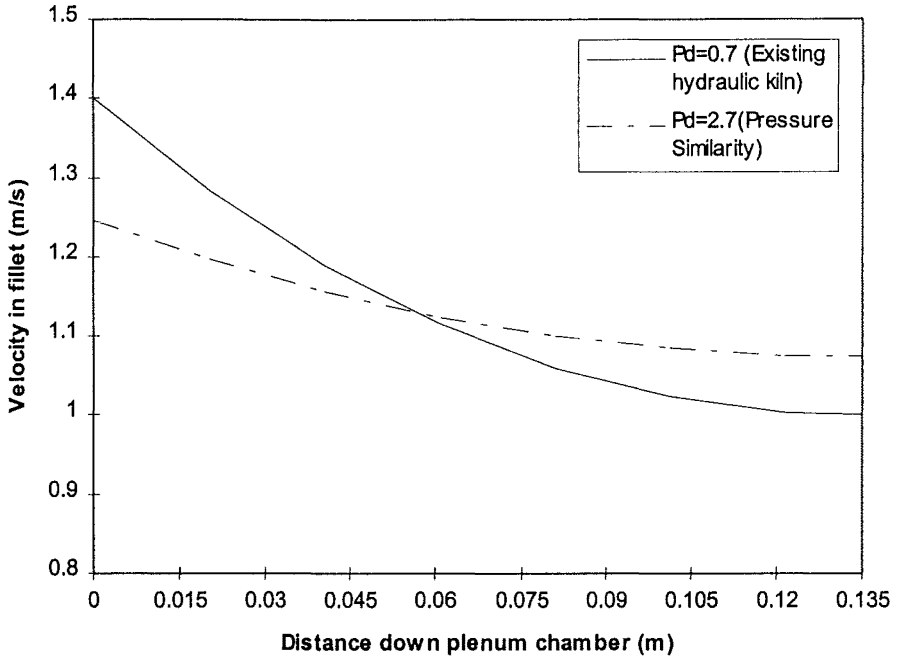

Figure 6.11. The effect of dimensionless pressure drop (P_d) over the stack in the hydraulic kiln on the flow distributions across stack of Perspex boards; equivalent average between-board air speed is 5.0 m/s at 300K; ratio of plenum-chamber width to sum of fillet-space widths A_r is unity.

Figure 6.8 shows that wall friction down the plenum chambers has very little effect on the distribution of flow across the stack for the plenum-chamber configuration tested; however, wall friction along the fillet path has a profound effect. Friction along the fillets, which results from board roughness, and in the case of a timber kiln, gaps between boards and variations in the thicknesses of boards in a particular row, tends to reduce the width of the flow distribution across the stack. Differences in velocities between the fillet spaces would be reduced even further if screens were placed over the inlet and outlet faces. The same effect can be achieved by reducing the fractional area for flow through the stack, for example, by reducing the width of the fillets. However, these solutions will tend to increase the fan power requirement of the fans in a timber kiln.

The contraction coefficient K_1 was not known for lateral branches (in this case, the fillet-space cross-sections) of rectangular cross-section. Therefore, K_1 was set equal to the value for branches with circular cross-section which was found experimentally by Pigford *et al.* [1983]. However, Figure 6.8 shows that the contraction coefficient has very little effect on the flow distribution across the stack in the hydraulic kiln. Clearly, wall friction swamps the frictional losses that occur in the contraction. Therefore, accurate knowledge of the contraction coefficient K_1 is not required.

Figure 6.9 shows that as the ratio A_r of the plenum chamber width to the sum of the widths of the fillets increases, the differences in airflow velocities through the fillet

spaces decrease. Increasing A_r for single-track kilns is only effective when A_r is less than unity and, therefore, very little advantage can be gained from increasing A_r beyond unity. Figure 6.10 shows that in a double-track kiln, A_r may be reduced to 0.75 and achieve a similar flow distribution as the single-track kiln with A_r set to unity. The added resistance through the timber stack of a double-track kiln allows a smaller value for A_r.

Figure 6.11 shows that disobeying the pressure similarity condition in the design of the hydraulic kiln has a significant but not critical effect on the flow distribution across the stack. The flow distribution in the lower half of the stack in the hydraulic kiln will not match closely the distribution in the lower half of the timber stack in an industrial timber kiln. However, the top half of the stack should produce similar distributions since this area is influenced predominantly by the vortex zone rather than the inertial and frictional effects. Dynamic and geometric similarity outside of the stack ensures that the vortex zone in the hydraulic kiln is similar to the vortex zone in an industrial timber kiln. Finally, the conclusion drawn in the previous chapter with the aid of the hydraulic kiln, that the width of the plenum chamber must be greater than or equal to the sum of the fillet space widths to minimise frictional and inertial effects, has been validated in this chapter.

6.3 Conclusions

A minimum entrance length equal to the width of the plenum chamber is required between the right-angled bend and the uppermost fillet space to allow the distribution in velocities across the width of the plenum chamber to become uniform. This entrance length will only remove the influence of flow non-uniformity that results from centrifugal forces induced in the right-angled bend. Longer entrance lengths are required for eliminating the influence of boundary-layer separation that occurs at the corners of a right-angled bend which has not been smoothed sufficiently.

A one-dimensional model for flows in timber drying kilns was calibrated against the experimental data found in the previous chapter. This model was used to develop design criteria for the plenum chambers of kilns with different configurations. It was found that the ratio of the width of the plenum chamber to the sum of the fillet-space widths, and the frictional resistance over the stack are the variables which most significantly affect the flow distribution across the timber stack. Narrow plenum chambers result in severe flow maldistribution across the timber stack. Therefore, it is recommended that, in single-track kilns, the width of the plenum chamber should be at least equal to the sum of the width of the fillets. This recommendation is in accordance with the results found in the previous chapter. In double-track kilns, the width of the plenum chamber should be at least equal to three-quarters of the sum of the fillet-space widths.

6.4 Symbols

A cross-sectional area of plenum chambers, m^2
A' cross-sectional area of control volume available for lateral flow, m^2

b coefficient for Blasius equation
c,d constants
D_H hydraulic diameter, m
f fanning friction factor
h height of ceiling space at inlet to sudden contraction
H total friction loss across stack
k inlet width of right-angled bend (height of ceiling space)
K contraction or expansion coefficient
K,L integration constant
L_c width of stack, m
m strength of source or sink, width of plenum chamber
n coefficient for Blasius equation
P pressure, Pa
r radius in the w plane
t integration variable
u coordinate in the w complex plane (real axis) or lateral velocity, m/s
U inlet veloicity to sudden contraction
v coordinate in the w complex plane (imaginary axis) or velocity in plenum chamber, m/s
V velocity vector or inlet velocity to right-angled bend
$|V|$ speed
$\overline{V}$ average speed
w complex variable, or depth of stack, m
x coordinate in the z complex plane (real axis)
y coordinate in the z complex plane (imaginary axis), or distance down plenum chambers, m
z complex variable

α parameter required for Schwarz-Christoffel tranformation, or momentum correction factor
β variable related to the equipotential function, or fillet friction coefficient
ε fractional area of stack available for flow
Φ complex potential
γ variable related to the stream function, or contraction/expansion coefficient
φ equipotential function
Π overall momentum correction coefficient
θ angle in the w or z plane, or plenum chamber friction coefficient
ρ density of fluid, kg/m^3
υ kinematic viscosity, m^2/s
ψ stream function

6.5 References

Bajura, R.A., Jones, E.H., 1976, Flow distribution manifolds, J. Fluids Engineering, Trans. ASME, 98:654-666.

Conte, S.D., de Boor, C., 1972, Elementary Numerical Analysis: an algorithmic approach, 2nd edition, McGraw-Hill.

Dow, W.M., 1950, The uniform distribution of a fluid flowing through a perforated pipe, J. Applied Mechanics, Trans ASME, 72:431-438.

Hildebrand, F.B., 1976, Advanced calculus for applications, 2nd edition, Prentice-Hall, Inc., Englewood Cliffs, New Jersey

Idelchik, I.E., 1991, Fluid Dynamics of Industrial Equipment: Flow distribution design methods, Hemisphere Publishing Corporation, New York.

Keller, J.D., 1949, The manifold problem, J. Applied Mechanics, Trans. ASME, 16:77-85.

Kröll, K., 1978, Trockner und Trocknungsverfahren, 2nd edition, Springer-Verlag, Berlin, Heidelberg, New York.

Langrish, T.A.G., 1996, *The effects of air bypassing in timber kilns on fan power consumption*, 24th Australian and New Zealand Chemical Engineering Conference (CHEMECA '96), Sydney, 103-108.

Massey, B.S., 1983, Mechanics of fluids, 5th edition, Van Nostrand Reinhold Co. Ltd, UK.

Milne-Thomson, L.M., 1960, Theoretical hydrodynamics, 4th edition, MacMillan & Co. Ltd., London.

Nijdam, J.J., Keey, R.B., 1998, Flow behaviour in timber (lumber) kilns, Proceedings of Industrial Drying Symposium (Greece).

Pigford, R.L., Ashraf, H., Miron, Y.D., 1983, Flow distribution in piping manifolds, Ind. Eng. Chem. Fundam., 22:463-471.

Plapp, J.E., 1968, Engineering Fluid Mechanics, Prentice-Hall, Inc., Englewood Cliffs, New Jersey

Vallentine, H.R., 1959, Applied Hydrodynamics, Butterworths Scientific Publications, London.

Wu, Q., 1989, An investigation of some problems in drying of Tasmanian Eucalypt timbers, M. Eng. Sci. Thesis, University of Tasmania at Hobart.

CHAPTER SEVEN

CONCLUSIONS AND RECOMMENDATIONS

The aim of this thesis was to develop and explore methods for more uniformly drying stacked timber boards in a kiln. In Chapter 1, two different aspects of the overall problem were identified: the *drying problem* and the *external-flow problem*. The *drying problem* deals with the design of kiln schedules that reduce final kiln-wide moisture-content variability. In this thesis, the *drying problem* was investigated by making use of Van Meel's [1958] batch drying equations which allow the overall moisture-transfer process throughout a kiln to be simulated. Thus, the influence of airflow reversals, flow maldistribution, bypass of air around the stack, and air-circulation speed on final moisture-content variability could be studied (Chapter 4). Before this investigation was carried out, the validity of Van Meel's theory was tested by comparing its predictions with the results of a more rigorous drying model. The development and exploration of the rigorous drying model were the focus of Chapters 2 and 3.

The *external-flow problem* is concerned with optimising the geometry of the kiln to reduce the degree of flow maldistribution across the inlet face of the timber stack and hence reduce the variability in final kiln-wide moisture contents. In Chapter 5, a hydraulic kiln was designed to determine the influence of various kiln configurations on the degree of flow maldistribution across the stack. A theoretical approach was taken in Chapter 6 in which mathematical flow models were used to optimise the geometry of the kiln.

Overall, this thesis has uncovered various methods for reducing the variability in the moisture content of kiln-dried timber. In this chapter, the achievements of the project will be summarised and directions for future research suggested.

7.1 The Drying Problem

In Chapter 2, one-dimensional heat and moisture transfer within a timber board was analysed by developing a comprehensive drying model based on Whitaker's [1977] volume-averaged drying equations. The drying model took into account effects such as bordered-pit aspiration, cell-wall shrinkage, and the hygroscopic nature of timber below fibre saturation. The drying of *Pinus radiata* timber was simulated because this species is of commercial importance in New Zealand.

It was argued that significant overpressures do not build up within *Pinus radiata* timber since it is very permeable compared with other softwood timbers. This simplified the analysis since the convective gaseous terms in the transport equations could be neglected. Correlations for the permeability and attenuation factor were derived from experimental data found in the literature. The permeability correlation showed that a large proportion of the pits aspirate near the green condition of the

timber. The attenuation of moisture movement below fibre saturation showed that progressive shrinkage of the cell wall as moisture is lost has a significant effect on the rate of diffusion of vapour through the woody substance. The diffusion data of Luikov [1966] indicated that moisture movement occurs between irreducible saturation, when liquid continuity ceases, and fibre saturation. By a process of elimination, it was suggested that a liquid 'diffusive' flux is the mechanism responsible for moisture transport within this range of moisture contents. Liquid water 'diffuses' either through any small-pore structure in the cell wall or by surface diffusion on the inside of the cell walls.

The computed results from the one-dimensional drying model agreed well with the experimental data of Pang [1994] despite the fact that heterogeneities in the timber were not accounted for, and that two-dimensional effects were shown to be significant, especially in the early stages of drying. However, the vapour-flux model in the dry zone tended to under-predict the surface moisture content, and was responsible for the surface temperature rising too quickly during the warming-up period. Thus, the vapour-flux model does not accurately describe the vapour-transport mechanism. However, employing a variable attenuation factor in the vapour-flux model clearly improved the accuracy of the simulation.

In Chapter 3, the one-dimensional drying model presented in Chapter 2 was extended to two dimensions and coupled with a turbulent flow model via interfacial continuity equations. The resultant set of equations formed a rigorous batch-drying model whose purpose was to test the validity of various assumptions made in the development of Van Meel's batch-drying model.

The most significant assumption associated with Van Meel's model is that the characteristic drying curve is independent of the external flow conditions. It was shown in Chapter 3 that the critical moisture content takes on a higher value for the first two or three boards from the leading edge and is almost constant for the remaining boards. This trend was attributed to the enhanced average transfer coefficients over the leading boards. The critical moisture content also rises with increasing air velocity because the transfer coefficients correspondingly increase; however, the rise in the critical point is very slight even for a large increase in the transfer coefficients. In addition, it was shown that the critical moisture content does not vary appreciably over the range of temperatures and humidities tested. Thus, the assumption that the characteristic drying curve is independent of the external conditions is valid over the range of conditions tested, except near the leading edge where the concept of the characteristic drying curve breaks down.

Two important results came out of this investigation. Firstly, it was shown that the characteristic drying curve is a strong function of the thickness of the timber board. Therefore, the characteristic drying curve used in Van Meel's model must be derived from timber of the same thickness as the timber which is being simulated. Secondly, it was shown that the two-dimensional drying behaviour of timber affects the magnitude of the critical moisture content. Enhanced drying rates over the leading portion of each board can cause the evaporative front to begin receding at the leading edge before it recedes at the trailing edge. In addition, kiln-stacking arrangements should be considered when conducting single-board tests in the laboratory. Comparisons between the results of the rigorous-drying model and the data of Pang [1994] suggest

that single-board tests produce more severe two-dimensional drying conditions than actually exist in a typical timber stack.

The results from the rigorous drying model and Van Meel's drying model compared well, especially when the variations in the mass-transfer coefficient with distance from the leading edge are taken into account. One difficulty with the simple model is that the surface humidity during the constant-rate period must be known in order to predict the kiln-wide drying behaviour. In timber, this surface humidity may not necessarily correspond to the saturation humidity at the given wet-bulb temperature. In fact, the presence of the thin-dry layer near the surface of the timber board ensures that the surface humidity is considerably less than the saturation humidity. In this thesis, it was assumed that the surface humidity used in Van Meel's model was equal to the saturation humidity at the wet-bulb temperature. This assumption does not affect the general trends observed.

Van Meel's batch drying model was used in Chapter 4 to model the kiln-wide drying behaviour of stacked *Pinus radiata* timber boards. The effects of flow maldistribution, progressive humidification of air through the stack, and bypass of air around the stack were investigated. Increasing the airflow rate sufficiently can mitigate the effect of flow maldistribution on final moisture content variability, provided that the range in fillet-space velocities across the stack does not widen significantly. It was shown that one well-timed airflow reversal can smooth the moisture content distribution as effectively as a number of reversals. The analysis illustrated the importance of eliminating paths for bypass of air around the stack.

7.2 The External-Flow Problem

In Chapter 5, it was shown that a significant contribution to flow maldistribution across the inlet face of a timber stack is the vortex zone generated by the sharp right-angled bend from the ceiling space, where the fan is located, into the inlet plenum chamber. Increasing the width of the plenum chamber reduces to a certain extent the effect of the vortex zone. However, the most effective method for controlling the vortex zone is rounding the sharp edges off the right-angled bend. A round-section with a radius equal to one-fifth of the ceiling space height, placed within the ceiling space at the corner of the right-angled bend, will remove the vortex zone completely, provided that the height of the ceiling space at the apex of the round-section is at least equal to the width of the plenum chamber.

Frictional and inertial effects down the height of the ceiling-space are also responsible for flow maldistribution across the inlet face of the stack. The results from a mathematical model developed in Chapter 6 showed that frictional and inertial effects are mitigated by ensuring that the width of the plenum chamber is at least equal to the sum of the fillet-space widths. It was also shown that an entrance length between the right-angled bend and the uppermost fillet space equal to the width of the inlet plenum chamber should be effective in narrowing the distribution of velocities downstream of a smooth right-angled bend, which are caused by centrifugal forces through the bend.

7.3 Recommendations

One recommendation for future work is to investigate in greater detail the mechanism for vapour transport below fibre saturation with the aim of improving the vapour-flux model. This could be initiated by repeating the work done by Choong [1963] for western fir (*Abies* sp.), except for *Pinus radiata* timber. Choong [1963] measured the steady-state temperature and moisture-content profiles in a timber board with fixed temperatures at opposite faces of the board. This enabled gradients in temperature, moisture content, and vapour pressure with respect to distance to be determined. These gradients form the building blocks of vapour and bound-moisture flux models. In addition, the extent of convective flow of gas inside the timber boards should be investigated more closely by including the gaseous convective expressions in the drying model, solving the resultant differential equations, and comparing the magnitude of the convective and diffusive fluxes.

Further work could be done to mathematically model the stress development within the timber board during drying. This model could then be used to assess kiln-schedules by evaluating the risk of stress-related degrade.

Attempts were made in Chapter 3 to rationalise the observations made, in particular with regards to the discontinuity that occurs in the results from the drying model and the trends in the transfer coefficients with time and distance along the fillet-space and their effect on the critical moisture content. It is recommended that, at a future date, these observations and rationalisations are scrutinised in more depth. A useful extension to the work covered in Chapter 3 would be simulate the drying of timber under lower temperature drying conditions, such as the accelerated conventional temperature schedules, thereby avoiding the problem associated with the upper limit of the boiling point placed on the wet-zone temperature. Furthermore, it would also be useful to switch from the high-Reynolds number turbulence model to a low-Reynolds number turbulence model so that the drying process can be modelled at air velocities between 5 and 10 m/s, which are typical of kiln operations in New Zealand.

The main supposition that the characteristic drying curve is independent of the external temperature and humidity has not been rigorously demonstrated in this thesis. Due to limitations with the high-Reynolds number turbulence model, and the great computational effort required in the numerical calculations, the air velocity between the boards and the width of the stack were set to 15 m/s and 1 m, respectively. Greater temperature and humidity variations than calculated in this thesis may be expected in practice due to lower velocities and wider timber stacks. It is recommended that the validity of the characteristic drying curve be tested over a greater range of external conditions and for wider timber stacks in the future.

It would be helpful to improve the hydraulic kiln design to make it more geometrically similar to industrial-scale kilns. The flow distributions extracted from the hydraulic kiln would then be more similar to the flow distributions that can be expected from an industrial-scale kiln. Any advances made in the hydraulic kiln for reducing flow maldistribution across the stack can then be applied directly to a timber kiln.

Finally, it is recommended that the experimental data from the hydraulic kiln be used to validate Computational Fluid Dynamics (CFD) calculations of the airflow in kilns of improved geometry. The CFD approach is particularly attractive since considerably less effort is required to obtain quantitative data about the airflow patterns in kilns.

7.4 References

Choong, E.T., 1963, Movement of moisture through a softwood in the hygroscopic range, *Forest Products Journal*, 13 (11): 489-498.

Luikov, A.V., 1966, Heat and mass transfer in capillary-porous bodies, Pergamon Press, Oxford.

Pang, S., 1994, High-temperature drying of *Pinus radiata* boards in a batch kiln. PhD Thesis, University of Canterbury, New Zealand.

Van Meel, D.A., 1958, Adiabatic Convection Batch Drying with Recirculation of Air, *Chem. Eng. Sci.* Vol 9, 36-44.

Whitaker, S., 1985, Moisture transport mechanisms during the drying of granular porous media, Drying '85 edited by Mujumdar, A.S., Hemisphere Publishing Corporation, New York, 21-32.